Journal of Healthcare Engineering

Big Data Intelligence in Healthcare Applications Based on Physiological Signals

Lead Guest Editor: Liang Zou
Guest Editors: Han Yu, Liang Zhao, and Yu Zhang

Big Data Intelligence in Healthcare Applications Based on Physiological Signals

Journal of Healthcare Engineering

Big Data Intelligence in Healthcare Applications Based on Physiological Signals

Lead Guest Editor: Liang Zou
Guest Editors: Han Yu, Liang Zhao, and Yu Zhang

Contents

G-Causality Brain Connectivity Differences of Finger Movements between Motor Execution and Motor Imagery

Chao Chen, Jiaxin Zhang, Abdelkader Nasreddine Belkacem, Shanting Zhang, Rui Xu, Bin Hao, Qiang Gao, Duk Shin, Changming Wang, and Dong Ming

Research Article (12 pages), Article ID 5068283, Volume 2019 (2019)

Hindawi
Journal of Healthcare Engineering
Volume 2020, Article ID 7963497, 18 pages
https://doi.org/10.1155/2020/7963497

Research Article

BMIVPOT, a Fully Automated Version of the Intravenous Pole: Simulation, Design, and Evaluation

Abbas Sayed-Kassem,[1] Nancy Kozah,[1] Georges Hajj-Moussa,[1] Reem Harb,[2] and Amira J. Zaylaa[3,4,5]

[1]*School of Engineering, Lebanese International University, Beqaa, Lebanon*
[2]*Galien Medical Services Company, Hazmiyeh, Lebanon*
[3]*Department of Electrical and Computer Engineering, Faculty of Engineering, Beirut Arab University, Beirut, Lebanon*
[4]*Neuroscience Research Center, Faculty of Medical Sciences, Lebanese University, Beirut, Lebanon*
[5]*Faculty of Public Health-I-V, Lebanese University, Beirut, Lebanon*

Correspondence should be addressed to Amira J. Zaylaa; amirazaylaa@gmail.com

Received 14 August 2019; Accepted 12 February 2020; Published 11 August 2020

Guest Editor: Han Yu

Robotic intravenous poles are automated supportive instrument that needs to be triggered by patients to hold medications and needed supplies. Healthcare engineering of robotic intravenous poles is advancing in order to improve the quality of health services to patients worldwide. Existing intravenous poles in the market were supportive to patients, yet they constrained their movement, consumed the time of both the patient and the nurse, and they were expensive in regard to what they offer. Although robotic poles overcame some of the movement limitations of the commercial/market poles, they were partially automated and did not offer additional technological features. The aim of our work was to develop a fully automated Biomedical Intravenous Pole Robot (BMIVPOT) to resolve the aforementioned limitations and to offer new technological features to intravenous poles, thereby promoting the health services. Several sensors and build-up materials were empirically chosen to be cost-effective and fulfill our needs. The new prototype was divided into three steps: simulated prototype, real implementation of the prototype, and testing and evaluation. Simulation results showed the best qualitative way to fit all the specifications in the robotic system, such as the shape, sensors, and connections in order to provide the proper functionality of the system. Experimental and real results provided the manufactured parts, implemented sensors, and the final robot. Testing the tracking and the flow sensor performances were provided. Evaluation of our Biomedical Intravenous Pole Robot with alternatives showed that our robot outperforms the other poles in many aspects including the features it offers, the percentage of interventions it comprised, the reliability, and cost-effectiveness. The overall percentage of features offered by our Biomedical Intravenous Pole Robot was 60% higher than that offered by peer research poles and 80% higher than that of the market poles. In addition, the average percentage of integration of interventions (architecture, sensor, wireless, tracking, and mechanical) in the Biomedical Intravenous Pole Robot was at least 56% higher than that of the alternative poles. According to the results, Biomedical Intravenous Pole Robot offers a cost-effective price as compared to the others. As a future prospect, we intend to add more features to this prototype in order to enhance it, such as vital signs detection, and improve the tracking system.

1. Introduction

Robotic intravenous (IV) poles are medical supportive instruments under research that could be partially automated and could hold IV medications to patients in an advanced way [1–3]. With the introduction of research IV poles, such as the so-called autonomous IV poles [1], and the robotic IV pole or novel robotic IV pole [2], some improvement to the commercial/market designs has occurred. The enhancement was centered on the IV poles' field of movement. In the autonomous IV pole designed by Binger et al., the so-called autonomous motion was achieved by the attachment of a nylon twine between the patient and the robotic system [1], while in the preliminary robotic IV pole designed by Sayed-Kassem et al., the automated motion was achieved via a joystick controlled by the patient [2, 3]. According to the

survey results showing the benefits of the robotic IV poles from the nurses, patients, and human resources points of view, there was a common agreement on the advantage of the robotic IV pole, which was designed to improve the comfort, cost, and feasibility. The majority of nurses (87.55%), patients (94.60%), and human resources (84%) agreed on the health benefits of the robotic IV pole as shown in Figure 1. Pertaining to the financial benefits of the robotic IV pole, 61.79% of nurses, 88.45% of patients, and 67.50% of human resources agreed on its reasonable price, while the additional benefits exhibited the higher percentage of agreement from patients (93.26%), nurses (91.66%), and human resources (83%), respectively [2].

Despite the survey and the enhancement related to the movement of research IV poles, the motion was not fully automated, and the problems of nurses' time consumption and sensors' lack were not solved completely. By comparing their presented features and their cost, the partially automated IV pole costs around $2000 [1], and the robotic IV pole costs around $300 [2]. Furthermore, the robotic IV poles were considered somehow costly as opposed to market poles [2].

Based on what preceded, the aim of our project was to design a new fully automated prototype for what we named a BioMedical IntraVenous Pole Robot (BMIVPOT). We hypothesize that BMIVPOT enhances the healthcare service to patients in hospitals and medical centers through its new, fully automated, user-friendly, and reasonably priced prototype. Our aim is to (i) improve the tracking system which provides the automated movement of the robot, (ii) enhance the detection of the saline's level, (iii) add new sensors to detect blood leakage in the IV tube, the saline's flow and thus increase the safety of the robot.

Our paper showcased the workflow for building the different parts of the fully automated system. The workflow comprised three main parts: simulation, hardware (combining system parts), and the testing and evaluation steps. The simulation of the system was implemented according to the AutoCAD drawings, which permit the visualization of the different building blocks of the full design. On the other hand, the real construction and hardware included the combination of the materials involved in the development of BMIVPOT. Moreover, the testing and evaluation of the performance and the cost-effectiveness of our prototype was revealed through the graphs and through comparing BMIVPOT to the existing designs and standards.

The remainder of this paper is organized as follows. In Section 2, the types of IV poles existing in the literature were provided. In Section 3, the BMIVPOT's materials and methods were introduced. In Section 4, the prototype's implementation was reported. In Section 5, the three types of results, simulation, real, and testing and evaluation results, were presented. In Section 6, the aforementioned results were discussed, and in Section 7, a general conclusion and future work were provided.

2. Existing Robotic Intravenous (IV) Poles

After our thorough review and research on the existing IV poles/stands, these stands can be divided into two main categories: the research IV poles and the IV poles present in the market (shortly market poles). The research IV poles were divided into two, the autonomous IV stand [1] and the robotic IV stand [2], while the market/commercial IV poles were divided into several designs, including, but not limited to, the ambulatory patient support stand [4], Homecare IV stand [5], hanging IV pole [6], Brewer stands [7], and Dyaun IV stand [8, 9] as shown in Figures 2(a)–2(g). The market IV poles are shown in Figures 2(a)–2(e), while research poles are shown in Figures 2(f) and 2(g).

2.1. IV Poles in Research. The common research IV pole designs are the autonomous IV stand developed by Binger et al. [1] and the robotic IV stand developed by Sayed-Kassem et al. [2, 3]. These two poles that were used in research are shown in Figures 2(f) and 2(g), respectively.

The autonomous IV stand allows mobile medicine delivery without the need for the patient to maneuver the system [1]. However, in the latter design the patient is tethered to the device via a nylon twine attached to a gait belt that the patient has to wear around the waist. The position of the patient and the angle of measurement are produced by two encoders: the potentiometer and the rotary encoder shaft [1].

Furthermore, the robotic IV pole allows the patient to move the stand using a joystick and releases an alarm whenever the IV bag is emptied [2]. However, the movement of this device depends mainly on the Radio Frequency (RF) communication between the controller (joystick) and the robotic base. This was achieved by sending commands to three Direct Current (DC) motors triggering three omni wheels, thereby controlling the translation and rotation of the robot. The emptiness of the IV bag was detected using a photodiode placed at the lower end of the IV bag [2].

2.2. IV Poles in the Market. Market/commercial IV poles are the most common poles used nowadays; they comprise a stand, wheeled base, and hooks assembled side by side, so that the hooks are attached to the top of the stand and the wheeled base is attached to its bottom [4]. These IV poles can be differentiated according to the added features. Ambulatory patient support, shown in Figure 2(a), is a stand associated with a horizontal support handle which aids in moving the stand feasibly. By pushing the pole while holding the handle, the patient exerts less force as opposed to the usual forces applied to push an ordinary IV pole [5] as shown in Figure 2(a). Homecare IV stand, shown in Figure 2(b), is designed by ensuring the center of mass at its base (bottom part), which is attached to two back supportive wheels and two front casters [5]. The latter design provides an easy assembly and disassembly of the device and allows the adjustment of the elevation of the IV bag depending on the patient's height [5]. Moreover, the hanging IV pole, shown in Figure 2(c), is a pole attached to the roof directly above the patient's bed. A drawback of such an IV stand is that it does not permit the patient to maneuver the pole; someone has to always hold the IV bag [6]. Besides, the Brewer stand, shown in Figure 2(d), is a free-standing

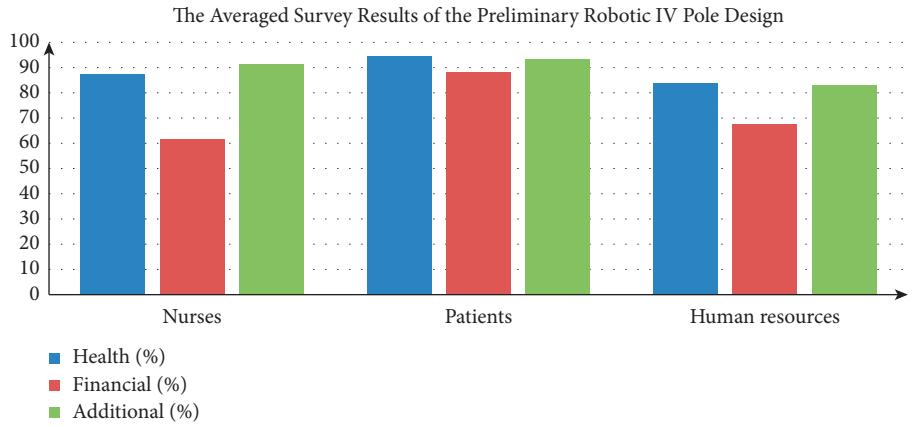

Figure 1: The averaged survey results of the preliminary robotic IV pole design [2].

Figure 2: Different intravenous (IV) stands available in the market (top) and in research (bottom). (a) Ambulatory patient support stand [4]. (b) Homecare IV stand [5]. (c) Hanging IV pole [6]. (d) The simple free-standing pole [7]. (e) Dyaun IV stand [9]. (f) Autonomous IV pole [1]. (g) Robotic IV pole [2].

mobile pole which includes improvement in hangers, accessories, and the adjustment of the stand's height. The primary difference of the Brewer stand as opposed to Figures 2(a)–2(c) is in the design of the base and the number of wheels included. A more advanced free-standing IV pole is the Dyaun IV pole, shown in Figure 2(e); however, it is no longer utilized nowadays [8, 9].

Both the advantages and drawbacks/disadvantages of the IV poles existing in the market and in research were provided in Table 1. The drawbacks reported for the existing poles were centered on its cost, the space it occupies, how it is maneuvered, and the absence of crucial features. Thereby, these reported drawbacks triggered the development of the fully automated BMIVPOT.

3. Biomedical Intravenous Pole Robot (BMIVPOT)

The materials used to develop the novel prototype of the robotic IV pole, i.e., BMIVPOT, were provided. The framework of this design is shown in Figure 3. The tracking system is composed of the camera, the TAG, and the controller of the image processing. The tracking system then drove four DC motors allowing the automated movement of the system. Moreover, the sensors of the saline level and blood leak detectors were implemented on the IV stand, and the parameters measured were displayed on an LCD screen. The measured results were planned to be sent wirelessly to the medical staff allowing them to monitor these parameters and control the flow. In addition to the emergency system, the DC motor was attached to four caster wheels to work traditionally when needed.

3.1. BMIVPOT Materials. The materials needed for the implementation of BMIVPOT prototype were selected to achieve the fully automated tracking and to provide new features. Noteworthily, the new features are the detected flow rate, detected blood leak, detected volume, detected obstacle, emergency alarm, linear velocity of BMIVPOT, angular velocity of BMIVPOT, and the distance covered by the BMIVPOT. These materials are listed as follows:

(i) The choice of the architecture materials was based mainly on both the material's weight and availability as compared to several designs. According to Figure 3, the architecture of the BMIVPOT comprised the IV stand, camera, and base. The Plexiglas material was employed due to its common availability, its hygienic property, ease of cleaning, and its cost-effectiveness [10].

(ii) The sensor materials were as follows:

(a) A load cell was used to detect the saline's level and thus volume, connected to a load cell amplifier module (HX711) [11] as shown in Figure 3.

(b) The blood leak detector and the flowmeter were Infrared Light-Emitting Diode (IR-LED) and photodetector, respectively [12].

(c) HC-SR04 ultrasonic sensor was used as an obstacle detector [13, 14].

(d) I2C 16×2 Arduino Liquid Crystal Display (LCD) module [15] was used to display the different detected and measured parameters.

(iii) The wireless materials included the use of the Wi-Fi NodeMCU shield which was used due to its feasibility and ability to send an analog signal and several digital signals [16, 17].

(iv) The patient's tracking materials were as follows:

(a) The Raspberry Pi 3 was used due to its capability in running multiple programs simultaneously and performing image processing at a reasonable pace [18, 19].

(b) An 8-megapixel camera module V2 was employed due to its compatibility with the Raspberry Pi 3 [20]. Thereby, this camera system could recognize the unique TAG, placed on the patient, at larger distances [21], while ensuring the security of each patient through the unique TAG.

(c) The TAG used was a square-colored image with a yellow background and red foreground as shown in the model in Figure 4. In order to obtain a unique identification of the patient, the camera was implemented to focus on the aforementioned image. Moreover, each side of the square in the TAG/image was 15 cm. The simple scenario of tracking the target was shown in Figure 4 through a direct straight line. Regardless of the scenario of tracking whether simple or complex, BMIVPOT was planned to maintain a safe distance between its boundaries and any obstacle present within its safety distance (D_{safety}). Also, the robot was planned to maintain the followed target's center of mass within its Field of View (FOV). BMIVPOT was also planned to maintain the target between the distance $d_{\min}$ and $d_{\max}$ in order to keep the target (patient) safe in the presence of static obstacles.

(v) The mechanical materials were as follows:

(a) The flow control system was composed of a stepper motor (controlled by a DRV8825 motor driver), screw, and bolt [22]. The stepper motor was controlled by DRV8825 motor driver. The hybrid stepper motor was selected due to its high holding torque and low power consumption [23, 24].

(b) Four DC motors were placed in the base and connected to four Mecanum wheels in order to provide a smooth movement associated with all the degrees of freedom [25–27]. The high torque DC geared motor was selected due to its high holding torque and low power consumption [28, 29]. In addition, two relay modules were

Table 1: The advantages and disadvantages of the IV poles existing both in research and in the market.

IV pole types	Method	Advantages	Disadvantages
Research IV poles	Autonomous IV stand	Automated movement	High cost (>2000); complex design; no wireless communication between the nurse and the IV pole; can carry only one IV bag, i.e., can withstand a low weight; consumes a lot of power
	Novel robotic IV pole	Semiautomated movement; saline sensor and alarm; can carry several IV bags; can be manually controlled	Needs patient training; not accurate sensing; no obstacle detection; power consuming
Commercial IV poles	Ambulatory patient support stand	Stable; resembles the walker; helpful for patients with walking difficulties	Occupies a lot of space
	Homecare IV stand	Easy assembly and disassembly; lightweight	Low load capacity, i.e., can hold slight weight merely
	Hanging IV pole	Occupies lower space; low probability of transporting bacteria	Limited mobility area; requires nurse assistance; absence of a place to attach a medical equipment
	Brewer stand	Simple design; high strength; high system stability; smooth movement; most popular	Limited mobility of patients; requires nurse assistance
	Dyaun IV stand	Brake on the wheels	Unstable design

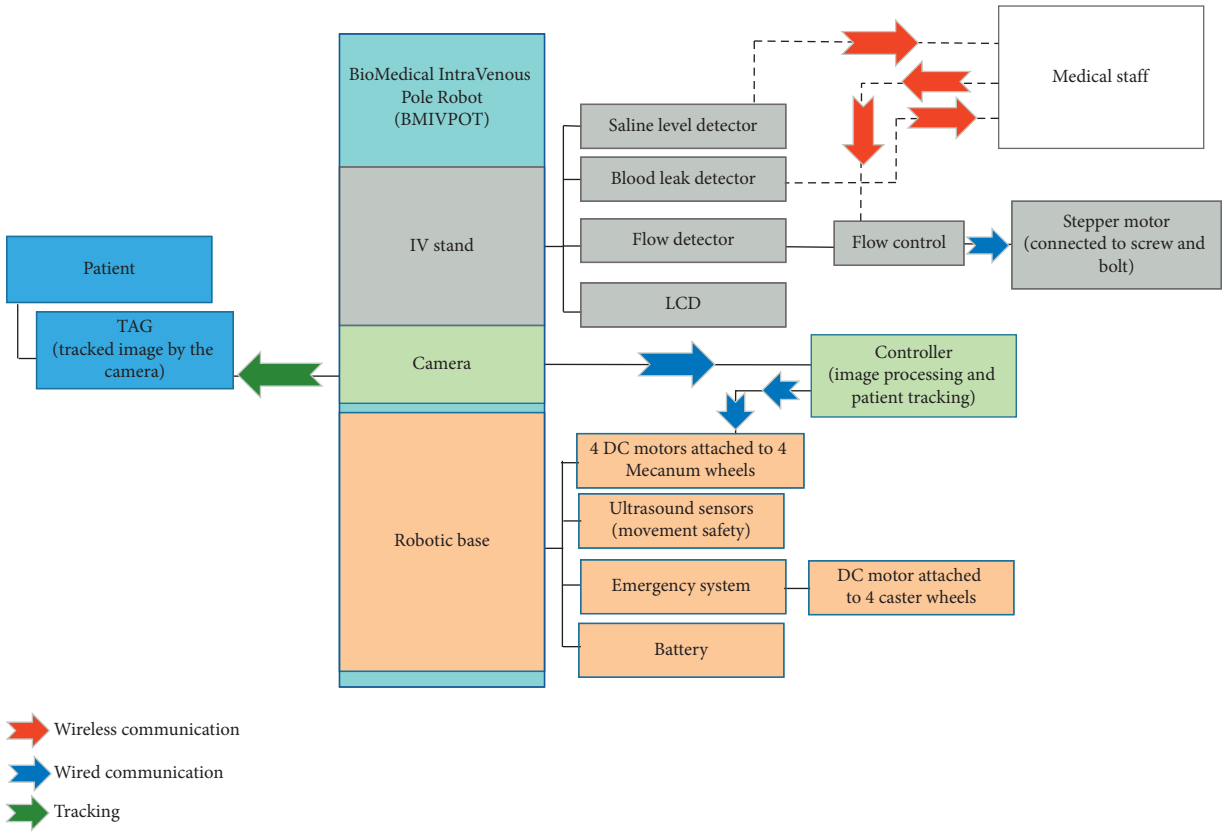

Figure 3: The block diagram of the Biomedical Intravenous Robot (BMIVPOT).

employed to provide the correct voltage polarity to the DC motors.

(c) The Arduino UNO was used to control the DC motors.

(d) Another DC motor [28, 30] and four caster wheels were used to form the emergency system.

3.2. BMIVPOT Development Method. In order to develop the BMIVPOT, first a simulation of the prototype was carried out using AutoCAD; then the real prototype construction was achieved. The interventions that we have done to provide the new fully automated BMIVPOT were divided into architecture (related to the shape), electronic (choice of sensors), mechanical (flow rate detection), communication (related to the Wi-Fi technology), and the tracking intervention.

3.2.1. Simulation Method. The AutoCAD simulated drawings were used to showcase the architecture intervention

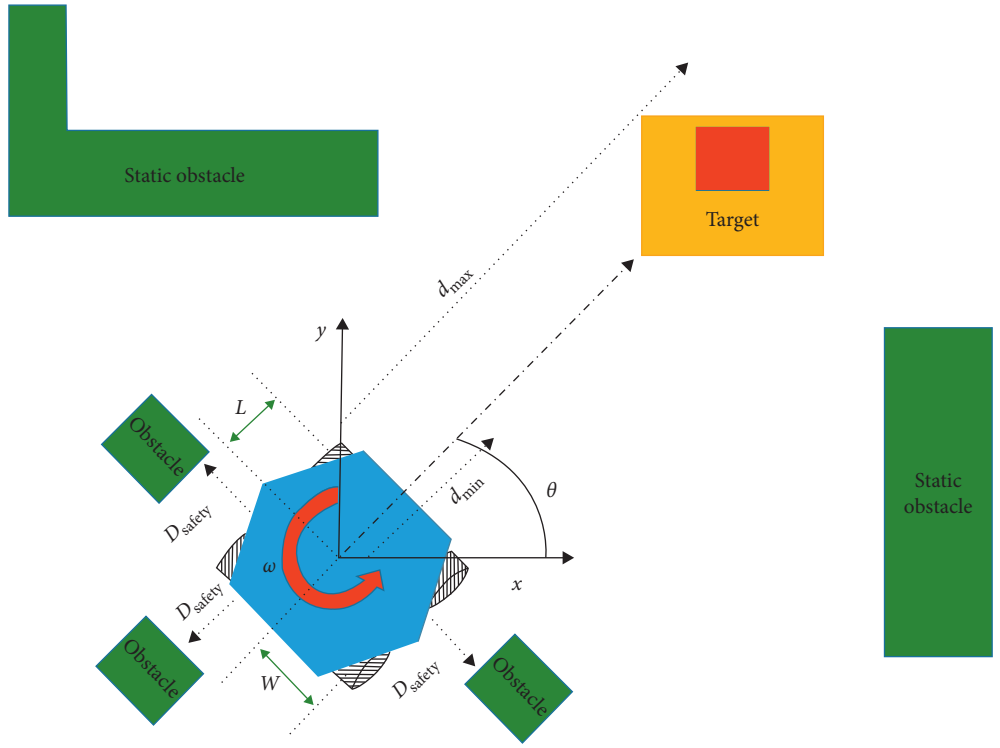

Figure 4: Model of the BMIVPOT, target distance, and TAG.

revealing the different geometric aspects of the design. The architecture of the prototype was mainly composed of the base and stand. The shape of the base was chosen to be surface efficient; the whole surface was used and filled with electronics. A large surface was required to realize the electronics. Therefore, according to the empirical inference [31], the octagonal shape, having a side of $a = 27.1$ cm and an area of $A = 2(1 + \sqrt{2})a^2 = 3540.81\,\text{cm}^2$ was the best design. This shape solved the trade-off between conserving a large surface and reducing the weight. The BMIVPOT's stand was planned to have a square shape in order to place the required objects on it as shown in the studies of Hajj-Moussa et al. and Kozah et al. [31–33].

Concerning the architecture intervention, it comprised the AutoCAD simulation steps needed to plan for the construction of the real BMIVPOT. The other interventions provided specific functions to the system; the assembly and the connection between all the materials are shown in Figure 3.

3.2.2. Real Prototype Method. The real construction method of BMIVPOT was based on the overall design (architecture), sensors, wireless communication, patient's tracking, mechanical, and healthcare communication services. To achieve the architecture intervention, apply the following:

(i) Use a total Plexiglas volume of $5.019296 \times 10^{-3} \cdot \text{m}^3$ and thus a base of overall weight of 5.9 kg according to $W = \rho V$, with $\rho_{\text{plexi}} = 1180\,\text{kg/m}^3$. Choose the stand to be aluminum with thin thickness.

Regarding the sensor's consideration,

(i) Measure the saline's weight to calculate the volume.

(ii) Detect the saline's droplet using the flow meter.

(iii) Count the droplet when it passes between the IR emitter and the receiver, through calculating the change in intensity values detected by the receiver.

(iv) Compute the flow rate by considering the number of drops per minute.

(v) Place the tube near the IV insertion in the blood detector system, in order to detect any backflow of blood from the patient's vein to the tube.

(vi) Detect the blood leakage when the intensity drop is recorded by the phototransistor, give an alarm, and send a notification to the nurse.

(vii) Place the ultrasound (US) sensors on the four sides of the base in order to detect at least obstacles at 10 cm away from the base and to provide more security to the system.

(viii) Display the parameters measured (flow volume, time) on an LCD screen connected to the main controller.

Regarding the wireless intervention,

(i) Integrate Wi-Fi shields on the volume detector, the flow meter, the blood leak detector, and the flow control system.

(ii) Provide the detected and calculated parameters (the volume and the flow of the saline) and the blood leakage on the cellphone of the nurses. Thereby, they could monitor and control the saline's flow.

Pertaining to the patient's tracking,

(i) Attach the chosen camera to the IV pole in order to track the patient's movement by TAG recognition. Recall that the TAG was a simple small image printed on the back of the patient's costume. The TAG has the shape of a square of side (b = 15 cm).

(ii) Take into consideration that the distance interval has to be maintained between the TAG and the camera based on the forthcoming calculations:

(a) Identify the TAG by taking 492 pixels/m as an assumption. This resolution was used for the identification of unknown faces in forensic applications.

(b) Calculate the FOV of the camera according to the study of Hajj-Moussa et al. [31].

(c) Calculate the maximum distance to get the FOV through the right triangle shown in Figure 5. The opposite side of the right triangle is FOV/2, and the angle (X) is half of the angle of the camera's lens. Thereby, the hypotenuse (H) is the distance taken from the camera's lens in order to ensure that the desired FOV is equal to 6.4533 m, where the desired horizontal FOV value was 6.67 m. The calculation was based on Figure 5 and the following equations:

$$\text{Radius: } R = \frac{C}{2\pi}, \tag{1}$$

where C is the circumference of the circle.

$$\text{Circumference: } C = S(360A), \tag{2}$$

where S was the approximated segment of the circle, R was the radius (the FOV), and A was the angle.

(d) Concerning the vertical FOV, repeat the same calculation by setting FOV at 5 m, the radius at 5.87, and the distance at 6 m, based on the lens's vertical angle. Thereby, the maximum distance that the 8 MP camera can identify an object was at 6.67 m along the horizontal direction and 5.87 m along the vertical direction, with 492 pixels/m, which was sufficient for the TAG identification [31].

(iii) Process using the Raspberry Pi 3 the captured images in order to identify the patient's position, send the coordinates of the patient to the Arduino UNO, and trigger the IV pole to follow the patient.

Regarding the mechanical intervention,

(i) Introduce and place a flow control system on the new BMIVPOT. While the motor rotates, the screw rotates performing a translational motion. This final motion causes a pressure on the IV tube which controls the saline's flow.

(ii) Use four DC motors to move the base.

(iii) Assume that the average acceleration of a walking human is 0.65 m/s^2, and the total mass of the system is approximately 40 kg, including an average additional load that can be attached to the system. The summation of forces has to be equal to the driving force which was 26 N. Thus, according to torque equation τ = (force) (radius of wheel), the total torque that the four motors have to handle was 1.3 N·m, i.e., 0.325 N·m for each motor.

(iv) Code the Arduino UNO to control the two relay modules, which then controls the DC motors.

(v) Drive the DC motor by two relay modules, in order to lift up the casters so that the system moves on the Mecanum wheels, or lower the caster down in case of emergency.

3.2.3. Testing and Evaluation Method. The testing of the system's performance, feature monitoring, and cost effectiveness was based on the accuracy and repeatability of the measurements. While the evaluation was based on comparing the results obtained from BMIVPOT to those existing in the market and in research. To check the function of each sensor, follow the upcoming steps:

(i) Test the volume meter by applying a series of known-weight stuff and checking if the measured values obtained by the balance were equal to them.

(ii) Test the flow meter by placing the drip chamber of the IV bag in the flow meter's housing and setting the saline at "slow flow" so that you could count the drops manually and check if the flow meter had counted the same number of drops.

(iii) Test the blood leak detector by checking if the alarm is triggered when blood passes in front of the LED and the phototransistor.

(iv) Test the flow control system by checking if the screw was pushing on the tube with the correct pressure to provide the intended flow rate.

(v) Test the LCD display to verify if the values displayed are the real ones.

(vi) Test the camera and TAG-recognition/tracking of the TAG by checking if the tracking image displayed the correct TAG and contour, also by checking the processing of the images for each frame. Test the TAG-recognition/tracking according to the schematic representation illustrated in Figure 4.

(vii) Test the movement of the system relative to the TAG by measuring the linear and angular velocities and the distance covered by BMIVPOT relative to time.

(viii) Test the wireless communication by verifying the establishment of the connection between the server and the sensor and by verifying the display of results on the server, i.e., whether they were consistent with the measured ones or not.

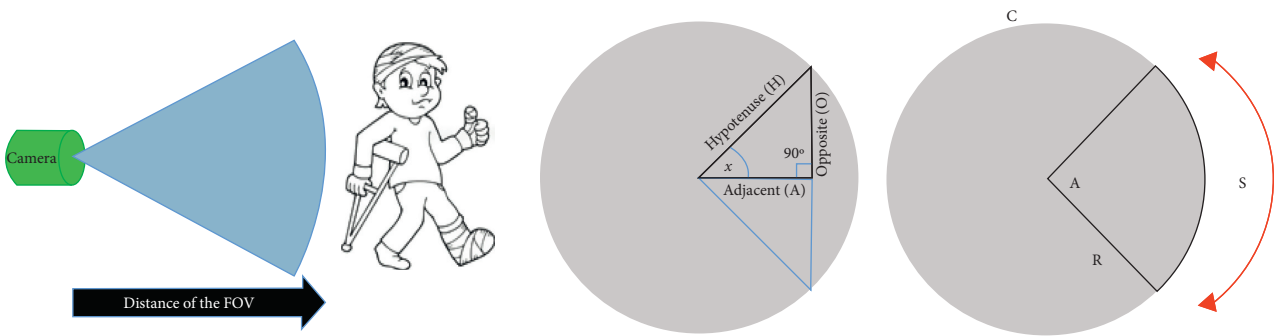

Figure 5: The patient's tracking method from the Field of View (FOV) showing the distance of pixels/m to the distance calculation.

3.3. BMIVPOT Implementation. This section includes the implementation process to build the BMIVPOT. It shows the base implementation, stand implementation, sensors' placement, and tracking system implementation.

3.3.1. Base Implementation. In order to build the base according to the simulated dimensions and overall design, the different parts forming the base were manufactured independently then reassembled. In order to mimic the assembly, apply the following steps:

(i) Assemble the DC motors to the Mecanum wheels, by inserting the motors' shafts each to a bearing fixed in the wheels.

(ii) Fix the four assembled motor-wheel parts to their specific position on the Plexiglas floor.

(iii) Connect the motors to their relays and to the Arduino Uno, which has to be connected to Raspberry Pi 3 via USB cable.

(iv) Attach the casters to their manufactured holders.

(v) Fix the motor, responsible for lifting the emergency casters up and down.

(vi) Fit the casters-holder assembly on the floor part, where their holes have to be drilled to provide an easy upward and downward movement for the casters.

(vii) Connect the casters' motor to its driver and to the Arduino and place the batteries inside the base then launch the stand implementation.

3.3.2. Stand Implementation. In order to assemble the stand, apply the following steps:

(i) Fix the stand to the holder.

(ii) Insert the pyramid-shaped part into the stand then fix it to the floor-casters assembly.

(iii) Fit the flow control stepper motor inside its box and place it on the stand.

(iv) Connect the flow control stepper motor to its driver and to the NodeMCU.

(v) Attach the hooks at the top of the stand then place the sensors.

3.3.3. Placement of Sensors. In order to achieve the intended functionality of the sensors, place a specific setup suitable for their measured parameters and apply the following steps:

(i) Connect the load cell to the HX711 module and then to a NodeMCU.

(ii) Fit the load cell circuit inside its box placed under the hooks.

(iii) Place the IR LED and phototransistor inside a black box, where the LED and the phototransistor have to be at the same level and facing each other.

(iv) Connect the LED and the photodetector to a NodeMCU. Then connect a 10 kΩ resistor to the analog reading coming from the phototransistor to the microcontroller pin.

(v) Place the three US sensors on the three sides of the base and connect them to the Arduino UNO.

(vi) Place the US sensor at the front side of the stand above the camera and connect it to the Raspberry Pi 3.

(vii) Connect the blood leak detector to the NodeMCU and place its circuit on the IV tube cable; then start with implementing the tracking system.

3.3.4. Tracking System Implementation. To synchronize the overall movement of the BMIVPOT with the movement of the patient, apply the following steps:

(i) Place the TAG on the back of the patient's costume.

(ii) Place the camera on the stand on the predefined height to track the TAG.

(iii) Connect the camera to the Raspberry Pi 3 in order to recognize the TAG and provide image processing.

4. Results of BMIVPOT

Herein, the results of BMIVPOT are provided. The results were divided into three parts, the simulation results in Section 4.1, the real results in Section 4.2, and the testing and evaluation results in Section 4.3. As for the testing and evaluation part, it included a comparison between BMIVPOT and existing poles based on the performance, the features it provides, and the cost.

4.1. Simulation Results. The AutoCAD simulation results of the different parts of the BMIVPOT were realized and were represented depending on the type of intervention.

The simulated Mecanum wheels and their motors are shown in Figure 6(a), and the simulated emergency system is shown in Figures 6(b)–6(d).

The architecture intervention was reflected by the simulated results of the system shown in Figures 7(a) and 7(b) which comprises the base and the pole. The base, shown in Figure 7(a), was divided into three parts: the floor, the casters' holder, and the stabilizing part (with three different views). The overall simulated system is shown in Figure 7(c).

The sensor's intervention was reflected by the housing for each sensor is simulated in order to accommodate for the electronics and materials required. The dimension of each box was chosen according to the size of the chosen electronics and the place they occupied. The simulated blood leak detector's box is shown in Figure 7(d). Moreover, the simulated flowmeter's housing is shown in Figure 7(e).

The tracking intervention was reflected by the simulated result of the camera and its FOV as shown in Figure 7(f). The simulated box that fits the camera and the circuitry is shown in Figure 7(g) in real dimensions. Furthermore, the mechanical intervention included the simulated flow control system shown in Figure 7(h).

4.2. Real Results. After providing the simulation results of the BMIVPOT, herein the real construction results are provided as shown in Figure 8.

4.2.1. Results according to the Type of Intervention. The architecture intervention results revealed the base of BMIVPOT, the whole base which was assembled as shown in Figure 8(a). The flow meter's electronics were fitted in their housing as shown in Figure 8(b). Moreover, the emergency system shown in Figure 8(c) included the lifting and lowering of the casters, so that the system can move on Mecanum wheels or on the casters, respectively. Besides, the mechanical intervention included the flow control, the motors and wheels, and the emergency system. The flow control system's stepper motor shown in Figure 8(d) was fitted inside the aluminum box and its circuitry was placed on this box. This base was made of three parts as shown in Figure 8(e), with the attached rods and with the casters attached to the system.

Furthermore, the sensors' intervention was reflected by the placement of the blood detector's components inside the Plexiglas box as shown in Figure 8(f).

The Wi-Fi intervention results showed the communication between the volume detector and the nurse's workstation through the web server and the nurse's workstation (see Figure 9). The flow meter percentages and rates were represented in Figure 9(a). As for the flow control, the wireless communication provided the nurse with the ability to control the flow from the workstation as shown in Figure 9(b). The blood leak detector sent wirelessly a notification to the nurse about any possible blood backflow in the tube as shown in Figure 9(c).

The tracking intervention result is shown in Figure 10, where the BMIVPOT was tracking the colored TAG placed on the patient in front of the camera.

4.3. Testing and Evaluation Results. The results for testing BMIVPOT tracking system are shown in Figure 11. Noteworthily, the robot could be centered in many ways; in the scenario shown in Figure 11, the center was set to be at the origin of the x-axis of BMIVPOT, and the five random targets and angles are shown in Figure 11(a). The results of tracking the TAG at Θ_{1-5} with respect to the x-axis are shown in Figure 11(b). The robot was tracking the target while staying centered. The change in the location of the target, i.e., the position of the patient, caused the BMIVPOT to deviate, and the deviation was associated with a change in the angle of movement accordingly. Thereby, the variation of the movement (tracking) of the BMIVPOT was tested as a function of the target location and time. The overall profile of the variation of the movement of the BMIVPOT as a function of the target location and time was aperiodic (see Figure 11(b)).

The positive sign of rotation was chosen to be the counterclockwise direction. Noteworthily, when the target was placed at 45° from the center of the BMIVPOT, the fully automated robot which was centered on y-axis, as shown in Figures 11(a) and 11(b), was able to detect the target, rotated 45°, and track the target in 1.2 seconds, merely.

As the target deviates at larger angles, such as Θ_2 and Θ_3, the tracking time increases from 2.2 seconds to 3.2 seconds, respectively, by an increment of 1. Thereby, it can be inferred that according to our test when $\Theta_{i+1} = \Theta_i + \Theta'$, $t_{i+1} = t_i + k$, where $k = 1$ s.

Furthermore, the results of testing the movement of BMIVPOT, i.e., the linear velocity, angular velocity, and distance relative to time features, are provided in Figures 12(a)–12(c), respectively. The graph of the variation of the linear velocity of robot versus time (Figure 12(a)) shows that at time $t = 0$ seconds, the robot was at rest; as time increases, the velocity increases gradually to reach to its highest value of 0.785 m/s at $t = 1$ sec. After 1 s, the robot moves at a constant velocity until $t = 15$ s when the patient stopped walking, so its velocity dropped to 0 m/s, while BMIVPOT kept walking with its constant velocity until $t = 15.618$ s to achieve the minimum distance with respect to the patient.

Besides, the graph shown in Figure 12(b) reveals the variation of angular velocity (rad/s) of robot versus time (s). The robot searches for a target by turning left, then returning back to its original position and then turning right. At $t = 0$, the robot is in its original position, where Wz value is 0 (rad/s). When the robot turns left, the angular velocity increases to reach 2.0138 (rad/s) at $t = 1$ s. Noteworthily, the angular velocity was calculated as in the study of Kim et al. [34]. At $t = 1$ s, the robot stops, so the value of Wz decreases back to 0 (rad/s) at $t = 2$ s. Then, the robot starts turning back to its original position at $t = 2$ s where Wz decreases to reach

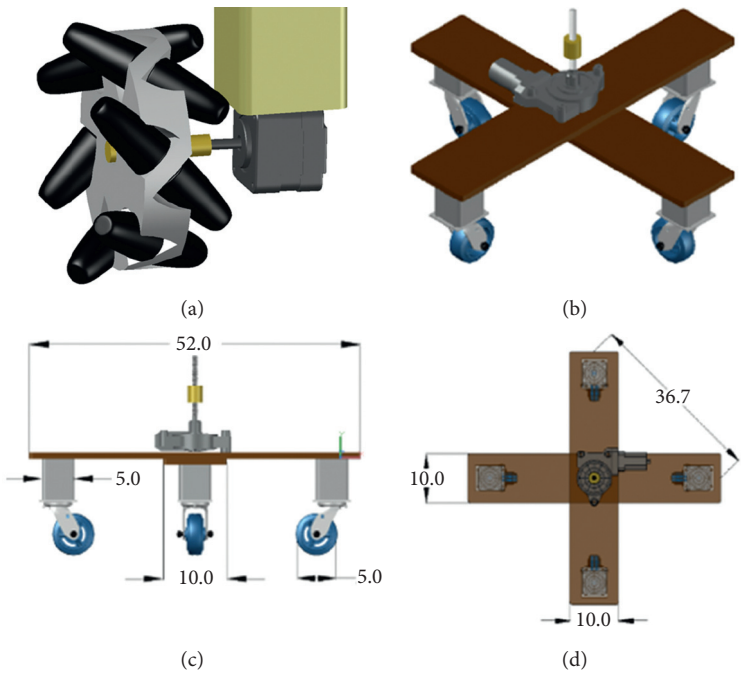

Figure 6: AutoCAD drawings of the BMIVPOT wheels. (a) Mecanum motor simulation. (b) 3-Dimensional view of emergency system simulation. (c) Side view of emergency system simulation. (d) Top view of emergency system simulation.

−2.0138 (rad/s) at $t = 3$ s since the moving direction is clockwise. At $t = 3$ s, the robot stops, so Wz increases to reach 0 (rad/s) at $t = 4$ s. At $t = 4$ s, the robot starts turning right, so Wz value decreases to reach −2.0138 (rad/s) at $t = 5$ s. BMIVPOT then stops at $t = 5$ s, so Wz value increases to reach 0 (rad/s) at $t = 6$ s. The robot then starts returning back to its original position, so Wz value increases to reach 2.0138 (rad/s) at $t = 7$ s. Then, the robot stops for 1 s at $t = 7$ s, so Wz values decrease to reach 0 (rad/s) at $t = 8$ s. Then, from $t = 8$ s to $t = 16$ s, the robot repeats the same rotation.

Moreover, the graph shown in Figure 12(c) reveals the distance (cm) covered by the BMIVPOT and patient versus time (s). At $t = 0$ s, both the patient and BMIVPOT were at the initial position close to each other, and the patient accelerates at 0.3925 (m/s^2). At $t = 1$ s, the distance covered by the robot remains at 0 cm, while the distance covered by the patient increases to reach 39.25 cm, i.e., greater than the minimum distance to keep between the robot and patient, so BMIVPOT starts moving uniformly and following the patient. At $t = 2$ s, the distance covered by the robot increases to reach 78.5 cm, and the distance covered by the patient increases to reach 157 cm. Both covered distances increase until $t = 15.618$ s, where the patient stops walking at a distance of 1147.5 cm, while BMIVPOT keeps moving to achieve the minimum distance $d_{\min}$ until $t = 16$ s where the distance covered by the patient remains constant at 1226 cm and the distance covered by the robot increases to reach 1196 cm. At $t = 16$ s, the robot stops moving since the distance between the robot and patient becomes 30 cm, i.e., roughly the minimum distance to keep between.

The graph, however, shown in Figure 12(d) reveals the flow rate versus the flow selectors. There were four selectors for indicating the flow of saline infusion. The flow at selector "very slow flow" is 14 drops/minute, so that the time to finish the saline will be 24 hours. The second selector "slow flow" will increase the flow to 28 drops/minute and decrease the time to finish the infusion of saline to 12 hours. Selecting "normal flow" will increase the flow to 42 drops/minutes and decrease the time to finish the saline to 8 hours. At selector "high flow," the flow will be 56 drops/minute, and the time to finish the saline infusion will be 4 hours. Besides, the results of testing the flow sensors are provided in Figure 12(d).

To evaluate our BMIVPOT, the comparison shown in Figure 13 was carried out between the BMIVPOT and the systems existing in the literature, including the novel robotic IV pole proposed by Sayed-Kassem et al., the autonomous IV pole proposed by Binger et al., and other market or commercial IV poles [1, 2].

A comparison perspective was taken into consideration concerning the number of features as shown in Figure 13(a). Noteworthily, all the features taken into consideration were the volume detection, flow rate detection, blood leak detection, flow control feature, wireless communication, emergency system, and the fully automated movement and tracking.

Furthermore, the comparison shown in Figure 13(b) provides the intervention's availability in the BMIVPOT, commercial, autonomous, and the robotic IV poles.

Concerning the architecture, the commercial IV poles were the reference and showed the lowest percentage of 40% (balanced base-pole and hooks design), while the BMIVPOT showed the highest rate of 90% (balanced base-pole with specific built-in material, practical pole design, Mecanum wheels, user-friendly architecture, and lack of hooks' design).

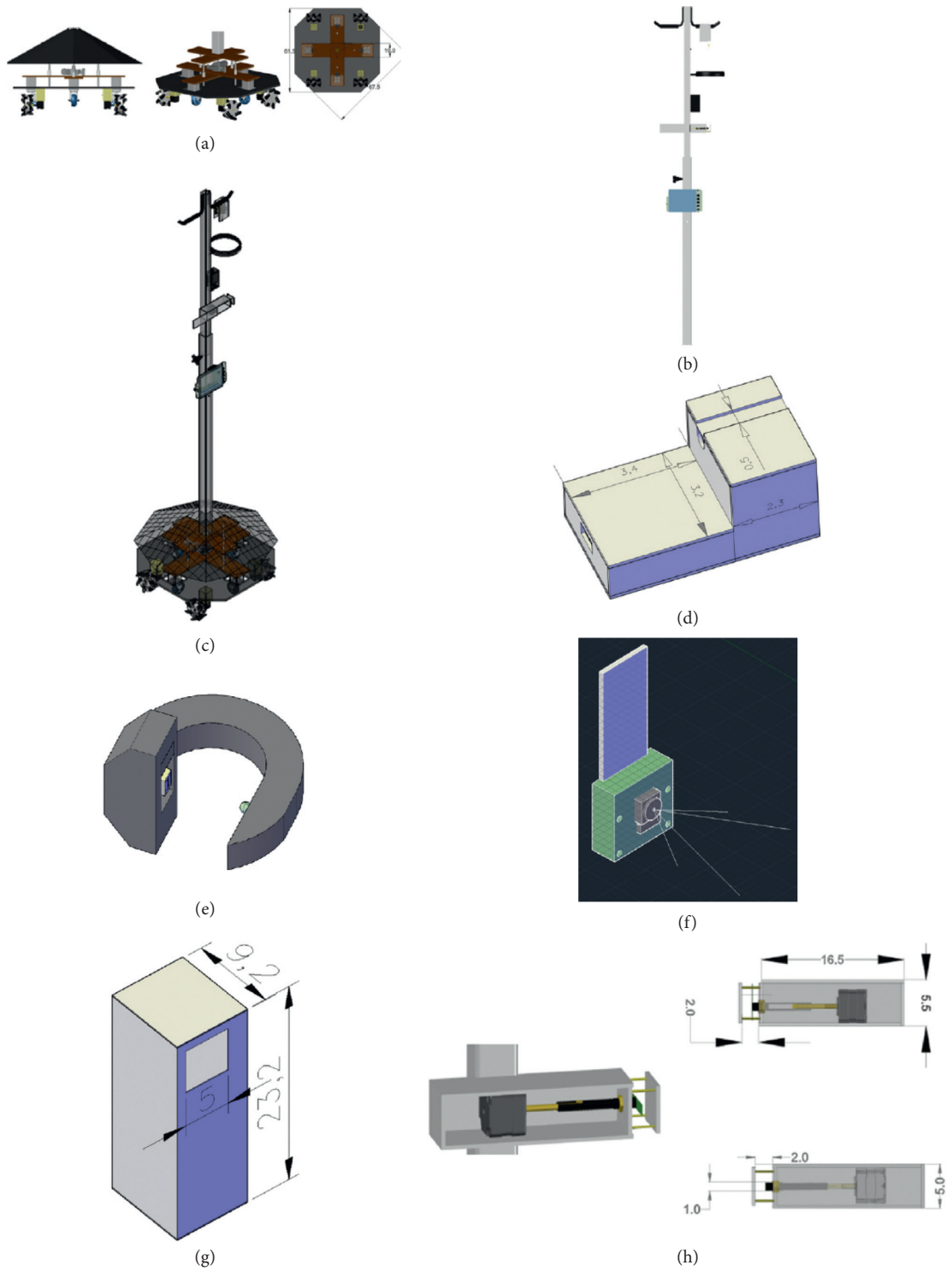

Figure 7: AutoCAD drawings of the BMIVPOTparts. (a) BMIVPOT base. (b) The pole. (c) Whole system. (d) Blood leak detector housing.(e) Flowmeter housing. (f) Camera and its field of view. (g) Raspberry Pi 3 and camera housing. (h) The flow control system.

Also for the electronic intervention reflected by the use of sensors, the commercial IV poles in the market showed the lowest percentage of 0% (absence of sensors), while the BMIVPOT showed the highest number of features of 80% (as it possessed 8 features out of 10: obstacle detector, volume detector, blood leak detector, flow meter, emergency alarm, linear velocity detector, angular velocity detector, and distance covered detector and lack of vital signs' sensors, i.e., temperature and blood pressure).

For the wireless intervention, BMIVPOT was exclusively the only system that had a wireless contribution feature (100%). As for the tracking, the BMIVPOT had the

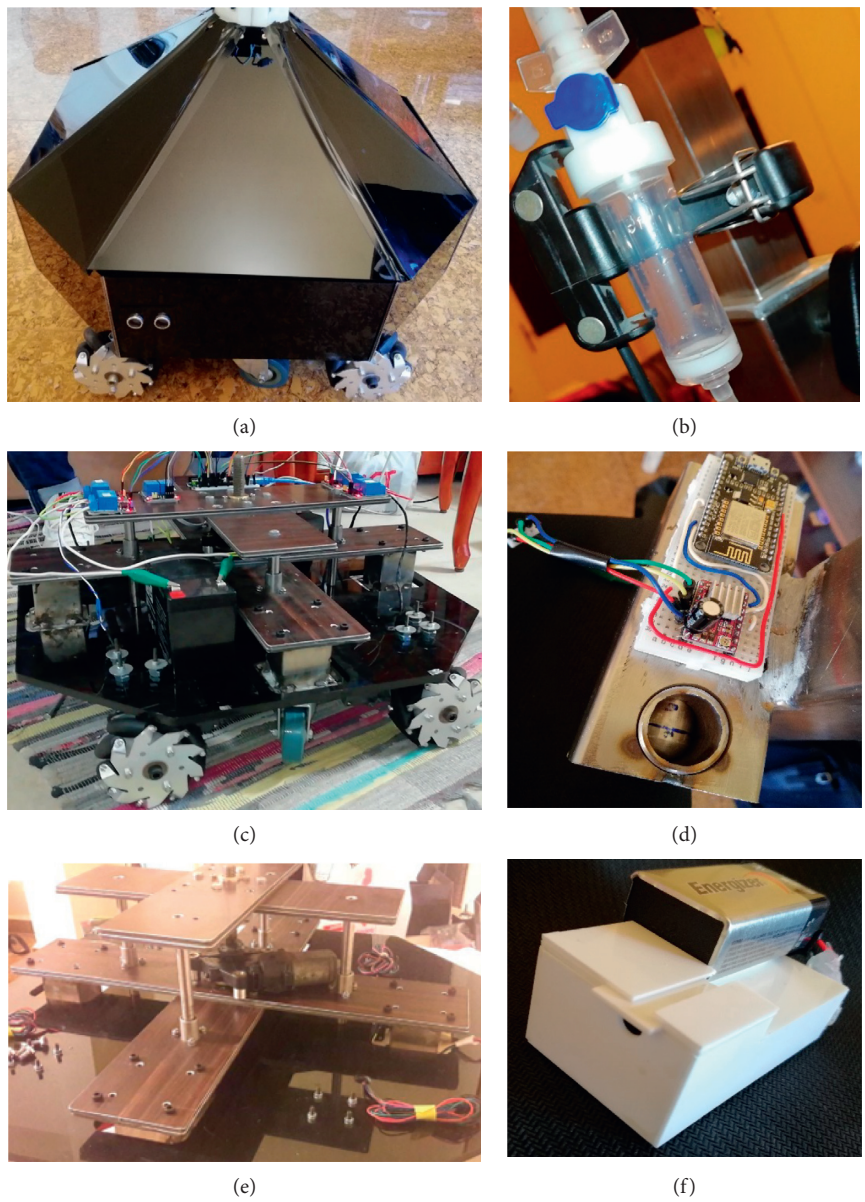

Figure 8: The real BMIVPOT construction results. (a) Whole base assembly. (b) The drip chamber inserted in the flow meter's housing. (c) The emergency system. (d) The flow control system. (e) The casters' holder system. (f) The blood leak detector.

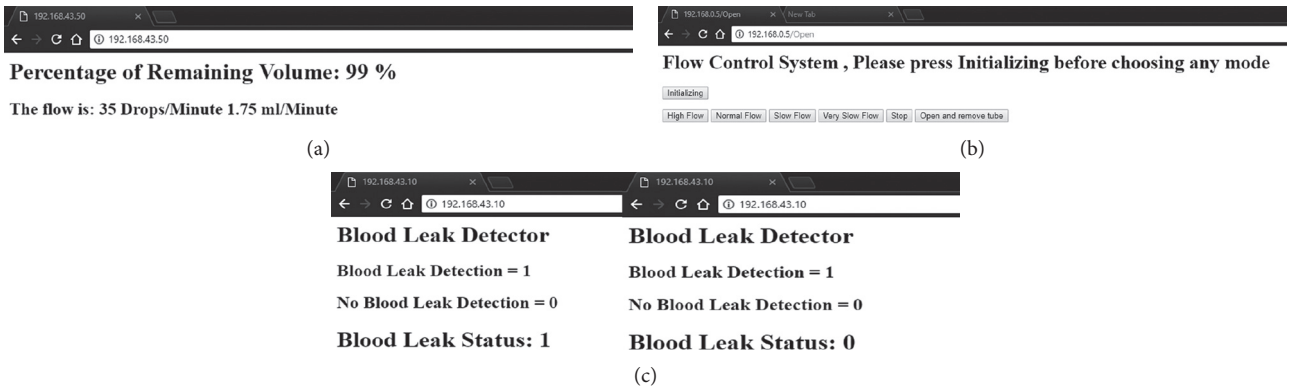

Figure 9: The web server results. (a) Web server showing the volume-flow detection. (b) Flow control server page. (c) Blood leak web server.

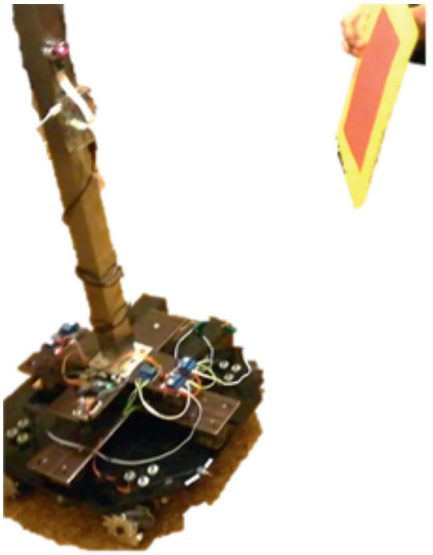

Figure 10: The Biomedical Intravenous Robot (BMIVPOT) tracking the TAG.

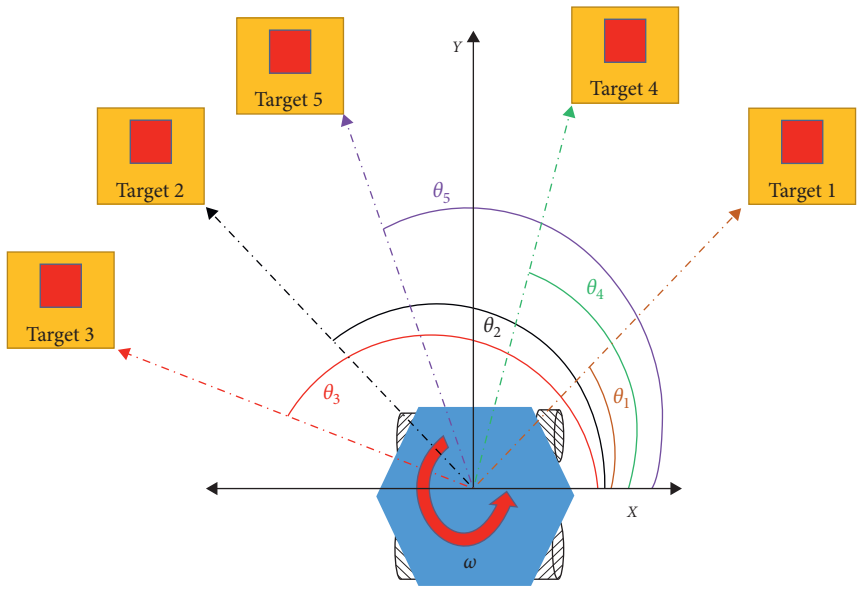

(a)

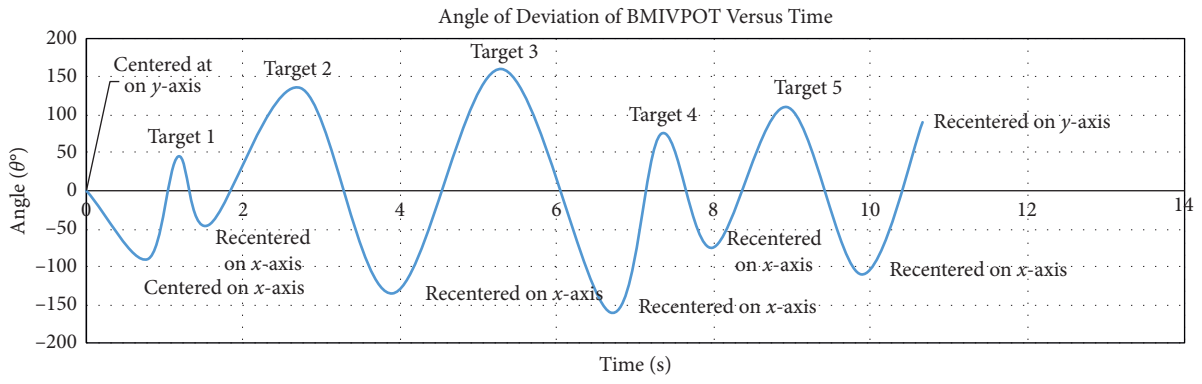

(b)

Figure 11: The variation of the movement of the BMIVPOT as a function of the target location and time. (a) The model of testing. (b) The overall profile of the variation of the angle of deviation of BMIVPOT relative to time and target.

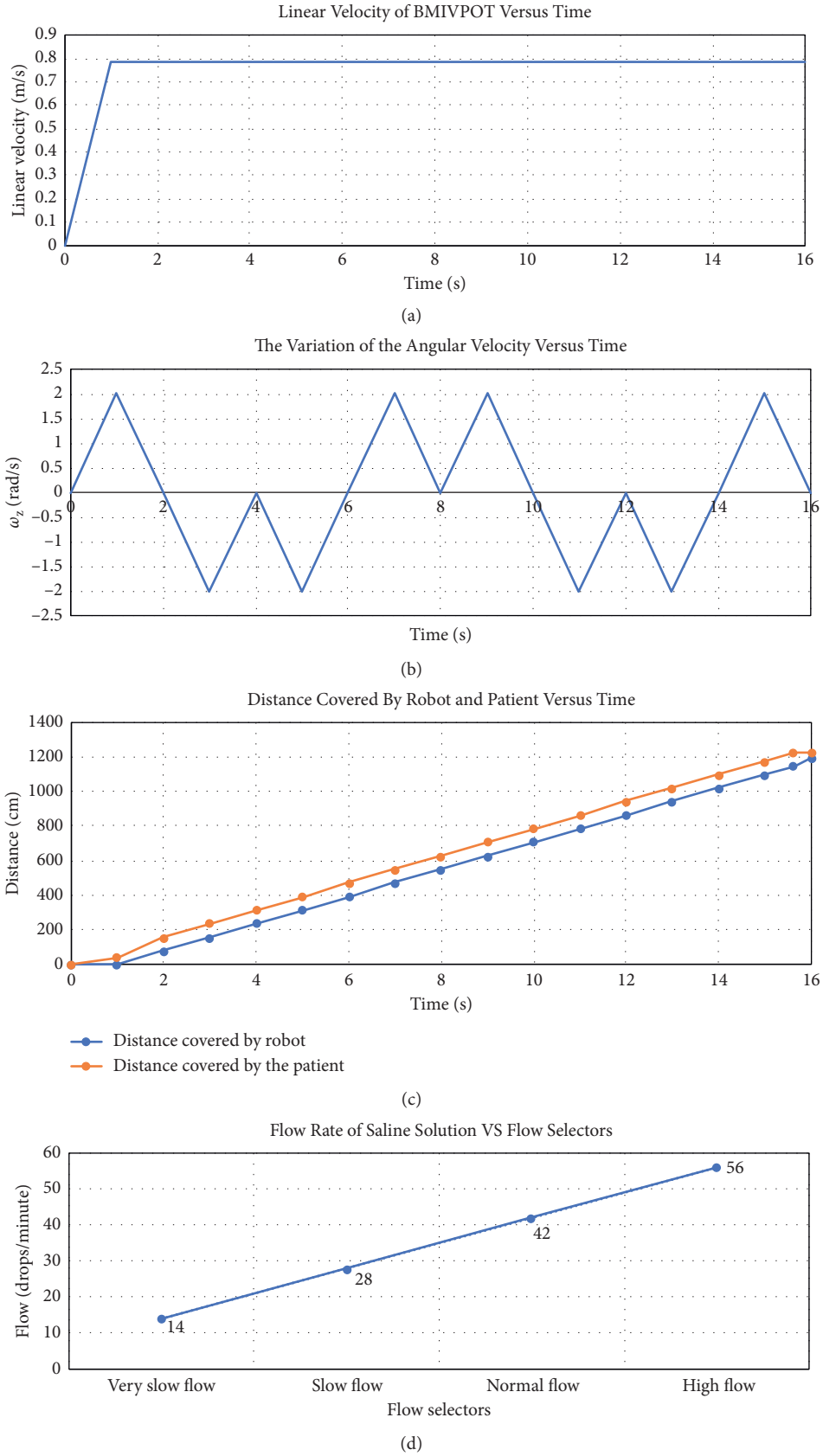

Figure 12: Testing results. (a) The linear velocity of BMIVPOT versus time. (b) The variation of the angular velocity versus time. (c) Distance covered by robot and patient versus time. (d) Flow rate of saline solution versus flow selectors.

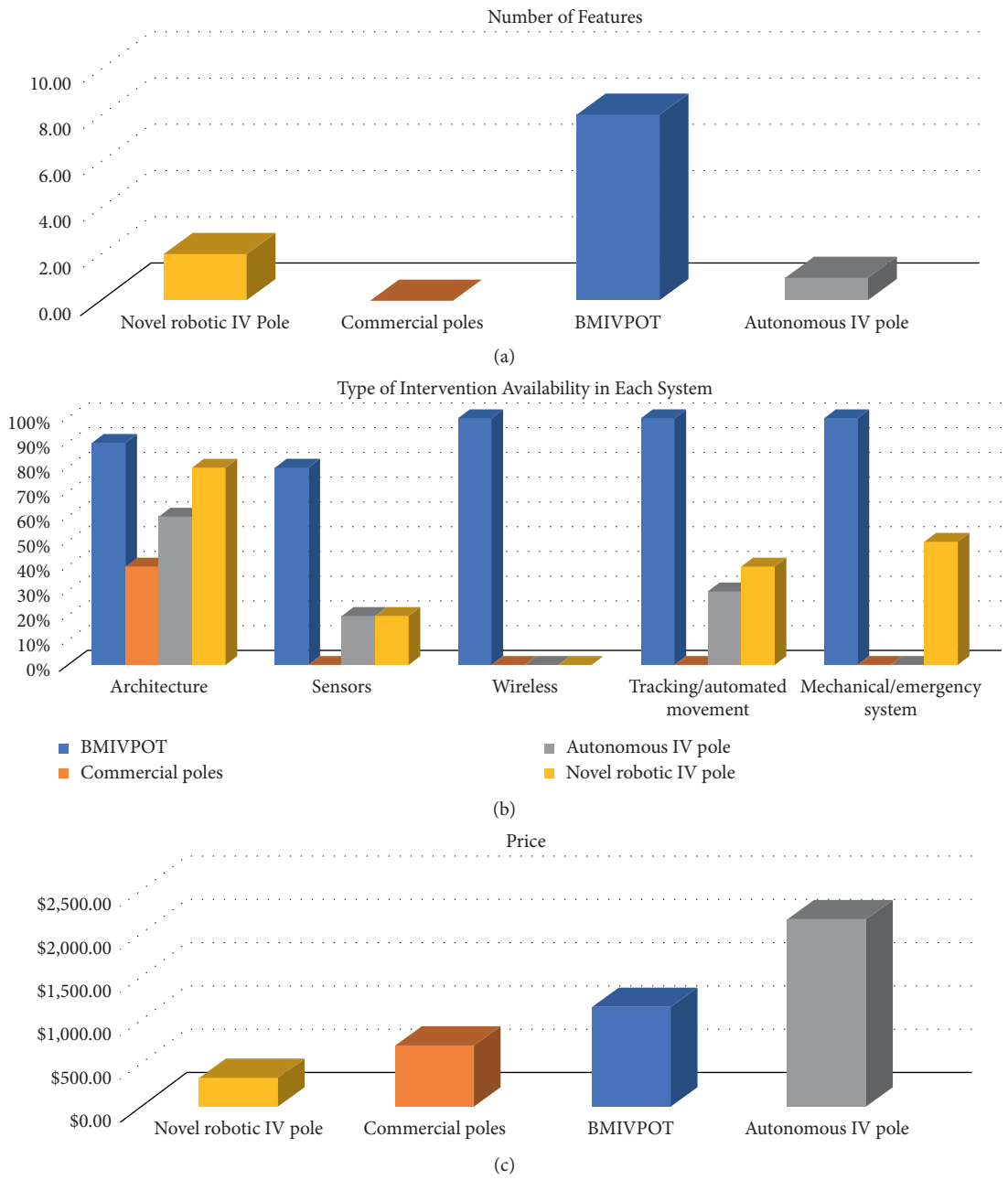

Figure 13: Comparison between different intravenous (IV) pole systems. (a) The number of features in each system in the novel robotic IV pole, commercial poles, BMIVPOT, and autonomous pole. (b) Interventions' availability in each pole. (c) The cost of the poles.

maximum percentage of 100% (fully automated), while the novel robotic IV pole had approximately half of the BMIVPOT's percentage 40% (semi-automated and requires prior training).

Concerning the mechanical or emergency system included in each design, the BMIVPOT took the highest rate 100% (since it is fully automated), while the robotic IV pole took the half of this rate (50%: semi-automated).

The evaluation of the price of BMIVPOT was compared to the IV poles designs as shown in Figure 13(c). According to our statistics, the market price of BMIVPOT is $1,155.29 and provided all the eight aforementioned features.

5. Discussion

According to our statistics and our thorough literature review, the BMIVPOT which costs $1,155.29 had all the eight aforementioned features. This could be considered as an advantage over the other systems that could cost more or less than the BMIVPOT, when these systems were not capable of providing the same number of features as BMIVPOT. For instance, Sayed-Kassem et al.'s system costs $4325.36 and offers two features [2] as shown in Figures 13(a)–13(c); the cost of each feature was approximately $162.68. Although the cost of our BMIVPOT system is $1,155.29, we had seven features; hence, the cost of each feature was approximately in

accordance to that for the novel robotic IV pole $165. As for the autonomous IV pole, it costs $2,167 and provides only one feature [1]. Thereby, our system is considered to be more cost-effective than the two existing alternatives.

Concerning the number of monitored and available features, our system provides seven features (considers 100% from the whole number of features) which surpasses the features monitored and available in other techniques as shown in Figure 13(a). While our system provides seven features, the novel robotic IV pole provides only two features (28.57% from the whole number of features), which are the semi-automated movement and the volume detection. On the other hand, the autonomous IV pole only includes one single feature, which is the automated movement (14.2% from the whole number of features).

In addition to what preceded, by comparing the accuracy of the volume measurement provided by the BMIVPOT to that of the novel robotic IV pole, the volume detection provided by the latter is limited to one volume level, which is the bag emptiness, while the detection provided by our BMIVPOT is based on a continuous volume monitoring for all levels represented by percentage value as shown in Figure 9(a).

Pertaining to the patient's safety and risk management, the BMIVPOT included US sensors which does not harm the patient; this safety measure was absent in the two other systems [1, 2]. According to Sayed-Kassem et al., the patient's safety was provided by the limited range of RF signals sent from the joystick to the pole, which constrain the distance of the patient from the pole [2], thereby giving safety to the IV tube, but does not take into consideration the patient's safety while present in the intended range of motion. Consequently, the BMIVPOT surpasses the novel robotic IV pole and the autonomous IV pole, in the safety and risk management. In addition, the US sensors provide safety for the system itself by keeping it away from obstacles.

By comparing our system to the ambulatory IV pole [4], the Homecare IV Pole [5], and the simple free-standing stands [7], our system included all interventions, while only one intervention, which is the architecture, was present in the commercial IV poles as shown in Figure 13(b). Concerning the architecture intervention, our system was similar in terms of stability, balance, and the overall concept (wheeled base and hooks) to the commercial IV poles [4, 5, 7]. However, BMIVPOT was not similar to the hanging IV pole [6], as the latter pole is attached to the roof merely. Concerning the number of monitored and available features, our system provides all advanced features as opposed to the commercial IV poles as shown in Figure 13(a). Although, commercial IV poles lacked most features, their average cost was above $500, which is considered expensive as shown in Figure 13(c).

The development of BMIVPOT was innovative and research oriented to provide a fully automated IV pole that tracks the patient while moving in a hospital. Several simulations were done in order to provide the appropriate system's architecture and design. Results showed that our BMIVPOT was user-friendly. The user-friendly notation was based on whether the patient and nurse fully trigger the IV pole by themselves, whether they partially trigger the IV pole [1, 2] or whether they do not need to trigger the IV pole (full automation). Thereby, the user-friendly BMIVPOT was associated with the fact that patient/nurse does not need any more to spend effort and time maneuvering the pole as opposed to the existing poles [1, 2]. The BMIVPOT system comprised various interventions, each providing a specific function. BMIVPOT showed up and provided higher performance percentage (80%) as compared to the other existing systems.

The fully automated robotic IV pole, BMIVPOT, exhibited an outstanding progress as compared to the commercial/market IV poles [4–7, 9]. The evolution of BMIVPOT was achieved by transforming the wheeled stand to a robot ready to be used in healthcare organizations. Moreover, the wireless communication provided transfer of eight features to the nurses' workbench. Although the patient tracking seemed to increase the on-chip computation cost, however, each pole followed a unique TAG printed on the back of the patient's costume. Upon testing the aforementioned tracking, the camera was successfully recognizing the tag and following it in the presence of obstacles, and at different angles as opposed to the limitations present in research poles [1, 2].

Furthermore, by comparing our system to the existing research poles, i.e., the autonomous IV pole developed by Binger et al. [1] and the novel robotic IV pole developed by Sayed-Kassem et al. [2], we found that our system surpassed these designs in vast ways, including the number of features, the cost-effectiveness, and the accuracy of the sensors' measurements.

According to Sayed-Kassem et al., the so-called novel robotic IV pole offered patients the ability to maneuver the poles with a joystick, making them move more freely [2], and according to Binger et al., their so-called autonomous system was able to follow the patient, by tethering the patient with a nylon twine to encoders and potentiometers present on the IV pole, which were able to determine the movement and direction of the patient while walking [1]. In comparison to what preceded, our system took into consideration fully automated tracking, movement, and recognition of the patient (100%); however, the motion of the IV pole in the Sayed-Kassem et al. system was semi-automated (50%), since the patient still needs to hold and control the pole by a joystick as shown in Figure 13(b). Moreover, the motion in the Binger et al. system could not be considered automated since the patient is still tethered to the pole, which presents a major limitation on his movement [1].

On the other hand, our BMIVPOT provides a fully automated movement (100%) of the IV pole, because it requires nothing from the patient except to be in the FOV of the camera. The overall percentage of features offered by our Biomedical Intravenous Pole Robot was 60% (80%–20%) higher than that offered by peer research poles and 80% (80%–0%) higher than the market poles. In addition, the average percentage of integration of interventions (architecture, sensor, wireless, tracking, and mechanical) in the Biomedical Intravenous Pole Robot was at least 56% (average interventions of BMIVPOT 94%-average interventions of Novel Robotic IV pole 38%) higher than the alternative poles.

6. Conclusion

This work was conducted in order to introduce a new and advanced version of the robotic IV pole, the fully automated BMIVPOT. BMIVPOT is an enhancement of the previous robotic IV pole systems in all terms, including the ease of motion of the patient, the reduced effort spent by the nurses to monitor the IV bag, and other vital signs.

An automated movement was provided and tested to make the patient move freely without the need for dragging his pole and the integration of monitoring sensors to help the nurses. The BMIVPOT was designed to include the tracking of the patient by camera which provides the ability to follow the patient by a fully automated motion.

Furthermore, a wireless communication between the sensors present on the BMIVPOT and their workstation was established, allowing the nurse to monitor the flow, volume and blood leakage wirelessly through the mobile phone. Also, the BMIVPOT has an electronic emergency system, which allows the switching between moving the system either manually on the casters or via the automated motion provided by the Mecanum wheels.

The BMIVPOT could improve the health outcomes for the patients and help the nurses to accomplish their duties and monitor the IV bag.

7. Future Work

The BMIVPOT offers many improvements; it could be subject to several enhancements concerning its tracking system, automated movement, the automation of the flow control, and the addition of new biomedical sensors.

The future work emerging from the BMIVPOT construction could be listed as follows:

(i) Utilizing a more powerful microprocessor able to perform image processing at a higher speed as opposed to the Raspberry Pi 3, also utilizing a specialized tracking camera to reduce the on-chip computation cost

(ii) Improving the overall architecture by making the base smaller

(iii) Utilizing motors and wheels with less noise

(iv) Controlling the automated flow control based on the communication between the volume detector and the flow meter

(v) Adding new sensors that provide measurements of the vital signs, such as the heart rate, patient's temperature, blood pressure, etc.

(vi) Reduce the on-chip cost of coding in Raspberry Pi 3

(vii) Implementing a mobile application which could be installed on the nurses' phones.

Data Availability

The data used to support the findings of this study are included within the article.

Conflicts of Interest

The authors declare no conflicts of interest regarding the publication of this paper.

Acknowledgments

The authors thank Dr. Mohamad Arnaout for his valuable feedback.

References

[1] M. Binger, C. Conway, N. Goddard, N. Jacobs, C. Pysher, and E. Whritenor, *Autonomous IV Stand (P15073)*, Rochester Institute of Technology, Rochester, NY, USA, 2015.

[2] A. Sayed-Kassem, A. Ghandour, L. Hamawy, and A. Zaylaa, "Cutting-edge robotic intravenous pole: preliminary design and survey in academic medical center in Lebanon," *Journal of Biomedical Engineering and Medical Devices*, vol. 2, no. 1, 2017.

[3] A. Ghandour, A. Sayed-Kassem, and A. Zaylaa, "Cutting edge wireless-based intravenous stand robot, Inserm (01575070)," 2016.

[4] J. W. Pryor, "Ambulatory patient support stand," US Patent 4332378A, 1982.

[5] G. Jost and C. C. Tseng, "Home care intravenous stand," US Patent 4905944A, 1990.

[6] B. J. Kunik, "Pole apparatus for hanging intravenous bags or other similar devices," US Patent 390952S, 2002.

[7] M. G. Vignali, *Intravenous Stand Design*, Worcester Polytechnic Institute, Worcester, MA, USA, 2015.

[8] K. L. Kramer and M. W. Weismiller, "Sliding IV pole," US Patent 5407163A, 1995.

[9] J. C. Schott, M. D. Schott, and J. D. Fox, "Intravenous stand support assembly," US Patent 6079678A, 2000.

[10] A. Polymers, "Plexiglas resist, Evonik performance materials GmbH," 2015.

[11] M. Thakur, "Measurement made simple with Arduino: 21 different measurements, covers all physical and electrical parameter with code and circuit," https://books.google.com.lb/books?id=g4deDwAAQBAJ.

[12] R. Marston, *Optoelectronics Circuits Manual: Newnes Circuits Manual Series*, Elsevier Science, Amsterdam, Netherlands, 2016, https://books.google.com.lb/books?id=TmiEDAAAQBAJ.

[13] A. Basu, *Intel Edison Projects*, Packt Publishing, Birmingham, UK, 2017, https://books.google.com.lb/books?id=bnc5DwAAQBAJ.

[14] E. Freaks, "Ultrasonic ranging module hc-sr04," https://cdn.sparkfun.com/datasheets/Sensors/Proximity/HCSR04.pdf.

[15] A. Pajankar, *Arduino made simple*, BPB Publications, Bengaluru, India, 2018, https://books.google.com.lb/books?id=7YxjDwAAQBAJ.

[16] N. Team, "Nodemcu," 2018, http://www.nodemcu.com/.

[17] A. Kurniawan, *NodeMCU Development Workshop*, PE Press, Riverside, CA, USA, https://books.google.com.lb/books?id=XP9ICgAAQBAJ.

[18] RP Foundation, Raspberry pi 3 model b, 2016, https://www.raspberrypi.org/products/raspberry-pi-3-model-b-plus/.

[19] E. Upton and G. Halfacree, *Raspberry Pi User Guide*, Wiley, Hoboken, NJ, USA, 2016, https://books.google.com.lb/books?id=WHPhDAAAQBAJ.

[20] P. Seneviratne and J. Sirach, *Raspberry Pi 3 Projects for Java Programmers*, Packt Publishing, Birmingham, UK, 2017, https://books.google.com.lb/books?id=tHc5DwAAQBAJ.

[21] M. Hawkins, "8-megapixel raspberry pi camera module v2," 2016, https://www.raspberrypi-spy.co.uk/.
[22] V. Ziemann, *A Hands-On Course in Sensors Using the Arduino and Raspberry Pi, Series in Sensors*, CRC Press, Boca Raton, FL, USA, 2018, https://books.google.com.lb/books?id=fmhQDwAAQBAJ.
[23] DFROBOT, Hybrid stepper motor, https://www.dfrobot.com/product-785.html?search=stepper motor.
[24] V. Athani, *Stepper Motors: Fundamentals, Applications and Design*, New Age International (P) Ltd., Publishers, Bengaluru, India, 1997, https://books.google.com.lb/books?id=0m8NTozFZL8C.
[25] N. Robot, "(6 inch) 152 mm aluminum mecanum wheels set (2 left, 2 right) basic 14165, your inspiration themes," 2012, https://www.nexusrobot.com/.
[26] T. Braunl, *Embedded Robotics: Mobile Robot Design and Applications with Embedded Systems*, Springer E-Books, Springer, Berlin, Germany, 2008, https://books.google.com.lb/books?id=1_rMmj9O-xYC.
[27] N. Dhengre, A. Mogra, S. Verma, and A. Gupta, "Design and manufacturing of mecanum wheel for omnidirectional robot," *International Journal of Mechanical and Production Engineering Research and Development*, vol. 2018, 2018.
[28] M. Scarpino, *Motors for Makers: A Guide to Steppers, Servos, and Other Electrical Machines*, Pearson Education, London, UK, 2015, https://books.google.com.lb/books?id=FpEFCwAAQBAJ.
[29] Techtonics, 12 v DC Square Gear/Geared Motor 150 rpm High Torque, 2019, https://techtonics.in/product/12v-dc-square-gear-geared-motor-150-rpm-high-torque/.
[30] J. T. Co and A. Baba, *Find Quality Wholesalers, Suppliers, Manufacturers, Buyers and Products from Our Award-Winning International Trade Site. Wholesale Products from china Wholesalers at aliexpress.Com*, 2010, http://www.aliexpress.com/item/GOOD-With-Hall-speed-measurement-DC-gear-motor-Big-torque-DC12V-75-1-High-grade-Car/32844986762.html.
[31] G. Hajj-Moussa, A. Sayed-Kassem, N. Kozah, R. Harb, M. Arnaout, and A. J. Zaylaa, "Prototype advancement of the robotic iv pole: preliminary simulation," in *Proceedings of the International Conference on Computer and Applications (ICCA)*, IEEE, pp. 71–74, Beirut, Lebanon, 2018.
[32] N. Kozah, A. Sayed-Kassem, G. H. Moussa, and A. J. Zaylaa, "Advanced prototype for an automated version of the robotic IV pole," in *Proceedings of the Lebanese International University Engineering Exhibition*, pp. 1-2, Beirut, Lebanon, 2018.
[33] A. Sayed-Kassem, N. Kozah, G. H. Moussa, and A. J. Zaylaa, *Advanced Robotic IV Pole Flyer, Inserm (01834529)*, 2018.
[34] J. Kim, J. Park, and S. Kim, "Inertial navigation system for omni-directional AGV with mecanum wheel," *Advances in Mechanical Engineering*, vol. 2, no. 1, 2012.

Hindawi
Journal of Healthcare Engineering
Volume 2020, Article ID 2452683, 17 pages
https://doi.org/10.1155/2020/2452683

Research Article

Merging RFID and Blockchain Technologies to Accelerate Big Data Medical Research Based on Physiological Signals

Xiuqing Chen, Hong Zhu, Deqin Geng, Wei Liu, Rui Yang, and Shoudao Li

School of Medicine Information, Xuzhou Medical University, Xu Zhou 221000, China

Correspondence should be addressed to Xiuqing Chen; xiuqingchen@126.com

Received 4 October 2019; Revised 20 December 2019; Accepted 16 January 2020; Published 14 April 2020

Guest Editor: Liang Zou

The proliferation of physiological signals acquisition and monitoring system, has led to an explosion in physiological signals data. Additionally, RFID systems, blockchain technologies, and the fog computing mechanisms have significantly increased the availability of physiological signal information through big data research. The driver for the development of hybrid systems is the continuing effort in making health-care services more efficient and sustainable. Implantable medical devices (IMD) are therapeutic devices that are surgically implanted into patients' body to continuously monitor their physiological parameters. Patients treat cardiac arrhythmia due to IMD therapeutic and life-saving benefits. We focus on hybrid systems developed for patient physiological signals for collection, storage protection, and monitoring in critical care and clinical practice. In order to provide medical data privacy protection and medical decision support, the hybrid systems are presented, and RFID, blockchain, and big data technologies are used to analyse physiological signals.

1. Introduction

The medical applications are continually increasing. For handling physiological signals efficiently, specific technologies, such as data gathering using RFID protocols, infrastructures, and distributed information storage based on blockchain frameworks, are required. The hospitals applications are adopting physiological signals to realize a quicker way to visit these records. The physiological signals are responsible to offer patient care, enhance the clinical performances, and promote the clinical data research [1–5].

Since the fog computing solves the secure storage issues of big data in the clinical data research with minimal cost, the fog computing technology is customizable and economical and offers infrastructure, platform, and software. Physiological signals' analysis and migration have been proposed for accessing and sharing physiological signal data by different research labs and health-care experts, which can enable exchange of physiological signals more rapid and suitable by using RFID technologies and smart phone app platforms. The advantages of RFID protocols [6–9], the fog computing, and blockchain in the medical applications provide security and privacy protection for storing and sharing physiological signal records. It can provide doctors with collaboration ways through IMD [10] and RFID to help patients in case of emergencies mode. The new model based on blockchain can support medical background rural healthcare and analyse data for medicines and medical research [11–15].

It is urgent for different research institutions to share the encrypted physiological signals. Therefore, privacy and security problems of physiological signals are the data owners and research institutions' primary focus, when the physiological signals include a lot of sensitive information and the attackers are continually trying novel approaches to steal the physiological signals. In order to handle these problems, the medical databases adapted blockchain, and fog computing are proposed [16, 17]. The medical application ecosystems allow the regulators to share and exchange physiological signal data in Figure 1. The introduction of the blockchain-fog-RFID based on data ecosystems ensures that the individuals take control over physiological signal information. The proposed sharing data-driven economy shares the

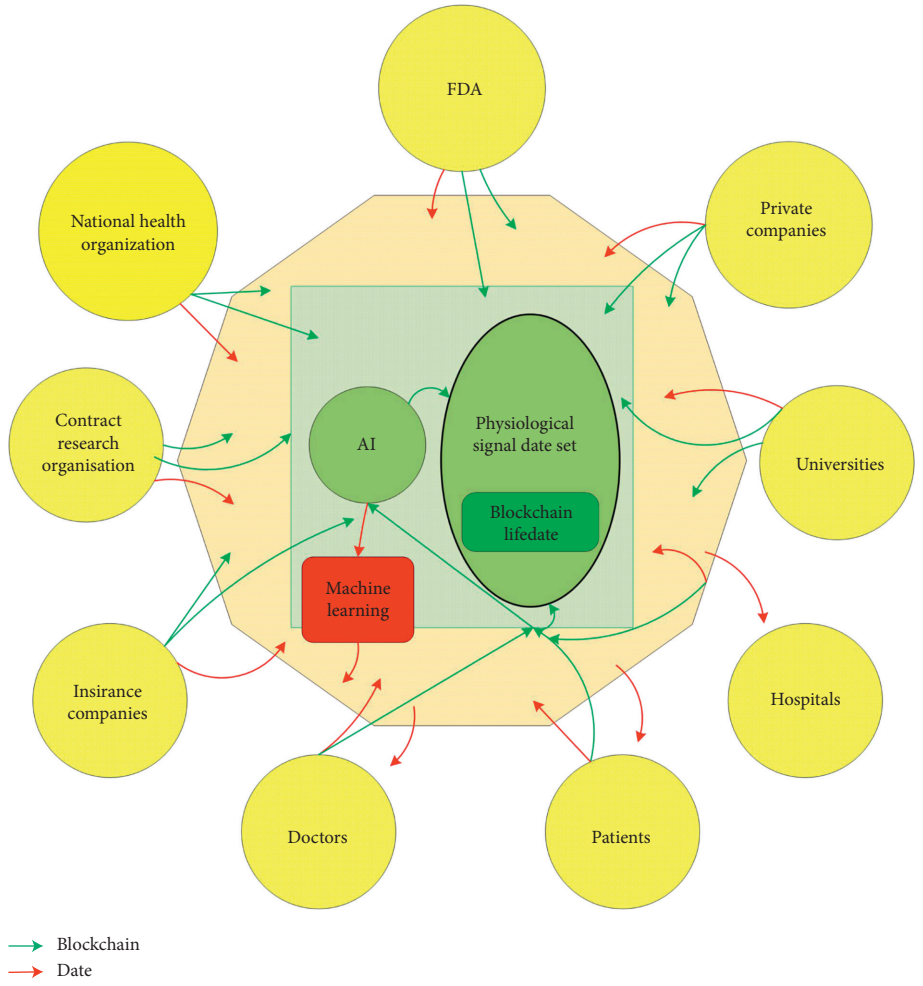

Figure 1: The flow of data from the individuals to the companies and research institutions.

physiological signals for research and commercial purposes in Figure 1.

In the paper, we protect cardiac IMD against security threats by presenting a security scheme. First, we verify and classify the IMD's major security attacks. Second, we introduce blockchain and the RFID systems to extend the IMD architecture [10] and discuss the structures of the interoperability in the medical environment, as shown in Figure 2.

The motivation of the blockchian-fog-RFID method for accelerating big data medical research based on physiological signal is as follows: the method is becoming more common due to the application of powerful computers and the availability of physiological signals from various sources. However, although the complexity of physiological signals makes the complex methods particularly applicable, their application of physiological signals is generally considered earlier than in other fields. Big data has become a buzzword in medical innovation. Rapid advances in artificial intelligence particularly promise to reform medical practice from the resource allocation to the complex diseases' diagnosis. However, big data brings huge risks and challenges, including major questions about patient privacy: the importance of fairness, consent, and patient management in data collection based on RFID; data storage based on fog computing; and dealing with data breaches by using blockchian. In the future, we will discuss the method's applications in physiological signals research: basic research; disease management; aetiology; detection and diagnosis; health services research; treatment development; and treatment evaluation. The possibilities of the blockchian-fog-RFID method for accelerating big data medical research in physiological signals are enormous.

The paper contribution consist of four parts as follows:

(1) The security scheme is a low energy cost RFID system in IMD. The applied authentication protocol is implemented on the RFID circuit without energy.

(2) The applied energy harvesting scheme uses the enhanced WISP, which performs computational functions and uses the harvested energy to go beyond passive RFID tags.

(3) The presented authentication protocol enables the authorized health-care professionals to obtain the access permission to cardiac IMD securely in the regular and emergency model which are determined according to the patient's ability to supply valid

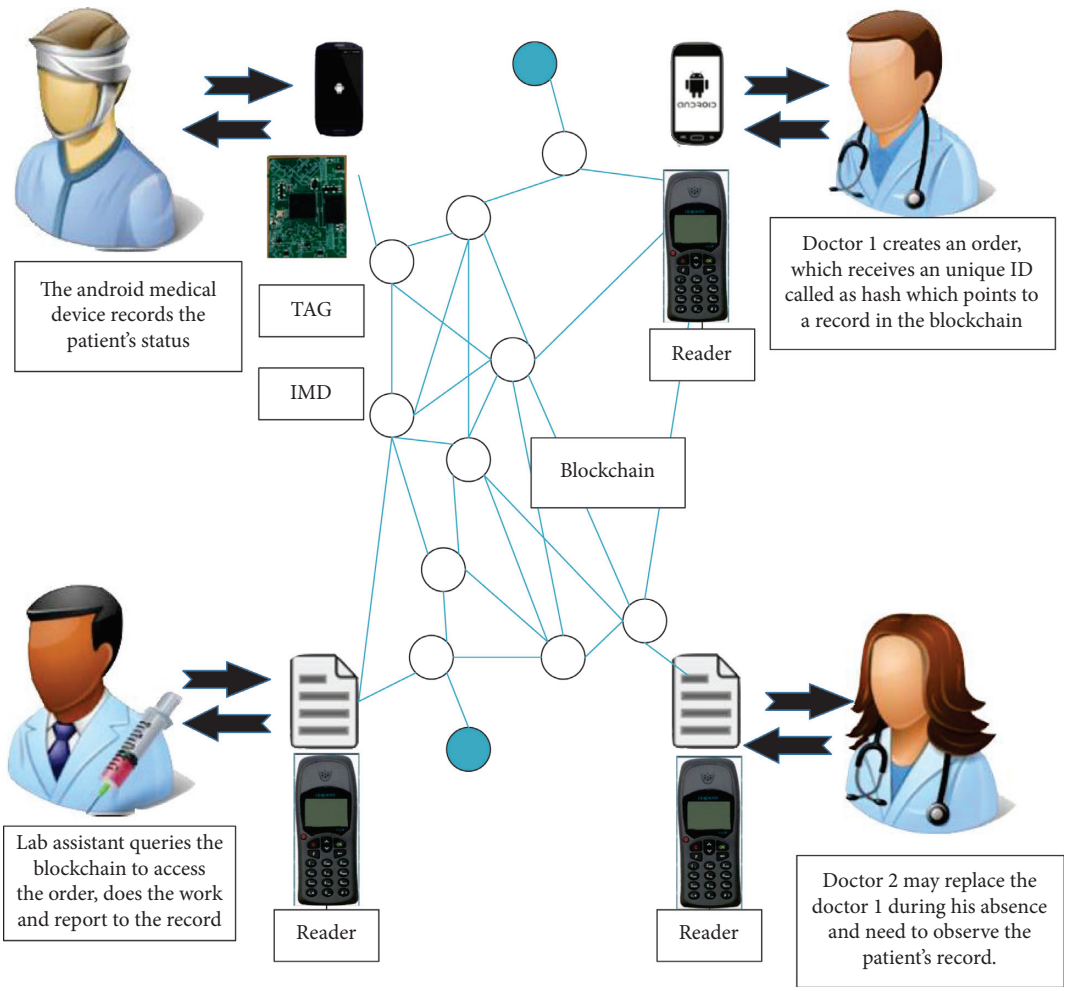

Figure 2: Blockchain in the medical environment.

credentials, thanks to a biometric key distribution scheme implemented.

(4) The schemes generate and share a master key securely based on the physiological sets of the patient collected by IMD. Monitoring and ensuring data integrity during clinical trials is not always feasible in current research systems. Blockchain makes the data collected immutable, traceable, and probably more trustworthy during clinical trials. We also improve the way we currently report adverse events.

In conclusion, we argue that the blockchain can improve the management of clinical trial data, enhance trust in the clinical research process, and simplify regulatory oversight of trials. Finally, we evaluate the security solution's security and performance.

The proposed model covers the many aspects of the health industry such as doctors, patients, and pharmacies to insurance suppliers and government. The paper shows the applications of using RFID, blockchain technologies, and fog computing for storing and managing the physiological signal data. A blockchain model for sharing physiological signals is proposed. In the next section, the combination of blockchain, RFID, and artificial intelligence (AI) technologies is suitable for collecting, storing, and handling heterogeneous physiological signal. The proposed model can be used for physiological signals management.

2. Related Work

The industry of healthcare has changed dramatically because of the boom in clinical research for physiological signal data sharing. We summarize the healthcare studies including physiological signal data, patient information obtained by fog computing, and improvements to blockchain technology. The health-care applications of physiological signal data adopt big data and deep learning technologies and provide with data confidentiality and identity authentication, so as to maintain patients' privacy. In order to more conveniently serve big data medical analysis, Rajan and Rajan [1] and Faust et al. [2] proposed the importance of medical big data privacy and the impact of data analysis on medical care.

Rajan and Rajan [1] proposed a physiological signal monitoring scheme by using the Internet of Things (IoT). Our schemes use IoT to improve the access method of physiological signals and the real-time dynamic monitoring method of the remote monitoring system, which enhances the efficiency of the remote monitoring systems. Faust et al.

[2] summarized the application of deep learning algorithms in physiological signals and pointed out that deep learning methods performed better than classical analysis and machine classification methods for large and diverse datasets. Shanthapriya and Vaithianathan [3] proposed the health monitoring system for human regional network. The steganography technologies monitor patients' health safety and provide patients with data confidentiality and identity authentication. Orphanidou [4] reviewed big data applications of physiological signals, pointed out how the applications use physiological signals to provide real-time support for medical decision making in both clinical and family settings, and need to be overcome in clinical practice. Tartan et al. [5] proposed a heart rate monitoring system based on mobile devices and geographical location, which can monitor physiological signals and send alarm information when abnormal heart rate changes.

The health-care systems [6–9] are data-distribution domains where many physiological signals are generated, stored, scattered, and accessed daily by using RFID. Yuri álvarez et al. [6] described that the contribution of RFID technology can improve medical services, can offer hospital tracking of patients, drugs, and medical assets, and can improve the efficiency and safety of electronic medical applications. Martinez Pérez et al. [7] used RFID technology in the ICU (information management system) to track ICU patients' admission, nursing plan, life monitoring, prescription, and drug management process, improving the quality of patients' care during hospitalization. Adame et al. [8] proposed the monitoring systems for intelligent healthcare which provides location status and tracks patients and health-care assets. Omar et al. [9] proposed the reliable, secure, and privacy-based medical automation and organizational information management system that can provide real-time monitoring of vital signs of patients during hospitalization for intelligent patient management.

The literatures [11–15] have been tremendous concentration in blockchain applications. Xu et al. [11] provided a decentralized resource management framework based on blockchain by studying resource management issues. Aiqing and Xiaodong [12] proposed a blockchain-based security and privacy protection sharing protocol to improve the diagnosis of electronic health systems. The private blockchain is responsible for storing personal medical information (PHI), while alliance blockchain keeps the secure index record of PHI. Dubovitskaya et al. [13] proposed a framework for sharing EMR data for cancer patients based on the blockchain and implemented. Lebech et al. [14] used multisignature blockchain protocol for diabetes data management and access control, as well as sharing and encryption. The new approach helps to share diabetes data more effectively in different institutions. Yue et al. [15] proposed the medical data gateway (HGD) architecture based on blockchain, which enabled patients to safely own, control, and share the data without infringing privacy.

When different research institutions share the physiological signals, the issues of privacy and security are the primary focus of research institutions because the physiological signals include the sensitive information, and the attackers are continually trying novel approaches to steal information. In order to meet the privacy needs and deal with the security problems, medical databases which use blockchain and fog computing technology are proposed.

The enhanced trusted sharing physiological signals model features highly secured data encryption and decryption schemes. The model requires permission from the blockchain network to share patient information among medical staff. The proposed model encrypts and analyzes the physiological signals through the blockchain network, big data analysis technology, and AI technologies. Kamel et al. [16] pointed out that blockchain technology is becoming more and more important in the research of medicine and medical care, proposed eight solutions of blockchain application in medical care, and predicted that blockchain and AI solve various medical problems in the future. Jen Hung et al. [17] used blockchain in the drug supply chain to create transparent drug transaction data, prevent counterfeit drugs, and protect public health.

The abovementioned research findings do not apply blockchain to RFID systems. However, the protocol [18] proposed the RFID system based on blockchain and did not apply fog computing to medical fields. It is our innovative work to propose RFID protocol based on fog computing and block chain technology in medical systems.

RFID protocol framework based on fog computing and blockchain is used for medical big data collection and data privacy protection [19–21]. Gu et al. [19] proposed a security and privacy protection solution for fog computing, which designs a framework for security and privacy protection using fog computing and a privacy leakage based on context-based dynamic and static information to improve health and medicine infrastructure. Silva et al. [20] proposed a medical records management architecture based on fog computing. The architecture used blockchain technology to provide necessary privacy protection and to allow fog nodes to execute authorization processes in a distributed manner. Guan et al. [21] discussed data security and privacy issues in fog computing. They pointed out that the data security and privacy challenges posed by fog layers and data protection technologies in cloud computing cannot be directly applied to fog computing. Patel added the fog computing in the original blockchain medical data sharing sequence model [22]. Tang et al. [23] proposed a new game theory framework to improve the mining efficiency of blockchain network and maximize the total benefits of blockchain network. In order to improve the diagnosis of an electronic medical system, Zhang and Lin [12] proposed a security and privacy protection based on the blockchain PHI sharing (BSPP) scheme. The consensus mechanism (private blockchain and joint blockchain) is constructed by designing a blockchain data structure.

3. Mutual Authentication Protocol Using IMDs

The presented mutual authentication protocols for the WISP have two modes: the regular mode shares the IMD and the same credentials; the emergency mode is initiated when one of the following status appear. The IMD credentials are not

shared by the programmer; the patients cannot communicate with the shared credentials; and the credentials configured are expired.

3.1. The Threats and Its Influence on the Medical Record. The threats and its influence on physiological signals are as follows: privacy, equity, consent, and patient governance in health information collection; discrimination in information applications; and handling data breaches.

Because of newly developing data collection and storage technologies to collect and analyse vast amounts of data, the technologies (RFID, blockchain, and artificial intelligence) enable more human experience. While strict clinical testing is still required for handling data breaches, the technologies will fuel a new age of precision medicine in various methods, as shown in Table 1.

3.2. Physiological Signals Data Privacy Rules. While physiological signals are the lifeblood of today's digital society, numerous people are not fully aware of appropriate data collection and processing. The privacy issues are the concerns in the process of generating data. It is more significant to be considered privacy protection in healthcare, where personal physiological signals consist of a large percentage of the data. The rules and regulations guide the process of data generation, transmission, access, and exchange. The privacy storage rules are as follows: entitles patients more control over physiological signals; establishes boundaries of physiological signals' use and release; protects the privacy of physiological signal; enables patients to make choices wisely; and enables patients to be aware of methods for preventing data leakage. It is completely important to maintain the security and privacy of physiological signals by using RFID, fog computing, and blockchain.

3.3. Security Attacks and Requirements for IMDs. This part shows IMDs' main security attacks [10] and discusses the security requirements in Figure 3. Table 2 explains the symbols and definitions of all the authentication protocols.

3.4. Mutual Authentication Scheme in the Emergency Mode. The IMD and programmer can securely produce and offer the major key which is extracted from the patient's data by executing the presented mutual authentication protocol's emergency mode in Figure 4.

Step1: the reader initiates the presented mutual authentication protocol's emergency mode by transmitting the synchronization request $M_1 = (ID_R, N_R,$ and flag) to the IMD.

Step2: WISP computes features $V = \text{RandPermute}(F_W \cup F' W)$ and sends V to the reader.

Step3: the reader computes $K_{bio} = H(Q)$ and sends $M_3 = (ID_R, I, \text{HMAC}(K_{bio}, I|Q|ID_R))$ to WISP.

Step4: if the number of matching characters is greater than the predefined threshold, the WISP calculates $K'_{bio} = H(Q)$, and verifies $K'_{bio} \stackrel{?}{=} K_{bio}$. If the key is successfully confirmed, WISP generates N_W and computes $K = H(K_{bio} | N_W)$ and $K' = H(K | N_W)$. WISP admits the reader by transmitting $M_4 = ((N_W, ID_W)_{Kbio}, \text{HMAC}(K_{bio}, N_R|N_W|ID_W))$.

Step5: in order to determine (N_W, ID_W), the reader decodes the message's first part using K_{bio}. After that, it verifies the authenticity of (N_W, ID_W) by employing HMAC function and comparing the result to the received message's second section. If they are equal, the reader calculates $K = H(K_{bio} | N_W)$ and $K' = H(K | N_W)$ and then sends $M_5 = (Seq_1, \text{HMAC}(K', N_W | Seq_1))$. The reader sends messages (K', Seq_1) to the programmer.

Step 6: WISP verifies the session keys' equality. IMD collects the key of session and the relevant sequence number.

Two modes (emergency mode and regular mode) have the same shortcomings. First, neither model talks about how to store large amounts of data on the database. Second, both models have secret key leakage attacks and tracking attacks. Third, neither model uses cloud storage technology or blockchain technology.

3.5. Attacks for Mutual Authentication Protocol in the Emergency Mode

3.5.1. The Reader Impersonation Attacks. The reader computes $K_{bio} = H(Q)$ and then sends $M_3 = (ID_R, I, \text{HMAC}(K_{bio}, I|Q|ID_R))$ to WISP.

In order to simplify the analysis steps, the steps 3–6 in Figure 4 are omitted here. The tracing attacks in the emergency mode have three phases.

(1) The testing phase: the attacker chooses the target tag R^*, monitors the first round $({}^1M_1, {}^1M_2, {}^1M_3)$ to R^*, and obtains the outputs keys ${}^1K_{bio} = H(Q)$, and the reader applies ${}^1M_3 = (ID_R, I, \text{HMAC}(K_{bio}, I|Q|ID_R))$ to WISP.

(2) The reader impersonation attacks phase: the attacker (the counterfeit reader R') chooses the monitored information ${}^1M_1$. The attacker monitors the output information $({}^2K_{bio} = H(Q), {}^2M_3 = (ID_R, I, \text{HMAC}(K_{bio}, I|Q|ID_R)))$ in the second round.

(3) The decision phase: the adversary obtained the values $({}^1K_{bio}, {}^1M_3)$ and $({}^2K_{bio}, {}^2M_3)$. If $({}^1K_{bio}, {}^1M_3) \neq ({}^2K_{bio}, {}^2M_3)$, and the attacker confirms that R^* is not R' with the probability 1; if $({}^1K_{bio}, {}^1M_3) = ({}^2K_{bio}, {}^2M_3)$, the attacker makes sure that R^* is the counterfeit R'. Therefore, the protocol does not meet the weak indistinguishability property and suffers from the reader impersonation attacks.

3.5.2. Reducing the Calculation Cost of Reader and WISP. In order to reduce the computation of the whole systems, the HASH computational expense of the reader and WISP are high, the proposed protocol uses the PRNG function to replace HASH function.

Table 1: Audiences and influence functions of medical record.

Audiences	Influence functions
Patients	Promote diagnoses and identification of physiological signals, facilitate preventive care, and reduce costs
Doctors	The rigorous diagnosis, treatment choices, monitoring disease progression, therapy response, and patient susceptibility
Researchers	Perform large-scale disease modelling and efficacious therapies
Clinics	Risk estimation, forecasting relapse possibility, designing criteria for discharge/readmission, predicting mortality, and conveying potential crisis episodes

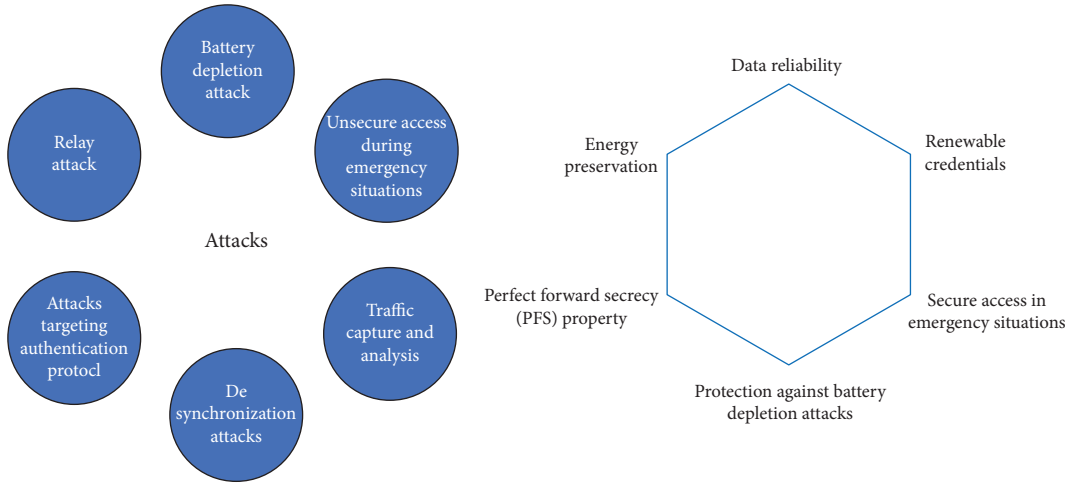

Figure 3: Security attacks and requirements for secure IMDs.

Table 2: Symbols and definitions of the enhanced RFID system privacy protection authentication protocol.

Symbols	Definitions
C_i; TID_T^i; COUNT	Challenge from the DB to reader; temporary identity; count
R_i; R_i^*; N_s	Response for the reader; $R_i \oplus N_s$; random number generated
Res_s; CRP $(C_i R_i)$; K_i	$h(\text{COUNT} + 1 \| Ri \| R_i^*)$; i^{th} challenge-response; i^{th} key
PUF_T;h (.); $\oplus$; $\|(\|)$	PUF for the tag T; one-way hash function; XOR; concatenation
K_H; K_P; K_D	Hospital; patient; doctor

3.6. Mutual Authentication in the Regular Mode. The regular mode ensures the secure data exchange, as shown in Figure 5.

Step1: the reader sends $M_1^{'} = (N_R, ID_R, \text{flag}, \text{HMAC}(K, N_R \,|ID_R))$ in the regular mode.

Step2: WISP can confirm the received request's freshness and the reader's authenticity. If the organized primary key has not run out, the received request from the keys is authenticated by the WISP. By contrary, the WISP rejects access by sending the denial message.

Step3: WISP computes $K' = H(K \,|\, N_W)$, and sends $M_2^{'} = ((\text{Nbr}, N_W, ID_W)_K, \text{HMAC}(K, N_R| N_W|ID_W))$ to reader.

Step4: when receiving the messages, the reader decodes the first part of the messages to obtain (Nbr, N_W, and ID_W).

Step5: after verifying successfully, the reader calculates the key value K' using N_W and sends the messages $M_3^{'} = (\text{Seq}_1, \text{HMAC}(K', N_W \,|\, \text{Seq}_1))$.

Step6: WISP can confirm the message's freshness and the keys' equality computed on both sides. WISP increments the Nbr parameter which represents the total number of session keys which originated from the primary key.

Step7: WISP delivers the messages (K', Seq_1, Nbr) to awaken IMD antenna.

The attacks for mutual authentication protocol in the regular mode.

3.6.1. Secret Key Disclosure Attacks. The attackers monitor the delivery messages and reveal the secret keys as follows:

In Step1, $M_1^{'} = (N_R, ID_R, \text{flag}, \text{HMAC}(K, N_R \,|ID_R))$, the attacker discloses ID_R

In Step3, $M_2^{'} = ((\text{Nbr}, \text{NW}, \text{IDW})\ K, \text{HMAC}(K, \text{NR}|\text{NW}|\text{IDW}))$, the attacker discloses IDW

In Step7, (K', Seq1, Nbr), the attacker discloses K'

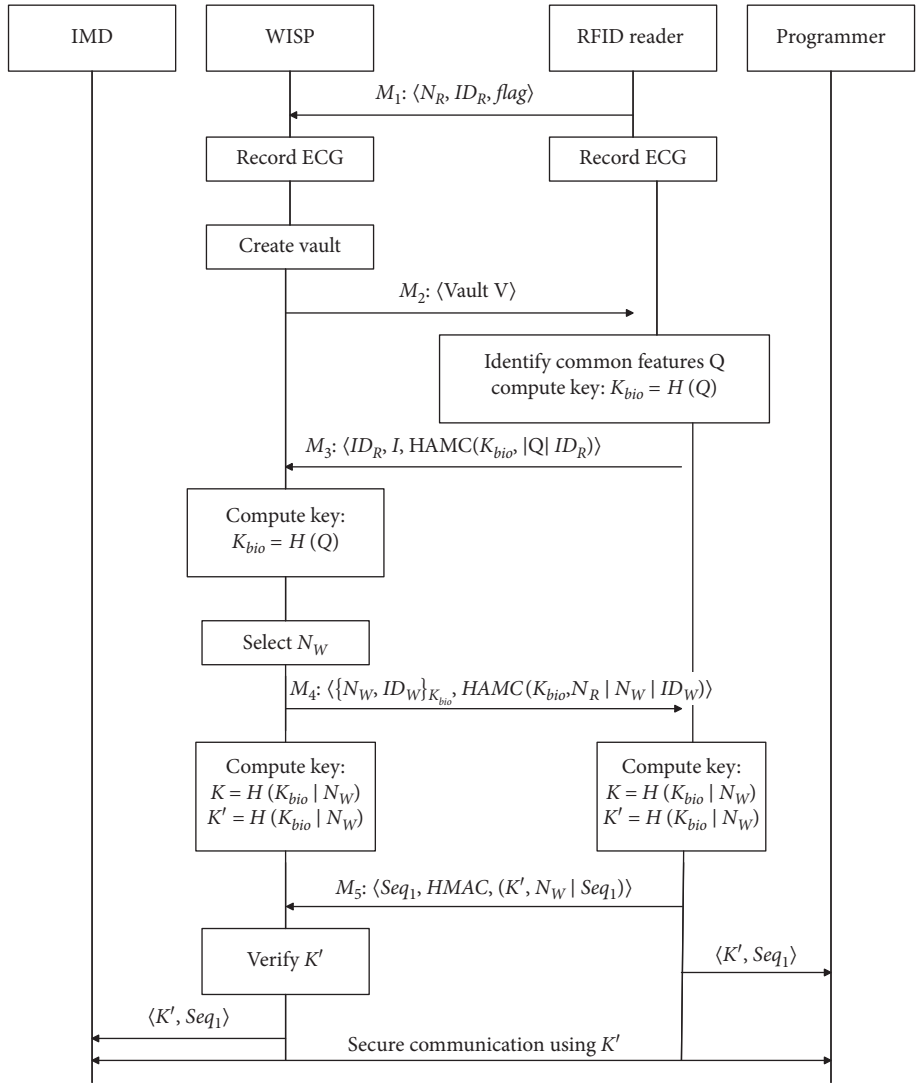

Figure 4: Mutual authentication protocol in the emergency mode (protocol 1).

3.6.2. The Tracing Attacks. In order to simplify the analysis process, the steps 3–6 in Figure 5 are omitted here. The tracing attacks have three phases.

(1) The testing phase: the attacker chooses the target tag T^*. Then, she/he monitors the first round ($^1M_1$, $^1M_2$, $^1M_3$, $^1M_4$) to T^* and obtains the outputs keys ($^1\mathrm{ID_R}$, $^1\mathrm{ID_W}$).

(2) The tracing attacks phase: we assume that the tag set (T^0, T^4,... T^i) includes T^* and the counterfeit tag T'. The attacker monitors the keys ($^2\mathrm{ID_R}$, $^2\mathrm{ID_W}$) in the second round.

(3) The decision phase: the adversary obtained the values ($^1\mathrm{ID_R}$, $^1\mathrm{ID_W}$) and ($^2\mathrm{ID_R}$, $^2\mathrm{ID_W}$). If ($^1\mathrm{ID_R}$, $^1\mathrm{ID_W}$) ≠ ($^2\mathrm{ID_R}$, $^2\mathrm{ID_W}$), the attacker confirms that T' is not T^* with the probability 1; if ($^1\mathrm{ID_R}$, $^1\mathrm{ID_W}$) = ($^2\mathrm{ID_R}$, $^2\mathrm{ID_W}$), the attacker makes sure that T^i is T^* (the counterfeit tag T'). Therefore, the original protocol in the regular mode does not meet the weak indistinguishability property and suffers from the tracing attacks.

3.6.3. Medical Framework Based on RFID, Blockchain, and Artificial Intelligence. At present, amounts of patients have the comprehensive datasets which consist of clinical history (the genetic, lifestyle data, drug, and blood biochemistry). In addition, the consumer companies and the pharmaceutical are willing to pay much money for the vast personal physiological signal data applied to train their AI model via using the machine learning. We proposed the medical framework based on RFID, blockchain, and artificial intelligence, as in Figure 6.

Previous researches based on RFID, blockchain, and artificial intelligence mainly focused on the medical application, respectively. The studies improve the time proficiency of physiological signal data processing and contribute to medical data management by combining three technologies. The effectiveness of the medical framework involves low resource usage, large computation time, more energy, less power, and low memory consumption (Algorithm 1).

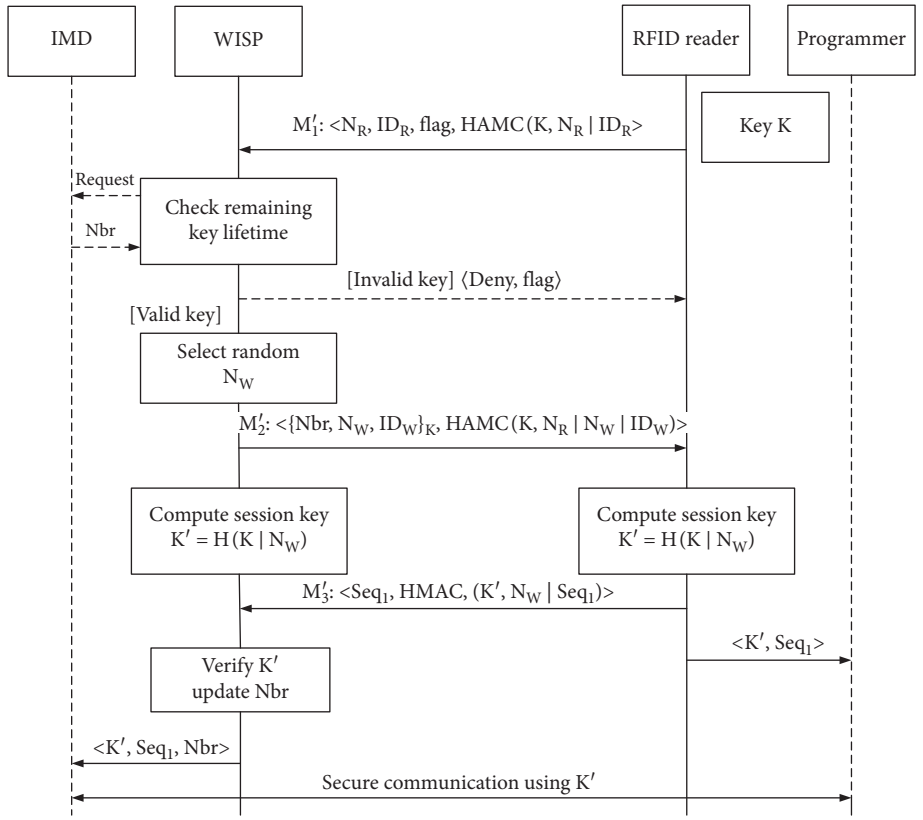

Figure 5: Mutual authentication in the regular mode (protocol 2).

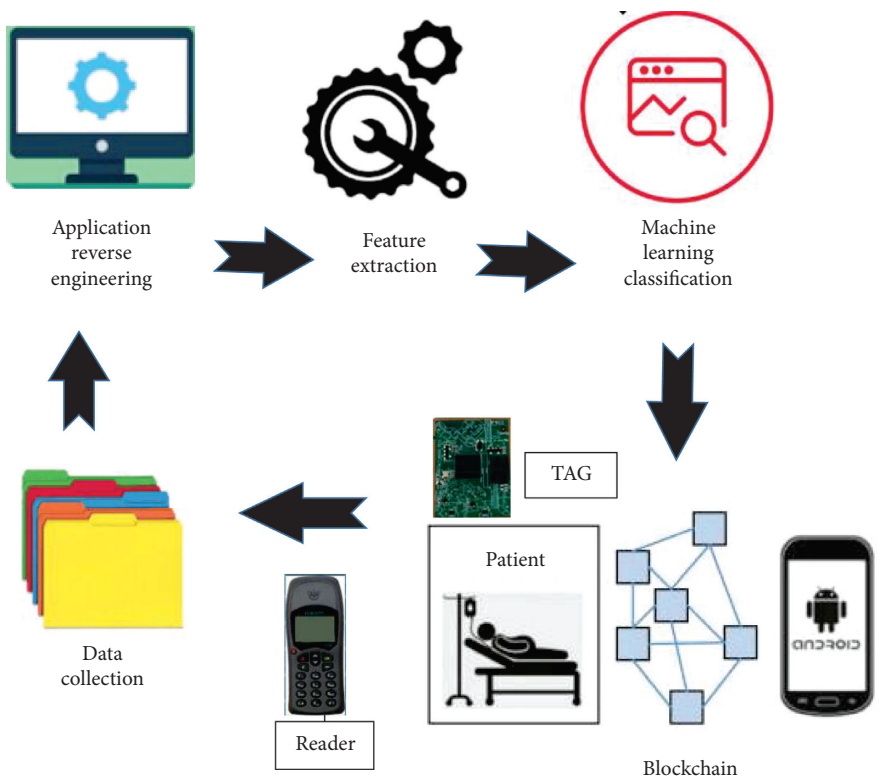

Figure 6: The medical framework based on RFID, blockchain, and artificial intelligence.

The proposed protocol in the emergency mode (Figure 7) is as follows:
(1) Step 1
(2) The reader initially generates the random numbers (N_R, ID_R, $flag = 1$);
(3) Calculate $A = N_R \oplus ID_R$;
(4) Broadcast M_1;
(5) Step 2
(6) Compare ID_R;
(7) if $ID_R \neq A \oplus N_R$ then
(8) Process termination;
(9) else
(10) {
(11) set up V=*RandPermute* ($F_W \cup F'_W$);
(12) Send M_2 to reader
(13) M_2 in V;
(14) Step 3
(15) for each f_r^i do
(16) if $f_r^i = F_R$ then
(17) The reader and the tag match each other;
(18) Calculate $K_{bio} = H(Q \| N_R)$;
(19) Send the message $M_3 = (I\ HMAC(K_{bio}, I|Q|ID_R))$;
(20) Step 4
(21) If the number of matched characteristics is greater than the predetermined threshold in WISP
(22) Calculate $K'_{bio} = H(Q||N_R)$;
(23) if $K'_{bio} = Kbio$ then
(24) if $HMAC(K'_{bio}, I|Q|ID_R) = HMAC(K_{bio}, I|Q|ID_R)$;
(25) Verify success, generate random number N_W, Calculate $B = N_W \oplus ID_W$;
(26) Calculate $K = H(K_{bio} | N_W)$, and new key $K' = H(K | N_W)$;
(27) Send $S1 = HMAC(K_{bio}, N_R | N_W | ID_W)$ $M_4 = <\{N_W, ID_W\}_{K_{bio}}, HMAC(K_{bio}, N_R | N_W | ID_W)>$
(28) Step 5
(29) if K_{bio} (reader) = K_{bio} (tag), obtain (N_W, ID_W);
(30) Calculate $S2 = HMAC(K_{bio}, N_R | N_W | ID_W)$;
(31) if S2 = S1 then
(32) Calculate (K, K′) $K = H(K_{bio} | N_W)$, $K' = H(K | N_W)$;
(33) Send $< Seq_1, HMAC(K', N_W | Seq_1) >$ to WISP
(34) Step 6
(35) WISP verifies the session keys' equality calculated by both sides (WISP, reader)
(36) If the session keys calculated on both sides are equal
(37) WISP records (K′, Seq1) to awaken the IMD antenna
(38) When IMD detects the request, begins to collect (K′, Seq1), and employs them to exchange data securely with the programmer
(39) };

Algorithm 1: The suggested mutual authentication protocol in the emergency mode.

4. Security and Performance Analysis of Protocol 3 and Protocol 4

The protocol 3 and protocol 4 are more suitable to store physiological signals in medical applications.

4.1. Security Analysis for Protocol 3. Scheme 3 overcomes the weaknesses of protocol 1, and the protocol 4 overcomes the weaknesses of protocol 2.

4.1.1. The Reader Impersonation Attacks Resistance. In order to resist the reader impersonation attacks, the reader calculates $K'_{bio} = PRNG(Q||N_R)$ using N_R. Even if the attacker monitors the output information ($^2K_{bio} = PRNG(Q||N'_R)$, $^2M_3 = (ID_R, I, HMAC(^2K_{bio}, I||Q||ID_R))$) using the new nonce N' R in the second round, the attacker cannot counterfeit the original reader.

4.1.2. Key Leak Attack Resistance. In order to resist the key leak attacks, WISP calculates $B = N_W \oplus ID_W$; the reader calculates $K = PRNG(K_{bio}||N_W)$; and $K' = PRNG(K||N_W)$.

4.1.3. Provision of Data Integrity Verification. In order to meet data integrity, the protocol 3 has used HMAC hash calculation to protect the integrity of messages ($K1$, Seq_1).

4.1.4. Provision of Scalability and Efficiency. In order to satisfy the scalability, each tag identifier does not match the corresponding key in DB. Therefore, the identifications of tag keys do not match one by one in DB of the improved

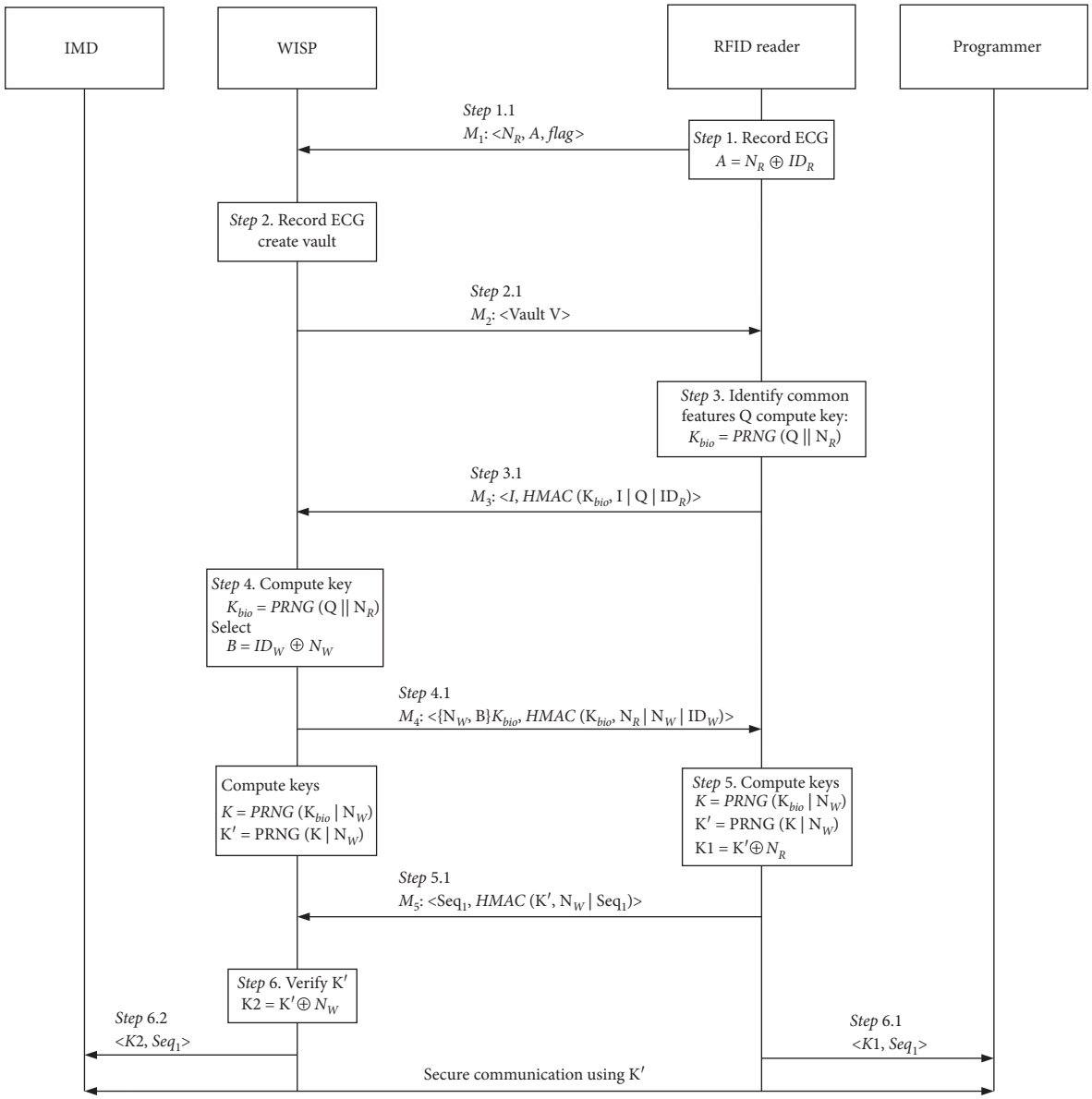

Figure 7: The proposed mutual authentication protocol in the emergency mode (protocol 3).

protocol, which guarantees the efficiency of tag authentication and satisfies the scalability property.

4.1.5. Replay Attacks Resistance. The attacker replays the messages to authenticate by monitoring the previous information. In order to resist replay attacks, all messages are encrypted by using the random numbers (*Nbr*, N_W, and N_R) and combined with PRNG function.

4.1.6. Provision of Data Integrity Verification. In order to achieve the property of data integrity, we have used PRNG calculation $K' = PRNG\ (K|N_W)$ to protect the integrity of K'.

4.2. Security Analysis for Protocol 4

4.2.1. Secret Key Disclosure Attacks Resistance. In order to achieve anonymous and privacy requirements in improved protocol 4, the protocol uses the XOR function to encrypt the transmitted keys as follows:

$$B = ID_W \oplus N_W,\ K1 = K' \oplus \mathrm{N_R},\ K2 = K' \oplus N_W.$$

4.2.2. Tracing Attacks Resistance. The key updating mechanism $K' = PRNG\ (K|N_W)$ involves the i^{th} keys and the nonces (N_W, K). The i^{th} key K_i cannot be cracked by the $(i+1)^{th}$ keys K_{i+1} and the i^{th} sessions. The reasons are that PRNG functions protect the parameters by the encrypted messages. Therefore, the enhanced protocols resist the tracing attacks.

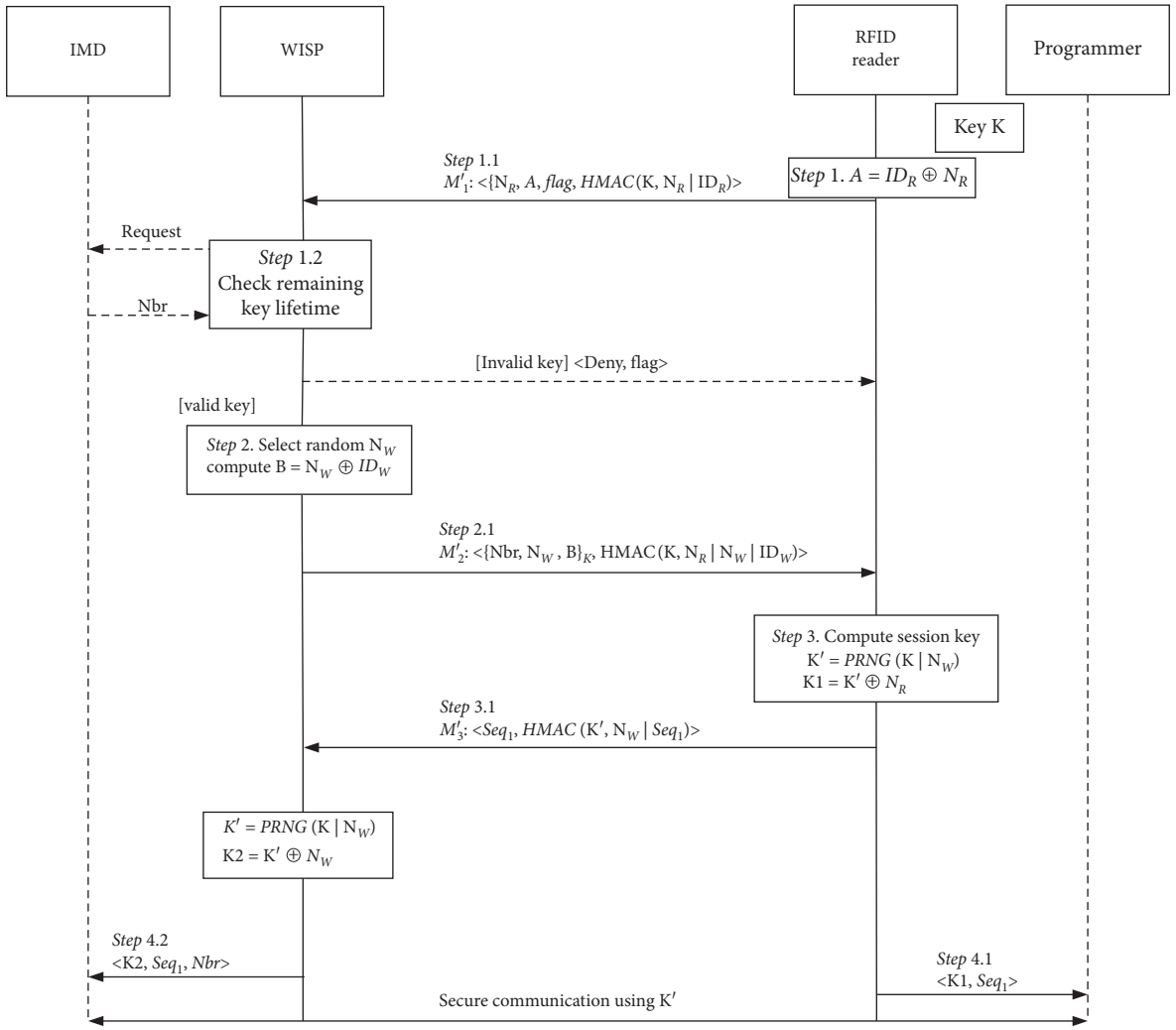

Figure 8: The proposed mutual authentication protocol in the regular mode (protocol 4) (Algorithm 2).

4.2.3. Availability and Desynchronization Attacks Resistance. In order to provide anonymity, the communication components (tag and DB) update the shared messages after completing the conversation. If the opponents destroy the updating process, the authentication scheme is subjected to desynchronization attacks. In order to guarantee the confidentiality and anonymity of K, the messages synchronously should be updated. In addition, the attacker knows the shared key K' during the updating processes, which is protected by the random numbers (N_W, N_R). The improved protocol is desynchronization resistance.

4.3. The Comparisons of Security and Performance Analysis. Table 3 lists the computational cost for five protocols. The computational costs of tags in protocol 3 are 3PRNG + Xor, and the computational costs of tags in protocol 4 are 2PRNG + Xor. The safety performances of the enhanced protocols are superior to other schemes. Compared with the original protocol 1 and protocol 2, the improved protocols support the security enhancements and ensure the function such as integrity, efficiency, and user privacy.

5. Blockchain Framework for Security and Privacy Storage and Sharing

A framework is developed to share physiological signals' cross domain and build the radiological studies' ledger and patient-defined access permissions by applying the blockchain as the distributed data store. Relative disadvantages of the framework include the privacy's complexity and security models. Ultimately, the large-scale feasibility of the approach remains to be demonstrated.

The peculiar health-care technologies are required, such as parallel processing, distributed data network, scalable storage, frameworks, and infrastructures. The fog computing is economical and customizable, since fog computing handles these complex problems in the virtual environment and only needs to pay for the used services and resources.

The sharing physiological signals systems are important in different medical institutions, but the current infrastructure for transmitting physiological signals relies on the trust third-party intermediaries. We propose the framework of cross-domain sharing image where the

The proposed mutual authentication protocol in the regular mode is in Figure 8 as follows:
(1) Step 1
(2) The reader generates (N_R, ID_R, flag = 0);
(3) Calculate $A = ID_R \oplus N_R$ and $K = H(N_R|ID_R)$;
(4) Transmit $M_1' = < N_R, ID_R, flag, HMAC(K, N_R \mid ID_R) >$
(5) When WISP receives the request, it confirms that the primary key is expired and verifies that how many session keys which originated from the primary key exceeds the predetermined threshold
(6) if t < T then
If the primary key has not expired, WISP receives the messages
(7) else the key expired, access denied;
(8) Step 2
(9) After WISP successful authentication, the random number N_W is generated;
(10) Calculate $K' = H(K \mid N_W)$, $B = ID_W \oplus N_W$;
(11) Transmit $M_2' = < \{Nbr, Nw, I\,Dw\}_k, HMAC(K, N_R|N_W|ID_w) >$
Calculate $S1 = HMAC(K, N_R|N_W|ID_w)$;
(12) Step 3
(13) After receiving the messages, the reader starts to parse the first part of the message through the key K to obtain (Nbr, NW, IDW);
(14) Calculate $S2 = HMAC(K, N_R|N_W ID_w)$;
If S2 = S1 then
The message is true;
Calculate $K' = PRNG(K|N_W)$, $K1 = K' \oplus NR$;
(15) Transmit $M_3' = Seq_1, HMAC(K', N_w|Seq_1)$
(16) Step 4
(17) Based on the received HMAC, WISP can confirm the timeliness of the message and the equality of the session keys calculated on both sides
(18) After verifying successfully, Nbr++, $K2 = = K' \oplus NW$;
(19) WISP records (K2, *Seq*1, *Nbr*) to awaken the IMD antenna
(20) When IMD detects the request, collects (K1, *Seq*1), and employs them to exchange data securely with the programmer.

Algorithm 2: The proposed mutual authentication protocol in the regular mode.

blockchain is used as the distributed data storage to establish patient-defined access rights. The blockchain framework is verified to eliminate the access permission of the third-party to protected physiological signal information, meets many standards of the interoperable medical system, and easily generalizes to fields beyond physiological signal. We summarize the framework based on blockchain to allow patients to securely grant electronic access permission to their physiological signal data and describe the advantages and disadvantages of the approach.

The actual transmission of physiological signals requires the physiological signals receiver who transmits the signed request to the URL endpoint. The individual service is the requesting entity that the access permission of the physiological signals study is authorized to by the owner (patient). The studies of all patients' physiological signals result in the huge blockchain, far too large to download, store, and validate for nodes running on mobile devices. The size of the blockchain has been proven to be the limiting element for chains storing the transactional data.

Considering all of these factors, sharing the physiological signals by using blockchain helps the interoperable health system and has greater ability to access patients' physiological signals electronically.

5.1. Physiological Signals Data Sharing Model Based on Blockchain [22]. Intelligent contract based on blockchain is used to promote the security analysis and management of medical sensors. Intelligent device invokes intelligent contract and writes records of all events on blockchain. The intelligent contract systems support real-time patient monitoring and medical intervention by sending notifications to patients and medical professionals. The provider of medical records can modify the physiological signals, but it needs patient's consent, and the patient can assign access authority to medical records.

When applying blockchain to the construction of the credit system, we promote the collection and supervision of credit information in the medical field and build the new relationship platform. It is significant to the improvement of the credit system construction. According to the unified evaluation criteria, the credit rating is evaluated, the result of the rating level is publicized on the platform of block chain, the credit rating is rewarded, and the violation of credit is punished, so as to strengthen the construction of the credit system in the medical field in the real sense.

The asymmetric information encryption methods need two keys: public key and private key. After the physiological signals are encrypted with public key, only the corresponding private key can be used for decryption. On the

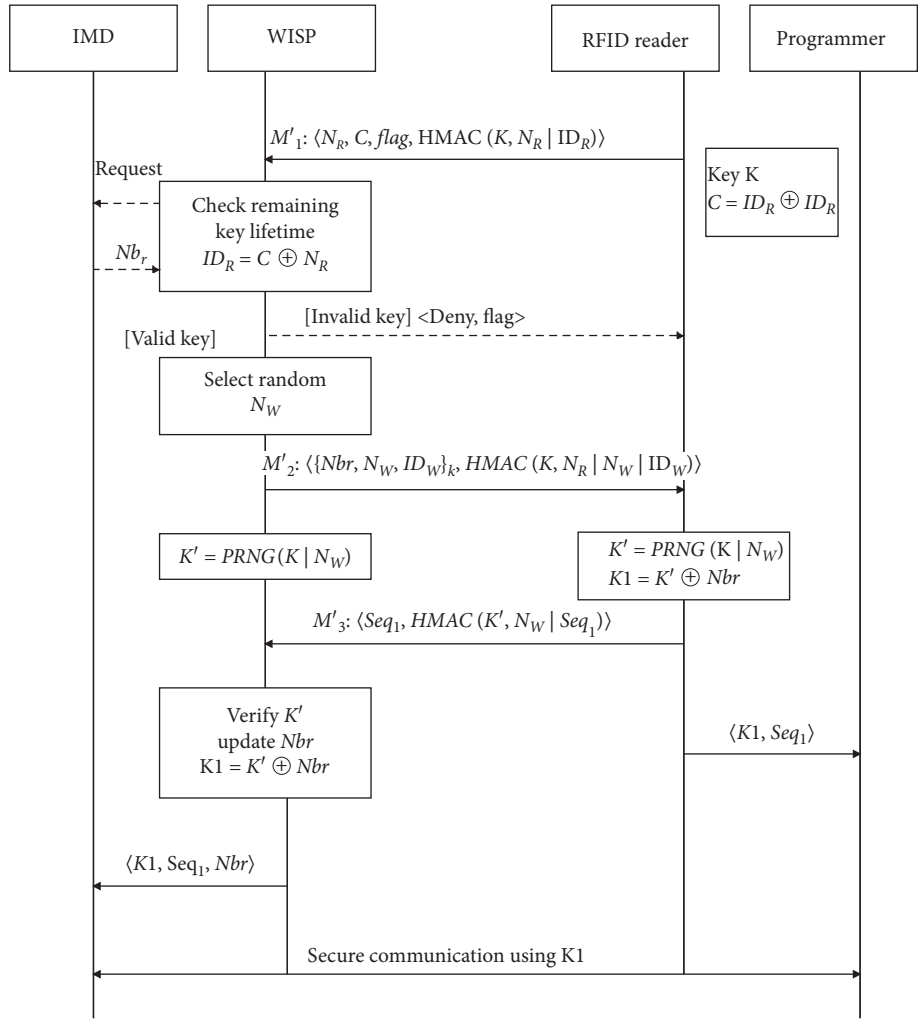

Figure 9: Secure communication protocol between the IMD and the programmer (protocol 5) (Algorithm 3).

contrary, if the private key is used to encrypt data, only the corresponding public key can be used for decryption. If the blockchain can be grafted, scientific research institutions understand the probability of disease occurrence, the occurrence of accidents, the level of hospital management, and claims cases and other actual situations.

(1) Use the fog-based blockchain and fog warehouse to store medical data, as shown in Figure 10.

  (1) List of medical research and patients in each institute.

  (2) Patients are authorized to access the entity set of each study. The entities are represented by the common part of the asymmetric key pair on the blockchain.

(2) Definition study: the transaction builds the patient as the master of a UID which is the specific unique identifier and the source as the creator. Tuples stored in block chains are transactions with double signatures, similar to documents with signatures from patients and hospital representatives. The patients claim that the definition study has received the medical diagnosis in the hospital, which confirms the statement and promised to provide the study in the previous block. The patient's signature declaration is obtained through the mobile application, which shares and stores the values required allowing access to the transaction in the future. Then, the hospital signs the follow-up information of the patients and broadcasts the transaction to the blockchain.

(3) Allow access: the transaction allows the owner of the medical information research to authorize the other party to retrieve its medical data. Patient K_P signs a transaction to grant the function to doctor K_D. The signed verification blocks are embedded in blockchains. As shown in Figure 11, patients publish the transaction after verifying the key with the doctor through the APP platform. The patient can be authorized to the legitimate doctor or institution, and the doctor can associate any medical information received with the correct local medical record number.

The middle column (Block Chain Medical Data Sharing Sequence) describes the interaction between entities and judgments in each stage and reflects the sharing medical

The programmer can use the session key calculated by the protocol to establish the secure communication after IMD authenticates the programmer in Figure 9.

(1) Step 1:
(2) The reader initially generates (K, $C = ID_R \oplus N_R$) and transmits the values $M_1^{'} = (N_R, C, flag, \text{HMAC (K, } N_R \mid ID_R))$ to the WISP.
(3) Step 2:
(4) The IMD returns *Nbr* and updates $ID_R = C \oplus N_R$.
(5) Step 3:
(6) If the key is valid then
(7) The WISP selects NW and transmits the values $M_2^{'}$=((*Nbr*, N_W, ID_W), HMAC (K, $N_R \mid N_W \mid ID_W$)) to the reader.
(8) else
(9) The WISP transmits the sequences (Deny, flag) to the reader.
(10) Step 4:
(11) The WISP updates K′ = PRNG (K | NW), and the reader updates K′ = PRNG ($K \mid N_W$) and $K1 = K' \oplus Nbr$. The reader sends the value M3 = (*Seq*1, HMAC (K′, N_W, *Seq*1)) to the WISP and sends the messages (K1, *Seq*1) to the programmer.
(12) Step 5:
(13) The WISP identifies K′ by comparing the value K′ of the WISP with the K′ value of the reader. The WISP updates *Nbr*, $K_1 = K' \oplus Nbr$, and sends (K_1, *Seq*1, *Nbr*) to the IMD.

Algorithm 3: Secure communication protocol between the IMD and the programmer.

Table 3: The comparisons of the performance analysis and safety performance.

Performance	Protocol 1	Protocol 3	Protocol 2	Protocol 4	Protocol 5
F0	No	Yes	No	Yes	No
F1	3H + Xor	3PRNG + Xor	2H + Xor	2PRNG + Xor	1PRNG+2Xor
F2	No	Yes	No	Yes	Yes
F3	No	Yes	No	Yes	Yes
F4	No	Yes	No	Yes	Yes
Attack types	Protocol 1	**Protocol 3**	Protocol 2	**Protocol 4**	Protocol 5
R1	No	Yes	No	Yes	No
R2	Yes	Yes	Yes	Yes	Yes
R3	Yes	Yes	Yes	Yes	Yes
R4	Yes	Yes	Yes	Yes	Yes
R5	No	Yes	No	Yes	Yes
R6	No	Yes	Yes	Yes	Yes

F0: provision of scalability and efficiency; F1: storage cost (tag); F2: blockchain-enabled; F3: cloud computing-enabled; F4: fog computing-enabled. R1: key leak attacks resistance; R2: replay attacks resistance; R3: desynchronization attacks resistance; R4: reader impersonation attacks resistance; R5: tracking attacks resistance; R6: tag impersonation attacks resistance.

information by supporting distributed block chains and out-of-block transactions.

The actual medical data transmission requires the medical data receiver to deliver the signature request to the medical source's URL endpoint which creates the research. Both requests and responses are transmitted through the secure link of the transport layer to prevent eavesdropping. The effective blocks are generated in the timely manner by generating the distributed database with access permissions and stimulating the block generator in some way. Only those nodes with security deposits can participate in the expansion of the chain, and any node with misconduct will be forced to abandon its investment. The nature of blockchain provides the direct audit of the activity of each node such as the number of blocks generated and the failure status of the blocks generated. The node operator can prove the node ownership by using the private key which is corresponded to the identity public key of the node to sign the message. The enhanced model adds the fog computing in the original blockchain medical data sharing the sequence model [22], which is used to construct the blockchain for medical data sharing.

We have showed the technology fundamentals of blockchain and provided a summarization of the blockchain application that can be used as a tool to allow the patient-controlled, physiological signal's cross-domain sharing without the central authority. In particular, we highlighted the way blockchain satisfies many requirements of the interoperable health system. However, these technologies also have several important limitations, and the relative merits of existing alternatives must be considered before any large-scale and blockchain-based application for sharing physiological signals.

When receiving query request, the physiological signal data source verifies the correctness of the signature, ensures that the hashed data matches the previously published data for K_P-owner via Block *B*, and confirms that the K_P-owner has allowed the requestor access to these physiological signal data via Block *C*. If meeting all the conditions, the response containing the physiological signal study is returned from

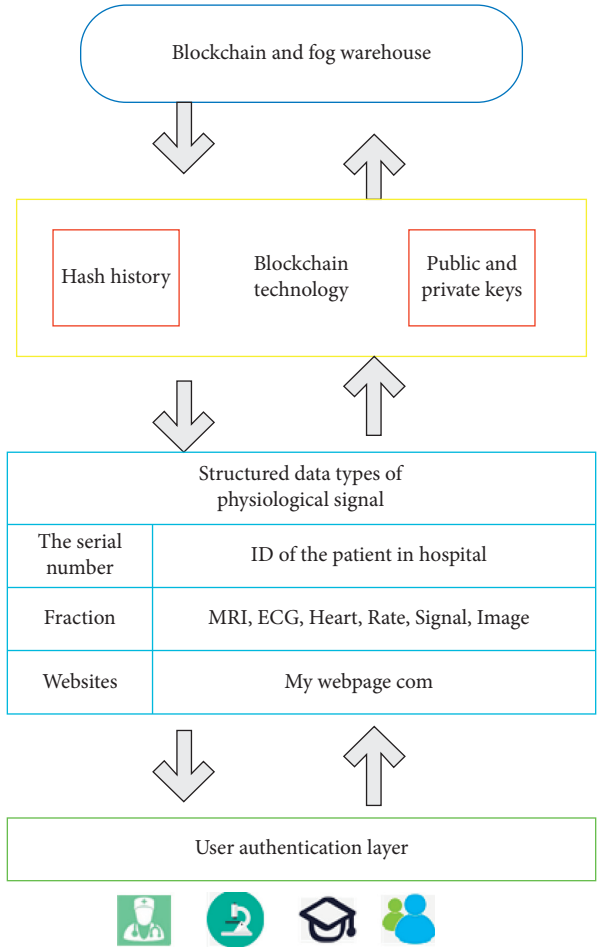

Figure 10: Blockchain based on fog warehouse.

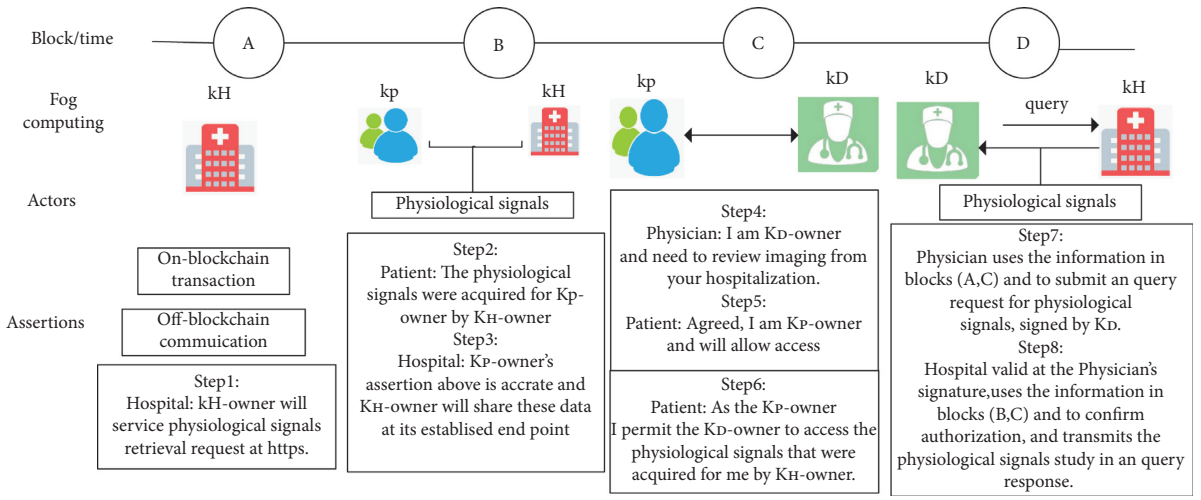

Figure 11: Blockchain medical data sharing sequence diagram based on fog computing.

the source. In order to prevent eavesdropping, the requests and responses are sent to prevent eavesdropping. The specific steps of blockchain medical data sharing sequence diagram are as follows:

Step 1: for hospital (K_H-owner), K_H-owner will service physiological signals retrieval requests at https by using on-blockchain transaction and off-blockchain communication.

Step 2: for the patient (K_P-owner), the physiological signals are acquired for KP-owner and KH-owner.

Step 3: for hospital, K_P-owner's assertion is accrate and KH-owner shares the physiological signals at the established endpoint.

Step 4: for physician (K_D-owner), K_D-owner reviews the physiological signals from the hospitalization.

Step 5: for patient, if the patients agree, they are K_P-owner and will allow access.

Step 6: for patient, the patient permit K_D-owner to access the physiological signals that were acquired by KH-owner.

Step 7: physician uses the information in blocks (*A*, *C*) to submit the query request for physiological signals, signed by K_D.

Step 8: hospital valid at the physician's signature, uses the data in blocks (*B*, *C*) to confirm authorization and transmits the physiological signals study in the query response. The requests are sent by the K_D-owner at timepoint *D*.

The ecosystem is consisted of the blockchain nodes and fog storage. For example, one of the main reasons for incorporating fog storage technology into the ecosystem is to supply the offline storage solution, especially for large physiological signals. For security and privacy, the client side would encrypt the physiological signals uploaded to the fog storage. With the maturity of the fog storage, personal storage may be replaced by it.

Most significantly, blockchain technology can create the physiological signal-driven marketplace, where patients can get real return by offering their data to research institutions, pharmaceutical and consumer companies, the application development community, and producing new physiological signal data.

6. Conclusions

We extend the architecture of the IMD with blockchain, RFID, and WISP, which increases the physiological signal data's confidentiality and authenticity. The enhanced RFID protocols provide protection against tracking attacks, readers' impersonation attacks, and secret disclose attacks.

The physiological signal records have proved the importance for the patients, and sharing and acquiring physiological signals is essential for intelligent and advanced medical services. The blockchain application of e-commerce has proven that trusted and auditable transaction in peer-to-peer networking is possible. In the paper, we have introduced a blockchain-based architecture model for physiological signal data on fog computing environment. Our contributions are mainly consisted of the proposed solution and introduction to future medical data directions in blockchain. The paper proposes the outline to show the framework and schemas for dealing with heterogeneous physiological signals. Once the hybrid technologies are integrated, big data systems and AI technology have the potential to offer privacy protection and data sharing and transform healthcare management. In the future, we will focus on heterogeneous physiological signal data issues through fog computing, blockchain, and AI technology in the realistic medical environment.

Data Availability

The paper gives an outline about the framework, and internal working and protocols for handling heterogeneous physiological signal data. Once the hybrid technologies are integrated, big data systems and AI technology have the potential to offer privacy protection and data sharing, transform healthcare management.

Conflicts of Interest

The authors declare no conflicts of interest.

Acknowledgments

This work was supported in part by Jiangsu Postdoctoral Science Foundation (Grant nos. 1701061B and 2017107007); Xuzhou Medical University Affiliated Hospital Postdoctoral Science Foundation (Grant nos. 2016107011, 183822, 53120225, and 53120226); Xuzhou Medical University Excellent Persons Scientific Research Foundation (Grant nos. D2016006, D2016007, and 53591506); the Practice Inovation Trainng Program Projects for the Jiangsu College Students (Grant nos. 20161031308H and 201610313043Y); the Natural Science Foundation of the Jiangsu Higher Education Institutions of China (Grant no. 16KJB180028); and 333 Project of Jiangsu Province (no. BRA2017278).

References

[1] J. P. Rajan and S. E. Rajan, "An internet of things based physiological signal monitoring and receiving system for virtual enhanced health care network," *Technology and Health Care*, vol. 26, no. 2, pp. 379–385, 2018.

[2] O. Faust, Y. Hagiwara, T. J. Hong, O. S. Lih, and U. R. Acharya, "Deep learning for healthcare applications based on physiological signals: a review," *Computer Methods and Programs in Biomedicine*, vol. 161, no. 1, pp. 1–13, 2018.

[3] R. Shanthapriya and V. Vaithianathan, "ECG-based secure healthcare monitoring system in body area networks," in *Proceedings of the 2018 Fourth International Conference on Biosignals, Images and Instrumentation (ICBSII)*, pp. 206–212, IEEE, Montreal, Canada, October 2018.

[4] C. Orphanidou, "A review of big data applications of physiological signal data," *Biophysical Reviews*, vol. 11, no. 1, pp. 83–87, 2019.

[5] E. O. Tartan and C. Ciflikli, "An android application for geolocation based health monitoring, consultancy and alarm system," in *Proceedings of the IEEE 2018 IEEE 42nd Annual Computer Software and Applications Conference (COMPSAC)*, pp. 341–344, IEEE Computer Society, Tokyo, Japan, July 2018.

[6] L. Yuri álvarez, F. Jacqueline, N. Guillermo álvarez et al., "RFID technology for management and tracking: e-health applications," *Sensors*, vol. 18, no. 8, pp. 2663–2678, 2018.

[7] M. Martínez Pérez, C. Dafonte, and Á. Gómez, "Traceability in patient healthcare through the integration of RFID

technology in an ICU in a hospital," *Sensors*, vol. 18, no. 5, pp. 1627–1641, 2018.

[8] T. Adame, A. Bel, A. Carreras, J. Melià-Seguí, M. Oliver, and R. Pous, "CUIDATS: An RFID–WSN hybrid monitoring system for smart health care environments," *Future Generation Computer Systems*, vol. 78, no. 2, pp. 602–615, 2016.

[9] H. Q. Omar, A. Khoshnaw, and W. Monnet, "Smart patient management, monitoring and tracking system using radio-frequency identification (RFID) technology," in *Proceedings of the Biomedical Engineering and Sciences*, vol. 1, no. 2, pp. 1–12, IEEE, Kuala Lumpur, Malaysia, December 2016.

[10] N. Ellouze, S. Rekhis, N. Boudriga, and M. Allouche, "Powerless security for cardiac implantable medical devices: use of wireless identification and sensing platform," *Journal of Network and Computer Applications*, vol. 107, no. 1, pp. 1–21, 2018.

[11] C. Xu, K. Wang, and M. Guo, "Intelligent resource management in blockchain-based cloud datacenters," *IEEE Cloud Computing*, vol. 4, no. 6, pp. 50–59, 2018.

[12] Z. Aiqing and L. Xiaodong, "Towards secure and privacy-preserving data sharing in e-health systems via consortium blockchain," *Journal of Medical Systems*, vol. 42, no. 8, pp. 140–154, 2018.

[13] A. Dubovitskaya, Z. Xu, S. Ryu et al., "Secure and trustable electronic medical records sharing using blockchain," in *Proceedings of the AMIA. Annual Symposium proceedings/ AMIA symposium*, vol. 1, no. 1, pp. 1–13, AMIA Symposium, Washington, DC, USA, January 2017.

[14] C. S. Lebech, S. M. Nibe, K. Thomas, P. Vestergaard, and O. Hejlesen, "How to use blockchain for diabetes health care data and access management: an operational concept," *Journal of Diabetes Science and Technology*, vol. 13, no. 2, pp. 1–14, 2018.

[15] X. Yue, H. Wang, D. Jin, M. Li, and W. Jiang, "Healthcare data gateways: found healthcare intelligence on blockchain with novel privacy risk control," *Journal of Medical Systems*, vol. 40, no. 10, pp. 218–242, 2016.

[16] B. M. N. Kamel, J. T. Wilson, and K. A. Clauson, "Geospatial blockchain: promises, challenges, and scenarios in health and healthcare," *International Journal of Health Geographics*, vol. 17, no. 1, pp. 1–19, 2018.

[17] T. Jen-Hung, L. Yen-Chih, C. Bin, and L. Shih-wei, "Governance on the drug supply chain via gcoin blockchain," *International Journal of Environmental Research and Public Health*, vol. 15, no. 6, pp. 1055–1067, 2018.

[18] K. Harleen, A. M. Afshar, J. Roshan, A. K. Mourya, and C. Victor, "A proposed solution and future direction for blockchain-based heterogeneous medicare data in cloud environment," *Journal of Medical Systems*, vol. 42, no. 8, pp. 156–167, 2018.

[19] J. J. Gu, R. C. Huang, L. Jiang, G. Qiao, X. Du, and M. Guizani, "A fog computing solution for context-based privacy leakage detection for android healthcare devices," *Sensors*, vol. 19, no. 5, pp. 1–16, 2019.

[20] C. A. Silva, G. S. Aquino, S. R. M. Melo, and D. J. B. Egídio, "A fog computing-based architecture for medical records management," *Wireless Communications and Mobile Computing*, vol. 2019, no. 1, pp. 1–16, 2019.

[21] Y. Guan, J. Shao, G. Wei, and X. Mande, "Data security and privacy in fog computing," *IEEE Network*, vol. 32, no. 5, pp. 1–6, 2018.

[22] V. Patel, "A framework for secure and decentralized sharing of medical imaging data via blockchain consensus," *Health Informatics Journal*, vol. 1, no. 1, pp. 1–14, 2018.

[23] C. Tang, C. Li, X. Yu, Z. Zheng, and Z. Chen, "Cooperative mining in blockchain networks with zero-determinant strategies," *IEEE Transactions on Cybernetics*, vol. 2, no. 3, pp. 1–6, 2019.

Hindawi
Journal of Healthcare Engineering
Volume 2020, Article ID 2389527, 8 pages
https://doi.org/10.1155/2020/2389527

Research Article

Research on Multi-Time-Delay Gene Regulation Network Based on Fuzzy Label Propagation

Haigang Li, Qian Zhang, and Ming Li

School of Information and Control Engineering, China University of Mining and Technology, Xuzhou, Jiangsu 221116, China

Correspondence should be addressed to Qian Zhang; zhangqian374@126.com

Received 22 August 2019; Revised 28 October 2019; Accepted 5 November 2019; Published 11 March 2020

Guest Editor: Liang Zhao

In view of time delay existing in gene regulation, by using the analysis idea and methods of complex network, this paper proposes a multi-time-delay gene regulation network analysis method based on the fuzzy label propagation. The algorithm takes the relative change trend coefficient, the correlation coefficient, and the mutual information as the similarity measurement indexes for the gene pair, fully reflecting the correlation of gene pairs and simultaneously obtaining the gene regulation relationship and the time delay through the fuzzy label propagation algorithm of the semisupervised learning. Experimental results of the cell cycle-regulated genes of yeast show that the proposed construction method of GRN can not only correctly select potential regulation genes but also provide details about the gene regulator model, thereby more accurately constructing gene regulation network.

1. Introduction

The interaction between the implicit genes in gene expression data can be used to construct gene regulatory network by analysing gene expression data [1]. The research of gene regulatory network is one of the topics of post-genomic informatics. It mainly analyses gene expression data, uses bioinformatics methods and technologies to identify the topological structure of gene network to deeply understand the structure and function of biology and the mechanism of pathological changes, and understands life phenomena in a systematic framework [2, 3]. Gene network research can be used to reveal the development process and mechanism of biological tissue system and help understand the regulation of internal substances, which can promote people to effectively identify the cause of disease. In particular, the study of human tumor gene regulatory network can make us have a deep understanding of the regulatory relationship of tumor related genes and then provide basis and guidance for tumor gene therapy. Gene regulatory network, as the molecular basis of basic cell life activities, has the biological characteristics of randomness, complexity, spatiotemporal specificity, and dynamic. This makes the construction of gene regulatory network very difficult.

The time-series gene expression data have been widely applied in the research on the gene regulation network, and attention to the time delay has been paid increasingly as the important factor for the gene regulation network construction [4]. The time-delay processing can be generally classified into two types: first type—firstly calculate the time delay among genes, then translate the time-series gene expression data to the calculated time delay to achieve the effect of removing delay, and finally construct the gene regulation network to analyse the regulation relationship among the genes; second type—directly construct the time-delay gene regulation network model and obtain the time delay and the regulation relationship through the time-delay regulation network method [5]. In the first type of analysis, Ahsen et al. [6] obtained the phase and frequency of two gene expression data in the frequency domain through the frequency domain change and calculated the time delay on the basis of the relationship between the phase and the frequency. Huang et al. [7] obtained the mutual time delay among 101 genes by using this time-delay estimation method, constructed the gene regulation network by adopting the concept of community detection, and obtained the better result. The delay time obtained by this method is not always the integer multiple of time interval, and it is

necessary to obtain the delay removed gene expression value by using the curve fitting method, which is not conducive to the follow-up study.

The regulation time of gene expression in cells is not synchronous, and the regulation delay length is also different [8]. The existing dynamic Bayesian network model of gene expression regulation network based on time-series gene expression data is difficult to model the asynchronous multi-time-delay regulation relationship [9]. In order to solve this urgent problem, this paper proposes a semisupervised learning method that can accurately model the asynchronous and multi-time-delay regulatory relationship between genes. It can learn the gene expression regulatory network with asynchronous and multi-time-delay characteristics from the time-series expression data of gene chip. In the learning process, it can use the known class data and the unknown class data to obtain more information and have better learning effect.

2. Related Work

The reconstruction of gene regulatory network based on expression data is also called reverse engineering or network inference. In recent years, various algorithms have been proposed by analysing gene expression data, such as GA [10], gene programming [11], evolutionary strategies [12], and ACO [13]. However, the GRNs modeled by the above algorithm consist of only a limited number of genes. How to reconstruct large-scale gene regulatory network is still an unknown biological problem.

At present, there are various models to model gene regulatory network. The simplest model is based on Boolean networks. In reverse engineering, Boolean networks are used to infer the underlying topology and the Boolean functions at the nodes from the observed gene expression data. In addition, continuous network is an extension of Boolean network [14], which is also widely used to model gene regulatory network. Nodes still represent the regulatory effect of genes and their connections on gene expression. Genes in biological systems show continuous range of activity levels, and it has been considered that continuous networks can capture some properties of gene regulatory networks that do not exist in Boolean models. Many methods based on continuous networks have been proposed to infer gene regulatory networks, for example, based on linear regression and based on mutual information. In Arachne algorithm, the specific information of each gene pair can be calculated in an appropriate way to get the actual value of mutual information, and compared with the fixed threshold value, a regulatory interaction can be inferred. In addition, many probabilistic graphical models have been proposed to measure the high-order dependence between different gene expression patterns. Bayesian network is one of the most popular methods to infer gene regulatory network. In Bayesian networks, directed acyclic graphs are used to indicate the conditional dependence between random variables [15].

Many researchers think that the time delay among the genes is constant value, and the time delay varies from gene pairs so that the analysis on the multi-time-delay gene regulation network was proposed in succession. To be favorable to construct the gene regulation network, the time delay is normally regarded as the integral multiple of time interval. Based on this, Yang et al. [16] firstly established the time-delay gene expression matrix to dig the time-delay regulation relationship among the genes through the decision tree classifier. Yang [17] constructed the multi-time-delay gene regulation network by using the high-order Markov dynamic Bayesian network. Raja Chowdhury and Chetty [18] constructed the multi-time-delay gene regulation network by using the correlation coefficient method. In this method, the time-delay correlation coefficient among the genes was firstly established, the maximum value of correlation coefficient in each gene pair and the time delay corresponding to this value were obtained through the dynamic threshold method, and finally the maximum value of correlation coefficient in the gene pair was compared with the given threshold to screen the correlation coefficient greater than the threshold and obtain the genes corresponding to these correlation coefficients and the time delay to complete the analysis on the multi-time-delay gene regulation network. This method is simple and can effectively handle the time-delay problem. Aderhold et al. [19] established the time-delay mutual information among the genes and constructed the multi-time-delay gene regulation network through the dynamic Bayesian network: firstly construct the multi-time-delay mutual information matrix to select the larger gene in the mutual information and then complete the analysis on the gene regulation relationship by the dynamic Bayesian network. Better effect has been obtained by this method. However, most of these time-delay methods start from the relationship between genes but ignore the characteristics of genes.

The single metrical scale was used when the similarity among the genes was measured by the above methods. When constructing the gene regulation network, Liu et al. [20] pointed that the single similarity evaluation scale cannot reflect the correlation among the genes very well, so they evaluated the correlation among the genes by using the combined method of correlation coefficient and interquartile range and obtained better gene regulation relationship through the vector analysis by taking the interquartile range of the gene pair as the horizontal ordinate and the correlation coefficient as the vertical coordinate. By reference to [21, 22], this paper combines the multi-time-delay correlation coefficient, the mutual information, and the relative change trend coefficient to construct the new gene pair correlation evaluation matrix and complete the analysis on the multi-time-delay gene regulation network through the semisupervised learning method of fuzzy label propagation.

3. Relevant Notes

The time-series gene expression data are denoted as $V = (x_{ij})_{N\times P}$, wherein x_{ij} expresses the expression value of gene i at the time point j and $j = 1, 2, 3, \ldots, P$. The maximum delay time among the genes is denoted as A times the time interval.

3.1. Time-Delay Relative Change Trend Coefficient. The matrix obtained by gene expression data discretization is denoted as $D = (b_{ij})_{N\times(P-1)}$.

$$b_{ij} = \begin{cases} 1, & \text{if } x_{ij} < x_{i(j+1)}, \\ 0, & \text{if } x_{ij} = x_{i(j+1)}, \\ -1, & \text{if } x_{ij} > x_{i(j+1)}, \end{cases} \tag{1}$$

where $j = 1, 2, 3, \ldots, P-1$.

For any two genes m and n in the dataset, the relative change trend coefficient for the gene n and the gene m at the time point j is denoted as $s_{mn,j}$ after the gene n is delayed by a unit of time and can be calculated by the following the formulas:

$$b'_{mn,j} = b_{mj} \times b_{n(j+a)}, \quad j = 1, 2, 3, \ldots, P-1-a, \tag{2}$$

$$s_{mn,j} = b'_{mn,j} \times b'_{mn,(j+1)}, \quad j = 1, 2, 3, \ldots, P-2-a. \tag{3}$$

The value of $s_{mn,j}$ is $-1, 0, 1$, wherein 1 indicates the similar change trend of two genes.

The relative change trend of two genes after delay is graded. The number of values equal to 1 is denoted as s'_{mn}, and the relative change trend score for the gene n and the gene m is denoted as score^a_{mn} after the gene n is delayed by a unit of time.

$$\text{score}^a_{mn} = \frac{s'_{mn}}{P-2-a}. \tag{4}$$

3.2. Time-Delay Correlation Coefficient. The correlation coefficient for the gene n and the gene m is denoted as r^a_{mn} after the gene n is delayed by a unit of time.

$$r^a_{mn} = \frac{\sum_{j=1}^{P-a}\left(x_{mj} - \overline{x}_m\right)\left(x_{n(j+a)} - \overline{x}_n\right)}{\sqrt{\sum_{j=1}^{P-a}\left(x_{mj} - \overline{x}_m\right)^2}\sqrt{\sum_{j=1}^{P-a}\left(x_{n(j+a)} - \overline{x}_n\right)^2}}, \tag{5}$$

where $\overline{x}_m$ expresses the mean value of the former $P-a$ expression values for the gene m and $\overline{x}_n$ expresses the mean value of the latter $P-a$ expression values for the gene n.

3.3. Time-Delay Mutual Information. Mutual information expresses the shared information amount between two genes, firstly performing interval partition for the gene expression dataset and then calculating the delay mutual information matrix among the genes. The mutual information for the gene n and the gene m is denoted as M^a_{mn} after the gene n is delayed by a unit of time.

$$M^a_{mn} = H(m) + H(n) - H(m,n), \tag{6}$$

where H is information entropy. The calculation method is as shown in formulas (7) to (9):

$$H(m) = -\sum p_m \log_2(p_m), \tag{7}$$

$$H(n) = -\sum p_n \log_2(p_n), \tag{8}$$

$$H(m,n) = -\sum p_{m,n} \log_2\left(p_{m,n}\right), \tag{9}$$

where m takes the former $P-a$ expression value and n takes the latter $P-a$ expression value.

3.4. Gene Pair Similarity Evaluation Matrix. The gene pair similarity evaluation matrix is $I = (i'_{mnfa})_{N\times N\times 3\times A}$, i'_{mnfa} expresses the expression value of the attribute f for the gene n and the gene m after the gene n is delayed by a unit of time, and $a = 0, 1, \ldots, A$, wherein the attributes of gene pair are, respectively, relative change trend, correlation coefficient, and mutual information. For the convenience of subsequent analysis, the time-delay similarity evaluation matrix is denoted as $I = (i'_{mna})_{N\times N\times A}$, wherein i'_{mna} expresses the similarity sample for the gene n and the gene m after the gene n is delayed by a unit of time.

4. Multi-Time-Delay Gene Regulation Network Based on Fuzzy Label Propagation

4.1. Algorithm Description. The converted datasets are classified by using the fuzzy label propagation algorithm of semisupervised learning. There are two label values: 1 and -1, wherein 1 indicates that the regulation relationship exists between two genes in the gene pair and -1 indicates that there is no regulation relationship.

In the fuzzy label propagation algorithm, firstly divide I into the labeled data set I_L and the unlabeled dataset I_U and calculate the similarity $S_{(mna)(m'n'a')}$ of any two samples i'_{mna} and $i'_{m'n'a'}$ by using RBP kernel function.

$$S_{(mna)(m'n'a')} = \begin{cases} 0, & m = m', n = n', a = a', \\ \exp\left(\dfrac{\left\|i'_{mna} - i'_{m'n'a'}\right\|^2}{2\sigma^2}\right), & \text{other}, \end{cases} \tag{10}$$

where σ expresses the variance of difference value between two samples.

Express the category of sample i'_{mna} with the vector $F_{(mna)}$ of 1×2 dimensions:

(1) If the sample $i'_{mna} \in I_L$,

$$F_{(mna)j'} = \begin{cases} 1, & i'_{mna} \in \text{the category } j', \\ 0, & i'_{mna} \notin \text{the category } j', \end{cases} \tag{11}$$

where $j' = 1, 2$.

(2) If the sample $i'_{mna} \in I_U$, the label value of i'_{mna} is propagated from the k' adjacent samples and the membership that i'_{mna} belongs to the category j' meets

$$\sum_{i'_{m'n'a'} \in N\left(i'_{mna}\right)} S_{(m'n'a')(mna)}\left(F_{m'n'a'} - F_{mna}\right) = 0, \tag{12}$$

where $N(i'_{mna})$ expresses the set composed of k' adjacent samples of i'_{mna}, and the results are obtained from formula (12):

$$F_{mna} = \sum_{i'_{m'n'a'} \in N(i'_{mna})} \frac{S_{(m'n'a')(mna)}}{\sum_{i'_{m'n'a'} \in N(i'_{mna})} S_{(m'n'a')(mna)}} F_{m'n'a'}. \tag{13}$$

As the category labels of unknown samples are continuously renewed, F_{mna} in formula (13) is required to be repeatedly calculated until the fuzzy category label values of all samples are not changed.

Obtain the fuzzy label value $F = (F_{mna})_{N \times N \times A}$ of all samples and convert the label value matrix by the following formula:

$$F_{mna} = \begin{cases} F_{mna}, & \text{if } F_{mna} > 0, \\ 0, & \text{if } F_{mna} > 0. \end{cases} \tag{14}$$

Convert the label value matrix by the following formula:

$$F_{mna} = \begin{cases} 1, & \text{if } F_{mna} \neq 0, F_{mna} = \max(F_{mn1}, F_{mn2}, \ldots, F_{mna}), \\ 0, & \text{otherwise.} \end{cases} \tag{15}$$

The regulation relationship exists between two genes corresponding to the samples with the label value of 1, and the time delay is a times the time interval.

4.2. Algorithm Steps

Step 1: estimate the missing value in the simulation data set by using the missing value estimation method [23] and construct the complete dataset.

Step 2: calculate the time-delay relative change trend coefficient matrix, the time-delay correlation coefficient matrix, and the time-delay mutual information matrix of all gene pairs in the complete dataset.

Step 3: obtain the similarity evaluation matrix of gene pair. This similarity evaluation matrix is a multidimensional space matrix. For simulation simplicity, the matrix is processed accordingly to be converted to the two-dimensional space matrix. Make $I = (i'_{m'f})_{(A \times c_N^2) \times 3}$, wherein the row sequence of the row vector $i'_{m'}$ is as follows: no delay between the gene 1 and the gene 1, delay 1 time unit between the gene 1 and the gene 1, and delay A time unit between the gene N and the gene N.

Step 4: add the label value to a small number of gene pairs, calculate the fuzzy label values of unknown gene pairs on the basis of fuzzy label propagation algorithm, and obtain the regulation relationship and the time delay between the genes.

4.3. Time Complexity Analysis of Algorithm. There are two main bottlenecks in the calculation of this algorithm. The first is to use mutual information to find the time delay between gene pairs, and the second is to use fuzzy label transfer algorithm to classify datasets. It is assumed that the number of genes is N, the length of gene time series is T, the maximum time delay is m, and the number of iterations of fuzzy label transfer algorithm is M. When we use equation (6) to find the mutual information of a target gene and its regulator under a certain time delay, we need to traverse the gene expression level matrix once, and the algorithm complexity is $O(N * T)$. So, the time complexity of the algorithm is $O(N^2Tm)$. The time complexity of initialization is $O(N^2)$. The time complexity of fuzzy label transfer algorithm using semisupervised learning is $O(M)$. The time complexity of calculating score function is $O(NT)$. Therefore, the total time complexity is $O(N^2Tm + MNT)$.

5. Results and Discussion

5.1. Simulation Dataset. The simulation dataset is selected from the yeast cell gene chip data [24, 25] provided by Spellman et al. in Stanford University, from which 6 genes are extracted to form a small gene regulation network. The data are as shown in Table 1.

Extract the regulation relationship among 6 genes based on the research of Hou et al. [26]. The regulation network structure is shown in Figure 1.

6. Results

In simulation, firstly we need to select part of samples to add the labels. In this paper, the sample label value is set to −1 when the delay between the genes Clb6 and Cln1 is 0, the sample label value is set to 1 when the delay between the genes Clb2 and Cln2 is 0, and the maximum time delay A is set to 2. The simulation results are shown in Table 2.

It can be seen from Figure 1 that there are 10 pairs of genes having the regulation relationship. Table 2 shows that the method of this paper can correctly identify 8 pairs of genes having the regulation relationship, accounting for 80% of the total gene pairs having the regulation relationship, and the accuracy is relatively perfect. In 8 pairs of genes correctly identified, there are two pairs of genes having time delay, namely, Swi5 and Cln2 and Cln2 and Clb1, and the time delay is 1 unit. The change relationship of expression values for 8 pairs of genes correctly identified is shown in Figure 2. Horizontal coordinates represent gene expression level and vertical coordinates represent time point of gene expression.

It can be seen from Figure 2 that the change relationships of the gene expression data in Figures 2(a) and 2(c)–2(e) are basically consistent and the change relationships of the gene expression data in Figures 2(b) and 2(f)–2(h) are basically contrary, and Figure 2(g) shows the change relationship between the gene Cln2 and the gene Clb1 after the gene Cln2 is delayed by 1 unit of time. On the left side, the time points corresponding to the peaks and troughs of Cln2 expression value and Clb1 expression value are basically the same, and the change trends are contrary; on the right side, the expression value changes of two genes are disordered to some extent, but except for the last three time points, the expression value changes of other time points substantially conform to the change contrary trends. Figure 2(h) shows the expression value change relationship between the gene

Table 1: The information of selected genes.

Gene	Dataset	Gene	Dataset	Gene	Dataset
Cln1	YMR199W	Clb2	YPR119W	Clb1	YGR108W
Cln2	YPL256C	Clb6	YGR109C	Swi5	YDR146C

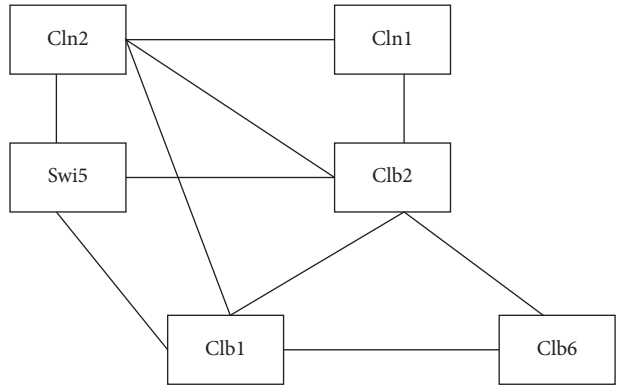

Figure 1: The structure of regulatory network formed by the 6 genes.

Table 2: The correctly identified gene pairs and the time delay.

Gene pairs	Cln1-Cln2	Swi5-Cln2	Swi5-Clb2	Cln2-Clb2	Cln1-Clb2	Cln2-Clb1	Swi5-Clb1	Clb2-Clb1
Time delay	0	1	0	0	0	1	0	0

Cln2 and the gene Swi5 after the gene Cln2 is delayed by 1 unit of time. It can be seen from the figure that the change trends of two gene expression values are contrary, wherein the first peak of the expression value for the gene Swi5 was obtained at the seventh time point and the first trough of the expression value for the gene Swi5 was obtained at the twelfth time point; the first peak of the expression value for the gene Cln2 was obtained at the seventh time point, and the first trough of the expression value for the gene Cln2 was obtained at the eleventh time point; the time points of peaks and troughs for the two genes are basically the same. Therefore, based on the premise and assumption, the result that the time delay between Swi5 and Cln2 and between Cln2 and Clb1 is 1 time interval in the regulation is reasonable.

7. Discussion

In order to have objective and scientific comparison results, hypothesis testing is used on the experimental results. Let the variables X_1, X_2, X_3, X_4 denote the classification error rate of algorithms proposed in this paper, reference [17], reference [20], and reference [27], respectively. Since the value of X_1, X_2, X_3, X_4 is subject to many random factors, we assume that they submit to normal distribution, $X_i \sim N(\mu_i, \sigma_i^2)$, $i = 1, 2, 3, 4$. Now, we compare the random variable mean of these algorithms, μ_i $(i = 1, 2, 3, 4)$. The smaller μ_i is, the lower the expected classification error rate is and the higher the efficiency is. Because the sample variance is the unbiased estimation of the overall variance, the sample variance value is used as an estimate of the generality variance. In this experiment, the significance level α is set as 0.01.

Table 3 shows the comparison process on μ_i and other parameters. We can see from Table 1 that the expectations of classification error rate in this paper are far below than other algorithms.

Next, we use some evaluation indexes to evaluate the algorithm. TP, TN, FP, and FN are abbreviations of true positive, false positive, true negative, and false negative, respectively. Perform the following operations on all target genes and regulatory genes. If the regulatory relationship between the target gene and regulatory gene is inferred by this algorithm and the previous literature has proved the regulatory relationship, then the value of TP is increased by 1. If the regulatory relationship between the target gene and regulatory gene is inferred by this algorithm, but the previous literature has not proved the regulatory relationship, then FP is increased by 1. If the algorithm in this paper does not infer the regulatory relationship between the target gene and the regulatory gene and no previous literature has proved that there is a regulatory relationship between the target gene and the regulatory gene, then the value of TN is increased by 1. And if the algorithm in this paper does not infer that there is a regulatory relationship between the target gene and the regulatory gene, but the previous literature has proved that the regulatory relationship exists, then add 1 to the value of FN. Each algorithm evaluation standard is evaluated by some combination of TP, FP, TN, and FN. The most common algorithms for predicting gene regulatory networks are sensitivity (Sn), specificity (Sp), and

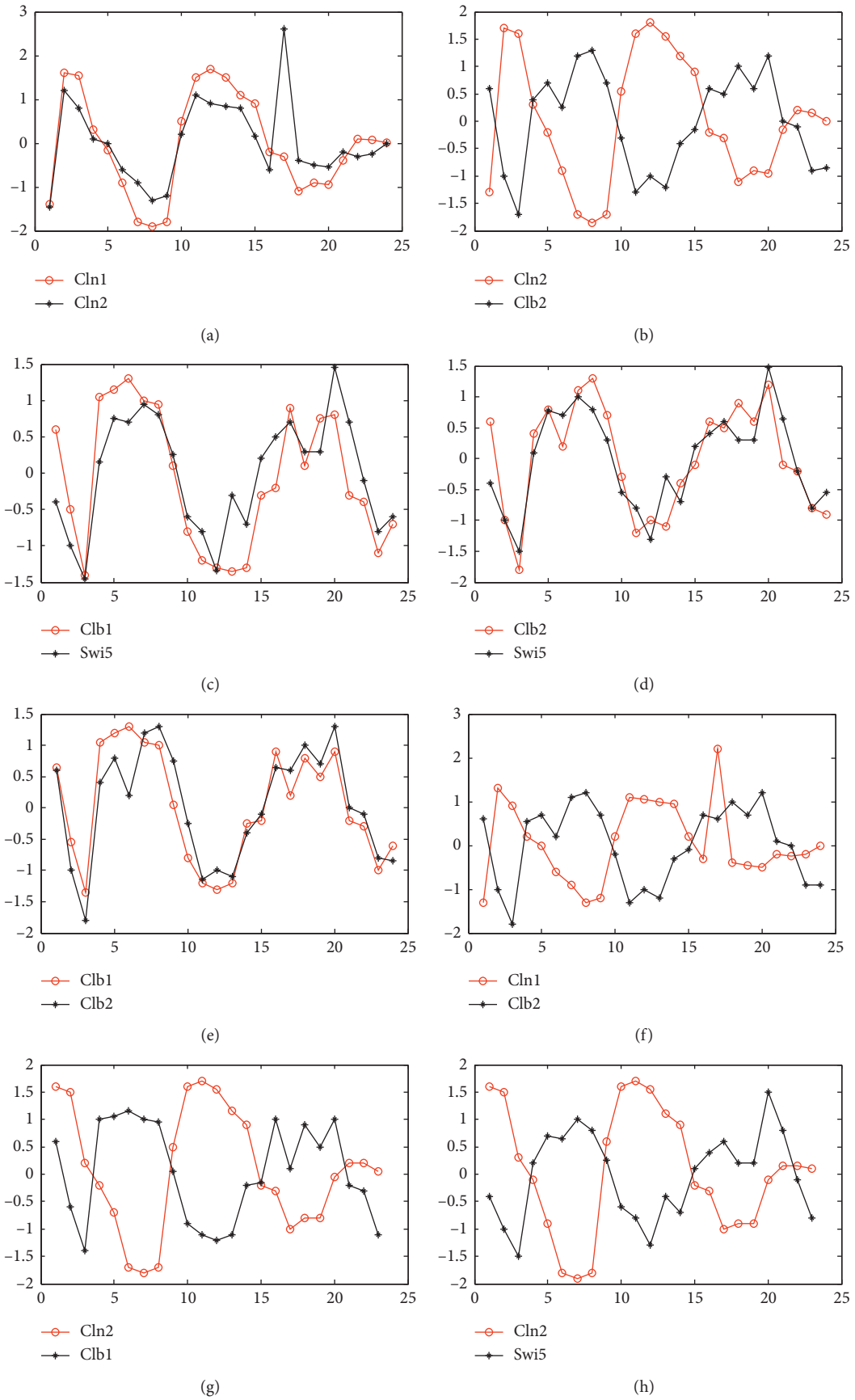

Figure 2: The changing relationship of the eight gene pairs. (a) The changing relationship of Cln1 and ln2. (b) The changing relationship of Cln2 and Clb2. (c) The changing relationship of Clb1 and Swi5. (d) The changing relationship of Clb2 and Swi5. (e) The changing relationship of Clb1 and sClb2. (f) The changing relationship of Cln1 and Clb2. (g) The change relationship between Cln2 and Clb1 after Cln2 is delayed by 1 unit of time. (h) The change relationship between Cln2 and Swi5 after Cln2 is delayed by 1 unit of time.

Table 3: Hypothesis testing for experimental results.

Hypothesis	$H_0: \mu_1 \geq \mu_2$ $H_1: \mu_1 < \mu_2$	$H_0: \mu_1 \geq \mu_3$ $H_1: \mu_1 < \mu_3$	$H_0: \mu_1 \geq \mu_4$ $H_1: \mu_1 < \mu_4$
Statistics	$U_1 = (\overline{X}_1 - \overline{X}_2)/(\sqrt{(\sigma_1^2/n_1) + (\sigma_2^2/n_2)})$	$U_2 = (\overline{X}_1 - \overline{X}_3)/(\sqrt{(\sigma_1^2/n_1) + (\sigma_3^2/n_3)})$	$U_3 = (\overline{X}_1 - \overline{X}_4)/\sqrt{(\sigma_1^2/n_1) + (\sigma_4^2/n_4)}$
Rejection region	$U_1 \leq -Z_\alpha = -2.325$	$U_2 \leq -Z_\alpha = -2.325$	$U_3 \leq -Z_\alpha = -2.325$
Value of the statistic	$U_1 = -36.24$	$U_2 = -58.32$	$U_3 = -76.65$
Conclusion	$H_1: \mu_1 < \mu_2$	$H_1: \mu_1 < \mu_3$	$H_1: \mu_1 < \mu_4$

Table 4: Comparison between the methods in this paper and other methods.

Algorithm	TP	TN	FP	FN	Sn (%)	Sp (%)	Acc (%)
Reference [17]	12	185	27	20	37.5	87.3	80.7
Reference [20]	12	183	28	21	36.4	86.7	79.9
Reference [27]	8	180	31	25	24.2	85.3	77.0
This paper	14	187	25	18	43.8	88.2	82.4

accuracy (Acc). Sn = TP/(TP + FN), Sp = TN/(TN + FP), and Acc = (TP + TN)/(TP + FP + TN + FN). The comparison results are shown in Table 4.

Table 4 compares the inference results of the four methods for gene regulatory network. The sensitivity of reference [17] method is only 37.5%, that of reference [20] method is 36.4%, that of reference [27] method is 24.2%, and that of the proposed method is 43.8%. It can be seen that in the network construction of this gene, the method proposed in this paper is better for identifying the right edge; it also shows that the addition of transcription factor linkage site data reduces the information loss in data processing. The data in accuracy are also optimal, which shows that the accuracy of network construction in this paper has been improved.

Therefore, each gene has a complex regulatory relationship in different cell cycles. The direction of regulation can be determined by using the method of multiple time delay, which is in line with the mechanism of biological time sequence activity. The introduction of transcription factor linked site data can reduce the network complexity and construct the regulatory network more effectively.

To sum up, the multi-time-delay gene regulation network method based on the fuzzy label propagation is feasible.

8. Conclusions

In consideration of the time delay existing in the interaction of genes, this paper constructs the multi-time-delay gene regulation network, uses the relative change trend coefficient, the correlation coefficient, and the mutual information as the evaluation indexes of the gene pair to construct the similarity matrix of the gene pairs, and then analyses the regulation relationship and the time delay among the genes by using the fuzzy label propagation algorithm. Due to the high complexity of algorithm in this paper, the method proposed in this paper is unsuitable for the construction of large network, and the error recognition ratio will be increased when the maximum time delay is set to high value. However, the method proposed in this paper is feasible. Therefore, how to effectively modularize the large network, divide the large network into many small networks, and integrate the small networks into the large network in the analysis will be an improvement direction of the method in this paper.

Data Availability

The yeast cell gene chip data used to support the findings of this study have been deposited by Spellman et al. in Stanford University.

Conflicts of Interest

The authors declare that there are no conflicts of interest regarding the publication of the paper.

Acknowledgments

This work was supported by the National Natural Science Foundation of China (grant nos. 61973304 and 61876185) and the Fundamental Research Funds for Central Universities (no. 2015QNB21).

References

[1] J. Watkinson, X. Wang, T. Zheng, and D. Anastassiou, "Identification of gene interactions associated with disease from gene expression data using synergy networks," *BMC Systems Biology*, vol. 2, no. 1, pp. 10–20, 2008.

[2] C. Wang, M. Yi, K. Yang, and L. Yang, "Time delay induced transition of gene switch and stochastic resonance in a genetic transcriptional regulatory model," *BMC Systems Biology*, vol. 6, no. 1, pp. 1–16, 2012.

[3] J. B. Furness, W. Kunze, and N. Clerc, "The intestine as a sensory organ: neural, endocrine, and immune responses," *American Journal of Physiology—Gastrointestinal and Liver Physiology*, vol. 277, no. 1, pp. 922–928, 1999.

[4] M. Khalid, S. Khan, J. Ahmad, and M. Shaheryar, "Identification of self-regulatory network motifs in reverse engineering gene regulatory networks using microarray gene expression data," *IET Systems Biology*, vol. 13, no. 2, pp. 55–68, 2019.

[5] J. Byrne, M. Nicola, and A. Brabazon, "An examination of synchronisation in artificial gene regulatory networks," in *Proceedings of the 2014 IEEE Congress on Evolutionary Computation*, pp. 2764–2769, Beijing, China, July 2014.

[6] M. E. Ahsen, H. Ozbay, and S.-I. Niculescu, "Analysis of a gene regulatory network model with time delay using the secant condition," *IEEE Life Sciences Letters*, vol. 2, no. 2, pp. 5–8, 2016.

[7] C. Huang, J. Cao, and M. Xiao, "Hybrid control on bifurcation for a delayed fractional gene regulatory network," *Chaos, Solitons & Fractals*, vol. 87, pp. 19–29, 2015.

[8] E. J. Bergholtz and Z. Liu, "Topological flat band models and fractional chern insulators," *International Journal of Modern Physics B*, vol. 27, no. 24, Article ID 1330017, 2013.

[9] C. A. Penfold and D. L. Wild, "How to infer gene networks from expression profiles, revisited," *Interface Focus*, vol. 1, no. 6, pp. 857–870, 2011.

[10] D. Repsilber, H. Liljenström, and S. G. E. Andersson, "Reverse engineering of regulatory networks: simulation studies on a genetic algorithm approach for ranking hypotheses," *Biosystems*, vol. 66, no. 1-2, pp. 31–41, 2002.

[11] R. Eriksson and B. Olsson, "Adapting genetic regulatory models by genetic programming," *Biosystems*, vol. 76, no. 1-3, pp. 217–227, 2004.

[12] Y. Fomekong, J. Kaandorp, and J. Blom, "Efficient parameter estimation for spatio-temporal models of pattern formation: case study of *Drosophila melanogaster*," *Bioinformatics*, vol. 23, no. 24, pp. 3356–3363, 2007.

[13] Y. Zhang, J. Liu, M. Zhou, and Z. Jiang, "A multi-objective memetic algorithm based on decomposition for big optimization problems," *Memetic Computing*, vol. 8, no. 1, pp. 45–61, 2016.

[14] A. A. Margolin, K. Wang, W. K. Lim, M. Kustagi, I. Nemenman, and A. Califano, "Reverse engineering cellular networks," *Nature Protocols*, vol. 1, no. 2, pp. 662–671, 2006.

[15] R. Prill, D. Marbach, and J. Saez, "Towards a rigorous assessment of systems biology models: the DREAM3 challenges," *Plos One*, vol. 5, no. 2, Article ID e9202, 2010.

[16] B. Yang, W. Zhang, H. Wang, C. Song, and Y. Chen, "Tdsdmi: inference of time-delayed gene regulatory network using s-system model with delayed mutual information," *Computers in Biology and Medicine*, vol. 72, pp. 218–225, 2016.

[17] B. Yang, "A new supervised learning for gene regulatory network inference with novel filtering method," *International Journal of Perform Ability Engineering*, vol. 14, no. 5, pp. 945–954, 2018.

[18] A. Raja Chowdhury and M. Chetty, "Network decomposition based large-scale reverse engineering of gene regulatory network," *Neurocomputing*, vol. 160, pp. 213–227, 2015.

[19] A. Aderhold, V. A. Smith, and D. Husmeier, "Biological network inference at multiple scales: from gene regulation to species interactions," *Pattern Recognition in Computational Molecular Biology*, Wiley, Hoboken, NJ, USA, pp. 525–554, 2015.

[20] F. Liu, Z. Zhang, X. Wang, and F. Sun, "Stability and synchronization control of fractional-order gene regulatory network system with delay," *Journal of Advanced Computational Intelligence and Intelligent Informatics*, vol. 21, no. 1, pp. 148–152, 2017.

[21] C. Zhang, L. Du, T. Wang, T. Yang, C. Zeng, and C. Wang, "Impact of time delay in a stochastic gene regulation network," *Chaos, Solitons & Fractals*, vol. 96, pp. 120–129, 2017.

[22] X. Wang, Q. Liu, and Y. Cheng, "Missing value estimation for gene expression profile data," *Chinese Journal of Electronics*, vol. 21, no. 4, pp. 673–677, 2012.

[23] A. Sefidmazgi and G. Ahmadi, M. Seid Abolghasem, Correlation analysis as a dependency measures for inferring of time-lagged gene regulatory network," in *Proceedings of the 2016 Eighth International Conference on Information and Knowledge Technology (IKT)*, pp. 6–11, Hamedan, Iran, September 2016.

[24] M. Zheng and M. Zhuo, "Gene regulatory network reconstruction from yeast expression time series," *Lecture Notes in Electrical Engineering*, Springer, vol. 542, pp. 1477–1481, , Berlin, Germany, 2019.

[25] W. Liu, D. Li, Q. Liu, Y. Zhu, and F. He, "A novel parametric approach to mine gene regulatory relationship from microarray datasets," *BMC Bioinformatics*, vol. 11, no. S11, p. S15, 2010.

[26] W. J. Hou and B. Ceesay, "Event extraction for gene regulation network using syntactic and semantic approaches," *Current Approaches in Applied Artificial Intelligence*, vol. 9101, pp. 559–570, 2015.

[27] A. Agrawal and A. Mittal, "A dynamic time-lagged correlation based method to learn multi-time delay gene networks," *Microbial Ecology*, vol. 50, no. 3, pp. 440–446, 2011.

Hindawi
Journal of Healthcare Engineering
Volume 2020, Article ID 3264801, 9 pages
https://doi.org/10.1155/2020/3264801

Research Article

Second-Generation Sequencing with Deep Reinforcement Learning for Lung Infection Detection

Zhuo Liu, Gerui Zhang, Zhao Jingyuan, Liyan Yu, Junxiu Sheng, Na Zhang, and Hong Yuan

The First Affiliated Hospital of Dalian Medical University, Dalian 116011, China

Correspondence should be addressed to Hong Yuan; yuanhonglab@163.com

Received 8 October 2019; Accepted 25 November 2019; Published 24 February 2020

Guest Editor: Liang Zou

Recently, deep reinforcement learning, associated with medical big data generated and collected from medical Internet of Things, is prospective for computer-aided diagnosis and therapy. In this paper, we focus on the application value of the second-generation sequencing technology in the diagnosis and treatment of pulmonary infectious diseases with the aid of the deep reinforcement learning. Specifically, the rapid, comprehensive, and accurate identification of pathogens is a prerequisite for clinicians to choose timely and targeted treatment. Thus, in this work, we present representative deep reinforcement learning methods that are potential to identify pathogens for lung infection treatment. After that, current status of pathogenic diagnosis of pulmonary infectious diseases and their main characteristics are summarized. Furthermore, we analyze the common types of second-generation sequencing technology, which can be used to diagnose lung infection as well. Finally, we point out the challenges and possible future research directions in integrating deep reinforcement learning with second-generation sequencing technology to diagnose and treat lung infection, which is prospective to accelerate the evolution of smart healthcare with medical Internet of Things and big data.

1. Introduction

Nowadays, smart healthcare has appeared to be an interdisciplinary subject by integrating mixed computing techniques into the health administration [1, 2]. The primary purpose of smart healthcare is to offer pervasive and personalized medical services and health protection to people. Computer-aided diagnosis and decision making of this personalized treatment plan is one of the current developments in precision medicine [3, 4]. Smart healthcare aims to provide intelligent comprehensive differentiation and prescription recommendation for the diagnosis and treatment of diseases by applying artificial intelligence technology and cloud computing to the practice of clinical medicine. It has been greatly developed through the applications of artificial intelligence, cloud computing, big data analysis, and Internet of Things (IoT), and has been applied to many medical fields such as intelligent Chinese medicine and intelligent testing. Medical big data is to integrate the IoT system into medicine and to integrate and classify the collected medical data information by creating the medical Internet of Things [5, 6]. The deep learning model and the deep reinforcement learning model are the most commonly used artificial intelligence models, which can be trained and simulated by providing a large number of training examples through medical big data. The computer aids of modern medicine and traditional Chinese medicine have matured. Thus, there are many well-trained deep learning models for clinical medicine.

Pulmonary infectious diseases are common respiratory diseases, whose clinical manifestations include cough, fever, and chills. However, pathogens of lung infections are complex, and it is difficult to carry out biological cultivation and identification. Particularly, complex lung infections have various clinical manifestations: the mortality rate is high and the treatment is difficult, the traditional pathogen detection methods have low positive rate; it is a long time-consuming and complicated operation, and it is difficult to

meet the requirements of diagnosis and treatment of complex infectious diseases. Classical pathogen detection methods include bacterial (fungal) culture, microscopy and antibody testing, and PCR-based pathogen-specific nucleic acid detection. These methods have made great progress in the diagnosis of pulmonary infectious diseases, but they have low sensitivity and poor timeliness; pathogen identification information and drug resistance information are not comprehensive, so it is impossible to identify unknown and rare pathogenic microorganisms. Therefore, clinical diagnosis of pulmonary infectious diseases is very difficult.

Second-generation sequencing (SGS), also known as next-generation sequencing technology and high-throughput sequencing, can simultaneously sequence billions of DNA molecules in parallel [7]. It is a group of sequencing with high throughput, low cost, short time, and automated sequencing technologies [8–10]. However, poor specificity is a major problem that restricts the clinical applications of SGS. Nonpathogenic pathogens, unrelated pathogens, and ambiguous pathogens are often seen in SGS reports. In order to clarify the diagnosis, the pathogen information detected by SGS needs to be verified and interpreted using more advanced methods [11, 12].

In this paper, we explore deep reinforcement learning for computer-aided diagnosis and treatment of complex pulmonary infectious diseases. We present several representative deep reinforcement learning models for the diagnosis and treatment of potential lung infections first, discuss the applications of the deep reinforcement learning model in the diagnosis of second-generation genetic testing for pulmonary infection, and summarize current status of pathogenic diagnosis of pulmonary infectious diseases and their main characteristics, and then we analyze the results of second-generation genetic testing and the main features of each type in common lung infections. Finally, we point out the open challenges and possible future research directions for intensive studies of second-generation genetic testing integrated with deep reinforcement learning in lung infections, which is expected to promote the development of intelligent healthcare and medical Internet of Things.

In the reminder of this paper, Section 2 introduces the deep reinforcement learning approaches that can be used for second-generation sequencing for lung diseases detection and treatment. Section 3 reviews the current status of pathogenic diagnosis of pulmonary infectious diseases and applications of SGS in detection of pulmonary pathogen infection are discussed in Section 4. Section 5 gives the challenges and possible future research directions for intensive studies of second-generation genetic testing integrated with deep reinforcement learning in lung infections. Finally, Section 6 concludes the paper.

2. Deep Reinforcement Learning

Deep reinforcement learning (DRL) is a new research hotspot in the field of artificial intelligence. It combines the perception of deep learning with the decision-making ability of reinforcement learning in a common form and enables direct control from raw input to output through end-to-end learning. With the rapid development of human society, in more and more complex real-world task tasks, deep learning (DL) is needed to automatically learn the abstract representation of large-scale input data and to use this representation as a basis for self-incentive reinforcement learning (RL) to optimize problem-solving strategies. DRL is an end-to-end sensing and control system with strong versatility. The learning process can be described as follows: (1) At each moment, the agent interacts with the environment to obtain a high-dimensional observation and uses the DL method to perceive the observation to obtain a specific state feature representation. (2) The value function of each action is evaluated based on the expected return, and the current state is mapped to the corresponding action through a certain strategy. (3) The environment reacts to this action and gets the next observation. By continuously cycling the above processes, the optimal strategy for achieving the goal can be finally obtained [13]. The framework of DRL is shown in Figure 1.

At present, DRL technology has been widely used in games, parameter optimization, machine vision, and other fields. Its application is considered as an important way to move toward general artificial intelligence [14, 15]. This paper explores the application of DRL in second-generation sequencing for lung infection detection.

2.1. Basic Concepts

2.1.1. Deep Learning. The concept of DL stems from artificial neural networks. The DL model is usually composed of multiple layers of nonlinear arithmetic units. It uses the output of the lower layer as the input of the higher layer; in this way, it automatically learns the abstract feature representation from the large amount of training data to discover the distributed characteristics of the data. Compared with shallow networks, multi-hidden-layer network models have better feature representation capabilities. It first uses the unsupervised learning to conduct greedy pretraining on layer by layer and then supervises the whole network with supervised learning. This pretraining method provides ideal initial parameters for deep neural networks and reduces the optimization difficulty of deep neural networks [16, 17]. Typical DL models include Stacked Autoencoder (SAE), Restricted Boltzmann Machine (RBM), Deep Belief Network (DBN), and Recurrent Neural Network (RNN). With the growth of training data and the improvement of computing power, Convolutional Neural Network (CNN) has been widely used in various fields.

2.1.2. Reinforcement Learning. Reinforcement learning (RL) is a kind of learning that maps from environmental state to action. The goal is to get the agent to get the maximum cumulative reward in the process of interaction with the environment [18]. The Markov decision process can be used to model the RL problem, which is usually defined as (S, A, ρ, f), where

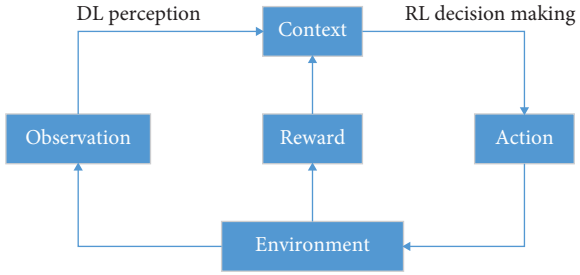

Figure 1: The framework of deep reinforcement learning.

(1) S is a collection of all environmental states. And $s_t \in S$ stands for the state of agent at time t.

(2) A is a collection of execution actions for agent. And $a_t \in A$ stands for the action that agent takes at time t.

(3) $\rho : S \times A \longrightarrow R$ is the reward function. And $r_t \sim \rho(s_t, a_t)$ stands for the immediate reward value of agent at state s_t when executing action a_t.

(4) $f : S \times A \times S \longrightarrow [0, 1]$ is the state transition probability distribution function. And $s_{t+1} \sim f(s_t, a_t)$ stands for the probability of agent transforming from state s_t to s_{t+1} when executing action a_t.

In RL, strategy $\pi : S \times A$ is a map from state space to action space, which indicated that the agent selects action a_t in state s_t, performs the action, and transforms to the next state s_{t+1} with probability $f(s_t, a_t)$, while accepting rewards r_t from environmental feedback. Assuming that the immediate reward for each time step in the future must be multiplied by a discount factor γ, then from the time t to the end of the time T, the sum of the rewards is defined as

$$R_t = \sum_{i=t}^{T} \gamma^{i-t} r_i, \tag{1}$$

in which $\gamma \in [0, 1]$ is used to weigh the impact of future rewards on cumulative rewards.

State action value function $Q^{\pi}(s, a)$ refers to the action a in the current state s and always follows the strategy π to the end of the plot, in which the cumulative return obtained by the agent is expressed as

$$Q^{\pi}(s, a) = \mathrm{E}\left[R_t \mid s_t = s, a_t = a, \pi\right]. \tag{2}$$

For all state action pairs, if the return of a strategy π^* is greater than or equal to the expected return of all other strategies, then the strategy π^* is called the optimal strategy. There may be more than one optimal strategy, but they share the same state action value function.

$$Q^{\pi}(s, a) = \max_{\pi} \mathrm{E}\left[R_t \mid s_t = s, a_t = a, \pi\right]. \tag{3}$$

It is called the optimal state action value function, and the optimal state motion value function follows the Bellman optimal equation; namely,

$$Q^{\pi}(s, a) = \mathrm{E}_{s' : S}\left[r + \gamma \max_{a'} Q(s', a') \mid s, a\right]. \tag{4}$$

In the traditional RL, the Q-value function is generally obtained by iterative Bellman equation:

$$Q_{i+1}(s, a) = \mathrm{E}_{s' : S}\left[r + \gamma \max_{a'} Q_i(s', a') \mid s, a\right]. \tag{5}$$

Herein, when $i \longrightarrow \infty$, π^*. By continuously iterating, the state action value function will finally converge, and the optimal strategy $\pi^* = \arg\max_{a \in A} Q^*(s, a)$ will be obtained. However, for practical problems, it is obviously not feasible to solve the optimal strategy by iterative updating (5), because in the large state space, the method of solving the Q-value function with the iterative Bellman equation is too expensive. To tackle it, in the RL algorithm, a linear function approximator is usually used to approximate the state action value function, $Q(s, a \mid \theta) \approx Q^*(s, a)$. Besides, nonlinear function approximators such as deep neural networks can also be used to approximate the value function or strategy. Therefore, DRL has attracted extensive attention in recent years. In the next subsection, we will discuss some deep reinforcement learning techniques that are potential for second-generation sequencing in lung infection detection and treatment.

2.2. DRL Techniques. In this section, we first describe three main types of deep reinforcement learning methods, including deep reinforcement learning based on value function, deep reinforcement learning based on strategy gradient, and deep reinforcement learning based on search and supervision. Afterwards, some potential deep reinforcement learning directions in SGS applications are summarized, such as hierarchical deep reinforcement learning, multitask deep reinforcement learning, multiagent deep reinforcement learning, deep reinforcement learning based on memory and reasoning, and so on.

2.2.1. DRL Based on Value Function. Mnih et al. [19] combined the convolutional neural network with the Q learning algorithm in the traditional RL and proposed the Deep Q-Network (DQN) model. This model is used to process visual perception-based control tasks and is a groundbreaking work in the field of DRL. The input of the DQN model is the four preprocessed images closest to the current time. The input undergoes a nonlinear transformation of 3 convolutional layers and 2 fully connected layers and finally produces a Q value for each action in the output layer. Figure 2 shows the architecture of DQN.

In order to alleviate the instability problem in the nonlinear network representation value function, DQN mainly made three improvements to the traditional Q learning algorithm. (1) DQN uses the experience replay mechanism during the training process to tackle the obtained transferred samples online. (2) In addition to using the deep convolutional network to approximate the current value function, DQN uses another network to generate the target Q value. (3) DQN reduces the bonus value and error term to a limited interval, which ensures that the Q value and

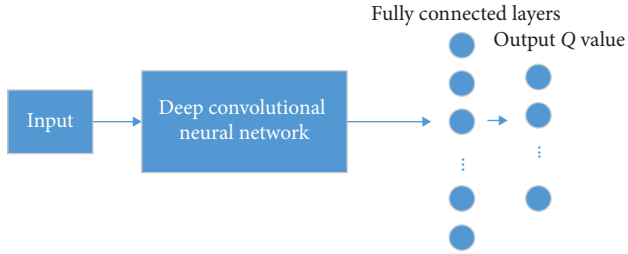

Figure 2: Architecture of DQN.

the gradient value are within a reasonable range, which improves the stability of the algorithm. Inspired by the DQN, many variants are proposed, such as deep dual Q network, deep Q network based on superior learning, deep Q network based on priority sampling, deep cycle Q network, and so on.

2.2.2. DRL Based on Strategy Gradient. Strategy gradient is a commonly used strategy optimization method, which updates the strategy parameters by continuously calculating the gradient of the strategy expectation total reward for the strategy parameters and finally converges to the optimal strategy. Therefore, when solving the DRL problem, a deep neural network with parameter θ can be used to parameterize the representation strategy, and the strategy gradient method is used to optimize the strategy. It is worth noting that when solving DRL problems, the first choice is to adopt a strategy-gradient-based algorithm. The reason is that it can directly optimize the expected total reward of the strategy and search for the optimal strategy directly in the strategic space in an end-to-end manner, eliminating the cumbersome intermediate links. Therefore, compared with DQN and its improved model, the DRL method based on strategy gradient is more applicable and the effect of strategy optimization is better.

Typical strategy-gradient-based DRL methods include deep strategy gradient based on actor critic, asynchronous dominant actor critic algorithm, and so on [20].

2.2.3. DRL Based on Search and Supervision. In addition to value-based DRL and strategy-gradient-based DRL, the process of strategy search can be promoted by adding additional manual supervision, which is the core idea of DRL based on search and supervision. Monte Carlo Tree Search (MCTS) [21], as a classic heuristic strategy search method, is widely used in action planning in game problems. Therefore, in the DRL method based on search and supervision, strategy search is generally done through MCTS. For example, the AlphaGo algorithm combines deep neural networks with MCTS to achieve remarkable results. Its main idea has two points: (1) using MCTS to approximate the value function of each state; (2) using the CNN based on value function to evaluate the current layout and walk of the board. AlphaGo's complete learning system consists of the following components:

(1) *Strategy Network*. It is divided into a strategy network for supervised learning and a strategy network for RL. The role of the strategy network is to predict and sample the next move based on the current situation.

(2) *Rollout Strategy*. The goal is also to predict the next step, but the speed of prediction is 1000 times that of the strategy network.

(3) *Value Network*. According to the current situation, the winning probability of both sides is estimated.

(4) *MCTS*. It integrates the strategy network, the rollout strategy, and the value network into the process of strategy search to form a complete system.

DRL based on search and supervision has achieved promising results in the game areas, which has prompted more and more researchers to transfer it to others.

2.2.4. Potential DRL in SGS. In addition to the above DRL methods, some outstanding methods have be proposed in recent years. In this subsection, we give a brief review of the potential DRL in SGS, which may be used for detecting of pulmonary pathogen infection.

(1) Hierarchical Deep Reinforcement Learning. In some complex DRL tasks, the strategy is optimized directly to the final goal, which is inefficient. Therefore, Hierarchical Reinforcement Learning (HRL) can be used to decompose the final goal into multiple subtasks to learn the hierarchical strategy and form a valid global strategy by combining multiple subtask strategies [22]. Figure 3 gives the structure of the hierarchical DQN.

Typical HRL methods include spatiotemporal abstraction and intrinsic-motivation-based methods, internal-option-based methods, and deep follow-up reinforcement learning. All the ideas can be used with the complex processes of SGS for detection of pulmonary pathogen infection.

(2) Multitask Transfer Deep Reinforcement Learning. In the traditional DRL method, the agent after completion of each training can only solve a single task. However, in some complex real-world scenarios, the agent needs to be able to handle multiple tasks at the same time. At this time, multitask learning and transfer learning are extremely important. In the RL field, Wilson et al. [23] used a hierarchical hybrid Bayesian model to provide prior knowledge of new tasks, enabling agents to better adapt to new task scenarios. For partially observable random multitasking scenarios, Li et al. [24] developed a regionalized policy representation to describe the behaviour of agents in different task scenarios. The method used the clustering properties contained in the Dirichlet process to share training scenarios between similar tasks and to pass valuable information between different tasks. Compared with the single-task learning mode, the multitask RL method has achieved more outstanding performance in both lattice world navigation and multitarget classification tasks. Taylor and Stone [25] proposed a way to transfer value functions between different tasks. Fernfindez

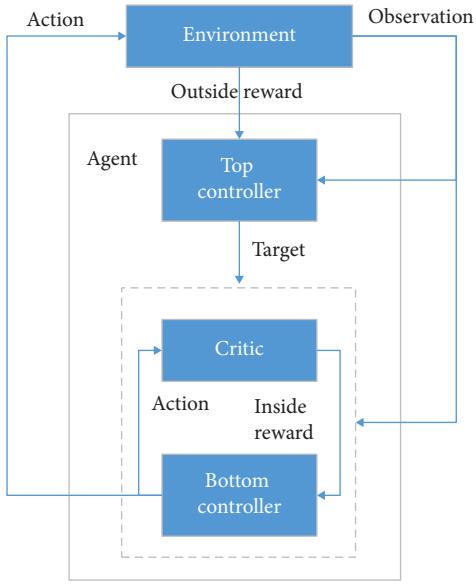

Figure 3: Architecture of hierarchical DQN.

Vdoso [26] used a mapping that reflects the relationship between the agent's current and past state action pairs, enabling the previously learned strategies to be transferred to new tasks in a timely manner. Wang et al. [27] concluded that the transfer learning in RL falls into two broad categories: behavioural transfer and knowledge transfer. These two types of transfer learning are also widely used in multitasking DRL algorithms.

Regarding SGS for detecting of pulmonary pathogen infection, multiple agents and multitask are promising. Therefore, the deep reinforcement learning based on multitask transfer learning is a feasible direction.

(3) Deep Reinforcement Learning Based on Memory and Reasoning. The traditional visual-perception-based DRL method is far worse than human beings in solving higher-level cognition-inspired tasks. That is to say, in solving some high-level DRL tasks, the agent not only needs strong perceptual ability, but also needs certain memory and reasoning ability to learn effective decision-making. Therefore, the ability to give active learning and reasoning to existing DRL models is very important.

In recent years, the research on neural network model of external storage has made substantial progress. Graves et al. [28] proposed a neural structure called Neural Turing Machines (NTM), which updates the parameters of memory structures by random gradient descent while reading and writing data to optimize the content of memory. By adding NTM, the neural network model has the ability to complete some simple tasks such as copying, inversion, addition, and subtraction, which shows that the deep neural network model has preliminary memory and reasoning ability. After that, Sukhbaatar et al. [29] proposed a memory network model based on NTM for question-and-answer system and language modelling tasks, which further improved the long-term memory ability of the network. Therefore, adding these external memory modules to the existing DRL model can give the network a certain high-level ability of long-term memory, active cognition, and reasoning. In addition, the development of cognitive neuroscience in recent years has also promoted the development of artificial intelligence. Researchers are simulating the auxiliary learning system of the human brain to construct an agent that can independently remember, learn, and make decisions.

3. Current Status of Pathogenic Diagnosis of Pulmonary Infectious Diseases

In recent years, as a result of the emergence of severe acute respiratory syndrome (SARS) in new pathogens, a variety of viruses, fungi, and resistant bacteria have emerged, and infectious diseases have once again received attention. However, there are many kinds of pathogens of infectious diseases [30–32]. Traditional immunological tests and cultivation of pathogenic microorganisms are limited; they are not efficient and timely to provide a reliable diagnosis basis for the clinic, especially the complex lung infection. How to judge the pathogens? Difficulties have made many patients with pulmonary infectious diseases fail to receive timely and effective treatment and even death. Pulmonary infections are mainly pneumonia and bronchiolitis and can also be manifested as lung abscesses and granulomas. Pulmonary infections are mainly collected from sputum and alveolar lavage fluid. Due to the special feeding environment of the lungs, routine detection of effective pathogen information in serum is limited. However, patients with severe pneumonia require mechanical ventilation, and lung tissue is difficult to obtain. The small amount of specimens limits the detection of pathogens of infectious lung diseases.

4. Application of SGS in Detection of Pulmonary Pathogen Infection

At present, pathogenic diagnostic methods based on microbial culture are still the main means for diagnosing the pathogenic diagnosis of pulmonary infectious diseases, but they are also largely influenced by culture conditions and antibiotic use, and the culture positive rate is low. For lung infections, second-generation sequencing technology can be used for the detection of a variety of pathogens, such as bacteria, fungi, viruses, mycoplasma, etc. Also, it can also be used for the detection of a variety of respiratory specimens, such as sputum, throat swab, alveolar lavage fluid and blood, and other specimens. The second-generation sequencing technology has a higher detection rate than the traditional culture method [33, 34]. Compared with the traditional single-plex PCR method, it not only reduces the sample nucleic acid requirement and expands the detection range, but also has better specificity and sensitivity [11, 12]. Detection of viral pathogens mainly includes virus antigen detection, nucleic acid detection, and virus isolation and culture. However, the traditional virus pathogen detection has a low positive rate; thus, it is difficult to promote and apply in clinical practice. Second-generation sequencing technology is superior to traditional virus detection

techniques in terms of sensitivity and accuracy. It theoretically reveals all microbial information in the sample, which can detect more virus types and its positive rate is higher [35]. Detectable viruses include well-known upper respiratory tract viruses and lower respiratory tract viruses such as HSV and CMV in immunosuppressed hosts. With the increasing range of pathogens based on second-generation sequencing technology, it is found that the proportion of viruses in respiratory infections is much higher than previously thought. The applications of SGS technology to detect in-hospital-acquired viral pneumonia in real time and rapid detection have shown that SGS technology can learn evidence faster than traditional methods, so that timely measures are taken to control outbreaks of nosocomial infections.

Pulmonary fungal infections are characterized by high lethality and difficulty in diagnosis and treatment. In recent years, with the abuse of antibiotics, more and more resistant bacterias and fungi have emerged. Pulmonary fungal infection has become the leading cause of death in ventilator-associated pneumonia, especially in patients with immunosuppression. Among patients with drugs, the incidence of fungal infections is also increasing [36]. Culture has long dominated the diagnosis of fungal infections, but traditional methods have inherent deficiencies in identifying mixed infections and analyzing the flora structure and dynamics of the flora and many fungi or undiscovered new ones. It is difficult or even impossible to cultivate the strain. These kinds of problems all suggest that we urgently need a new method to assist clinical diagnosis more accurately and quickly. Different from the bacterial DNA extraction method, the second-generation technology in the fungal flora structure spectrum method mainly through the amplification, sequencing, and analysis of the fungus ITS1 (internal transcribed spacer) and ITS2 gene fragments, using ITS1/ITS2 gene sequencing technology, generally, 50 to 60 genera were detected, and the sequence of fungal ITS gene obtained by sequencing can be matched by the existing gene database. However, for the most common clinical genera of *Candida* and *Aspergillus*, ITS gene sequencing can well identify their ITS gene sequences, and some pathogen strains can be distinguished at the species level. Fungi not only cause lung dysfunction, but also because of the long treatment time, affect the prognosis of the disease, and the second-generation sequencing technology helps to understand the whole picture of airway microbes from the overall structure of the community and in complex lung infections, especially AIDS, etc. The diagnosis of *Pneumocystis* is important in immunodeficient patients [37].

Mycobacterium tuberculosis also occupies an important position in the pathogens of lung infection. At present, the commonly used PCR method for collection of mycobacterium tuberculosis has low sensitivity and low positive rate. The T-SPOT detection method is also applied clinically, but the specificity is low, and the false positive rate is high. However, the second-generation sequencing technology, the pathogen detection, epidemiology, and typing of mycobacterium tuberculosis have made a leap forward. The second-generation sequencing technology can be applied not only to conventional sputum, alveolar lavage fluid and blood, but also to the detection of pleural effusion and pericardial effusion, which greatly improves the accuracy and sensitivity of detection, especially improving the diagnosis of tuberculous pleural effusion. At the same time, SGS can classify the detected *M. tuberculosis*, greatly improve the typing efficiency, and also determine the variation and propagation source among the strains in the transmission chain.

It is well known that the clinical microbiology laboratory's real-time PCR technology for screening and confirming suspected viruses must be based on known pathogen gene sequences, but not for unknown viral pathogens. The second-generation sequencing technology not only discovers known pathogens, but also discovers completely unknown pathogens [38, 39]. About 70% of patients with infectious diseases cannot determine pathogen information due to traditional detection methods and cannot be treated in a timely and effective manner, thus worsening the condition. Therefore, rapid and accurate pathogen detection methods are of great significance for effective diagnosis and timely control of infectious diseases. There are many types of modern molecular typing techniques, and the most commonly used molecular techniques in the traceability and monitoring of infectious diseases are multisequence typing (MLST), pulsed-field gel electrophoresis (PFGE), and multisite tandem repeats. Sequence analysis (MLVA), etc., and the emerging high-resolution WGS technology guarantee the accurate traceability and monitoring of infectious diseases and can also complement each other with multiple molecular technologies to improve the accuracy of detection. WGS technology can track the prevalence of pathogens and more accurately identify possible sources of pathogens [40, 41]. And with the continuous development of this technology, the current traceability and monitoring capabilities for unknown pathogens are becoming more and more prominent. The pathogens of severe pulmonary infection are usually unclear. Currently, the clinical use of antigen/antibody immunology methods and traditional microbial culture techniques is used for diagnosis. However, these methods have problems of long culture period and low culture positive rate. The second-generation sequencing technology is a novel DNA/RNA sequencing method based on the detection of nucleic acid molecules, which has high sensitivity and short time-consuming, and does not depend on traditional pathogenic culture. The application of antibiotics in the early stage has little effect on the detection results. Accurate and rapid identification of microbial pathogens in patients with lung infections may result in targeted antibacterial therapies, with fewer side effects and lower costs. In particular, patients with tracheal intubation are measured by sputum extraction from the lower respiratory tract of the bronchus, which can more accurately provide pathogenic bacteria analysis of ventilator-associated pneumonia, further guiding clinical treatment and prognosis. With the development of second-generation sequencing technology, processing and sequencing time will be further reduced. The SGS method will eventually provide clinicians with rapid, accurate, independent

culture-based identification of bacterial, fungal, and viral pathogens and their antimicrobial sensitivity characteristics [42].

Although the blood and alveolar lavage SGS tests have revolutionized the pathogens of complex lung infections, there are still many problems with the detection and interpretation of SGS. Different from the application of SGS detection in hereditary diseases, the complex composition of infectious disease specimens and the low level of nucleic acid of pathogenic microorganisms all restrict the detection of SGS in pathogenic microorganisms of lung infection. The first problem is sensitivity. Although SGS detection shows great advantages over traditional methods in diagnosing rare and rare pathogens, the sensitivity of common pathogens such as *Cryptococcus* is not stronger than traditional methods. Even if these pathogens detected by traditional methods, SGS may not detect or detect only a very small number of specific fragments, which affects the results. For example, for the metagenomics detection of *M. tuberculosis*, the current optimal solution is still to perform SGS sequencing on the basis of MGIT960 liquid culture. The reason may be that the *Mycobacterium tuberculosis* are intracellular bacteria, and the current detection method is mainly to detect the intracellular infection with *M. tuberculosis* by using the sputum supernatant; and *M. tuberculosis* due to nucleic acid of GC is relatively high (60% higher), and the melting method of most bacteria cannot fully dissociate the nucleic acid strand of *M. tuberculosis*. Therefore, under the condition of specimen processing suitable for most pathogenic microorganisms, the detection of tuberculosis cannot be effectively achieved. At present, direct SGS testing of clinical specimens to diagnose *M. tuberculosis* infection is very difficult. As an alternative, it is often the case that the clinical specimens are cultured for tuberculosis and then SGS is detected to improve the positive rate of clinical specimen detection, which increases the financial burden of the patient.

5. Discussion

Although SGS is a high-throughput test and can theoretically detect almost all pathogenic microorganisms, it does not completely replace all clinical pathogen detection methods. This requires us to continue to optimize the detection method of SGS on the one hand, so that it can cover the range of pathogens as much as possible and improve the detection rate. On the other hand, we must understand that SGS technology has limitations and cannot be completely dependent on SGS detection [43]. At the same time, traditional methods cannot be ignored, and other effective pathogen detection methods should be retained or explored as supplements or verifications. For patients with partial lung abscess or granuloma, because the disease is confined to the lungs, the amount of pathogens released into the blood and alveolar lavage fluid is limited, so for these diseases, pathogens can only be detected by SGS detection of tissue samples. Deep reinforcement learning can fully learn the potential results by simulating human brain learning and decision making based on the given complex data. Thus, it is a good choice to integrate DRL with SGS for clinical pathogen detection.

Poor specificity is another major problem that restricts the clinical application of SGS. Nonpathogenic, unrelated pathogens, and ambiguous pathogens are often seen in SGS reports. The lungs are an open environment, connected to the outside world, there are airway and oral colonization bacteria, many fragments of different species can be detected in the sputum and alveolar lavage fluid, and many unexplained samples can often be detected in the specimen. Part of the reason may be the contamination of specimens and reagents, such as environmental microbes (such as plants, plant viruses, etc.), which are difficult to discriminate. For these contaminations, it is necessary to eliminate the comparison between the laboratory quality control and the data between the specimens. DRL can combine all the related data to learn a favorable result through training and decision making; thus, it may effectively solve the poor specificity of the clinical application of SGS.

In summary, by combining the deep reinforcement learning techniques with SGS, it can eliminate the valueless results and analyze and evaluate the meaningful results of SGS. The core of SGS testing for the diagnosis of lung infections is the identification of responsible pathogens. Since SGS testing often yields a large number of backgrounds or unrelated microbial fragments, it is critical to find or identify responsible pathogens. It is first necessary to establish a knowledge database of common microorganisms for lung infections: a database of background microorganisms common to each laboratory and testing unit in SGS testing and record the number of common fragments detected. If a suspected pathogen fragment that is not in the range of common background bacteria appears in the SGS test of clinical specimens, or the number of fragments of a certain microorganism is significantly higher than the data in the background microbial database, it is included in the suspected responsible pathogen, and further methods are used for authenticating. In the alveolar lavage fluid, possible responsible bacteria, fungi, or virus fragments were detected by SGS, and the proportion of the total fragments was often extremely low, even only a few fragments, which is difficult to be diagnosed. SGS testing is often only useful in the diagnosis of pulmonary systemic infections, and when pathogens for nonclinical routine screening are detected, further use of classical pathogen detection methods is needed for diagnosis. This requires the development of a well-developed pathogen verification test system, especially for pathogenic microorganisms that are not easily detected by some common methods. Because the current SGS testing cost is still high, it cannot be widely used in the clinic, and it also affects its timeliness. SGS is also only a pathogen detection method, and it has just been applied in clinical practice. Therefore, there are also blind spots and misunderstandings of its monitoring. The excessive expectation and interpretation of SGS detection results can not only push up the cost of clinical testing, but also make it effective. The examination could not be carried out smoothly, which also led to misdiagnosis and missed diagnosis.

However, because the optimal processing conditions and bioinformatics analysis required for sequencing of different specimens and pathogenic microorganisms are different, it is currently not possible to adapt an SGS detection procedure to all infectious pathogens. Moreover, the difference in the location and method of the specimen will also affect the test results. Therefore, using the deep reinforcement learning, based on the patient's medical history and clinical examination, the possible pathogens are presumed, the specimens are preprocessed and then sequenced, and even different strategies are adopted for the biosignal analysis of the sequencing results. Taking into account various unknown pathogens, the detection rate of specific pathogens and the interpretation of the results are improved. The deep reinforcement learning is a diagnostic basis to reduce errors. It sets certain standards and procedures to determine whether the detected pathogen is a responsible pathogen, and designing targeted evaluation sequencing methods based on different types of pathogens to improve the effectiveness of SGS. Therefore, the deep reinforcement learning combined with knowledge graph is a promising direction for SGS in the application of pulmonary infectious diseases.

6. Conclusion

In this paper, we explore deep reinforcement learning for computer-aided diagnosis and treatment of complex pulmonary infectious diseases. We first present several representative deep reinforcement learning models for the diagnosis and treatment of potential lung infections. Moreover, we discuss the applications of the deep reinforcement learning model in the diagnosis of second-generation genetic testing for pulmonary infection and summarize the current status of pathogenic diagnosis of pulmonary infectious diseases and their main characteristics. After that, we analyze the results of second-generation genetic testing and the main features of each type in common lung infections. Finally, we point out the open challenges and possible future research directions for intensive studies of second-generation genetic testing integrated with deep reinforcement learning in lung infections, which may help the related researchers and medical workers.

Data Availability

The data used to support the findings of this study are currently under embargo, while the research findings are commercialized. Requests for data will be considered by the corresponding author.

Conflicts of Interest

The authors declare no conflicts of interest regarding the publication of this paper.

Acknowledgments

This study was partially funded by the National Natural Science Foundation of China (81871725).

References

[1] Q. Zhang, C. Bai, L. T. Yang, Z. Chen, L Peng, and H. Yu, "A unified smart Chinese medicine framework for healthcare and medical services," *IEEE/ACM Transactions on Computational Biology and Bioinformatics*, 2019.

[2] Q. Zhang, C. Bai, Z. Chen et al., "Deep learning models for diagnosing spleen and stomach diseases in smart Chinese medicine with cloud computing," *Concurrency and Computation: Practice and Experience*, p. e5252, 2019.

[3] Z. Liu, C. Bai, H. Yu et al., "An adaptive deep learning model to differentiate syndromes of infectious fever in smart medicine," *Future Generation Computer Systems*, 2019.

[4] Z. Liu, C. Yao, H. Yu, and T. Wu, "Deep reinforcement learning with its application for lung cancer detection in medical internet of things," *Future Generation Computer Systems*, vol. 97, pp. 1–9, 2019.

[5] L. Zhao, Z. Chen, Y. Yang, Z. Jane Wang, and V. C. M. Leung, "Incomplete multi-view clustering via deep semantic mapping," *Neurocomputing*, vol. 275, pp. 1053–1062, 2018.

[6] L. Zhao, Z. Chen, and Z. J. Wang, "Unsupervised multiview nonnegative correlated feature learning for data clustering," *IEEE Signal Processing Letters*, vol. 25, no. 1, pp. 60–64, 2018.

[7] K. Zhou, M. Lokate, R. H. Deurenberg et al., "Use of whole-genome sequencing to trace, control and characterize the regional expansion of extended-spectrum beta-lactamase producing ST15 *Klebsiella pneumoniae*," *Scientific Reports*, vol. 6, no. 1, Article ID 20840, 2016.

[8] M. J. Dark, "Whole-genome sequencing in bacteriology: state of the art," *Infect Drug Resist*, vol. 2013, no. 6, pp. 115–123, 2013.

[9] A. Sboner, X. Mu, D. Greenbaum, R. K. Auerbach, and M. B. Gerstein, "The real cost of sequencing: higher than you think!" *Genome Biology*, vol. 12, no. 8, p. 125, 2011.

[10] B. Steuernagel, S. Taudien, H. Gundlach et al., "De novo 454 sequencing of barcoded BAC pools for comprehensive gene survey and genome analysis in the complex genome of barley," *BMC Genomics*, vol. 10, no. 1, p. 547, 2009.

[11] S. Jünemann, F. J. Sedlazeck, K. Prior et al., "Updating benchtop sequencing performance comparison," *Nature Biotechnology*, vol. 31, no. 4, pp. 294–296, 2013.

[12] N. J. Loman, R. V. Misra, T. J. Dallman et al., "Performance comparison of benchtop high-throughput sequencing platforms," *Nature Biotechnology*, vol. 30, no. 5, pp. 434–439, 2012.

[13] Q. Liu, J. Zhai, Z. Zhang et al., "A survey on deep reinforcement learning," *Chinese Journal of Computers*, vol. 41, no. 1, pp. 1–27, 2018.

[14] L. Zhao, Z. Chen, Y. Yang, L. Zou, and Z. J. Wang, "ICFS clustering with multiple representatives for large data," *IEEE Transactions on Neural Networks and Learning Systems*, vol. 30, no. 3, pp. 728–738, 2019.

[15] L. Zhao, Z. Chen, L. T. Yang, M. J. Deen, and Z. J. Wang, "Deep semantic mapping for heterogeneous multimedia transfer learning using co-occurrence data," *ACM Transactions on Multimedia Computing, Communications, and Applications*, vol. 15, no. 1s, pp. 1–21, 2019.

[16] Y. LeCun, Y. Bengio, and G. Hinton, "Deep learning," *Nature*, vol. 521, no. 7553, pp. 436–444, 2015.

[17] G. E. Hinton, S. Osindero, and Y. W. Teh, "A fast learning algorithm for deep belief nets," *Neural Computation*, vol. 18, no. 7, pp. 1527–1554, 2006.

[18] R. S. Sutton and A G. Barto, *Reinforcement Learning, An Introduction*, MIT Press, Cambridge, MA, USA, 1998.

[19] V. Mnih, K. Kavukcuoglu, D. Silver et al., "Human-level control through deep reinforcement learning," *Nature*, vol. 518, no. 7540, pp. 529–533, 2015.

[20] N. Heess, G. Wayne, D. Silver, T. Lillicrap, Y. Tassa, and T. Erez, "Learning continuous control policies by stochastic value gradients," in *Proceedings of the Advances in Neural Information Processing Systems*, pp. 2944–2952, Montreal, Canada, October 2015.

[21] R. Coulom, "Efficient selectivity and backup operators in Monte-carlo tree search," in *Proceedings of the International Conference on Computers and Games*, pp. 72–83, Berlin, Germany, November 2006.

[22] T. D. Kulkarni, K. R. Narasimhan, A. Saeedi, and J. B. Tenenbaum, "Hierarchical deep reinforcement learning: integrating temporal abstraction and intrinsic motivation," in *Proceedings of the Conference on Neural Information Processing Systems*, pp. 3675–3683, Barcelona, Spain, May 2016.

[23] A. Wilson, A. Fern, S. Ray et al., "Multi-task reinforcement learning:a hierarchical Bayesian approach," in *Proceedings of the International Conference on Machine Learning*, pp. 1015–1022, Corvallis, OR, USA, June 2007.

[24] H. Li, X. Liao, and I. Carin, "Multi-task reinforcement learning in partially observable stochastic environments," *Journal of Machine Learning Research*, vol. 10, no. 3, pp. 1131–1186, 2009.

[25] M. E. Taylor and P. Stone, "Behavior transfer for value function based reinforcement learning," in *Proceedings of the International Joint Conference on Autonomous Agents and Muhiagent Systems*, pp. 53–59, Utrecht, Netherlands, July 2005.

[26] F. Fernandez and M. Vdoso, "Probabilistic pohcy reuse in a reinforcement learning agent," in *Proceedings of the International Joint Conference on Autonomous Agents and Multiagent Systems*, pp. 720–727, Istanbul, Turkey, May 2015.

[27] H. Wang, Y. Gao, and X. Chen, "Transfer of reinforcement learning:the state of the art," *Acta Electronica Sinica*, vol. 36, no. s1, pp. 39–43, 2008.

[28] A. Graves, G. Wayne, and I. Danihelka, "Neural turing machines," 2014, http://arxiv.org/abs/1 410·5401.

[29] S. Sukhbaatar, J. Weston, and R. Fergus, "End to-end memory networks," in *Proceedings of the Advances in Neural Information Processing Systems*, pp. 2440–2448, Montreal, Canada, December 2015.

[30] S. R. Head, H. K. Komori, S. A. LaMere et al., "Library construction for next generation sequencing: overviews andchallenges," *Biotechniques*, vol. 56, no. 2, pp. 66–68, 2014.

[31] D. H. Parks, M. Imelfort, C. T. Skennerton, P. Hugenholtz, and G. W. Tyson, "CheckM: assessing the quality of microbial genomes recovered from isolates, single cells, and metagenomes," *Genome Research*, vol. 25, no. 7, pp. 1043–1055, 2015.

[32] D. E. Wood and S. L. Salzberg, "Kraken: ultrafast metagenomic sequence classification using exact alignments," *Genome Biology*, vol. 15, no. 3, p. R46, 2014.

[33] S. Ranque, A.-C. Normand, C. Cassagne et al., "MALDI-TOF mass spectrometry identification of filamentous fungi in the clinical laboratory," *Mycoses*, vol. 57, no. 3, pp. 135–140, 2014.

[34] A. Wieser, L. Schneider, J. Jung, and S. Schubert, "MALDI-TOF MS in microbiological diagnostics-identification of microorganisms and beyond (mini review)," *Applied Microbiology and Biotechnology*, vol. 93, no. 3, pp. 965–974, 2012.

[35] P. Tang, M. A. Croxen, M. R. Hasan, W. W. L. Hsiao, and L. M. Hoang, "Infection control in the new age of genomic epidemiology," *American Journal of Infection Control*, vol. 45, no. 2, pp. 170–179, 2017.

[36] S. R. Harris, E. J. Cartwright, M. E. Török et al., "Whole-genome sequencing for analysis of an outbreak of meticillin-resistant *Staphylococcus aureus*: a descriptive study," *The Lancet Infectious Diseases*, vol. 13, no. 2, pp. 130–136, 2013.

[37] C. U. Koser, M. T. Holden, M. J. Ellington et al., "Rapid whole-genome sequencing for investigation of a neonatal MRSA outbreak," *New England Journal of Medicine*, vol. 366, no. 24, pp. 2267–2275, 2012.

[38] A. T. Saeb, M. Abouelhoda, M. Selvaraju et al., "The use of next-generation sequencing in the identification of a fastidiouspathogen: a lesson from a clinical setup," *Evolutionary Bioinformatics*, vol. 13, 2017.

[39] C Guo, L. L. Zhong, Y. HL et al., "Clinical value of fluorescence lateral flow immunoassay in diagnosis of influenza a in children," *Zhongguo Dang Dai Er Ke Za Zhi*, vol. 18, pp. 1272–1276, 2016.

[40] E. Franz, P. Delaquis, S. Morabito et al., "Exploiting the explosion of information associated with whole genome sequencing to tackle Shiga toxin-producing *Escherichia coli* (STEC) in global food production systems," *International Journal of Food Microbiology*, vol. 187, pp. 57–72, 2014.

[41] M. Laabei, M. Recker, J. K. Rudkin et al., "Predicting the virulence of MRSA from its genome sequence," *Genome Research*, vol. 24, no. 5, pp. 839–849, 2014.

[42] M. Willmann, M. El-Hadidi, D. H. Huson et al., "Antibiotic selection pressure determination through sequence-based metagenomics," *Antimicrobial Agents and Chemotherapy*, vol. 59, no. 12, pp. 7335–7345, 2015.

[43] L. Falgenhauer, S.-E. Waezsada, Y. Yao et al., "Colistin resistance gene mcr-1 in extended-spectrum β-lactamase-producing and carbapenemase-producing gram-negative bacteria in Germany," *The Lancet Infectious Diseases*, vol. 16, no. 3, pp. 282-283, 2016.

Hindawi
Journal of Healthcare Engineering
Volume 2020, Article ID 1051394, 11 pages
https://doi.org/10.1155/2020/1051394

Research Article

Modified Immune Evolutionary Algorithm for Medical Data Clustering and Feature Extraction under Cloud Computing Environment

Jing Yu,[1] Hang Li,[2] and Desheng Liu[3]

[1]*Luxun Academy of Fine Arts, No. 19, Miyoshi Street, HePing District, Shenyang P. C 110000, China*
[2]*Software College, Shenyang Normal University, Shenyang 110034, China*
[3]*College of Information and Electronic Technology, Jiamusi University, Jiamusi 154007, Heilongjiang, China*

Correspondence should be addressed to Hang Li; lihangsoft@163.com and Desheng Liu; zdhlds@163.com

Received 9 October 2019; Revised 26 November 2019; Accepted 10 December 2019; Published 20 January 2020

Guest Editor: Liang Zou

Medical data have the characteristics of particularity and complexity. Big data clustering plays a significant role in the area of medicine. The traditional clustering algorithms are easily falling into local extreme value. It will generate clustering deviation, and the clustering effect is poor. Therefore, we propose a new medical big data clustering algorithm based on the modified immune evolutionary method under cloud computing environment to overcome the above disadvantages in this paper. Firstly, we analyze the big data structure model under cloud computing environment. Secondly, we give the detailed modified immune evolutionary method to cluster medical data including encoding, constructing fitness function, and selecting genetic operators. Finally, the experiments show that this new approach can improve the accuracy of data classification, reduce the error rate, and improve the performance of data mining and feature extraction for medical data clustering.

1. Introduction

Through the support of existing technologies, relevant medical research organizations only rely on coupled dictionary technology to classify and store medical images [1]. However, with the continuous increase of the number of slices, some images begin to show serious frame rate overlap phenomenon, which not only causes the sharp decline of the original image gray level but also causes a series of image data redundancy problems. It brings great trouble to the mining and scheduling of the following image information. The so-called image data redundancy refers to the phenomenon of uneven or excessive storage caused by data repetition in the process of data imaging that can lead to the real information loss in the image and cause a certain negative impact on the image sharpness. Frame rate overlap is a common image fault problem, which is often associated with image data redundancy. Under certain circumstances [2], a certain degree of frame rate overlap may lead to a small increase of the image sharpness. But excessive frame rate overlap will lead to serious damage to the modal property of the medical image, which will lead to a large increase of the redundant region in the medical image data. Diagnosis in medicine is related to the patient's medication and treatment. Many diseases are more complex. Data clustering analysis is integrated into the diagnosis of diseases, such as clinical urology and breast cancer, so that doctors can greatly enhance the diagnosis accuracy of patients.

With the fast growth of information science, the research of biological applications has been used for computational science to analyze the intelligent bionic optimization algorithm design and improve the ability of processing big data and analysis [3]. Intelligent bionic algorithms mainly include ant colony algorithm [4], particle swarm optimization (PSO) algorithm [5], and the quantum swarm algorithm [6–8]. Swarm intelligence optimization algorithms have a good application value in artificial intelligence design, data clustering analysis, computer control, and other fields.

Clustering technology is an important part in data mining and machine learning. Domestic researchers mainly focus on the following two aspects: (1) a clustering algorithm dynamically determines the number of clustering centers and (2) a clustering algorithm improves the accuracy of clustering. Zhao et al. [9] presented a new dynamic clustering method based on genetic algorithm; the main idea of the method was that, in order to effectively overcome the sensitivity to the initial state value clustering algorithm, it used the maximum attribute value range partitioning strategy and two stages and dynamic selection method in mutation, which obtained the optimal clustering center.

Clustering analysis is a kind of unsupervised model in pattern recognition. The task of cluster is to divide an unmarked pattern according to the certain criteria into several subsets, which requires that similar samples have the most similar cluster center and dissimilar samples should be divided in different classes. Therefore, it is also called unsupervised classification. Clustering analysis has been extensively used in data mining, image processing, object detection, radar target detection, etc. [10, 11]. Zhang et al. [12] proposed a Geometric-constrained multiview image matching method based on semiglobal optimization. It was obvious that some features had more information than others in a dataset. So it was highly likely that some features should have lower importance degrees during a clustering or a classification algorithm due to their lower information, their higher variances, etc. So, it was always a desire for all artificial intelligence communities to enforce the weighting mechanism in any task that identically used a number of features to make a decision. Parvin and Minaei-Bidgoli [13] proposed a weighted locally adaptive clustering algorithm that was based on the locally adaptive clustering algorithm.

Nowadays, different clustering methods are being used to resolve several machine learning problems. According to the clustering criterion, different clustering algorithms can be divided into clustering algorithm based on fuzzy relations including hierarchical clustering and graph clustering and clustering algorithm based on the objective function [14–16]. For the objective function of optimization clustering algorithms, it generally uses the gradient method to solve the extremum problem. The search direction of gradient method is always along the direction of the energy reduction, which prompts the algorithm easily falling into local minimum value. Methods are sensitive to the initialization of clustering algorithm in the objective function which is a serious defect. To overcome the above shortcomings, all proposed algorithms are used to optimize objective function. Meng et al. [17] presented that the MapReduce programming model was adopted to combine Canopy and K-means clustering algorithms within cloud computing environment, so as to fully utilize the computing and storing capacity of Hadoop clustering. Large quantities of buyers on taobao were taken as application context to do case study through the Hadoop platform's data mining set Mahout. Zhang et al. [18] proposed a high-order possibilistic c-means algorithm (HOPCM) for big data clustering by optimizing the objective function in the tensor space. Li et al. [19] proposed a task scheduling algorithm based on fuzzy clustering algorithms. However, there are still some problems, such as long convergence time.

Moreover, deep learning-based methods are used for feature selection. Minaei-Bidgoli et al. [20] proposed an ensemble based approach for feature selection. The results showed that, although the efficacy of the method was not considerably decreased in most of cases, the method became free from setting of any parameter. Some algorithms could not properly represent data distribution characteristics when datasets were imbalanced. In some cases, the cost of wrong classification could be very high in a sample of a special class, such as wrongly misclassifying cancerous individuals or patients as healthy ones. Hu and Du [21] tried to present a fast and efficient way to learn from imbalanced data. This method was more suitable for learning from the imbalanced data having very little data in class of minority. Gao et al. [22] was devoted to the exploration of brain images for early detection of Parkinson's disease. All brain images were analyzed to extract Gabor 2D features. It was also shown that the models created on Gabor features outperform the ones created without Gabor features. Zhao et al. [23] analyzed the triple-negative breast neoplasm gene regulatory network using gene expression data. We collected triple-negative breast neoplasm gene expression data from the Cancer Genome Atlas to construct a triple-negative breast neoplasm gene regulatory network using least absolute shrinkage and selection operator regression. In addition, it constructed a triple-positive breast neoplasm network for comparison. Nejatian [24] presented that the available additional information at different times and conditions and gold-standard protein complexes was employed to determine fitting thresholds. By doing so, the problem was converted into an optimization problem. Thereafter, the problem was solved using the firefly metaheuristic optimization algorithm.

Hence, we propose a new medical big data clustering algorithm based on modified immune evolutionary method under cloud computing environment to overcome the above disadvantages in this paper. The reminder of this paper is organized as follows: Section 2 presents big data structure analysis in cloud computing environment. Immune evolutionary algorithm is stated in Section 3. Section 4 describes the improved clustering method in detail, Section 5 provides the MapReduce framework, and Section 6 manifests the experiments results. Finally, the conclusion is given in Section 7.

2. Analysis on Storage Mechanism and Structure of Medical Big Data in Cloud Computing Environment

Cloud computing [25–28] is through the Internet to provide dynamic data to extend large storage space and the structure model. In order to evaluate the data clustering and mining in the cloud computing environment, it needs to build a big data storage system architecture in cloud computing environment. Big data storage structure adopts virtualized storage pool and depends on the computer cluster. From top to bottom, these are the I/O (input/output) virtual computer, USB interface layer sequence,

and disk layer, respectively. Enterprise data center through all kinds of terminal accesses the application service, which makes the calculation of distribution on a large number of distributed computers. When all the cloud computing virtual machines are assigned to the physical machine, it uses the following formula to calculate the global optimal solution in this clustering process. And, it also can assign big data feature clustering center $\mathrm{BF}_{\mathrm{M}_i}$ of the cloud computing on the physical machine P_{M_i} according to the optimal solution:

$$N = \frac{1}{n}\sum_{j=1}^{n}\left|U_{t_j^{\mathrm{CPU}}} - U_{t_{\mathrm{avg}}^{\mathrm{CPU}}}\right| + \frac{1}{n}\sum_{j=1}^{n}\left|U_{t_j^{\mathrm{Mem}}} - U_{t_{\mathrm{avg}}^{\mathrm{Mem}}}\right| + \frac{1}{n}\sum_{j=1}^{n}\left|U_{t_j^{\mathrm{bw}}} - U_{t_{\mathrm{avg}}^{\mathrm{bw}}}\right|. \tag{1}$$

The sample is collected and analyzed to determine whether the sample belongs to a typical sample. Assuming that data information stream sample $S = (\overline{X}_1, \overline{X}_2, \ldots, \overline{X}_k)$ makes sampling in time $(T_1, T_2, \ldots, T_k)$. We divide big data set X in cloud environment into c clusters, $1 < c < n$. The data segmentation can be transformed as space segmentation. Storage structure central vector of big data is obtained:

$$V = \left\{ v_{ij} \,\middle|\, i = 1, 2, \ldots, c,\ j = 1, 2, \ldots, s \right\}, \tag{2}$$

where V_i is the i-th vector of object cluster feature.

Fuzzy division matrix can be presented as

$$U = \left\{ \mu_{ik} \,\middle|\, i = 1, 2, \ldots, c,\ k = 1, 2, \ldots, n \right\}. \tag{3}$$

Redundant data reduction is processed for a single data source. In the process of multichannel QoS demand virtual machine clustering, some parameters are defined as virtual machine set $V_{\mathrm{MS}} = \left\{V_{\mathrm{M}_1}, V_{\mathrm{M}_1}, \ldots, V_{\mathrm{M}_m}\right\}$ and physical machine set $P_{\mathrm{MS}} = \left\{P_{\mathrm{M}_1}, P_{\mathrm{M}_1}, \ldots, P_{\mathrm{M}_n}\right\}$. Inspiring factor is α, and the expect of inspiring factor is β. Biggest mining number is $I_{\max}$. As a result, uploaded data blocks provide a fixed size of data blocks, which is beneficial to analyze the cloud clustering. Through the big data storage mechanism analysis in cloud computing environment, it provides the accurate data for big data clustering.

Supposing that the time series of information stream is $\{x(t_0 + i\Delta t)\}, i = 1, 2, \ldots, N-1$. X and Y are attribute sets. The vector expression of big data clustering space in the cloud computing environment is

$$\mathfrak{R} = \left[r(t_0), r(t_0 + \Delta t), \ldots, r(t_0 + (K-1)\Delta t)\right], \tag{4}$$

where $r(t)$ is information stream time series of big data clustering in cloud computing environment and Δt is data sampling interval. The spectral characteristic $X_{\mathrm{p}}(u)$ of discrete samples of big data can be calculated as

$$X_{\mathrm{p}}(u) = s_{\mathrm{c}}(t)e^{2\pi f_0 t} = \frac{1}{\sqrt{T}}\mathrm{rect}\frac{t}{T}e^{(2\pi(f_0 t + Kt^2)/2)}, \tag{5}$$

where $s_{\mathrm{c}}(t)$ is the characteristic scalar time series of big data, $e^{2\pi f_0 t}$ is the discrete sample center of big data clustering, and (F, Q) is sample data high-order Bessel function statistics of data set $\{X_1, X_2, \ldots, X_N\}$. So, we can get the confidence and confidence interval:

$$\begin{aligned} z_{i,d}^{k+1} &= x_{\mathrm{r}_1}^{k} + F \cdot \left(x_{\mathrm{r}_2}^{k} - x_{\mathrm{r}_3}^{k}\right), \\ u_{i,d}^{k+1} &= \begin{cases} x_{i\,d}^{t+1}, & f_{\mathrm{fit}}^{t} < f_{\mathrm{fit}}', \\ z_{i,d}^{k+1}, & f_{\mathrm{fit}}^{t} \geq f_{\mathrm{fit}}'. \end{cases} \end{aligned} \tag{6}$$

Suppose the information flow time series in the cloud computing environment is $\{x(t_0 + i\Delta t)\}, i = 0, 1, \ldots, N-1$. Let X and Y be the set of properties. The expression of clustering space state vector of big data in cloud computing environment is as follows:

$$\begin{aligned} X &= \left[x(t_0), x(t_0 + \Delta t), \ldots, x(t_0 + (K-1)\Delta t)\right] \\ &= \begin{bmatrix} x(t_0) & x(t_0 + \Delta t) & \cdots & x(t_0 + (K-1)\Delta t) \\ x(t_0 + J\Delta t) & x(t_0 + (J+1)\Delta t) & \cdots & x(t_0 + (K-1)\Delta t + J\Delta t) \\ \vdots & \vdots & & \vdots \\ x(t_0 + (m-1)J\Delta t) & x(t_0 + (1 + (m-1)J)\Delta t) & \cdots & x(t_0 + (N-1)\Delta t) \end{bmatrix}, \end{aligned} \tag{7}$$

where $x(t)$ is the information flow time series of big data clustering system in cloud computing environment, J is the time window function of phase space reconstructed by big data in cloud computing environment, M is the target clustering regulator, and Δt is the data sampling interval.

The discrete sample spectral characteristic $X_{\mathrm{p}}(u)$ of big data is calculated, and the main feature component is

$$X_{\mathrm{p}}(u) = s_{\mathrm{c}}(t)e^{j2\pi f_0 t} = \frac{1}{\sqrt{T}}\mathrm{rect}\left(\frac{t}{T}\right)e^{j2\pi(f_0 t + Kt^2)/2}, \tag{8}$$

where $s_{\mathrm{c}}(t)$ is the characteristic scalar time series of big data and $e^{j2\pi f_0 t}$ is the center of discrete sample of big data clustering.

The data set is $\{X_1, X_2, \ldots, X_n\}$. (F, Q) is the high-order Bessel function statistics of the sample data to determine the confidence of node data packets and establish the confidence

interval. The obtained confidence and confidence intervals are

$$z_{(i,d)}^{(k+1)} = x_{r_1}^k + F \cdot \left(x_{r_2}^k - x_{r_3}^k\right),$$
$$u_{(i,d)}^{(k+1)} = \begin{cases} x_{id}^{(t+1)}, & f_{\text{fitness}}^t < f_{\text{fitness}}^*, \\ z_{(i,d)}^{(k+1)}, & f_{\text{fitness}}^t \geq f_{\text{fitness}}^*. \end{cases} \quad (9)$$

3. Immune Evolutionary Algorithm (IEA)

IEA consists of crossover and mutation operator which represent two strategies with group search and information exchange. It provides optimization opportunities for each individual. However, this inevitably produces the degradation phenomenon in some cases, and the degradation phenomenon is quite obvious.

IEA uses some features or knowledge in original problems to suppress the degradation phenomenon appeared in the process of optimization. The key operation of IEA is to construct the structure of immune operator that is finished through vaccination and immune selection. The immune evolutionary algorithm can improve the fitness of the individual and prevent the group degradation, so as to reduce the original wave phenomenon in the late evolutionary algorithm and improve the convergence speed. The main steps for immune evolutionary algorithm are as follows, and the detailed information can be obtained from [29, 30].

(1) Randomly generate the initial parent group A_1.

(2) Extract the vaccine according to prior knowledge.

(3) If the current group contains the best individual, it stops running the process and outputs the result. Otherwise, the procedure continues to work.

(4) Cross operation of the current k-th group A_k is conducted, and it obtains the population B_k.

(5) It makes mutation operation for B_k and obtains the population C_k.

(6) It executes vaccination for C_k and gets group D_k.

(7) It executes immune selection for D_k and obtains new parent group A_{k+1}. Then back to step 3.

4. Modified Immune Evolutionary Algorithm for Data Clustering

Fuzzy clustering is regarded as one of the commonly used approaches for data analysis. The Fuzzy C-means (FCM) algorithm is the most well-known and widely used method for fuzzy clustering and provides an optimal way to construct fuzzy information granules [31]. Cluster prototypes and membership values of data across all clusters can be developed by optimizing the FCM clustering model. Basically, the FCM is a steepest-descent algorithm with variable step length that is adjusted according to the majorization principle for the step length, showing the simplicity and efficiency of the algorithm. Therefore, we combine immune evolutionary algorithm and FCM to optimize the cluster result [32, 33]. The detailed improved data clustering processes are as follows:

The objective function of FCM is

$$J(X;U,V) = \sum_{k=1}^{n}\sum_{i=1}^{c} u_{ik}^m D_{ik}^2, \quad (10)$$

$$D_{ik}^2 = \left(x_k - v_i\right)^T \left(x_k - v_i\right), \quad (11)$$

where D_{ik} is the distance from k-th data point to i-th cluster center, $V = (v_1, v_2, \ldots, v_c)$ denotes the cluster center of each class, and $v_i \in R$ and $m \in (1, \infty)$ are fuzzy index:

$$X = \left(x_1, x_2, \ldots, x_n\right) \subset R,$$
$$U = \left\{ U \in R^{c\times n} \middle| u_{ik} \in [0,1]; \sum_{i=1}^{c} v_{ik} = 1; 0 < \sum_{k=1}^{n} v_{ik} < n \right\}. \quad (12)$$

4.1. Encoding. According to $J(X;U,V)$, the aim of cluster is to obtain fuzzy division matrix U and cluster prototype V of sample X. U and V are associated with each other. So we have two encoding methods. First, we encode U. Suppose that n samples need to be divided into c clusters. Gene cluster $a = \{\alpha_1, \alpha_2, \ldots, \alpha_n\}$ denotes one clustering result; $\alpha_i \in \{1, 2, \ldots, c\}$. When $\alpha_i = k\,(1 \leq k \leq c)$, then x_i belongs to k-th cluster. Its search space is c^n. If the data samples are bigger, the search space of this encoding is very big too. Therefore, we adopt the second encoding method for V. The quantized values are encoded into strings according to their respective values. $a = \{\alpha_1, \alpha_2, \ldots, \alpha_l\}$, $l = c \times p$. The former p quantized values denote the first p dimension cluster center. But it does not change with the data sample n.

4.2. Constructing Fitness Function. According to $J(X;U,V)$, if the clustering effect is better, the object function value is smaller. The formula (10) is used for constructing fitness function f:

$$f = \frac{1}{J(X;U,V) + 1}. \quad (13)$$

4.3. Genetic Operator Selection. Genetic operator has a point crossover, two-point crossover, and multipoint crossover methods. The immune operator inverts the selected individual genes based on certain probability. We can also adopt a reverse genetic mutation operator, namely, it randomly generates a gene in the parent group and the gene is reverted. It basically prevents premature phenomenon. In genetic selection methods, it adopts the roulette wheel selection method and ranking selection. Crossover probability $p_c \in [0.75, 0.95]$, $p_m \in [10^{-3}, 10^{-2}]$.

4.4. Immune Vaccine Selection. The immune vaccine selection properly describe two ways. It is not clear. Specifically, the first method, after collecting information,

executes the immune vaccine. The other is an adaptive method, namely, in the process of group evolution from the best individual genes. It extracts useful information and then executes the vaccine. The former is restricted due to two reasons. The first one is it is difficult to form a mature approach for a prior knowledge. It cannot get effective immune vaccine. The second is, to extract the vaccine, the work costs too much. Therefore, in the clustering algorithm based on immune evolution, we adopt the adaptive method to extract the vaccine.

Therefore, we get the new cluster algorithm as follows (Figure 1).

Step 1. Fix cluster class number c, $1 \le c \le n-1$. Set fuzzy index $m \in (1, +\infty)$, stop condition τ, total population number p_n, crossover probability p_c, mutation probability p_m, vaccination probability p_v, and vaccine update probability p_u.

Step 2. Randomly generate group $P(k)$ with p_n individuals.

Step 3. Compute fitness of every individual.

(1) Each individual is decoded to calculate each prototype parameter v_i, $1 \le i \le c$.
(2) Use v_i and (8) to calculate D_{ik}^2.
(3) Calculate $U = [u_{ik}]_{c\times n}$.
If $I_k = \varphi$,

$$u_{ik} = \frac{1}{\sum_{j=1}^{c} \left[d_{ik}^2 / d_{jk}^2 \right]^{(1/(m-1))}}. \tag{14}$$

If $I_k \neq \varphi$,

$$u_{ik} = 0, \quad \forall i \in {}^{-}I_k, \qquad \sum_{i \in I_k} u_{ik} = 1, \tag{15}$$

where $I_k = \{i \mid 1 \le i \le c, d_{ik} = 0\}$ and ${}^{-}I_k = \{1, 2, \ldots, c\} - I_k$.

(4) Use U, D_{ik}, and (7) to calculate object function $J(X; U, V)$, and then it can get f for each individual.

Step 4. Make statistics for parent group, determine the best individual, then decompose the best individual, and extract immune vaccine $H = \{h_i \mid i = 1 - m\}$.

Step 5. Use p_c and p_m to make crossover, mutation operation for $P(k)$, and get group $P\prime(k)$.

Step 6. Execute vaccination and immunization selection for $P(k)$ and get group $P(k+1)$.

Step 7. If it satisfies τ, return to Step 8. Otherwise, return to Step 3.

Step 8. Then, it decodes the best individual, the clustering prototype v_i is calculated, the classification results of each sample are calculated, and this classification result is the clustering result of data set X.

5. MapReduce Framework

In order to improve the efficiency of modified immune evolutionary algorithm (MIEA) in processing large datasets, this paper designs the implementation scheme of MIEA in the MapReduce model. There are two main operations in the mechanism processing big data clustering tasks: updating the center of the class and fitness evaluation. Class center is updated based on MIEA. Fitness evaluation is to calculate the sum of Euclidean distance between each object and the center of mass and then find the global optimal value. The clustering program divides data objects into clusters, minimizes the sum of Euclidean distances between all objects and the center of mass, and takes it as the fitness function of MIEA. The data clustering process based on MIEA is shown in Figure 2.

6. Experiments and Analysis

In order to verify the performance of clustering and data mining in cloud computing environment, we conduct abundant experiments. Medical data are taken from http://archive.ics.uci.edu/ml/. The database is constantly updated. Donations of data are also accepted. The database type involves life, engineering, science, etc.; the record number is from several to hundred thousand pieces. The data selected in this paper are Breast Cancer Wisconsin (Original) Data Set. These data sets are from the clinical case reports of the university of Wisconsin hospital in the United States, and each data has 11 attributes.

Due to limited space, we display only few results in here. The computing platform is configured with Intel Core I7 4.0 GHz CPU, 16G Memory, and NVIDIA GTX 780 GPU. The algorithm is compiled by Apache Hadoop platform. The sampling frequency of big data is $f_s = 20$ kHz. The time center of big data clustering is $t_0 = 20$ s. Size of the data is from 50 MB to 2 GB. Cross probability $p_c = 0.95$, variation probability $p_v = 0.3$, and fuzzy index $m = 2$. We also select three state-of-the-art clustering methods to make comparisons including HGM [34], WPC [35], and ACCH [36].

6.1. Result 1. Table 1 is the description of 11 attributes of this dataset.

In this paper, the proposed algorithm is adopted to calculate the weight of each feature. Features with the weight less than a certain threshold will be removed. According to the actual situation in this paper, 2 and3 with the smallest weight will be removed. In the process of the algorithm, we will randomly select sample R. Different random numbers will lead to certain discrepancy in the weight of the result. Therefore, this paper adopts the average method by running it for 20 times. Then, we summarize the results to calculate the average value of each weight as shown in Figure 3.

By analyzing the data set, the importance of attribute weight can be obtained, which has some reference values for clinical diagnosis and can be used for the analysis of actual cases. This can avoid misdiagnosis as far as possible and

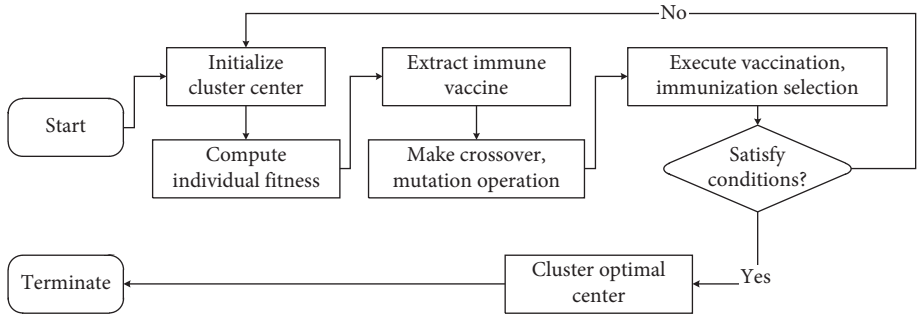

Figure 1: Proposed clustering algorithm flow diagram.

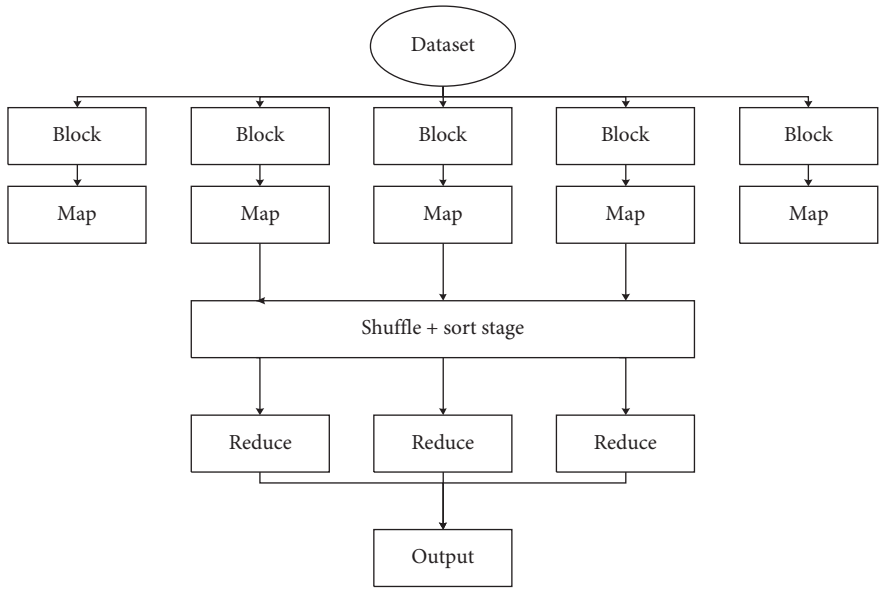

Figure 2: Data clustering flow based on MIEA.

Table 1: Attribute description.

Name of attributes	Description	The serial number of characteristics
Lumps thickness	1–10	1
Cell size uniformity	1–10	2
Cell morphology uniformity	1–10	3
Marginal adhesion	1–10	4
Single epithelial cell size	1–10	5
Bare nucleus	1–10	6
Bland chromatin	1–10	7
Normal nucleoli	1–10	8
Mitosis	1–10	9

improve the diagnosis speed and accuracy. According to the attributes, we obtain the object function optimal value as given in Table 2.

6.2. Result 2. To evaluate the performance of proposed algorithm, the composite data sets given in Table 3 are adopted. The four public data sets are assembled into a large data set, all of which are from UCI Machine Learning Repository with different attributes. Four data sets are randomly copied into several backups to form a large data set with 10^7 records.

F-measure is adopted as the evaluation index of clustering quality. *F*-measure is calculated from two information indexes, precision, and recall rate, defined as

$$F(i,j) = \frac{2 \cdot r(i,j) \cdot p(i,j)}{r(i,j) + p(i,j)}, \tag{16}$$

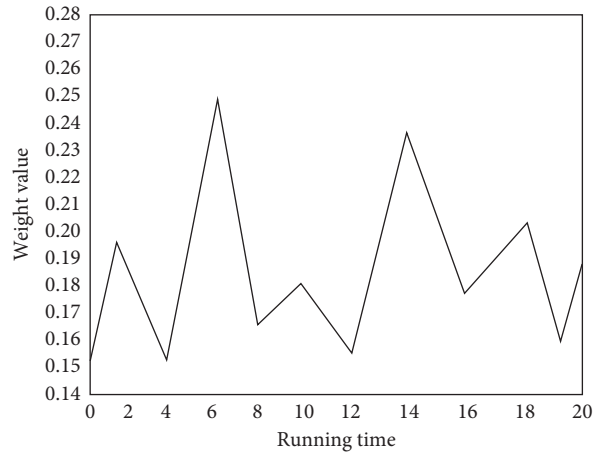

Figure 3: Weight change in 20 times.

Table 2: Performance comparison.

Method	HGM	WPC	ACCH	Proposed
Accuracy (%)	65	72	76	**85**
Optimal value	12.54	10.31	8.75	**6.59**

Table 3: Attributes of experimental datasets.

Number	Dataset	Sample number	Dimensionality	Cluster number
1	Iris	10000050	3	4
2	CMC	10000197	3	9
3	Wine	10000040	3	13
4	Vowel	10000822	6	3

Table 4: F comparison with different methods.

Dataset number	HGM	WPC	ACCH	Proposed
1	0.678	0.796	0.853	**0.912**
2	0.312	0.336	0.398	**0.423**
3	0.493	0.528	0.735	**0.796**
4	0.597	0.654	0.678	**0.817**

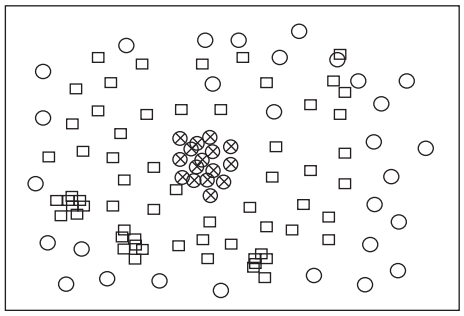

Figure 4: Big data two-dimensional feature distribution in cloud computing.

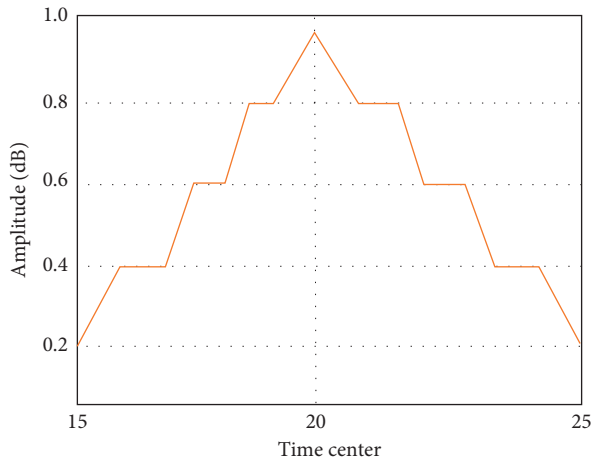

Figure 5: Feature extraction result with the proposed method.

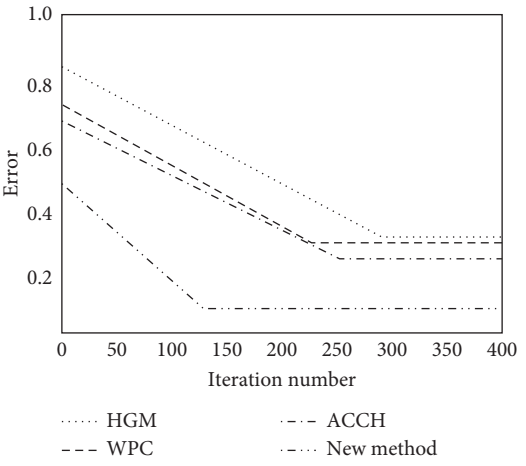

Figure 6: Comparison results.

where j represents the class generated by the cluster method, i denotes the class label of original dataset, and r and p represent recall rate and precision, respectively. Recall rate is defined as $r(i, j) = n_{ij}/n_i$. Precision is defined as $p(i, j) = n_{ij}/n_j$. Here, n_{ij} represents the divided class number of class i. n_i and n_j are the data sizes of class i and

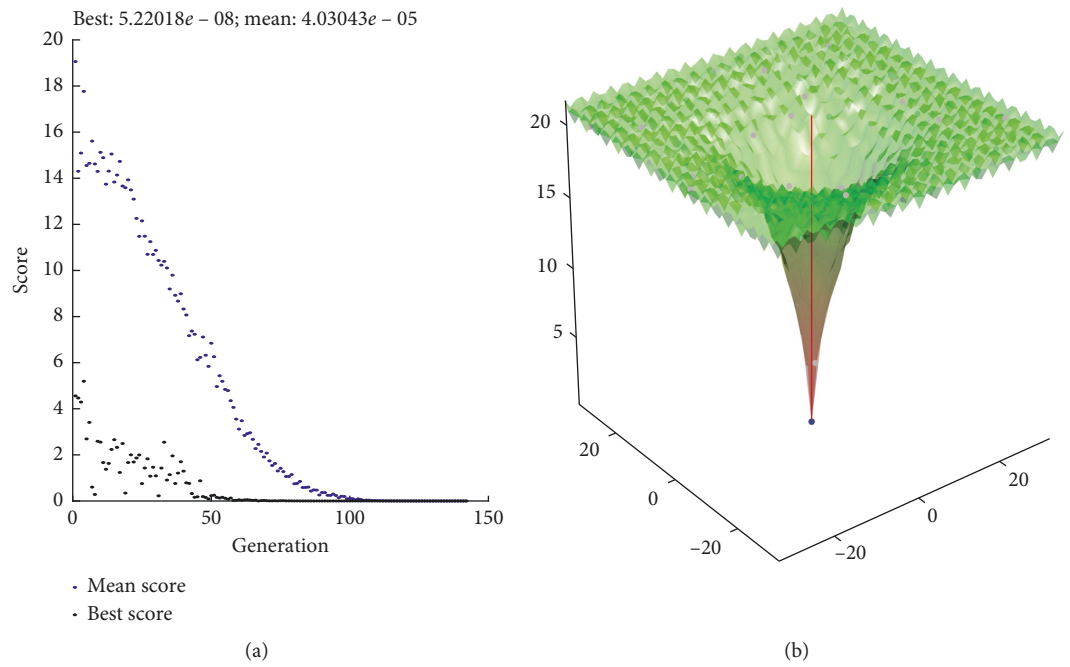

Figure 7: HGM method.

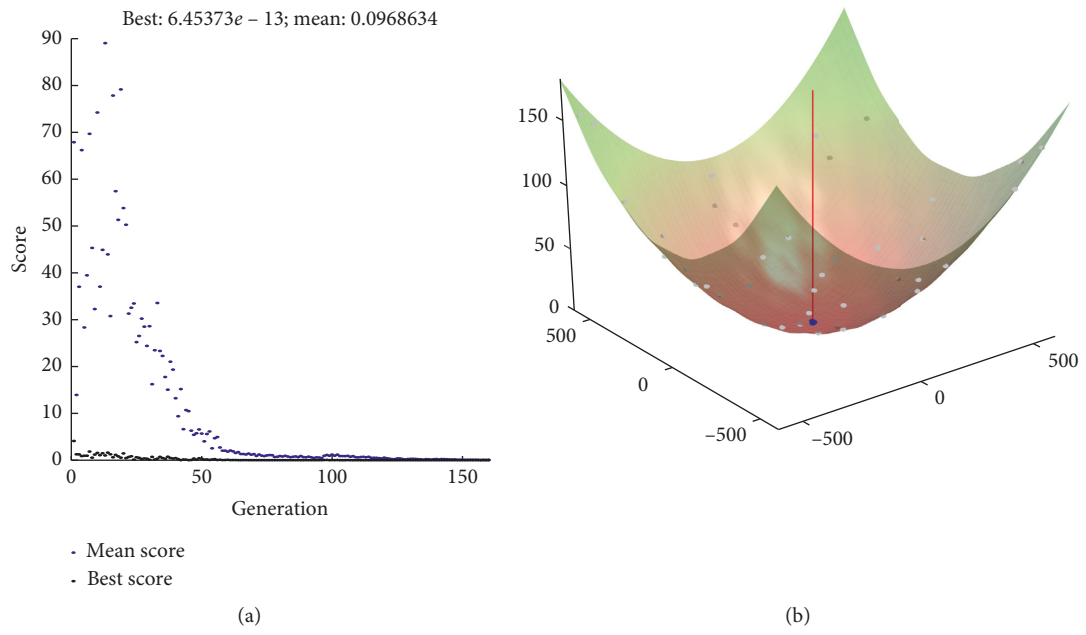

Figure 8: WPC method.

class j, respectively. For the data set with size n, the calculation formula of F-measure is

$$F = \sum_i \frac{n_i}{n} \max_j (F(i, j)), \tag{17}$$

where the upper bound of F is 1. If the F-measure value is larger, then the clustering quality will be higher as shown in Table 4. With the increase of dataset number, the F value is slightly on the whole. However, the value of 0.817 of the proposed method is still higher than that of HGM, WPC, and ACCH.

The following experiments are for the feature extraction under cloud computation.

The original big data feature distribution is random as shown in Figure 4, and it is difficult to achieve feature extraction in the two-dimensional space regularity. We use the proposed algorithm for feature extraction and processing data clustering to build big data feature extraction model.

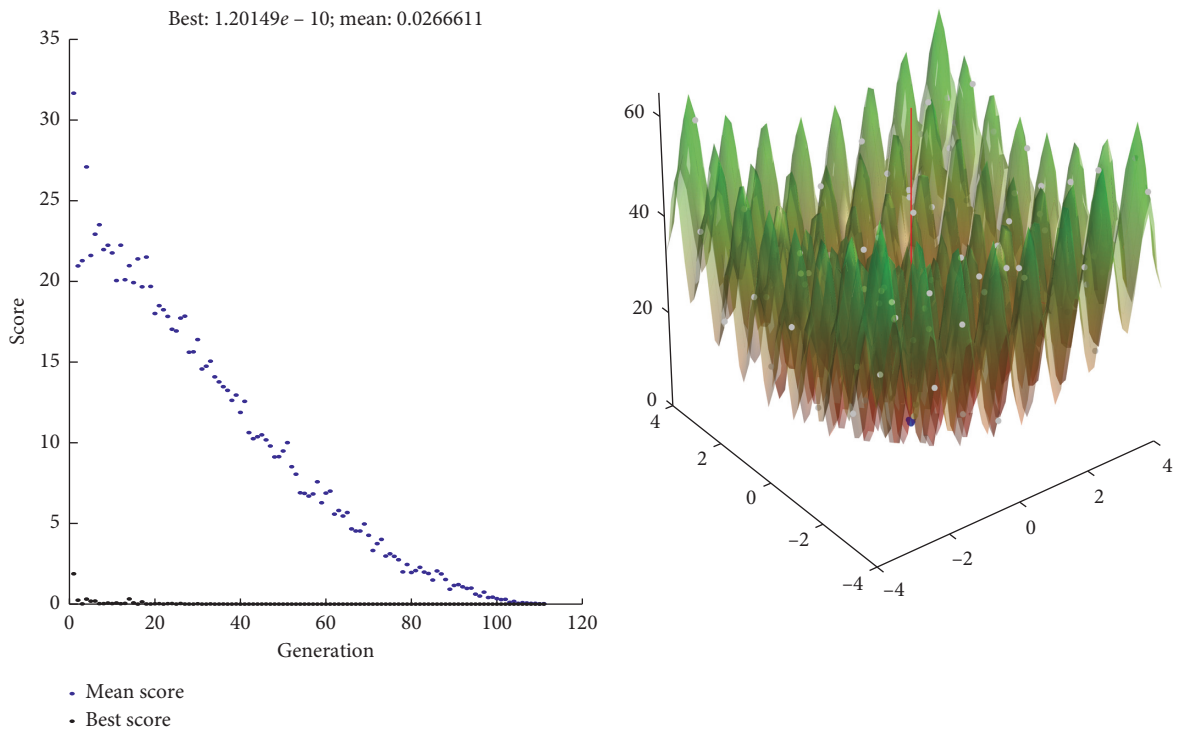

Figure 9: ACCH method.

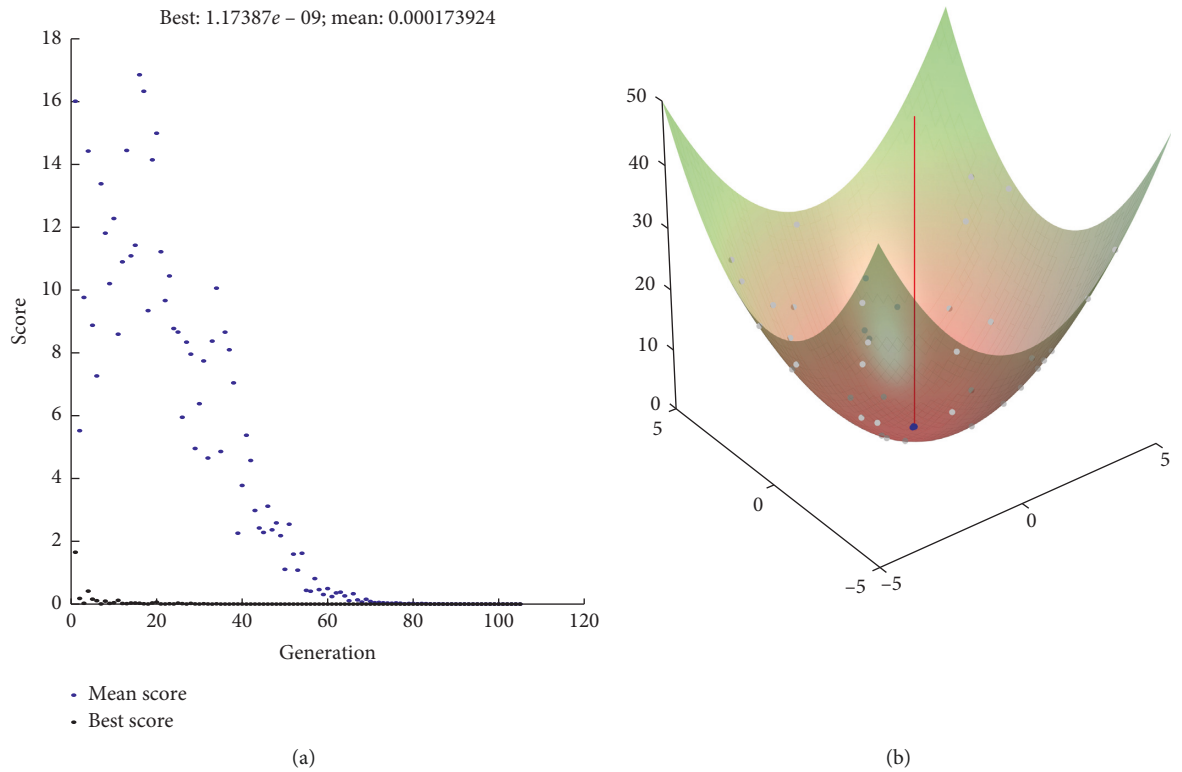

Figure 10: Proposed method.

The obtained feature extraction results are shown in Figure 5.

As can be seen in Figure 5, the proposed algorithm can effectively evaluate the feature extraction of big data in cloud computing; the beam focusing performance is good, which provides accurate basis for the data optimal clustering. Using different big data clustering optimization algorithms, we get the clustering center optimal performance curve as shown in Figure 6.

We also get the best value and mean value within 200 iterations as shown in Figures 7–10. And, we can know that the best value is with our proposed method.

7. Conclusions

In cloud computing environment, vast amounts of data need to be scheduled and accessed aiming at achieving the goal of medical data mining. This paper puts forward a new medical big data clustering algorithm based on modified immune algorithm. It firstly analyzes the big data structure model in the cloud computing environment to build big data feature extraction and information model. Designing immune optimization algorithm for clustering, it achieves the goal of optimization clustering for big data. Simulation results show that the proposed algorithm improves the clustering performance of big data in cloud computing environment. The new algorithm is used for IoT data clustering, which reduces the error rate and exhibits better performance. In the future, we will research the deep learning methods and apply them into actual engineering projects.

Data Availability

The data used to support the findings of this study are available from the corresponding author upon request.

Conflicts of Interest

The authors declare that there are no conflicts of interest regarding the publication of this paper.

Acknowledgments

This research was funded by the Heilongjiang Province Science Found for Returnees (grant number: LC2017027), Jiamusi University Science and Technology Innovation Team Construction Project (grant number: CXTDPY-2016-3), and Basic Research Project of Heilongjiang Province Department of Education (grant number: 2016-kyywf-0547).

References

[1] V. Kisekka and J. S. Giboney, "The effectiveness of health care information technologies: evaluation of trust, security beliefs, and privacy as determinants of health care outcomes," *Journal of Medical Internet Research*, vol. 20, no. 4, p. e107, 2018.

[2] L. Zhao, Z. Chen, L. T. Yang, M. Jamal Deen, and Z. Jane Wang, "Deep semantic mapping for heterogeneous multimedia transfer learning using co-occurrence data," *ACM Transactions on Multimedia Computing, Communications, and Applications*, vol. 15, no. 1s, pp. 9–21, 2019.

[3] Q. Zhang, C. Bai, L. T. Yang, Z. Chen, P. Li, and H. Yu, "A unified smart Chinese medicine framework for healthcare and medical services," *IEEE/ACM Transactions on Computational Biology and Bioinformatics*, 2019.

[4] S. Yin, J. Liu, and L. Teng, "An improved artificial bee colony algorithm for staged search," *TELKOMNIKA Telecommunication, Computing, Electronics and Control*, vol. 14, no. 3, pp. 1099–1104, 2016.

[5] T. Liu and S. Yin, "An improved particle swarm optimization algorithm used for BP neural network and multimedia courseware evaluation," *Multimedia Tools and Applications*, vol. 76, no. 9, pp. 11961–11974, 2016.

[6] L. Jie, L. Teng, and S. Yin, "An improved discrete firefly algorithm used for traveling salesman problem," in *Proceedings of the International Conference in Swarm Intelligence*, pp. 593–600, Springer, Fukuoka, Japan, July–August 2017.

[7] S.-L. Yin and J. Liu, "A K-means approach for map-reduce model and social network privacy protection," *Journal of Information Hiding and Multimedia Signal Processing*, vol. 7, no. 6, pp. 1215–1221, 2016.

[8] L. Peng, Z. Chen, L. T. Yang et al., "Deep convolutional computation model for feature learning on big data in Internet of things," *IEEE Transactions on Industrial Informatics*, vol. 14, no. 2, pp. 790–798, 2018.

[9] L. Zhao, Z. Chen, Y. Yang, L. Zou, and Z. J. Wang, "ICFS clustering with multiple representatives for large data," *IEEE Transactions on Neural Networks and Learning Systems*, vol. 30, no. 3, pp. 728–738, 2019.

[10] J. Gao, P. Li, and Z. Chen, "A canonical polyadic deep convolutional computation model for big data feature learning in internet of things," *Future Generation Computer Systems*, vol. 99, pp. 508–516, 2019.

[11] J. Yang, Y. Xie, and Y. Guo, "Panel data clustering analysis based on composite PCC: a parametric approach," *Cluster Computing*, vol. 22, no. S4, pp. 8823–8833, 2019.

[12] Q. Zhang, C. Bai, Z. Chen et al., "Deep learning models for diagnosing spleen and stomach diseases in smart chinese medicine with cloud computing," *Concurrency and Computation: Practice and Experience*, no. e5252, 2019.

[13] H. Parvin and B. Minaei-Bidgoli, "A clustering ensemble framework based on elite selection of weighted clusters," *Advances in Data Analysis and Classification*, vol. 7, no. 2, pp. 181–208, 2013.

[14] L. Zhao, Z. Chen, Y. Yang, Z. Jane Wang, and V. C. M. Leung, "Incomplete multi-view clustering via deep semantic mapping," *Neurocomputing*, vol. 275, pp. 1053–1062, 2018.

[15] W. Zhao, L. Yan, and Y. Zhang, "Geometric-constrained multi-view image matching method based on semi-global optimization," *Geo-spatial Information Science*, vol. 21, no. 2, pp. 115–126, 2018.

[16] P. Li, Z. Chen, L. T. Yang, L. Zhao, and Q. Zhang, "A privacy-preserving high-order neuro-fuzzy c-means algorithm with cloud computing," *Neurocomputing*, vol. 256, pp. 82–89, 2017.

[17] Z. Meng, J.-S. Pan, and L. Kong, "Parameters with adaptive learning mechanism (PALM) for the enhancement of differential evolution," *Knowledge-Based Systems*, vol. 141, pp. 92–112, 2018.

[18] Q. Zhang, L. T. Yang, Z. Chen, and P. Li, "PPHOPCM: privacy-preserving high-order possibilistic c-means algorithm for big data clustering with cloud computing," *IEEE Transactions on Big Data*, no. 99, p. 1, 2017.

[19] J. Li, T. Ma, M. Tang, W. Shen, and Y. Jin, "Improved FIFO scheduling algorithm based on fuzzy clustering in cloud computing," *Information*, vol. 8, no. 1, p. 25, 2017.

[20] B. Minaei-Bidgoli, M. Asadi, and P. Hamid, "An ensemble based approach for feature selection," in *Proceedings of the International Conference on Engineering Applications of Neural Networks*, pp. 240–246, EANN, Corfu, Greece, September 2011.

[21] G. Hu and Z. Du, "Adaptive kernel-based fuzzy C-means clustering with spatial constraints for image segmentation," *International Journal of Pattern Recognition & Artificial Intelligence*, vol. 33, no. 1, 2018.

[22] J. Gao, J. Li, and Y. Li, "Approximate event detection over multi-modal sensing data," *Journal of Combinatorial Optimization*, vol. 32, no. 4, pp. 1002–1016, 2016.

[23] L. Zhao, Z. Chen, Z. J. Wang, and Jane, "Unsupervised multiview nonnegative correlated feature learning for data clustering," *IEEE Signal Processing Letters*, vol. 25, no. 1, pp. 60–64, 2018.

[24] S. Nejatian, H. Parvin, and E. Faraji, "Using sub-sampling and ensemble clustering techniques to improve performance of imbalanced classification," *Neurocomputing*, vol. 276, pp. 55–66, 2018.

[25] M. Tavana, H. Parvin, and F. Rezazadeh, "Parkinson detection: an image processing approach," *Journal of Medical Imaging and Health Informatics*, vol. 7, no. 2, pp. 464–472, 2017.

[26] H. C. Jung, S. H. Kim, J. H. Lee, J. H. Kim, and S. W. Han, "Gene regulatory network analysis for triple-negative breast neoplasms by using gene expression data," *Journal of Breast Cancer*, vol. 20, no. 3, pp. 240–245, 2017.

[27] M. Mohammadi Jenghara, H. Ebrahimpour-Komleh, and H. Parvin, "Dynamic protein–protein interaction networks construction using firefly algorithm," *Pattern Analysis and Applications*, vol. 21, no. 4, pp. 1067–1081, 2018.

[28] B. Langmead and A. Nellore, "Cloud computing for genomic data analysis and collaboration," *Nature Reviews Genetics*, vol. 19, no. 5, 2018.

[29] M. Abdel-Basset, M. Mohamed, and V. Chang, "NMCDA: a framework for evaluating cloud computing services," *Future Generation Computer Systems*, vol. 86, pp. 12–29, 2018.

[30] P. Li, Z. Chen, L. T. Yang et al., "An incremental deep convolutional computation model for feature learning on industrial big data," *IEEE Transactions on Industrial Informatics*, vol. 15, no. 3, pp. 1341–1349, 2018.

[31] G. Zilong, W. Sun'an, and Z. Jian, "A novel immune evolutionary algorithm incorporating chaos optimization," *Pattern Recognition Letters*, vol. 27, no. 1, pp. 2–8, 2006.

[32] Q. Zhang, L. T. Yang, Z. Yan, Z. Chen, and P. Li, "An efficient deep learning model to predict cloud workload for industry informatics," *IEEE Transactions on Industrial Informatics*, vol. 14, no. 7, pp. 3170–3178, 2018.

[33] P. Li, Z. Chen, L. T. Yang, J. Gao, Q. Zhang, and M. J. Deen, "An improved stacked auto-encoder for network traffic flow classification," *IEEE Network*, vol. 32, no. 6, pp. 22–27, 2018.

[34] G. Manogaran, V. Vijayakumar, R. Varatharajan et al., "Machine learning based big data processing framework for cancer diagnosis using hidden markov model and GM clustering," *Wireless Personal Communications*, vol. 102, no. 3, pp. 2099–2116, 2018.

[35] Q. Zhang, L. T. Yang, A. Castiglione et al., "Secure weighted possibilistic c-means algorithm on cloud for clustering big data," *Information Sciences*, vol. 479, pp. 515–525, 2019.

[36] H. Li, H. Li, and K. Wei, "Automatic fast double KNN classification algorithm based on ACC and hierarchical clustering for big data," *International Journal of Communication Systems*, vol. 31, no. 16, p. e3488, 2018.

Hindawi
Journal of Healthcare Engineering
Volume 2020, Article ID 3965961, 6 pages
https://doi.org/10.1155/2020/3965961

Research Article

Analysis of Anesthesia Methods in Percutaneous Kyphoplasty for Treatment of Vertebral Compression Fractures

Jie Liu,[1] Lin Wang,[1] Mei Chai,[1] Junjie Kang,[2] Jie Wang,[2] and Yanjun Zhang[1]

[1]*Department of Anesthesia, Second Affiliated Hospital of Dalian Medical University, Dalian, China*
[2]*School of Software Technology, Dalian University of Technology, Dalian, China*

Correspondence should be addressed to Jie Wang; wangjie1003@163.com and Yanjun Zhang; zhangyanjun8893@126.com

Received 23 August 2019; Revised 12 November 2019; Accepted 10 December 2019; Published 9 January 2020

Guest Editor: Liang Zou

Aim. Percutaneous kyphoplasty (PKP) is a routine operation for the treatment of vertebral compression fracture (VCF). Both local anesthesia and general anesthesia are widely used for PKP. However, which type of anesthesia is better for PKP still remains uncertain. This study aimed to find out whether local anesthesia or general anesthesia is more suitable for PKP. *Methods*. This is a retrospective clinical trial. A total of 85 single-level VCF patients who received PKP 12 months ago were recruited in this study. 45 patients who received local anesthesia were in group L, and 40 patients with general anesthesia were in group G. Clinical, radiological, and economic data between the two groups were collected. *Results*. No difference was found on preoperative data between the two groups. The duration of operation time in group L was longer than that in group G. Within 12 months after PKP, more complications happened in group G than those in group L. *Results*. This study found that there was no difference between group L and group G before the operation in terms of baseline. The operation time in group L was shorter than that in group G and the difference was significant. The VAS pain score in group L was significantly higher than that in group G. Clinical and radiological indicators were all improved after surgery, while no other difference was detected between the two groups. More severe complications happened in group G within 12 months after PKP, and the cost in group L was significantly less than that in group G. *Conclusion*. Both local anesthesia and general anesthesia were reliable for PKP. However, local anesthesia was more efficient and safer with less expense and more bearable pain when compared with general anesthesia.

1. Introduction

It is well known that vertebral compression fracture (VCF) can cause severe and long time pain [1], and it may lead to nerve injury, mental disease, and even disability without proper treatment [2]. The incidence of VCF has been increasing and the patients are becoming younger recently [3, 4]. VCF can also cause height loss and kyphosis, which always reduces the quality of life [5]. Long-term bedridden can even cause deadly hypostatic pneumonia and decubitus ulcer. Percutaneous kyphoplasty (PKP) is a good treatment for patients of VCF who cannot bear the pain or do not get well from conservative treatment [6]. Nowadays, both local anesthesia and general anesthesia are widely used in the PKP process [7–12]. However, the controversy about the best type of anesthesia for PKP has never been stopped. As far as we know, there were few studies focusing on this topic.

The purpose of this study is to find the best type of anesthesia for PKP.

2. Materials and Methods

The study was authorized by the Ethics Committee of the Second Hospital of Dalian Medical University (DMU).

2.1. Patient Population. PKP for all patients was performed at the First Operating Room of the Second Affiliated Hospital of DMU from Jan 2014 to Jan 2017. All data were retrospectively reviewed from the medical records and bills.

The inclusion criteria [13] were planned as follows:

(1) The compression was over 15% of the height of the injured vertebra
(2) Single-level VCF was diagnosed by doctors

(3) The severe back pain had been treated by conservative treatments for 14 days before PKP, but not effective enough

(4) The pain was over 5, measured by visual analogy score (VAS)

(5) Percussion and tenderness on the posterior midline were detected

(6) In magnetic resonance imaging (MRI), a hypointense signal on T1-weighted images was observed at the injured level

(7) In MRI, a hyperintense signal on T2-weighted stir fat-suppressed images was observed at the injured level

The exclusion criteria [13] were planned as follows:

(1) The fracture was caused by secondary osteoporosis

(2) The patient got coagulopathy

(3) The patient was in cachexia or ASA IV-V

(4) There was no pain caused by VCF

(5) The fracture was caused by metastatic cancer

(6) There was a symptomatic neurologic injury

According to the inclusion and exclusion criteria, a total of 85 patients (45 patients who received local anesthesia were in group L and 40 patients with general anesthesia were in group G) were recruited in this study.

The demographic data of patients were collected one day before the operation from medical records at the ward. They included but are not limited to age, gender, body weight, height, body mass index (BMI), and smoking history. Injury mechanisms were divided into fall, traffic, sports, and others. Compensation was recorded according to the bills. The fracture level and operator were also collected.

2.2. Outcome Measures. The outcomes indicators were set in accordance with published research [13]. Clinical outcome was measured by operation time, severe complications, and VAS pain score of before, during, and after the operation. Operation time was obtained from anesthesia records. Severe complications consisted of myocardial ischemia, lung disease, and delirium.

Zero of VAS indicated no pain. Ten of VAS meant an ultimate pain. The VAS of patients was measured by a researcher who did not know this study. Anteroposterior and lateral radiographs were obtained before and after the operation. Vertebral height and kyphotic angle (KA) were calculated by measuring the radiographs as described in the published article [13]. Briefly, the posterior height (PH) of caudal vertebra under the injured level was set as 100%. Then, the anterior height (AH) and posterior height (PH) of the injured vertebra were calculated similarly and presented as percentage of PH. The KA was defined as an acute angle between the upper endplate of the head-end vertebra and the lower endplate of the tail-end vertebra.

2.3. Expenditures. Total expenditure and expenditures for anesthesia, device, drugs, and nursing were collected from medical bills of each patient. The medical expenditures outside of our institution were not involved. All participants declared that they had no extra medical expenditure outside of our institution from Jan 2014 to Jan 2017. Expenditures were collected 12 months after the operation. All expenditures were calculated as RMB.

2.4. Statistical Analysis. All data were analyzed by SPSS (Version 12, SPSS Cooperation, Chicago, IL). The classified variable was calculated by chi-square test and Fisher's exact test. They were shown as a figure with percentage. The continuous variable was calculated by Mann–Whitney test, paired or unpaired t-test with or without Welch's correction. Continuous variable was shown as mean ± standard deviation. All statistical results are presented as tables. $P < 0.05$ indicates the difference is statistically significant.

3. Results

3.1. Subject Characteristics. According to the inclusion and exclusion criteria, a total of 85 patients were included in this study (Table 1). 45 patients who received local anesthesia were recruited in group L and 40 patients undergoing general anesthesia were in group G. Table 1 presents the indicators of both groups at the baseline. The differences of indicators between the two groups were not significant ($P > 0.05$, all).

3.2. Clinical Results. The operation time and severe complications are shown in Table 1. The VAS of pain score before, during, and after PKP was also recorded (Table 2). The operation time in group L was significantly shorter than that in group G ($P < 0.05$). The incidence of severe complications in group L was significantly lower than that in group G ($P < 0.05$). Myocardial ischemia occurred in two patients with history of coronary heart disease during the operation in group G. One patient with history of asthma developed asthmatic attack just after intubation and recovered by spraying salbutamol aerosol and intravenous methylprednisolone in group G. Another patient of 80 years old developed delirium after the operation and got well 4 days later.

In both groups, the pain was significantly relieved after the operation when compared with that before the operation ($P < 0.05$). However, the degree of pain relief between the two groups had no significant difference ($P > 0.05$). There was no significant difference in VAS pain score before and after the operation between the two groups ($P > 0.05$). During the operation, the VAS pain score in group L was 2.939 ± 0.9934, while it could not be assessed in group G because of general anesthesia. However, after the operation, no patients said they feel pain in the period of the operation, so we still consider VAS pain score during the operation to be 0. Thus, the VAS pain score during the operation in group L was significantly higher than that in group G ($P < 0.05$).

Table 1: Characteristics of the study population.

Characteristics	Group L ($n = 45$)	Group G ($n = 40$)	P	Statistical method
Age	73.43 ± 7.181	75.01 ± 9.653	0.4320	Mann–Whitney test
Male	25 (55.6)	19 (47.5)	0.5179	Fisher's exact test
Body mass index (kg/m^2)	21.98 ± 2.511	22.99 ± 2.719	0.1109	Mann–Whitney test
Smoking	8 (17.8)	8 (20.0)	0.6123	Fisher's exact test
Injury mechanism			0.3596	Chi-square
Fall	29	21		
Traffic or sports injury	6	10		
Others	10	9		
Compensation	25 (55.6)	21 (0.525)	0.8295	Fisher's exact test
Fracture level			0.4778	Chi-square
T	15	10		
L	30	30		
Operator			0.4157	Chi-square
No. 1	11	10		
No. 2	16	18		
No. 3	9	6		
No. 4	7	2		
No. 5	2	4		
Operation time	40.89 ± 29.91	59.09 ± 21.11	0.0441	Mann–Whitney test
Severe complications	0	4	0.0451	Fisher's exact test

Data are presented as mean ± standard deviation and number (percentage values).

Table 2: Comparison of VAS pain scores before, during, and after the operation in group L and group G .

Group	VAS before the operation	VAS during the operation	VAS after the operation
Group L	7.332 ± 0.8761	2.939 ± 0.9934[a]	0.4472 ± 0.6121[b]
Group G	7.502 ± 0.9874	0[a]	0.4459 ± 0.7136[b]

Data are presented as mean ± standard deviation. VAS, Visual Analogue Scale. [a]$P < 0.05$ when compared with preoperative VAS; [b]$P < 0.05$ when compared with preoperative VAS.

3.3. Radiological Results. Radiological data were obtained as described above. AH and PH were analyzed (Table 3). AH KA in both groups was also compared (Table 4). All these radiological indicators showed there was no significant difference between the two groups at the same time point ($P > 0.05$, respectively). In the meantime, there was no significant difference in PH presented before and after the operation ($P > 0.05$). After the operation, AH in group L was significantly increased (94.10 ± 21.19) than that before the operation (80.92 ± 31.64) ($P < 0.05$), and AH in group G was significantly increased after the operation (93.17 ± 14.02) than that before the operation (80.10 ± 9.169) ($P < 0.05$). KA in group L was significantly decreased after the operation (6.344 ± 8.431) than that before the operation (12.04 ± 7.093) ($P < 0.05$), and KA in group G was significantly decreased after the operation (7.051 ± 4.711) than that before the operation (12.01 ± 3.183) ($P < 0.05$). The data shown above demonstrated that the PKP in both groups were effective on deformity correction.

3.4. Expenditures. The expenditures of both groups are shown in Table 5 and Figure 1. In group L, total expenditure and anesthesia expenditure were significantly lower than those in group G ($P < 0.05$). There was no significant difference between the two groups when it came to device, drug, or nursing expenditures ($P > 0.05$).

4. Discussion

A desired method for the treatment of VCF should offer pain relief and a deformity correction fast and safely [14–16]. Percutaneous vertebroplasty (PVP) and PKP have been widely used recently, which can meet the needs of patients who want to relief the pain and correct the deformity [17, 18]. Some researches demonstrated that PVP and PKP had similar effects on pain killing and function improving [19–21]. However, recently published meta-analysis [22] showed that PKP has more merits compared with PVP. So, PKP should be recommended to people for the treatment of VCF.

However, there was still controversy about which kind of anesthesia was better for PKP as both local anesthesia and general anesthesia are used widely at present [11, 12]. In this study, patients with single-level VCF were included. Clinical outcomes, radiological outcomes, and expenditures were compared between local and general anesthesia.

Though the VAS pain score in group L during the operation is higher than that in group G, there are still several other reasons supporting the usage of local anesthesia for PKP. First, the pain of local anesthesia during the operation is relatively bearable (the VAS in L group is about 2.939, Table 2). Second, the sense of pain during the operation can be used as a protection for severe nerve injury because patients will give feedback to the operator when the nerve is

Table 3: Comparison of anterior and posterior heights before and after the operation in L and G groups.

Group	AH before the operation	AH after the operation	PH before the operation	PH after the operation
Group L	80.92 ± 31.64	94.10 ± 21.19[a]	91.15 ± 16.99	93.17 ± 14.02
Group G	80.10 ± 9.169	90.98 ± 12.24[a]	89.91 ± 8.951	91.67 ± 9.714

Data are presented as mean ± standard deviation. AH, anterior height; PH, posterior height. [a]$P < 0.05$ when compared with preoperative VAS.

Table 4: Comparison of kyphotic angles before and after operation in L and G groups.

Group	KA before the operation	KA after the operation	Change of KA
Group L	12.04 ± 7.093	6.344 ± 8.431[a]	3.504 ± 6.011
Group G	12.01 ± 3.183	7.051 ± 4.711[a]	3.772 ± 4.221

Data are presented as mean ± standard deviation. KA, kyphotic angle. [a]$P < 0.05$ when compared with preoperative VAS.

Table 5: Comparison of expenditure in group L and group G .

Expenditure	Group L ($n = 45$)	Group G ($n = 40$)	P	Statistical method
Total expenditure (RMB)	43170 ± 5831	52920 ± 6012	**<0.0001**	Mann–Whitney test
Anesthesia expenditure (RMB)	6221 ± 3112	14989 ± 7231	**<0.0001**	Mann–Whitney test
Device expenditure (RMB)	34841 ± 7493	35773 ± 7804	0.1665	Mann–Whitney test
Drug expenditure (RMB)	1099 ± 399.5	1120 ± 509.5	0.3127	Mann–Whitney test
Nursing expenditure (RMB)	128.5 ± 39.55	132 ± 44.75	0.7091	Mann–Whitney test

Data are presented as mean ± standard deviation.

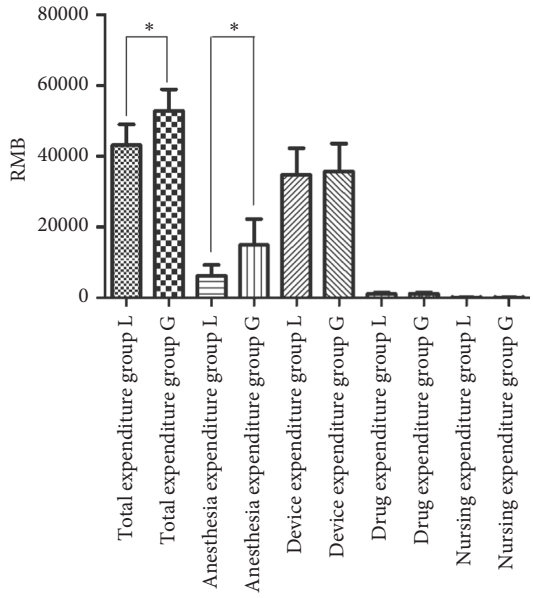

Figure 1: Comparison of expenditures between L group and G group. Error bars represent +1 SD from the mean. *Statistically significant ($P < 0.05$).

going to be hurt. Third, the AH and KA between the two groups had no significant difference, which is in consistence with the previous published studies [23–26] and indicates that the type of anesthesia has no impact on the treatment effect of PKP. Therefore, local anesthesia, instead of general anesthesia, should be adopted for PKP for the treatment of VCF.

We also found more advantages in local anesthesia for PKP. The operation time in group L was shorter than that in group G. Group L needed less expenditure when compared with group G. More severe complications happened in group G such as myocardial ischemia and infection of the lung after the operation, while fewer happened in group L. This was also an important reason for high expenditure in group G too. According to the above data, local anesthesia showed its advantages, such as shorter operation time, lower incidence of severe complications, and less expenditure.

However, local anesthesia might not be good for all patients with VCF. In this study, we chose patients with single-level VCF which caused short operation time and less expenditure. While for multiple-level VCFs, general anesthesia may be a good choice because of the complicated operation and longer operation time and uncomfortable feeling of the prone position. So the anesthesia choice is relative and it should be planned by the patient's VCF condition and the patient's desire.

Expenditures can be divided into micro- and macrocosts [27, 28]. Macrocost focuses on the sum of the expenditures in a specific period. The merit of macrocost is that its data are easier to collect and calculate than that of microcost. But the details in the macrocost will be ignored, which is its internal drawback. In comparison, microcost lists all the items of the expenditures in a specific period, including the resources and the categories. So the expenditures of our study were collected and analyzed in the method of microcost.

According to the opinion of the published article [29], direct and indirect expenditures are supposed to be collected for cost analysis. However, the guidelines from the UK, Netherlands, and South Korea indicate that it is also acceptable to do the cost analysis with only direct expenditures [30, 31]. Therefore, we collected only direct expenditures in this study.

Referring to the published research [32], recommendations for medical procedures can be various from A to E. Grade A means the new procedure is cheaper and equally or more effective than the old one, which should be recommended strongly. Grade E means the new procedure is less or equally effective but more expensive, which should be rejected. The degrees of recommendations of grades B, C, and D are between A and E. The local anesthesia for PKP is supposed to be scored as grade A, which means the procedure should be strongly recommended.

There are still several points for consideration. Firstly, inherent limitations for retrospective study are not able to be avoided. Prospective studies should be better to verify the conclusions in the future. Secondly, the methods for appraising clinical outcomes such as cost-utility analysis were not applied in this study. Other researches focusing on this topic had better apply the cost-utility analysis to get a more affirmed conclusion [32]. Lastly, patients undergoing local anesthesia, who still felt pain and were nervous, should use conscious sedation, such as dexmedetomidine plus some opioids to make patients comfortable, which needs an anesthesiologist to keep patients safe and more expenditure.

5. Conclusions

PKP is an effective treatment for patients with VCFs. General anesthesia led to more serious complications, while local anesthesia was more effective, safer, and cost less. Therefore, although patients may endure tolerable pain, local anesthesia is more suitable for PKP for patients with single-level VCF when compared with general anesthesia.

Data Availability

The data used to support the findings of this study are included within the supplementary information files.

Ethical Approval

The study was authorized by the Ethics Committee, Dalian Medical University (DMU).

Consent

Before anesthesia, anesthetists explained the plan carefully to the patients until they understood it totally. Informed consent was signed by all patients.

Disclosure

Jie Liu, Lin Wang, and Mei Chai are the co-first authors.

Conflicts of Interest

Jie Liu, Lin Wang, Mei Chai, Junjie Kang, Jie Wang, and Yanjun Zhang have no conflicts of interest.

Authors' Contributions

Jie Liu, Lin Wang, and Mei Chai contributed equally to this study.

Acknowledgments

This work was supported by the National Nature Science Foundation of China (no. 61472100). Our team collected all the data and performed all the experiments. Thanks are due to Junyu Xiong, the head of our department, who provided general support.

Supplementary Materials

PKP for all patients was performed at the First Operating Room of the Second Affiliated Hospital of DMU from Jan 2014 to Jan 2017. All data were retrospectively reviewed from the medical records and bills. Research data include characteristics of the study population, comparison of VAS pain scores before, during, and after operation in L and G groups, comparison of anterior and posterior heights before and after the operation in L and G groups, comparison of kyphotic angles before and after the operation in L and G groups, comparison of expenditure in L and G groups. *Statistical Analysis.* All data were analyzed by SPSS (Version 12, SPSS cooperation, Chicago, IL). The classified variable was handled by chi-squared test and Fisher's exact test. They were shown as figure with percentage. The continuous variable was treated by Mann–Whitney test, paired or unpaired t-test with or without Welch's correction. The continuous variable was shown by mean ± standard deviation. All statistical approaches were presented by the tables of the article. $P < 0.05$ indicates the difference is statistically significant. (*Supplementary Materials*)

References

[1] X. Mei, Z. y. Sun, F. Zhou, Z. p. Luo, and H.-l. Yang, "Analysis of pre- and postoperative pain variation in osteoporotic vertebral compression fracture patients undergoing kyphoplasty," *Medical Science Monitor*, vol. 23, pp. 5994–6000, 2017.

[2] X. H. Zuo, X. P. Zhu, H. G. Bao et al., "Network meta-analysis of percutaneous vertebroplasty, percutaneous kyphoplasty, nerve block, and conservative treatment for nonsurgery options of acute/subacute and chronic osteoporotic vertebral compression fractures (OVCFs) in short-term and long-term effects," *Medicine*, vol. 97, no. 29, Article ID e11544, 2018.

[3] E. Lau, K. Ong, S. Kurtz, J. Schmier, and A. Edidin, "Mortality following the diagnosis of a vertebral compression fracture in the Medicare population," *The Journal of Bone and Joint Surgery-American Volume*, vol. 90, no. 7, pp. 1479–1486, 2008.

[4] M. Shengzhong, W. Dongjin, W. Shiqing et al., "Modification of percutaneous vertebroplasty for painful old osteoporotic vertebral compression fracture in the elderly: preliminary report," *Injury*, vol. 43, no. 4, pp. 486–489, 2012.

[5] J. McCarthy and A. Davis, "Diagnosis and management of vertebral compression fractures," *American Family Physician*, vol. 94, no. 94, pp. 44–50, 2016.

[6] X. Chen, W. Guo, Q. Li et al., "Is unilateral percutaneous kyphoplasty superior to bilateral percutaneous kyphoplasty for osteoporotic vertebral compression fractures? Evidence

from a systematic review of discordant meta-analyses," *Pain Physician*, vol. 21, no. 4, pp. 327–336, 2018.

[7] X. L. Ru, Z. H. Jiang, B. S. Song, X. G. Gui, H. Lin, and J. He, "Treatment of senile osteoporotic vertebral compression fractures with percutaneous kyphoplasty under local anesthesia," *Zhongguo Gu Shang*, vol. 26, no. 10, pp. 824–828, 2013, in Chinese.

[8] L. Liu, S. Cheng, R. Lu, and Q. Zhou, "Extrapedicular infiltration anesthesia as an improved method of local anesthesia for unipedicular percutaneous vertebroplasty or percutaneous kyphoplasty," *BioMed Research International*, vol. 2016, Article ID 5086414, 4 pages, 2016.

[9] J. V. Cuchillo-Sastriques, M. Monsma-Muñoz, N. García-Claudio, and M. Barberá-Alacreu, "Anestesia subaracnoidea hipobárica metamérica para las técnicas de refuerzo vertebral. Experiencia en 6 casos," *Revista Española de Anestesiología y Reanimación*, vol. 61, no. 6, pp. 328–331, 2014.

[10] M. Stevenson, T. Gomersall, M. Lloyd Jones et al., "Percutaneous vertebroplasty and percutaneous balloon kyphoplasty for the treatment of osteoporotic vertebral fractures: a systematic review and cost-effectiveness analysis," *Health Technology Assessment (Winchester, England)*, vol. 18, no. 17, pp. 1–290, 2014.

[11] Medical Advisory Secretariat, "Percutaneous vertebroplasty for treatment of painful osteoporotic vertebral compression fractures: an evidence-based analysis," *Ontario Health Technology Assessment Series*, vol. 10, no. 19, pp. 1–45, 2010.

[12] M. Luginbühl, "Percutaneous vertebroplasty, kyphoplasty and lordoplasty: implications for the anesthesiologist," *Current Opinion in Anaesthesiology*, vol. 21, no. 4, pp. 504–513, 2008.

[13] Z. Jing, Q. Sun, J. Dong et al., "Is it beneficial to reuse the balloon in percutaneous kyphoplasty for the treatment of non-neoplastic vertebral compression fractures?," *Medical Science Monitor*, vol. 23, pp. 5907–5915, 2017.

[14] L. D. Kong, P. Wang, L. F. Wang, Y. Shen, Z.-K. Shang, and L.-C. Meng, "Comparison of vertebroplasty and kyphoplasty in the treatment of osteoporotic vertebral compression fractures with intravertebral clefts," *European Journal of Orthopaedic Surgery & Traumatology*, vol. 24, no. Suppl 1, pp. S201–S208, 2014.

[15] R. S. Taylor, R. J. Taylor, and P. Fritzell, "Balloon kyphoplasty and vertebroplasty for vertebral compression fractures," *Spine*, vol. 31, no. 23, pp. 2747–2755, 2006.

[16] B. B. Pradhan, H. W. Bae, M. A. Kropf, V. V. Patel, and R. B. Delamarter, "Kyphoplasty reduction of osteoporotic vertebral compression fractures: correction of local kyphosis versus overall sagittal alignment," *Spine*, vol. 31, no. 4, pp. 435–441, 2006.

[17] C. H. Hu, Q. P. Li, C. Wang, Q. P. Liu, and H. G. Long, "Analysis of clinical effects of three operative methods for osteoporotic vertebral compression fracture," *Zhongguo Gu Shang*, vol. 29, no. 7, pp. 619–624, 2016, in Chinese.

[18] D. Yan, L. Duan, J. Li, C. Soo, H. Zhu, and Z. Zhang, "Comparative study of percutaneous vertebroplasty and kyphoplasty in the treatment of osteoporotic vertebral compression fractures," *Archives of Orthopaedic and Trauma Surgery*, vol. 131, no. 5, pp. 645–650, 2011.

[19] K. Kumar, R. Nguyen, and S. Bishop, "A comparative analysis of the results of vertebroplasty and kyphoplasty in osteoporotic vertebral compression fractures," *Operative Neurosurgery*, vol. 67, no. 3 Suppl Operative, pp. ons171–ons188, 2010.

[20] J. T. Liu, W. J. Liao, W. C. Tan et al., "Balloon kyphoplasty versus vertebroplasty for treatment of osteoporotic vertebral compression fracture: a prospective, comparative, and randomized clinical study," *Osteoporosis International*, vol. 21, no. 2, pp. 359–364, 2010.

[21] F. R. Santiago, A. P. Abela, L. G. Álvarez, R. M. Á. Osuna, and M. d. M. C. García, "Pain and functional outcome after vertebroplasty and kyphoplasty. A comparative study," *European Journal of Radiology*, vol. 75, no. 2, pp. e108–e113, 2010.

[22] H. Wang, S. S. Sribastav, F. Ye et al., "Comparison of percutaneous vertebroplasty and balloon kyphoplasty for the treatment of single level vertebral compression fractures: a meta-analysis of the literature," *Pain Physician*, vol. 18, no. 3, pp. 209–222, 2015.

[23] Z.-Y. Sun, X.-F. Li, H. Zhao et al., "Percutaneous balloon kyphoplasty in treatment of painful osteoporotic occult vertebral fracture: a retrospective study of 89 cases," *Medical Science Monitor*, vol. 23, pp. 1682–1690, 2017.

[24] X. T. Fang, F. Yu, S. L. Fu et al., "Clinical outcomes of percutaneous kyphoplasty under local anesthesia for osteoporotic vertebral compression fractures," *Zhonghua Yi Xue Za Zhi*, vol. 93, no. 33, pp. 2654–2658, 2013, in Chinese.

[25] A. Krüger, L. Oberkircher, J. Figiel et al., "Height restoration of osteoporotic vertebral compression fractures using different intravertebral reduction devices: a cadaveric study," *The Spine Journal*, vol. 15, no. 5, pp. 1092–1098, 2015.

[26] G. H. Shi, P. C. Li, and X. C. Wei, "Progress on treatment of osteoporotic vertebral compression fracture," *Zhongguo Gu Shang*, vol. 26, no. 10, pp. 878–882, 2013, in Chinese.

[27] N. R. Powe and R. I. Griffiths, "The clinical-economic trial: promise, problems, and challenges," *Controlled Clinical Trials*, vol. 16, no. 6, pp. 377–394, 1995.

[28] Y. Kim, Y.-W. Kim, I. J. Choi et al., "Cost comparison between surgical treatments and endoscopic submucosal dissection in patients with early gastric cancer in Korea," *Gut and Liver*, vol. 9, no. 2, pp. 174–180, 2015.

[29] S. Birch and A. Gafni, "Economics and the evaluation of health care programmes: generalisability of methods and implications for generalisability of results," *Health Policy*, vol. 64, no. 2, pp. 207–219, 2003.

[30] E.-Y. Bae, "Guidelines for economic evaluation of pharmaceuticals in Korea," *Journal of Preventive Medicine and Public health*, vol. 41, no. 2, pp. 80–83, 2008.

[31] P. H. M. Van Baal, T. L. Feenstra, R. T. Hoogenveen, G. Ardine de Wit, and W. B. F. Brouwer, "Unrelated medical care in life years gained and the cost utility of primary prevention: in search of a "perfect" cost-utility ratio," *Health Economics*, vol. 16, no. 4, pp. 421–433, 2007.

[32] A. Laupacis, D. Feeny, A. S. Detsky, and P. X. Tugwell, "How attractive does a new technology have to be to warrant adoption and utilization? Tentative guidelines for using clinical and economic evaluations," *CMAJ: Canadian Medical Association Journal*, vol. 146, no. 4, pp. 473–481, 1992.

Hindawi
Journal of Healthcare Engineering
Volume 2020, Article ID 6484129, 18 pages
https://doi.org/10.1155/2020/6484129

Research Article

Fatigue Evaluation through Machine Learning and a Global Fatigue Descriptor

G. Ramos[1], **J. R. Vaz**[2,3,4], **G. V. Mendonça**[4], **P. Pezarat-Correia**[4], **J. Rodrigues**[5], **M. Alfaras**[1,6] **and H. Gamboa**[5,7]

[1]*PLUX Wireless Biosignals S.A, Avenida 5 Outubro 70, 1050-59 Lisbon, Portugal*
[2]*Department of Biomechanics and Center for Research in Human Movement Variability, University of Nebraska at Omaha, Omaha, NE, USA*
[3]*Universidade Europeia, Laureate International Universities, Lisbon, Portugal*
[4]*Neuromuscular Research Lab, CIPER, Faculty of Human Kinetics, University of Lisbon, Lisbon, Portugal*
[5]*Laboratory for Instrumentation, Biomedical Engineering and Radiation Physics (LIBPhys-UNL), Faculty of Sciences and Technology of NOVA University of Lisbon, Caparica, Portugal*
[6]*Universitat Jaume I, Castelló de la Plana, Spain*
[7]*Department of Physics, Faculty of Sciences and Technology of NOVA University of Lisbon, Caparica, Portugal*

Correspondence should be addressed to G. Ramos; gramos@plux.info

Received 26 August 2019; Revised 19 October 2019; Accepted 11 November 2019; Published 7 January 2020

Guest Editor: Liang Zou

Research in physiology and sports science has shown that fatigue, a complex psychophysiological phenomenon, has a relevant impact in performance and in the correct functioning of our motricity system, potentially being a cause of damage to the human organism. Fatigue can be seen as a subjective or objective phenomenon. Subjective fatigue corresponds to a mental and cognitive event, while fatigue referred as objective is a physical phenomenon. Despite the fact that subjective fatigue is often undervalued, only a physically and mentally healthy athlete is able to achieve top performance in a discipline. Therefore, we argue that physical training programs should address the preventive assessment of both subjective and objective fatigue mechanisms in order to minimize the risk of injuries. In this context, our paper presents a machine-learning system capable of extracting individual fatigue descriptors (IFDs) from electromyographic (EMG) and heart rate variability (HRV) measurements. Our novel approach, using two types of biosignals so that a global (mental and physical) fatigue assessment is taken into account, reflects the onset of fatigue by implementing a combination of a dimensionless (0-1) global fatigue descriptor (GFD) and a support vector machine (SVM) classifier. The system, based on 9 main combined features, achieves fatigue regime classification performances of 0.82 ± 0.24, ensuring a successful preventive assessment when dangerous fatigue levels are reached. Training data were acquired in a constant work rate test (executed by 14 subjects using a cycloergometry device), where the variable under study (fatigue) gradually increased until the volunteer reached an objective exhaustion state.

1. Introduction

Fatigue occurs frequently in several functional tasks performed on a daily basis [1]. Fatigue can be classified as objective or subjective, taking into consideration its nature [2].

Objective fatigue is a physical phenomenon, not only on its origins but also in the effects that it produces (generating a decrease in the capability to exert mechanical work), in opposition to subjective fatigue, which can be directly caused by intense or stressful mental tasks and, indirectly, by physical activities whose consequences, as De Luca [3] affirmed, are "*...characterized by a decline of alertness, mental concentration, motivation, and other psychological factors...*".

Taking into consideration the relevance of sports in the modern society and the fact that it is also a valuable example of how physical activities may force the human body to reach its limits, the brave effort of athletes to reach their maximum performance was a great inspiration for this study.

However, in spite of the great preponderance of the physical component, athletes can only reach their full potential when mentally and physically healthy, reason why studying both subjective and objective fatigue becomes interesting to achieve a global evaluation of the consequences of fatigue and eventually adjust the training programs.

Through the previous descriptions, these two types of fatigue (objective and subjective) gradually rises due to an intense physical or mental activity, causing the body to reach its limit breaking the homeostasis state, due to the deficit between the metabolic energy production/consumption and the accumulation of metabolic waste at cellular level, conditioning the normal functioning of the organic system. The perturbation of the homeostasis state becomes a potential/transient cause of damage to the organism or, in more drastic situations, the effect of fatigue may be prolonged leading to overwork, chronic fatigue syndrome, overtraining syndrome, and immunity dysfunctions, as stated by Wan et al. [4].

In the specific case of objective fatigue, it reflects the inability of the organism to maintain homeostasis [4, 5] and may result from the physiological consequences of exercise (e.g., accumulation of metabolites, such as lactic acid [4], within the exercising muscle). Objective fatigue can be subdivided accordingly to its physiological origin in central fatigue, which reflects changes at the neuronal level that affect nerve conduction to the exercising muscle and in peripheral fatigue that is typically associated with changes in sarcoplasmic ionic concentrations [4, 6]. Regardless of its origin, fatigue is consistently accompanied by decreased physical performance [4, 7] caused by the imbalance between the rate of energy production/consumption and also by a deficit in the recycling of metabolic waste [8]. Objective fatigue (muscle level) may be more or less transient, depending on the characteristics of the exercise stimulus (i.e., intensity, duration, and volume) [9].

Regarding subjective fatigue, its effects were well defined since early studies, namely, drowsiness, inability to concentrate, and physical discomfort [10]; so, a possible definition that aggregates these three types of effects will establish subjective fatigue as a physical incapacity caused by psychological factors, conducting to subjective feelings of exhaustion influenced by loss of motivation or concentration [7, 11, 12].

In spite of these valuable definitions, for evaluating fatigue in a precise and reliable way, more concrete and unbiased approaches are needed, something achievable by the conjugation of machine and human powers.

Nowadays, artificial decision support systems extend the capabilities of the natural ones. With the help of machines, solving complex challenges delineated by the human brain is now much more reliable and time inexpensive. As knowledge benefits from the processing power of machines, incredible discoveries may arise, with great impact to the daily life of populations.

Following this line of thought, the current research article tries to explore fatigue, both as an objective and subjective physiological phenomenon (research variable) through the powerful capabilities of computational systems, using a conjugation of electromyographic (EMG) and electrocardiographic (ECG) signal processing methodologies together with the training of an exploratory machine-learning system.

Since past research has shown that muscle injuries are more frequently associated with prolonged forms of muscle fatigue [13], there is clearly a need for a monitoring system to identify the onset of fatigue, both in objective and subjective terms, using an indirect and noninvasive approach.

The proposed detection model included both electromyographic signals and heart rate variability (HRV) parameters because fatigue develops at the muscle level whenever the rate of oxygen delivery and utilization become imbalanced [5]. This global monitorization of the fatigue phenomenon (objective and subjective types) may have a major impact on the training programs of high-performance athletes, taking into consideration that, as previously mentioned, the maximum performance can only be achieved when subjects are physically and mentally healthy [14–16].

Fatigue can be evaluated through different methodologies (beyond EMG and HRV), distinguishable by the nature of studied events. As a practical example, muscle contraction is triggered by an (1) electrical impulse that generates (2) chemical changes at cellular level during its propagation in order to produce (3) a mechanical event, i.e., the muscular contraction. The previous three points are an illustrative demonstration of how fatigue acquisition is dependent on (1) electrical, (2) chemical, and (3) mechanical phenomena.

Interesting studies were also conducted regarding the mechanical and chemical nature of fatigue, namely, the research studies of Faller et al. [17] and Kimura et al. [18] (mechanical perspective) using accelerometric and acoustic sensors, respectively. It was concluded that, typically, the amplitude of the mechanical signal decreases as fatigue was being acquired.

From the chemical point of view, the use of near-infrared spectroscopy arises as a noninvasive methodology to measure relative changes in the oxygen levels at the muscular level. In spite of the concentrations of oxyhemoglobin and deoxyhemoglobin not evolving in a linear way, a specific 4-stage pattern was found by Taelman et al. [19].

The choice of ECG/HRV and EMG data to study fatigue is framed on the set of studies focused on the "electrical" nature of fatigue, providing a way to understand this phenomenon from its source and through multiple fatigue categories (objective and subjective types).

However, the current study is not restricted to a quantitative point of view, which may not be appropriate, taking into consideration that a specific value of consensual indicators of fatigue may flag the existence of fatigue for a segment of subjects, while for others it is innocuous, i.e., fatigue-related values may vary accordingly to the subject and experimental conditions under analysis. Due to this difficulty, it was decided to explore fatigue phenomenon from a qualitative and more universal point of view, through the analysis of how certain parameters evolve in time, instead of focusing on its absolute values. Since median frequency represents a valid parameter for monitoring muscle

fatigue [5], the median frequency of the EMG signal power spectrum was one of the parameters where trends were searched, together with other documented wavelet parameters [20].

We extended this trend evaluation to linear and nonlinear HRV parameters (e.g., low- and high-frequency power as well as short- and long-term dispersion derived from the Poincaré analysis, respectively) extracted from the cardiac epochs (RR) obtained on a cardiopulmonary cycloergometry trial above the second ventilatory threshold (VT_2). After identifying the most significant EMG and HRV parameters to evaluate fatigue, we aim to objectively classify the physiological impact of fatigue in the performance of athletes. A successful achievement of this purpose may ensure a way to study possible adaptations on training programs responsible for simultaneously improving athletes' physical indexes and minimizing the long-term impact of fatigue, avoiding severe injuries.

As previously mentioned, a preventive approach that ensures the monitorization of fatigue-related patterns can be followed by developing a computational system capable of extracting individual fatigue descriptors (IFD) from EMG and HRV signals, obtained during a cycloergometer exercise performed above the second ventilatory threshold.

EMG parameters may ensure a local/muscular monitorization of this phenomenon, while HRV indexes are quite relevant for a generalized/mental evaluation of the fatigue state [4, 16, 21]. The implemented system reflects the gradual onset of fatigue by incorporating a global fatigue descriptor (GFD) and a support vector machine (SVM) classifier, both supported by the evolution time series of IFD's (such as EMG median frequency) generated along the cycling exercise trial.

2. Materials and Methods

It should be taken into account that the following experimental environment/protocol replicated some conditions and procedures described on a past research work. One of the authors gave his contribution in the design of the study and also in the analysis of the results [64].

2.1. Participants. Fourteen healthy, young men (age: 24.5 ± 3.6 years; body mass index: 23.7 ± 1.7 $kg{\cdot}m^{-2}$) were included in this study. Participants were recruited from a local university and community population through direct invitation or flyers. From this population, a primary group of study was chosen and all volunteers were accustomed to cardiopulmonary exercise.

All participants were nonsmokers and normotensive (systolic and diastolic blood pressure values repeatedly < 120/80 mmHg) [22].

Participants were all nonoverweight and free of any known cardiovascular or metabolic disease, as assessed by medical history. None of the participants were currently using prescription or taking any medications or nutritional supplements. Taking into consideration one of the previously mentioned inclusion criteria, participants were already accustomed to cardiopulmonary exercise testing using a cycloergometer. For this reason, there were no familiarization sessions for this specific group of participants.

Each participant was requested to avoid heavy exercise for at least 24 h before testing and to have nothing to eat from midnight until the testing session on the subsequent morning (fasting conditions). Participants were also asked to refrain from caffeine ingestion and to empty their bladders before testing.

Participants were fully informed of the purposes, risks, and discomfort associated with the experiment before providing written informed consent. Informed consent was obtained from all individual participants included in the study. This study was carried out with the approval from the University's Institutional Review Board and in accordance with the Declaration of Helsinki.

2.2. Protocol. Participants were evaluated over the course of 2 visits on separate days (within a 7-day period). Testing was separated by at least 48 h and, to minimize the effects of circadian and other similarly induced variations in performance, was performed at approximately the same time of the day (between 07.00 and 11.00 a.m.).

During the first visit, standing height and weight measurements were taken with participants wearing light-weight clothing and no shoes. Height was obtained using a stadiometer with measures obtained to the nearest 0.5 cm. Weight was measured by using a digital scale (BG 42; Beurer GmbH, Söflinger, Germany). Body mass index was calculated by dividing the participants' mass in kilograms by the square of their height in meters. Subsequently, participants performed a treadmill-graded exercise test to determine their VT_2 and peak oxygen uptake (VO_{2peak}).

On the second visit, each participant performed one bout of cycloergometer exercise above the VT_2 to volitional exhaustion. All tests were performed on the same cycloergometer (Monark Ergomedic 839E, Varberg, Sweden). Expired gas measurements were made using a portable mixing chamber (Metamax® I, Cortex, Leipzig, Germany), which was calibrated before each test with a known volume and with known gas concentrations. Testing was carried out in the laboratory with an environmental temperature between 21–24°C and a relative humidity between 44–56%.

In synthesis, *Day 1* dedicated to the execution of a "Graded Exercise Test" was focused on the assessment of participants' work rate (WR) near the second ventilatory threshold (VT_2), through an incremental power test, where the cardiorespiratory fitness level was inferred.

As stated by Mourot et al. [23], the second ventilatory threshold is *"...the point where high-intensity exercise can no longer be sustained..."*. This parameter can be determined through the collection and monitorization of exhaled air, focusing the analysis on changes in oxygen and carbon dioxide concentrations. With this continuous monitorization, the determination of VE/VCO_2 and VE/VO_2 ventilatory equivalent parameters can be achieved and consequently the VT_2.

On *Day 2*, a "Constant Work Rate Test" was conducted, taking into consideration the $WR_{VT_{2+15\%}}$ power, producing for each participant a set of physiological signals (EMG and HR analysis), where fatigue pattern search took place through digital processing.

2.2.1. Graded Exercise Test (Day 1). Graded exercise testing was performed using an incremental cycloergometer ramp protocol. Following a 3 min warm-up period at 60 W, work rate was increased by 15 $W \cdot min^{-1}$ until the participant was unable to continue. The participants cycled at a self-selected pedal rate between 60–90 $rev \cdot min^{-1}$, being constantly encouraged by the researcher to proceed the exercise in the desired rhythm.

The test was stopped when the pedaling rate could no longer be maintained. VO_{2peak} was defined as the highest VO_2 attained in a 20 s average. Participants were considered to have reached VO_{2peak} if at least three of the following four criteria were met: (1) plateau (increase of no more than 150 $mL \cdot min^{-1}$) in VO_2 with an increase in workload, (2) respiratory exchange ratio greater than 1.1, (3) peak heart rate within 10 bpm of the age predicted maximum, and (4) visible exhaustion [24].

All participants met at least three of these criteria. The peak heart rate was identified as the highest value recorded during each test. Additionally, using the time course of the relationship between the ventilatory equivalents for oxygen (Ve/VO_2) and carbon dioxide (Ve/VCO_2), the VT_2 for each participant was determined by two independent investigators [25].

The VT_2 was defined as the minimal work rate at which the Ve/VO_2 as well as the Ve/VCO_2 exhibited a systematic increase. The VT_2 was expressed in absolute (W) intensity and used for defining the work rate to be used by each participant in the trial of Day 2 ($WR_{VT_{2+15\%}} = 1.15 \times P_{VT_2}$). Participants included in this study exhibited a VO_{2peak} of $52.5 \pm 5.7\ mL\ kg^{-1} \cdot min^{-1}$ and work rate at $VT_{2+15\%} = 204.5 \pm 33.7$ W.

2.2.2. Constant Work Rate Test (Day 2). On the second day, cycloergometry was performed at a constant work rate ($WR_{VT_{2+15\%}}$) and with a periodical encouragement by the researcher until volunteer reaches a volitional exhaustion.

During exercise, the cycling cadence was kept constant after setting the most appropriate value in response to a brief warm-up phase that preceded the test.

The participants were instructed to synchronize their right lower limb to an auditory metronome provided through speakers. Specifically, warm up was divided in 2 sets of 3 min, separated by 1 min rest, during which the participants exercised at their preferred cycling cadence. Then, the mean cadence recorded during the 6 min of warm up was used as the reference cadence for performing the constant work rate test.

The EMG signals from five lower limb muscles (*rectus femoris, vastus lateralis, vastus medialis, semitendinosus*, and *biceps femoris*) were acquired during exercise.

In the current stage of the research, as it will be explained with more detail, only the *rectus femoris* and *vastus medialis* data were taken into consideration during the formal definition of the proposed solutions (GFD and SVM) and methodologies (fatigue trend identification).

The acquisition was carried out using Ag/AgCl disposable electrodes and a signal acquisition system (biosignalsplux, PLUX S.A., Lisbon, Portugal) of PLUX Wireless Biosignals [26], following the recommendations of SENIAM (surface EMG for noninvasive assessment of muscles) [27]. The acquisition system followed the directives of the International Society of Electrophysiology and Kinesiology (acquisition at a sampling frequency of 1000 Hz, filtering using a band-pass filter between 10 and 500 Hz and common mode rejection ratio of 110 dB). In parallel, we also obtained HRV data using a Polar RS 800 G3 heart rate monitor (Polar R-R recorder, Polar Electro, Kempele, Finland).

Among the 14 participants of the study population, HRV data of 3 of them, collected from the constant power test of "Day 2," were compromised due to loss of heart rate signal, so all HRV analysis and subsequent conclusions took into consideration a smaller population. Thus, when a combined analysis of EMG and HRV parameters was needed, it only included the participants with valid EMG and HR data, which were 11.

2.3. Signal Processing and Analysis. Besides data collection, our study was divided into three stages: (a) *Processing Stage*, (b) *Analysis Stage*, and (c) *Proposed Solutions*.

In the *Processing Stage*, a list with commonly extracted parameters from an EMG signal and HRV data was identified together with the computational methodology used to explore the existence of trends in these parameters over time.

The subsequent *Analysis Stage* covers the identification of which EMG and HRV parameters evolve over time in a characteristic trajectory with the progression of fatigue. First, we generated the evolution series of each parameter contained in the EMG and HRV *Processing Stage* preliminary list using a sliding window mechanism. We implemented an algorithm similar to Thongpanja et al. [28] and subsequently identified trends in the series using a linear regression model [29].

2.3.1. Processing Stage - Features and Sliding Window Mechanism. From the EMG signal and HRV data, specific events had been selected (muscular activation periods and *R* peak positions, respectively).

For EMG, we followed the approach proposed by Pimentel et al. [30], which uses the Teager–Kaiser Energy Operator (TKEO).

For HRV, the *R* wave peaks, which we used to build the tachogram (time series with the duration of each RR interval along the acquisition – $RR_{tachogram}$) were identified through the algorithm proposed by Pan and Tompkins [31].

After this process, a sliding window model was used for extracting samples of a set of EMG and HRV parameters over time, in order to explore trends. The window of dimension WS_z slides over each sample of the time series, taking into consideration a defined overlapping factor, dependent of the chosen time-step TS_y, between consecutive windows [32]. Table 1 lists the parameters that were extracted from the EMG signal and HRV data.

A detailed description of HRV parameters can be found in Acharya et al. study [33] and Task Force of The European Society of Cardiology and the North American Society of Pacing and Electrophysiology [34]. A more exhaustive explanation for the EMG parameters, both from the temporal and the frequency domains, can also be found in Cifrek et al. [5].

Table 1: List of the various EMG and HRV parameters studied.

EMG			ECG/HRV	
Time domain	Frequency domain	Time-frequency domain	Time domain	Frequency domain
RMS[†]	Median frequency	Median frequency	Maximum RR interval	Power inside ULF band[∠]
	Total power	Major frequency	Minimum RR interval	Power inside VLF band[∆]
		Major time	Average RR interval	Power inside LF band[◁]
		Mean power	SDNN[‡]	Power inside HF band[*]
		Area	rmsSD[*]	Median frequency
		Volume	Triangular index	
		Time dispersion	SD1[*]	
		Frequency dispersion	SD2[*]	
			SD1/SD2	

[†]RMS, root mean square; [‡]SD, standard deviation of NN intervals; [*]rmsSD, root mean square of successive differences; [*]Poincaré Standard Deviation/Dispersion of points perpendicular (SD1) or along (SD2) the axis of line-of-identity (ellipse semiaxes 1 and 2). [∠]ULF, ultralow frequency band ([0; 0.003] Hz); [∆]very low-frequency band ([0.003; 0.040] Hz); [◁]low-frequency band ([0.040; 0.150] Hz); [*]high-frequency band ([0.150; 0.400] Hz).

Time-frequency information can be gathered through the wavelet transform, which shares some principles with the conventional Fourier analysis, namely, the decomposition of a signal into multiple elementary frequency components, mathematically ensured by a sequence of inner products between the signal and the "base" function (measuring their similarity).

However, while the "basis" of the Fourier analysis are sinusoidal functions, the wavelet transform provides more freedom to the researcher, taking into consideration that the elementary decomposition function (wavelet) can be chosen according to the characteristics of the signal to be decomposed.

Additionally, in the wavelet domain, some temporal information is preserved, in contrast with the Fourier domain being the Morlet mother wavelet (used on the current study) explicitly defined as a function of time:

$$\psi(t) = \frac{1}{\sqrt{b\pi}} e^{-(t/b)^2} e^{j2\pi f_c t}, \quad (1)$$

where $j = \sqrt{-1}$, f_c corresponds to the center frequency of the mother wavelet, and b is a bandwidth parameter related to the energy spread in the frequency domain.

This mother wavelet will be progressively compressed/stretched in a process called "scalling," providing a way to decompose the signal in multiple time and frequency scales.

The EMG parameters from time-frequency domain were obtained from the scalogram (image) processing, after applying the wavelet transform through the **Morlet** family and using a scale array $(1/f)$ defined from a set of pseudofrequencies (in Hz) related with the typical EMG informational content (0–500 Hz), i.e, $1/f = [1/499, 1/497, 1/495, \ldots, 1/9, 1/7, 1/5] = [1.628, 1.635, 1.641, \ldots, 90.278, 116.071, 162.5]$, as described by Graham et al. [20].

According to this approach, *Major Time* and *Major Frequency* define the coordinates of the centroid:

$$\text{Major Time} = \frac{\sum_{f=1}^{F}\sum_{t=1}^{T} t \times S(t,f)}{T \times F}, \quad (2)$$

$$\text{Major Frequency} = \frac{\sum_{f=1}^{F}\sum_{t=1}^{T} f \times S(t,f)}{T \times F}, \quad (3)$$

where $S(t, f)$ defines the scalogram (2D coordinate system with a third virtual coordinate established by the pixel values/colors) pixel value at coordinates (t, f), t the time coordinate of the pixel, f is linked with the frequency dimension, and T and F are, respectively, the number of available columns and rows of the scalogram (dependent on the chosen frequency and temporal resolutions of the wavelet decomposition $\Delta t = 1/F_s = 1/1000 = 0.001\,s$ and $\Delta f = 2\,\text{Hz}$, where F_s is the data acquisition sampling rate).

Mean Power corresponds to the average power obtained at scalogram entries' values. *Volume*, *Area*, *Time Dispersion*, and *Frequency Dispersion* are all dependent on a scalogram segmentation phase using the Otsu methodology, excluding low-intensity values [35]. For the remaining values, the convex volume and the convex area were then determined using *Time Dispersion* and *Frequency Dispersion* as the parameters that defined the maximum length of the convex area according to the time and frequency dimensions. The processing scheme used is depicted in Figure 1.

This scheme mainly consists in an iterative procedure where, in each iteration, EMG and HRV data from each participant (Par_i) are analyzed in order to extract all individual parameters (P_k) contained in the primordial set (Table 1), using different sliding window mechanism configurations, varying the window size ($\text{WS}_z \mid \text{WS}^{\text{EMG}} = [5, 10, 15, 20, 25]$ muscular activation periods and $\text{WS}^{\text{HRV}} = [30, 40, 50, 60, 70, 80, 90, 100, 110, 120]s$) and time-step ($\text{TS}_y \mid \text{TS} = [0, 10, 25, 50, 75, 90]\%$ of WS_z).

Regarding the window sizes of EMG data, a brief explanation should be provided, taking into consideration that each window is composed by a set of muscular activation periods.

However, the muscular activation periods are analyzed individually, i.e., from each muscular activation period the parameter under evaluation is extracted. Then, the generated set of results is averaged, giving rise to a single value, which represents the overall data inside the window.

Each parameter P_k produced a set of $Y \times Z$ time series, where our meta-analysis took place. Taking into consideration the size of the population under study (11 or 14 subjects), the number of EMG (11 indexes on all 5 muscles) and HRV (14 indexes) parameters, and, obviously, the number of window size ($Z^{\text{EMG}} = 5$ and $Z^{\text{HRV}} = 10$) and time-step ($Y = 6$)

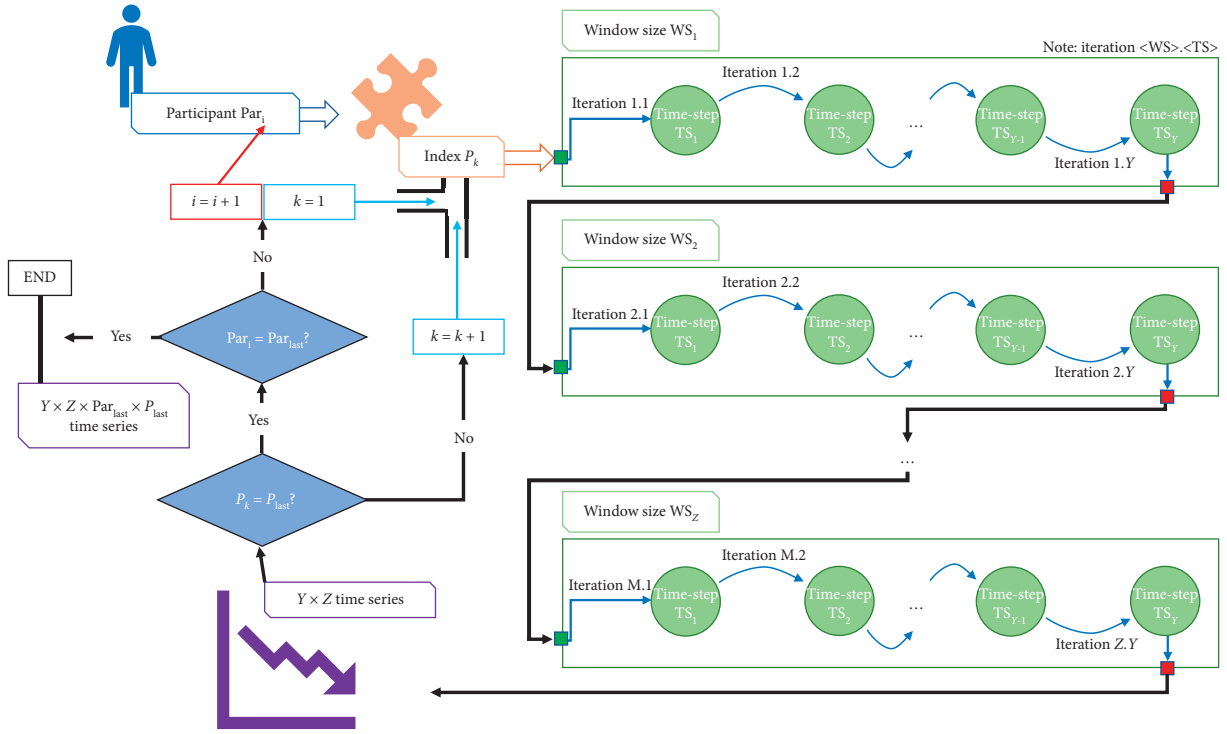

FIGURE 1: Illustration of the iterative process followed during data processing, so that for each participant all parameters were extracted using the various combinations of window sizes and time-steps (Par$_i$ | Participant i; Par$_{last}$ | Last participant; P_k | Index/parameter k; P_{last} | Last index/parameter; WS | Window size; WS$_z$ | Last window size; TS | Time − step; TS$_y$ | Last time − step).

configurations, it means that we were dealing with a big volume of data to be analyzed, i.e., more than 27390 time series.

2.3.2. Analysis Stage Identification of Trends and Potential Fatigue Descriptors

(1) Identification of Trends. Using an adaptation of a meta-analysis procedure, by combining the descriptions of Becker and Wu [29] and Borenstein et al. [36], we identified trends in different time series generated in the *Processing Stage* (by the application of the sliding window mechanism).

Trends were derived from the fitting of a linear regression model to the time series of each parameter (providing a slope value and standard error) and converted to two classes, either as increasing or decreasing trajectory patterns.

Despite the fact that some EMG and HRV parameters may not evolve linearly due to changes on our fatigue variable, by using a linear regression model we decrease the number of degrees of freedom in our analysis, since a relatively complex time series is synthesized in a simple regression line.

Subsequently, the slopes of all participants were reduced into a single combined slope. This final slope was extracted to reflect the overall trajectory of change in the parameter P_k under analysis (generic parameters are used on this section in order to present the applied processing methodology) over time synthesizing in a single value the population trend. This was carried out by combining the slope of parameter P_k for each participant (11 participants for HRV and 14 participants for EMG) and computing a weighted average (of 11 slopes for the HRV indexes and of 14 slopes for the EMG parameters). The weights were computed as the inverse of the square of the respective standard errors (equation (6)). For each participant Par$_i$, the evolution time series of the index P_k has been generated through a sliding-window mechanism (with the window size WS$_z$ and time-step TS$_y$). For the generated time series, the linear regression model was fitted, returning a slope m_i and a variance $\sigma^2_{m_i}$. These individual slopes and variances (1 per participant) are joined in a combined slope (weighted average described in equation (4)) that reflects the global behavior of P_k evolution for our population sample.

This method was applied to each one of the previously specified parameters shown in Table 1 and combinations of window sizes (WS$_z$) and time-steps (TS$_y$), presented in Section 2.3.1.

$$m_{\text{comb}} = \frac{\sum_{i=1}^{\text{NS}} m_i w_i}{\sum_{i=1}^{\text{NS}} w_i}, \tag{4}$$

$$\sigma^2_{\text{comb}} = \frac{1}{\sum_{i=1}^{\text{NS}} w_i}, \tag{5}$$

where NS is the number of participants/subjects ($\text{NS}^{\text{HRV}} = 11$ and $\text{NS}^{\text{EMG}} = 14$) and w_i is

$$w_i = \frac{1}{\sigma^2_{m_i}}. \tag{6}$$

Using combined slope (4) and variance (5), we then calculated the associated 95% confidence interval as follows:

$$IC^{m_{\text{comb}}}_{(1-\alpha)\times 100\%} = \left[\hat{m}_{\text{comb}} - F^{-1}_{t_{(n-2)}}\left(1-\frac{\alpha}{2}\right)\sqrt{\hat{\sigma}^2_{m_{\text{comb}}}}\,;\hat{m}_{\text{comb}} + F^{-1}_{t_{(n-2)}}\left(1-\frac{\alpha}{2}\right)\sqrt{\hat{\sigma}^2_{m_{\text{comb}}}}\right], \tag{7}$$

where $\hat{m}_{\text{comb}}$ and $\hat{\sigma}^2_{m_{\text{comb}}}$ are the estimated values of the combined slope and variance, respectively; $F^{-1}_{t_{(n-2)}}$ corresponds to the value of the t-test statistic for $n-2$ degrees of freedom; and n represents sample size. The combined slope and the confidence interval were also analyzed graphically using the *Forest Plots* [37].

The computation of the combined slope and variance associated with P_k was repeated for various windows of different sizes and time-step pairs (WS_z and TS_y, respectively). Then, to assess the quality of each combination, we calculated the coefficient of variation (CV) of WS_z and TS_y, using the combined standard deviation (σ_{comb}) and slope (m_{comb}):

$$\text{CV}\left[\text{WS}_z, \text{TS}_y\right] = \frac{\sigma_{\text{comb}}}{m_{\text{comb}}}. \tag{8}$$

The rationale behind the choice of CV as a statistical indicator of the quality of window-size and time-step combination is related with the fact that well-defined trends should be characterized by (1) representative variations (monitored by the slope) and (2) also by a small uncertainty linked to the regression model fitting stage (monitored by standard deviation).

(2) Potential Fatigue Descriptors. As detailed in Section 2.2.2, the experimental protocol also included an acquisition of the heart rate data during recovery from submaximal cycloergometry performed above the VT_2. The stage of data collection occurring during cycloergometry was termed "acquisition +" and that occurring during postexercise recovery was termed "acquisition −." These data were used to identify all the parameters that were sensitive to variations in the magnitude of fatigue.

As described on some research works, while the *vastus medialis* muscle exhibits a high level of fatigue-resistance to cycling exercise, this is not the case for the *rectus femoris* muscle [38, 39]. Thus, for the EMG parameters, "acquisition +" and "acquisition −" data were obtained in the *rectus femoris* and *vastus medialis*, respectively (two antagonistic conditions, where fatigue patterns will be more evident or undefined/nonexistent, respectively).

On the current stage of the project we focused our analysis on 2 of our 5 muscles' protocols, the choice of 5 muscles is intended to expand, in the near future, the analysis of the pilot study; however, the data processed for the remaining 3 muscles were extremely useful to confirm the theoretical expectations collected from other research articles that fatigue-induced patterns on EMG parameters are more accentuated on the *rectus femoris* and less prominent on the *vastus medialis* muscle [38–40].

In scientific terms, there is a general agreement that the study of a single case/participant or, in our case, a single trend is not enough to draw definitive physiological conclusions [41]. To overcome this problem, we established two criteria to distinguish between generic- and fatigue-associated trends for each one of the EMG and HRV indexes under analysis.

Premise: For each parameter P_k, the trend evaluation procedure will be restricted to the most representative combination of (WS_z and TS_y) that describes the evolution of P_k (i.e., the combination that minimized the CV).

Trend Acceptability Criteria:

(1) Taking into consideration the previous premise, for the "acquisition +", it is considered the existence of a trend only if the confidence interval, linked to the combined slope estimate of parameter P_k, did not cross the center of the *Forest Plot* (zero slope), belonging exclusively to one of its two domains (Figure 2(a))

(2) The trend identified on "acquisition +" is only considered a fatigue-related trend when it was verified in the "acquisition −", a combined slope reversal in P_k vs. that seen in "acquisition +", or at least a state of uncertainty, where confidence intervals included values of the two domains of the *Forest Plot* (Figure 2(b))

These criteria were applied sequentially. We established that P_k descriptor did not correspond to a fatigue indicator whenever one of these criteria was not fulfilled.

Therefore, a parameter P_k is considered an individual fatigue descriptor (IFD) if the provided algorithm steps (section A of Supplementary Material (available here)) are followed.

2.4. Proposed Solutions: Global Fatigue Descriptor and Binary Classifier. Finally, the *Proposed Solutions* (third stage of the research process, defined on Section 2.3) included the definition of a global fatigue descriptor (GFD) and implementation of a binary classification system. At this point, all the information provided by the EMG and HRV indexes was modeled into a single value that characterized the GFD. Then, we generated a classifier with the ability to process the information of the *Processing Stage*, i.e., the selected features derived from the identified IFD as an input and returning an output containing one of the two classes (+ fatigue vs. − fatigue).

The GFD corresponds to a weighted average, where each of the individual fatigue descriptors was normalized. It defines an input with a weight equivalent to the inverse of the CV, determined at the end of the application of the trend identification methodology (equation (9)).

GFD is a dimensionless parameter that may present a value between 0 and 1:

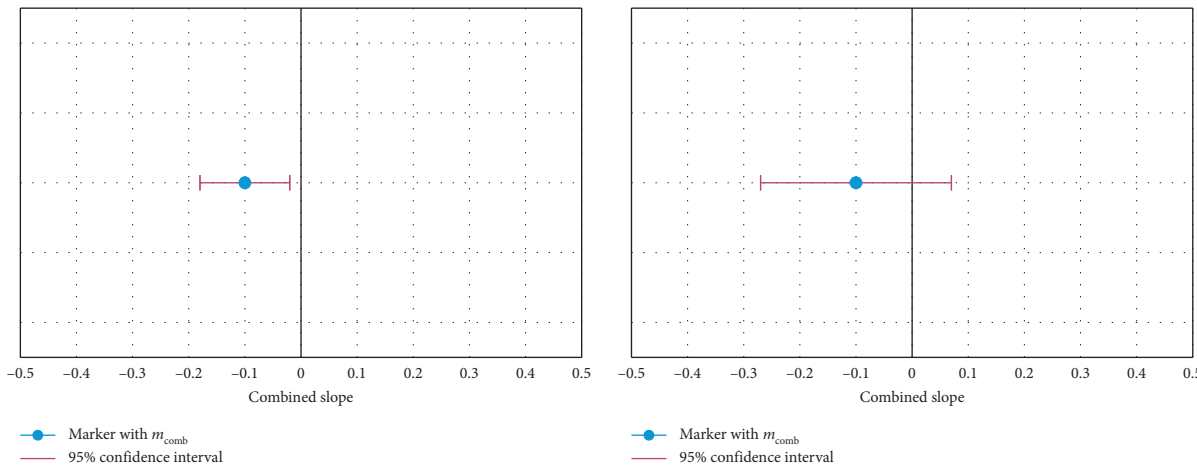

FIGURE 2: *Forest Plots* graphically synthesizing the results of the meta-analysis, based on the estimate of the combined slope and the respective confidence interval. (a) Graphical result of the meta analysis when a trend exists. (b) Graphical result of the meta analysis when no trend exists.

$$\mathrm{GFD}[i] = \frac{\sum_{k=1}^{K} \mathrm{IFD}_k[i] \times \mathrm{CV}_k^{-1}}{\sum_{k=1}^{K} \mathrm{CV}_k^{-1}}, \tag{9}$$

where K is the number of fatigue descriptors to be considered, $\mathrm{IFD}_k[i]$ being a sample of the fatigue descriptor k, and CV_k being the CV for the most favorable window-size and time-step combination for the extraction of the IFD_k descriptor.

A calibration protocol, similar to the one described in Section 2.2.2, was applied to each participant's data. This allowed representing the evolution of GFD over time in a graphical figure. The calibration provided the maximum values of each IFD used for normalization. Afterwards, its distribution was computed and graphically translated into a *boxplot* (Figure 3). Consequently, a profile of each participant became available to the system based on the segmentation of the GFD into three regions (green, yellow, and red), using two thresholds corresponding to the 25% percentile and the median value. These regions were set to assess the magnitude of fatigue.

The proposal of 50% (median) and 25% as GFD thresholds was mainly based on statistical concepts.

In first place, the 50% threshold was defined, taking into consideration the intention of segmenting the GFD values into two equally probable regions (for the known population being the median value, less susceptible to outliers when compared with the mean), i.e., the green and red zones, representative of innocuous and dangerous fatigue levels, respectively.

Nevertheless, after analysing the first results (Figure 4) it was concludedthat, in a great majority of the cases, the GFD evolution is characterized by a first stage of abrupt decline followed by a prolonged interval of stability, something that could be related with the fatigue acquisition mechanism specificities.

In fact, the physiological process of fatigue acquisition can also be divided into two stages: (1) aerobic and (2) anaerobic, accordingly to the dominant mechanism of cellular energy production.

In the beginning of the exercise, the dominant energy production mechanism is the aerobic respiration, being considerably more efficient, but also slower than the anaerobic type.

After reaching the maximum rate of aerobic energy production, the fastest anaerobic respiration gradually starts becoming dominant, in order to suppress the energetic needs.

The beginning point of this aerobic-anaerobic transition period is defined as the first lactate threshold, which may be linked with the start of the identified "stability" period in the GFD evolution [42, 43].

However, in this transitional period, it is neither a severe/dangerous (red) or innocuous (green) state of fatigue, creating the need of including an additional category, i.e., the yellow zone.

Replicating the splitting logic applied to green and red regions, the original red region was divided into two equally probable intervals, through the 25%, giving rise to the final scale composed of three fatigue levels.

With regard to the binary support vector machine fatigue classifier (the creation and training were implemented based on Python Scikit-learn, a library specialized in machine learning), the two implemented classes corresponded to "nonfatigued" and "fatigued," identifying when each participant was in its optimal physical condition or under fatigued conditions, respectively.

The SVM model is very attractive and intuitive, taking into consideration that it essentially works based on a Cartesian logic, where each example is a point (contained inside the Cartesian space) univocally defined by N coordinates, i.e., each feature corresponds to a dimension of the space.

This supervised machine-learning model should be included in the hyperplanes' class, where, through a finite but representative set of training examples, the major aim is to

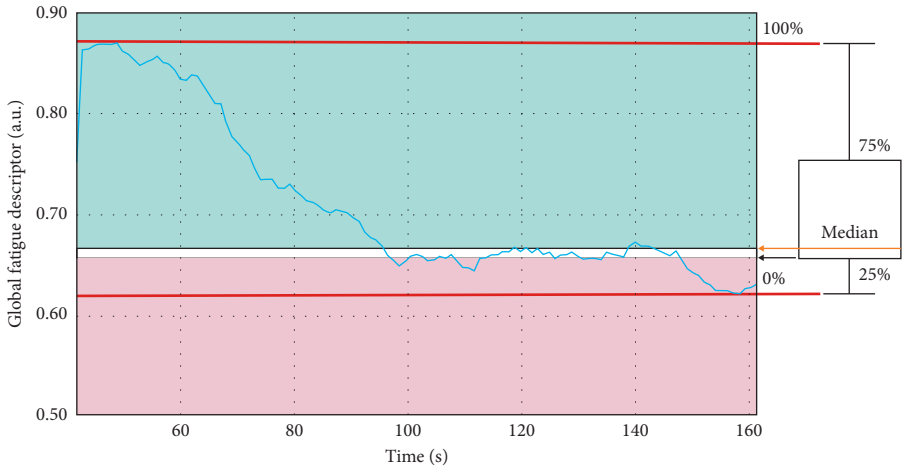

Figure 3: Graphical correspondence between the thresholds defining the fatigue zones and their origin in the *box plot*.

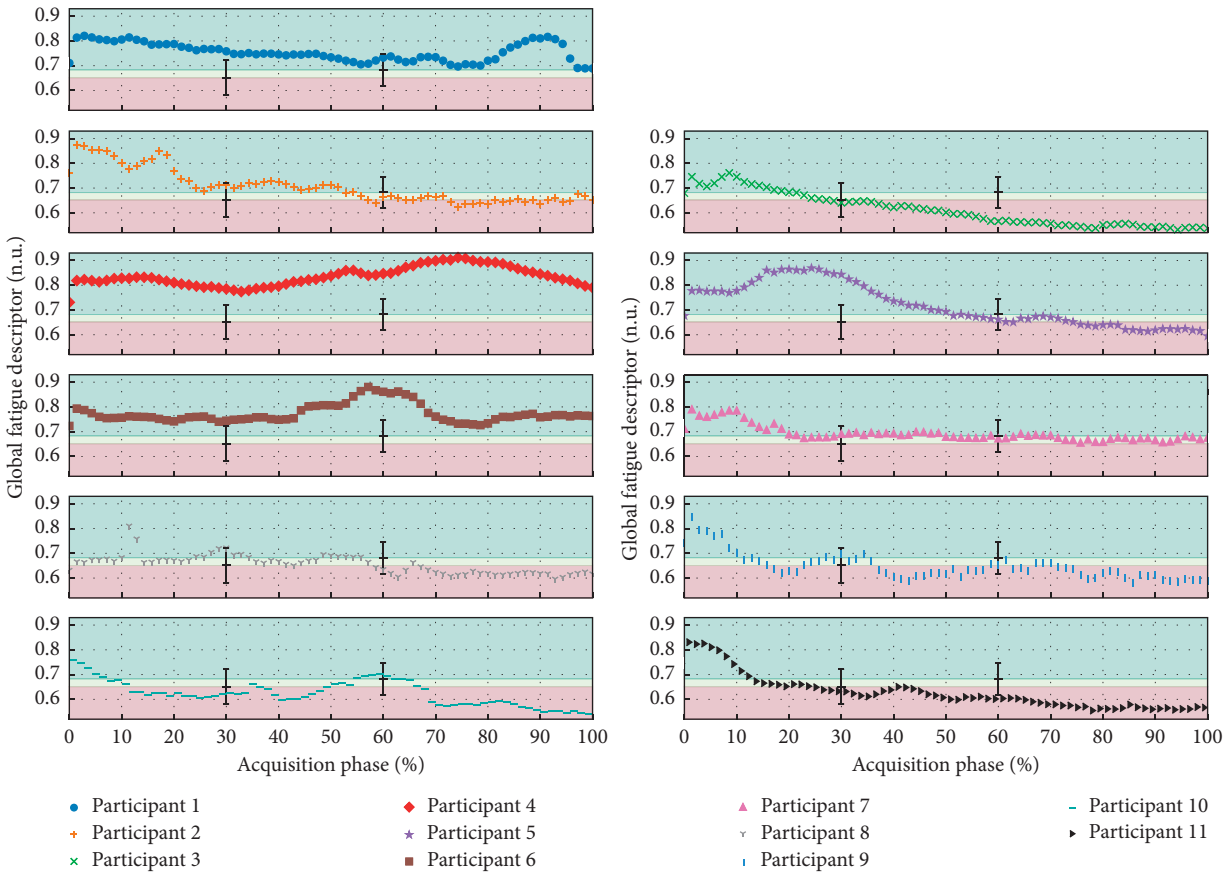

Figure 4: Presentation of the evolution of the GFD for the various participants that compose the population sample ("acquisition +"), highlighting the regions of separation between fatigue levels.

find a function f (decision function) capable of properly returning an output/prediction (class) after receiving a new testing example as input [44].

In order to achieve this end (identification of the decision function f), the training phase of a SVM is based on the search for the hyperplane $(\vec{w} \cdot \vec{x} + b = 0, \vec{w} \in R^N, b \in R$, $\vec{x}$ being the vector with the value of the features associated with the testing example and $\vec{w}$ and b being the parameters determined during the classifier training phase) that ensures the maximization of the separation between the two groups of training examples, which are geometrically defined by two convex hulls.

With the two groups of training examples well delimited, the next stage consists in an optimization procedure intended

to identify the smallest segment that links the boundaries of the two convex hulls. The optimum hyperplane is perpendicular to this segment and crosses its central point.

The previous logic will produce the pretended decision function f:

$$f(\vec{x}) = \text{sign}(\vec{w}.\vec{x} + b), \vec{w} \in R^N, b \in R. \quad (10)$$

This type of classifier was initially intended for binary problems [45], which fully meet our needs to categorize fatigue state into two classes.

Our aim is not focused on defining an absolute threshold of fatigue, but instead a qualitative measure of when fatigue is being acquired or not and the respective relative level of installation.

Returning to the specific implementation of the binary classifier, the procedure for preparing the set of training examples was based on the segmentation of EMG and HRV signals, from the 11 available participants into two temporal segments with equal duration. From the first segment, the features of the "nonfatigued" class examples were extracted, while the other half segment (related to the final period of the trial) was used to extract the information for the training examples of the "fatigued" class.

Two features were extracted from each time series for the $N + M$ fatigue descriptors ($N = 4$ and $M = 10$ being the number of EMG and HRV fatigue descriptors, respectively). This was carried out to include information about their absolute values and trends in the training phase. The formulation of these features corresponds to the average value of the normalized series (equation (11)) and the relative variation rate (equation (12)):

$$\text{feature}_1 = \frac{\sum_{j=1}^{L} P_k[j]/\max_{P_k}}{L}, \quad (11)$$

$$\text{feature}_2 = \frac{\left(P_k^{\text{end}}/P_k^{\text{start}}\right) - 1}{t_{\text{end}} - t_{\text{start}}}, \quad (12)$$

where L represents the number of samples of the parameter P_k extracted from the analyzed segment of the EMG or $\text{RR}_{\text{tachogram}}$ and $\max_{P_k}$ represents the maximum value of the P_k descriptor for normalization. The terms of feature_2, P_k^{start}, and P_k^{end} correspond to the P_k parameter in the first and last sample of the time series and t_{start} and t_{end} to the respective time instants.

The training phase was preceded by the selection of features using recursive feature elimination [46]. Before feature selection, each one of the 22 training examples (11 for the "nonfatigued" class and 11 for the "fatigued" class) was characterized by an array with $2 \times (N + M) = 28$ entries (Figure 5).

The classifier provides an assigned class together with an estimate of its degree of certainty (i.e., a qualitative and quantitative output).

3. Results

Using the methods described in Section 2.3.2, we obtained a list of potential fatigue descriptors (that we previously refer as IFD) consisting of 4 EMG and 10 HRV parameters, as summarized in Table 2.

Table 2 shows the typical evolution trend, the combination of window size, and time-step that provides a more efficient analysis of the descriptor and the respective CV.

Due to the GFD definition, as almost all of its inputs (IFD) decrease with the onset of fatigue, this is the typical behavior for the GFD in most participants. Figure 4 emphasizes the observed evolution for the 11 participants, presenting valid EMG and HRV acquisitions, while Table 2 defines the identified weights contained inside the formal definition of GFD. The threshold values, between colored zones, were determined by averaging the thresholds obtained for each participant on the calibration protocol. The error bars illustrate the standard deviation associated with the calculated mean value. As for the classification, the results highlight how class and GFD evolve in parallel for most of the participants.

Regarding the feature selection stage, the original training array was composed by 28 entries. The feature selection procedure generated a considerable reduction in the number of meaningful features, which decreased to 9.

We executed a recursive feature elimination stage through a Leave One Out cross-validation strategy. With this strategy, different sets of features were tested sequentially, removing in each iteration the less meaningful feature until reaching the limit case, where only one feature remained. The performance of the trained classifiers (1/iteration of the cross-validation procedure) was evaluated. The complete list of classifiers' score provided a way to understand which is the most effective set of features to train the binary classifier.

The feature_1 was considered the most relevant for a set of 9 parameters correspondent to **HRV Group** | *Average RR*, *SDNN*, *Triangular Index*, *SD2*, *Fourier Median Frequency*, *Power in LF Band* and *Power in HF Band*, **EMG Group** | *Wavelet Median Frequency* and *Wavelet Major Frequency*.

Regarding the results of the trained classifier, we found that, in the initial phase of the test, the "nonfatigued" class was assigned with a high degree of certainty. Then, the certainty of assignment of this class decreased gradually until the "fatigued" class began to be dominant towards the end of the exercise trial (Figure 6). Feature extraction in the test examples differs slightly from the training phase procedure, disregarding averages and using instantaneous values so that classes can be returned over time, during the real-time processing of data.

For evaluating the quality of the classifier, a cross-validation method based on a *Stratified K-Fold* ($K = 11$ folds) strategy was applied, providing an accuracy score of 0.82 ± 0.24 with a 95% confidence interval between [0.68; 0.96].

4. Discussion

In this study, we implemented a monitoring system capable of showing trends on the evolution of EMG and HRV parameters during cycloergometry, using an indirect and noninvasive approach to qualitatively evaluate the fatigue progression.

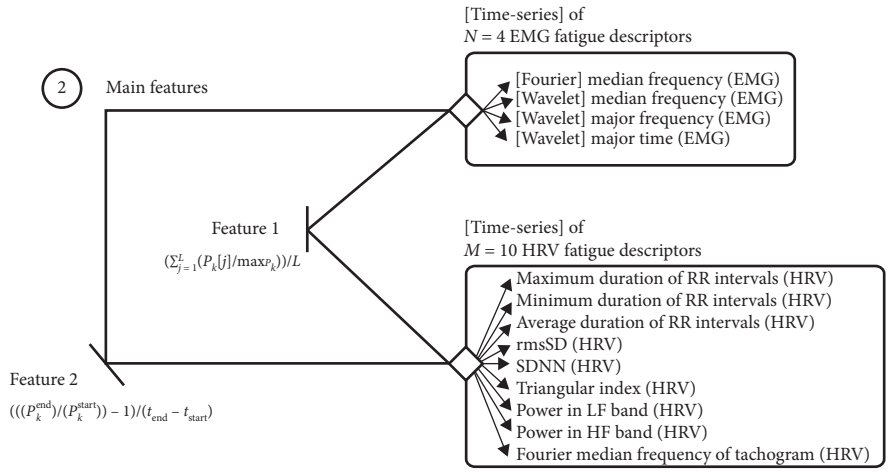

Figure 5: Diagram presenting the initial set of 28 features (before feature selection), obtained through the extraction of 2 parameters ($feature_1$ and $feature_2$) from the time series of $N = 4$ EMG and $M = 10$ HRV fatigue descriptors (described in Section 2.3.1 and identified on Section 3).

Table 2: List of the various EMG and HRV fatigue descriptors with the typical evolution trend in fatigue conditions and the most appropriate combination of window size and time-step.

Signal	Domain	Parameter	Window size	Time-step	Coefficient of variation	m_{comb} ± Half length of 95% CI♠	Typical evolution
EMG	Frequency	Median frequency	10 muscular activations	1 muscular activation	1.22×10^{-2}	$-3.01 \times 10^{-2} \pm 8.02 \times 10^{-4}$	↓
EMG	Time frequency	Median frequency	10 muscular activations	1 muscular activation	2.42×10^{-2}	$-2.87 \times 10^{-2} \pm 1.52 \times 10^{-3}$	↓
EMG	Time frequency	Major frequency	10 muscular activations	1 muscular activation	1.70×10^{-2}	$-3.39 \times 10^{-2} \pm 1.26 \times 10^{-3}$	↓
EMG	Time frequency	Major time	25 muscular activations	0 muscular activations	3.94×10^{-2}	$-5.19 \times 10^{-4} \pm 4.46 \times 10^{-5}$	↓
HRV	Time	Maximum duration of RR intervals	30 s	3 s	1.25×10^{-2}	$-1.82 \times 10^{-1} \pm 5.16 \times 10^{-3}$	↓
HRV	Time	Minimum duration of RR intervals	30 s	3 s	8.94×10^{-3}	$-1.71 \times 10^{-1} \pm 3.46 \times 10^{-3}$	↓
HRV	Time	Average duration of RR intervals	30 s	3 s	9.13×10^{-3}	$-1.76 \times 10^{-1} \pm 3.64 \times 10^{-3}$	↓
HRV	Time	rmsSD*	50 s	45 s	1.92×10^{-2}	$-3.87 \times 10^{-3} \pm 1.68 \times 10^{-4}$	↓
HRV	Time	SDNN‡	30 s	3 s	5.17×10^{-2}	$-6.09 \times 10^{-3} \pm 7.12 \times 10^{-4}$	↓
HRV	Time	Triangular index	60 s	30 s	2.04×10^{-2}	$-4.01 \times 10^{-2} \pm 1.85 \times 10^{-3}$	↓
HRV	Time	SD2*	30 s	3 s	4.25×10^{-2}	$-1.09 \times 10^{-2} \pm 1.05 \times 10^{-3}$	↓
HRV	Frequency	Power in LF band◁	30 s	3 s	5.78×10^{-2}	$-1.51 \pm 1.97 \times 10^{-1}$	↓
HRV	Frequency	Power in HF band*	30 s	3 s	5.41×10^{-2}	$-8.51 \times 10^{-1} \pm 1.04 \times 10^{-1}$	↓
HRV	Frequency	Median frequency	30 s	3 s	1.51×10^{-2}	$3.65 \times 10^{-3} \pm 1.25 \times 10^{-4}$	↑

♠m_{comb} refers to the combined slope and CI to the confidence interval (m_{comb} ± **half length of 95% CI**). ‡SDNN refers to standard deviation of NN intervals; *rmsSD refers to root mean square of successive differences; *Poincaré Standard Deviation/Dispersion of points perpendicular (SD1) or along (SD2) the axis of line-of-identity (ellipse semiaxes 1 and 2). ◁Low-frequency band ([0.040; 0.150] Hz); *high-frequency band ([0.150; 0.400] Hz).

One of our main concerns was related with the applicability of EMG parameters extracted from the Fourier domain, taking into account that we were dealing with dynamic muscular contractions, where the stationarity criterium can be affected due to changes in force, speed, muscle length, and electrode relative location along the cycling trial [47–49].

In order to avoid a possible problem of nonstationarity EMG, wavelet analysis was conducted, considering that it is not based on the assumption of stationarity [50–52].

However, we are still interested on exploring methodologies that require less computational resources, such as short-time Fourier transform (STFT), which is based on the conventional Fourier transform but applied on a sequence of short sliding windows. Direct application of the Fourier transform in EMG data collected during dynamic/cyclic tasks is not appropriate [48], but STFT will be viable if the size of the time windows under analysis is sufficiently short to avoid the effect of nonstationarities during the application of the Fourier transform [47, 49, 50, 52–54]. The common

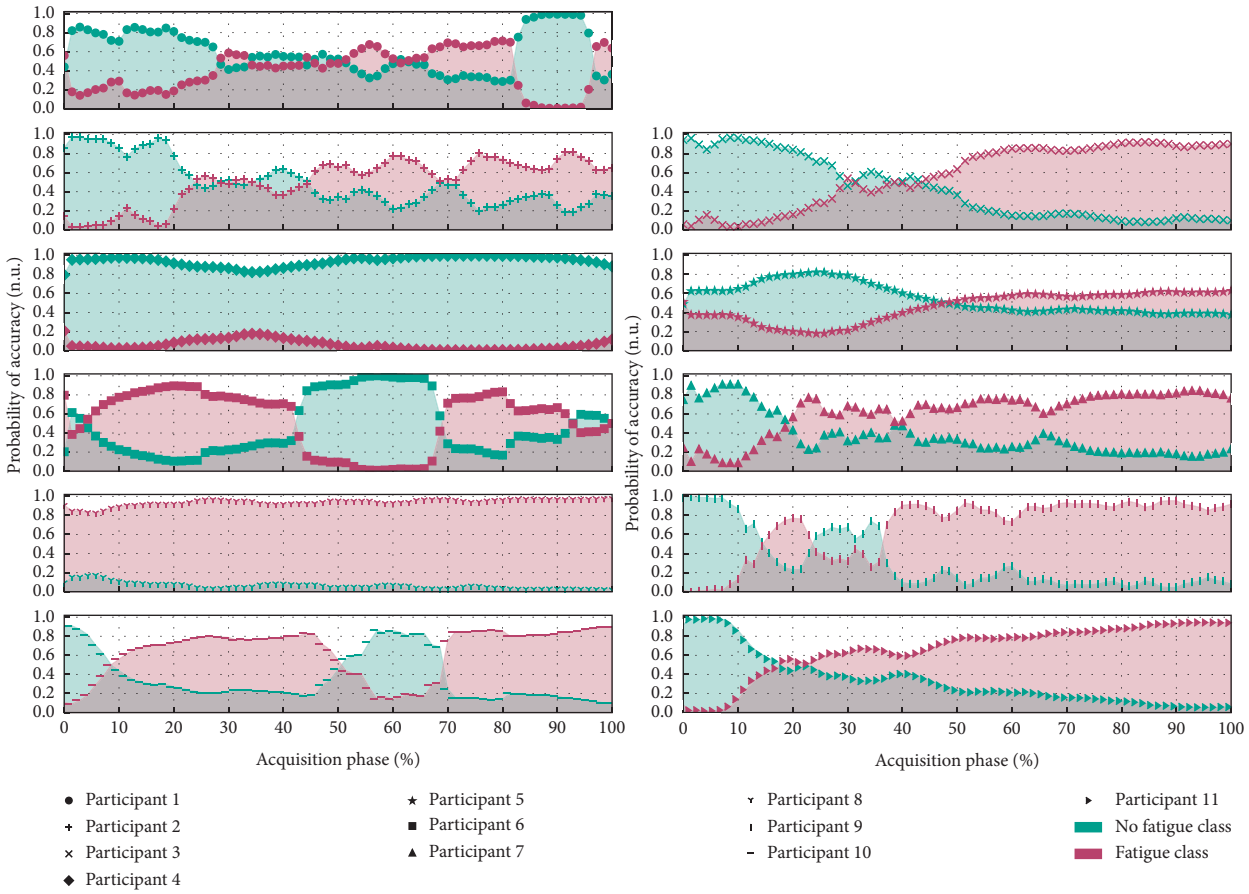

Figure 6: Demonstration of the evolution in the classification attributed by the support vector machine throughout the "acquisition +" collected in the various elements of the population sample.

size of our EMG processing windows is approximately equal to 1 second, corresponding to the muscular activation period, which is in accordance with some studies executed in similar experimental conditions [49, 52].

Before proceeding with the discussion, it should be noted that, in our analysis, each window is composed by multiple muscular activation periods. As an illustrative example, the most favorable window-size configuration to extract *Fourier Median Frequency* (Table 2) will be composed by a set of 10 muscular activation periods.

Each muscular activation period is a subwindow, and from each of these subwindows, the respective Fourier power spectrum is generated and the *Fourier Median Frequency* is determined.

So, returning to our illustrative example, each window originally generates 10 *Fourier Median Frequency* values, which will be averaged, giving rise to an overall *Fourier Median Frequency* value for the window under analysis.

With this approach, in each window, it is ensured that (1) the stationarity conditions are fulfilled, taking into account that each power spectrum was generated from subwindows (individual muscular activation's) with less than 1 second and (2) the average of the set of *Fourier Median Frequency* values minimizes the influence of outliers.

Regarding HRV analysis, in spite of the fact that a relationship between physical fatigue and HRV patterns can be established [55–56], the most common applications are related with subjective/mental fatigue [57–59].

As declared before, the projection of our computational system with both EMG and HRV parameters was intended to collect patterns related with physical and subjective fatigue, ensuring a global evaluation of the fatigue state.

So, with HRV parameters, we believe that it is possible to reach subjective/mental fatigue patterns and also complement the physical/local information gathered with EMG.

Taking these concerns into consideration, several EMG and HRV parameters were modeled with the purpose of identifying trends described by the global fatigue index that was extracted from the data obtained during and after exercise performed above the VT_2.

The trend identification phase gave rise to an extensive list of fatigue descriptors.

Identified trends were reasonably supported by past study results, namely, the decrease of EMG median frequency [3, 5], wavelet parameters [20], SD2, absolute power in LF and HF bands [56, 60, 61] and increase of heart rate (inverse of RR interval duration) [60].

Then, the descriptor list was refined, through a pretraining feature selection methodology, to avoid redundancies in the definition of the global fatigue descriptor and in the training of the support vector machine (Table 2). As referred previously and taking into account that the global fatigue descriptor is defined as an average of these individual fatigue descriptors, it denotes a decreasing trend with the progression of the trial, evolving in parallel with the probability of accuracy in the decision returned by the binary classifier.

These results (trend identification, evolution of the global fatigue descriptor, and training of the binary classifier) show different dependencies with regard to the coefficient of variation. The coefficient of variation enabled detecting the best sliding window mechanism combination (window size and time-step) for generating the evolution time series of each EMG and HRV index contained in the preliminary list (Table 1). This is fundamental for all the subsequent research, since it is from these time series that trends were identified and individual fatigue indexes were found and used next at the definition of the global fatigue descriptor and during the training of the classifier. Among the different assessment possibilities and considering the combined slopes and standard deviations here obtained, our approach emerged as a reasonable method to optimize the sliding window mechanism procedure for extracting each descriptor. Regarding the trained classifier, its main purpose is to distinguish data into two extreme conditions: Fatigued and Nonfatigued, but we were also concerned in tracking how the system behaves in the intermediate state between these two extreme conditions, which, as stated in Section 2.4, can be achieved through a quantitative metric: Degree of Certainty.

So, the classifier has two outputs: (1) a qualitative result (class: [Fatigued, Nonfatigued]) and (2) a quantitative result (degree of certainty).

If the main focus was only the qualitative result, the chosen training approach (splitting the training data into two half-size temporal segments) could create some problems, because, in practical terms, it will be possible that data collected in the beginning of the trial and in the middle will produce the same qualitative result (Nonfatigued class). But, if both qualitative and quantitative outputs (returned by the classifier) are taken into account, the previous undesirable situation can be avoided and the system is able to distinguish data collected from the beginning and middle of the trial, because the degree of certainty in the middle will be considerably lower than in the beginning (as demonstrated by almost the full set of results available on Figure 6).

In spite of the binary nature of the classifier, when it returns the Nonfatigued class as a result of input test data, the system is not stating in an absolute way that the test data are related to a Nonfatigued state, giving, instead, a probability of this state.

Of course, to guarantee the reliability of the used approach (for segmenting the training data), some assumptions were needed:

(1) At the beginning of the trial, the volunteer should be in an absolute Nonfatigued state, which was guaranteed by the resting hours and absence of intense physical activity on the hours precedent to the trial

(2) The variable under study ("Fatigue") is incremented during the trial, which means that the volunteer state is gradually becoming away from the Nonfatigued class and entering in the Fatigued one

(3) At the end of the trial, it is assumed that the volunteer was in an absolute Fatigued state, which is a reasonable consideration taking into account the exhaustion and inability to proceed when the exercise was reached

(4) Fatigue is acquired in a constant rate, condition reasonably ensured by the constant work rate used on the cycloergometry test

In terms of the feature selection stage of the SVM classifier, it should be refined in the future (removing some redundant components), taking into consideration that after performing a Principal Component Analysis (PCA), it was concluded that 79% of the informational content intrinsic to the 9 features can be ensured by using only 2 principal components, i.e., the dimensionality of our classifier can be considerably reduced (as demonstrated by PCA and by the produced graphical results presented in Figure 7).

In fact, reducing the dimensionality of the classifier produced very interesting results in the performance evaluation stage through a *Stratified k-Fold Strategy*. The average classification accuracy decreased a little (from 82% to 77%), but the 95% confidence interval has shrunk from $\pm 24\%$ to $\pm 19\%$, which means that the classification system was simplified but kept its effectiveness.

After a careful analysis of the original results, it was noticed that the classification accuracy could be further improved.

This increase of accuracy was achievable with a simple adjustment in the training stage of the classifier. Instead of splitting the acquired EMG and HRV signals into two halves (the first half, representative of the "nonfatigued" class, while the second is linked to the "fatigued" class), training data from the "nonfatigued" class can be extracted from the 1st quarter and the "fatigued" data from the 4th quarter segment of the original full-time acquisitions.

With the previous approach, for each class, an increase on the specificity of the training examples is ensured, taking into consideration that the excluded EMG and HRV data (from the 2nd and 3rd quarter segments of each trial) are related to a transition stage between "nonfatigued" and "fatigued" classes and not exclusively to one of these two classes.

Through the previous adjustments in the feature selection/training stage, the estimated overall classification accuracy increased to $95\% \pm 8\%$, while the practical results, using a sliding-window mechanism to evaluate the evolution of fatigue instantaneous classification, were maintained (as demonstrated in Figures 6 and 8).

The combination of information from different fatigue descriptors relied on the GFD and support vector machine.

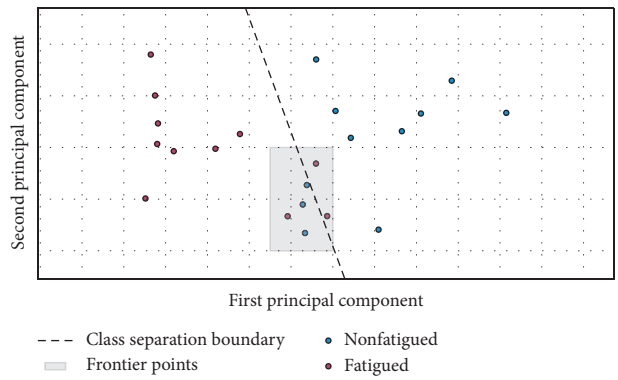

Figure 7: Demonstration of viability of reducing the dimesionality of the classification system, taking into consideration that with only 2 principal components a very reasonable separation between "Fatigued" and "Nonfatigued" class is ensured.

Nevertheless, it should be considered that the GFD corresponds to an exploratory approach that still needs a more profound validation. For instance, the definition of GFD thresholds is based on a statistical criterion, while deeper physiological correspondences could be relevant, i.e., the present results are promising, although a strong physiological connection/meaning should be found, in order to achieve a more solid interpretation.

4.1. Limitations. Currently, this classification system is tuned for acquisitions similar to those reported in the experimental protocol (during a cycling task with the monitoring of *rectus femoris* muscle). In a first look, it could be expected that this restrictive training procedure would entail an undesired biased behavior of the classifier (with more false positives). We believe that the choice of using only one muscle at the training phase will not cause a biased behavior, which would be problematic, because we have two well-defined acquisition segments representative of "nonfatigued" and "fatigued" classes. However, it is probable that the classifier reveals an excess of specificity (working well for data acquired from *rectus femoris* and worst for other muscles).

When tested with other muscles, or motor tasks, the classifier accuracy might be compromised because the manifestation of fatigue varies substantially between different muscles and exercise paradigms [62]. In line with this concept, new acquisitions will be extremely important to further overcome these limitations and allow a more generalized and accurate tool for monitoring the onset of fatigue noninvasively.

The present version of the system also requires a calibration test for a correct operation, which is essential for IFD normalization. Normalized values, used as inputs of GFD and for generation of the support vector machine training arrays, decrease the impact of the variability in the fatigue acquisition process, typical between participants.

Additionally, the dimension of the population sample should be increased in order to achieve more solid generalizations and to reduce unexpected behavior of the binary classifier and global fatigue descriptor. This need is reinforced by the results reported for participants 1, 6, and 10, where the binary classifier suddenly flags an abrupt recovering period in the middle/end of the trial.

As previously referred, physiological patterns of fatigue are considerably subject specific, which means that by increasing the training population, the resultant model will ensure a better generalization.

However, the size of the population sample is probably not the only reason for the reported short-term (participants 1, 6, and 10) and long-term (participants 4 and 8) behavior. The trained SVM model was based on a linear kernel due to its computational elegance and simplicity [44].

In spite of requiring less computational resources, its simplicity may create some rigidity on the definition of the hyperplane responsible for separating the two classes under analysis ("nonfatigued" vs "fatigued"), taking into account that geometrically it corresponds to a straight line in a 2D space.

For increasing the generalization/adaptability of the model, in the future, the kernel could be changed to a polynomial or a radial basis function (RBF) type, which could achieve a better separation of frontier points (as the ones highlighted on Figure 7), decreasing the occurrence of incorrect classification results.

5. Practical Applications

The described functionalities were implemented as a plugin of *OpenSignals* software, which emerges as an intuitive tool for processing physiological signals acquired by the systems designed and marketed by PLUX Wireless Biosignals, namely, in the *biosignalsplux* (PLUX Wireless Biosignals, 2015). The interface provides some sections for user interaction intended to the configuration of the processing algorithms, presenting the results divided into four zones, including EMG and HRV events detected (periods of muscle activation and *R* peaks) and the evolution of each of the IFD, the GFD, and the support vector machine class assigned.

With these processing functionalities, the computational system defines an interesting solution that can be applied in research studies and even by coaches and athletes, helping to prevent overtraining condition and ultimately the occurrence of muscular injuries.

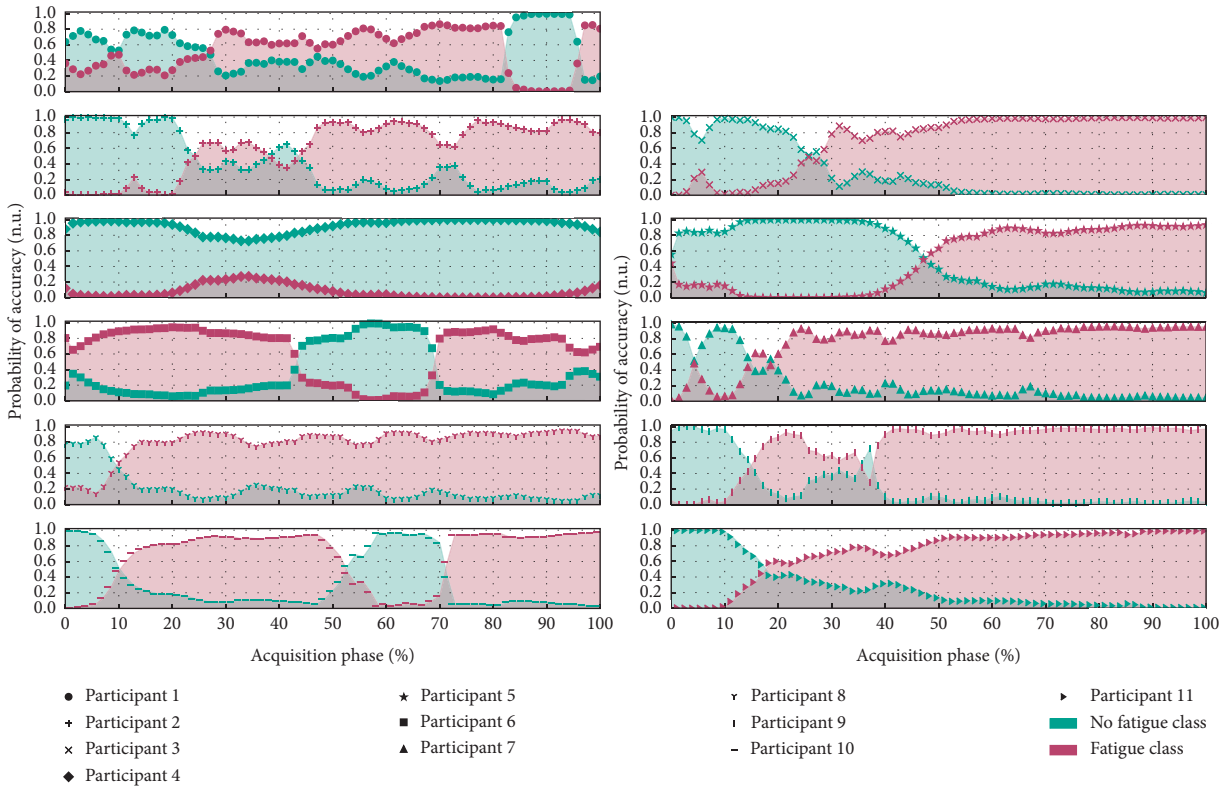

Figure 8: Evolution in the classification attributed by the support vector machine throughout the "acquisition +" collected in the various elements of the population sample after reviewing the segmentation methodology of the training data.

6. Conclusion

In the final analysis, we can conclude that 4 EMG (*Median Frequency*, from Fourier and Wavelet analysis; *Major Frequency*; *Major Time*) and 10 HRV parameters (*Maximum*, *Minimum* and *Average RR Interval*; *SDNN*; *rmsSD*; *Triangular Index*; *SD2*; *Power in LF* and *HF Band*; *Median Frequency*), i.e., 14 individual fatigue descriptors, exhibited a tendentious behavior over time in the participants included in our population. This tendentious behavior, according to the proposed trend evaluation methodology, is a demonstration of the correlation between the variable under study (fatigue) and the selected EMG and HRV parameters.

Taking into consideration the previously stated importance of the coefficient of variation to qualify the degree of correlation between changes in the experimental variable and the evolution of the extracted parameters, it can be concluded that *Fourier Median Frequency* will be the best EMG fatigue descriptor while *Average and Minimum RR Intervals* duration are the most meaningful HRV parameters, due to the lower CV values.

Combined information from these descriptors was achieved by the definition of our own global fatigue descriptor, an index that reflects the simultaneous impact of fatigue at the neuromuscular and cardiac autonomic level (objective nature) and also in a more global perspective when including HRV parameters, relevant indicators of mental/subjective fatigue. Since the implemented processing system extracts all information using a sliding window mechanism, a future adaptation of the system to a real-time analysis can be facilitated. The actual version is interesting within the context of exercise training because it may aid the estimation of the optimal individual workload during an acute exercise session. Ultimately, within the context of chronic endurance exercise, we speculate that this approach might be valuable for prophylaxis against overtraining and its negative side effects [63, 64].

A future implementation could benefit from the previously mentioned real-time algorithm. This would provide the user an automatic and immediate *feedback* about fatigue development.

In the work presented, our promising results on combined fatigue indices and the related classification approach are already providing novel tools for fatigue assessment that pave the way for broader, more robust, studies with larger populations that could potentially be established as preventive fatigue assessment mechanisms.

Data Availability

The acquired physiological data used to support the findings of this study are also restricted, in order to protect patient privacy. However, data may become accessible in some exceptional cases for researchers who meet the criteria for access to confidential data, through the corresponding author Guilherme Ramos (gramos@plux.info).

Conflicts of Interest

The authors declare that there are no conflicts of interest.

Acknowledgments

The authors thank Ms. Carolina Teodósio for assistance during the data collection. The acquired data were collected within the projected PTDC/DTP-DES/5714/2014-Contralateral effects of low intensity resistance training combined with blood flow restriction, funded by Fundação para a Ciência e Tecnologia (FCT), and J. R. Vaz was supported by NIH-P20GM109090 and by the University of Nebraska at Omaha Office of Research and Creative Activity. João Rodrigues participates in "iNOVA4Health-Programme in Translational Medicine" with a FCT grant I&D 2015-2020, while Guilherme Ramos was supported in the first phase by AHA CMUP-ERI/HCI/0046. The authors acknowledge the support that Miquel Alfaras received from ITN AffecTech, under the Marie Skłodowska Curie Actions (ERC H2020 Project ID: 722022).

Supplementary Materials

A. Algorithm for Identification of IFD. (*Supplementary Materials*)

References

[1] R. M. Enoka and J. Duchateau, "Translating fatigue to human performance," *Medicine & Science in Sports & Exercise*, vol. 48, no. 11, pp. 2228–2238, 2016.

[2] M. Gruet, J. Temesi, T. Rupp, P. Levy, G. Y. Millet, and S. Verges, "Stimulation of the motor cortex and corticospinal tract to assess human muscle fatigue," *Neuroscience*, vol. 231, pp. 384–399, 2013.

[3] C. J. De Luca, "Myoelectrical manifestations of localized muscular fatigue in humans," *Critical Reviews in Biomedical Engineering*, vol. 11, no. 4, pp. 251–279, 1984.

[4] J.-j. Wan, Z. Qin, P.-y. Wang, Y. Sun, and X. Liu, "Muscle fatigue: general understanding and treatment," *Experimental & Molecular Medicine*, vol. 49, 2017.

[5] M. Cifrek, V. Medved, S. Tonković, and S. Ostojić, "Surface EMG based muscle fatigue evaluation in biomechanics," *Clinical Biomechanics*, vol. 24, no. 4, pp. 327–340, 2009.

[6] M. J. Zwarts, G. Bleijenberg, and B. G. M. van Engelen, "Clinical neurophysiology of fatigue," *Clinical Neurophysiology*, vol. 119, no. 1, pp. 2–10, 2008.

[7] J. Shi, Y. P. Zheng, X. Chen, and Q. H. Huang, "Assessment of muscle fatigue using sonomyography: muscle thickness change detected from ultrasound images," *Medical Engineering & Physics*, vol. 29, no. 4, pp. 472–479, 2007.

[8] W. Ament and G. J. Verkerke, "Exercise and fatigue," *Sports Medicine*, vol. 39, no. 5, pp. 389–422, 2009.

[9] B. Bigland-Ritchie and J. J. Woods, "Changes in muscle contractile properties and neural control during human muscular fatigue," *Muscle & Nerve*, vol. 7, no. 9, pp. 691–699, 1984.

[10] H. Yoshitake, "Three characteristic patterns of subjective fatigue symptoms," *Ergonomics*, vol. 21, no. 3, pp. 231–233, 1978.

[11] B. Pageaux and R. Lepers, "Chapter 16-the effects of mental fatigue on sport-related performance," in *Sport and the Brain: The Science of Preparing, Enduring and Winning, Part C*, vol. 240, Elsevier, Amsterdam, Netherlands, 2018.

[12] C.-E. Benoit, O. Solopchuk, G. Borragán, A. Carbonnelle, S. Van Durme, and A. Zénon, "Cognitive task avoidance correlates with fatigue-induced performance decrement but not with subjective fatigue," *Neuropsychologia*, vol. 123, pp. 30–40, 2019.

[13] S. L. Rozzi, S. M. Lephart, and F. H. Fu, "Effects of muscular fatigue on knee joint laxity and neuromuscular characteristics of male and female athletes," *Journal of Athletic Training*, vol. 34, no. 2, pp. 106–114, 1999.

[14] J. Borresen and M. Ian Lambert, "The quantification of training load, the training response and the effect on performance," *Sports Medicine*, vol. 39, no. 9, pp. 779–795, 2009.

[15] E. Tønnessen, Ø. Sylta, T. A. Haugen, E. Hem, I. S. Svendsen, and S. Seiler, "The road to gold: training and peaking characteristics in the year prior to a gold medal endurance performance," *PloS One*, vol. 9, no. 7, Article ID e101796, 2014.

[16] L. Schmitt, J. Regnard, and G. P. Millet, "Monitoring fatigue status with HRV measures in elite athletes: an avenue beyond RMSSD?," *Frontiers in Physiology*, vol. 6, p. 343, 2015.

[17] L. Faller, G. N. Nogueira Neto, V. L. S. N. Button, and P. Nohama, "Avaliação da fadiga muscular pela mecanomiografia durante a aplicação de um protocolo de EENM," *Brazilian Journal of Physical Therapy*, vol. 13, no. 5, pp. 422–429, 2009.

[18] T. Kimura, M. Fujibayashi, S. Tanaka, and T. Moritani, "Mechanomyographic responses in quadriceps muscles during fatigue by continuous cycle exercise," *European Journal of Applied Physiology*, vol. 104, no. 4, pp. 651–656, 2008.

[19] J. Taelman, J. Vanderhaegen, M. Robijns, G. Naulaers, A. Spaepen, and S. Van Huffel, "Estimation of muscle fatigue using surface electromyography and near-infrared spectroscopy," *Oxygen Transport to Tissue XXXII*, vol. 701, pp. 353–359, 2011.

[20] R. B. Graham, M. P. Wachowiak, and B. J. Gurd, "The assessment of muscular effort, fatigue, and physiological adaptation using EMG and wavelet analysis," *PLoS One*, vol. 10, no. 8, pp. 1–13, 2015.

[21] H.-G. Kim, E.-J. Cheon, D.-S. Bai, Y. H. Lee, and B.-H. Koo, "Stress and heart rate variability: a meta-analysis and review of the literature," *Psychiatry Investigation*, vol. 15, no. 3, pp. 235–245, 2018.

[22] P. K. Whelton, R. M. Carey, W. S. Aronow et al., "2017 ACC/AHA/AAPA/ABC/ACPM/AGS/APhA/ASH/ASPC/NMA/PCNA guideline for the prevent ion, detection, evaluation, and management of high blood pressure in adults: a report of the American College of Cardiology/American Heart Association Task Force on Clinical Practice Guidelines," *Hypertension*, vol. 71, no. 6, pp. e13–e115, 2017.

[23] L. Mourot, N. Fabre, A. Savoldelli, and F. Schena, "Second ventilatory threshold from heart-rate variability: valid when the upper body is involved?," *International Journal of Sports Physiology and Performance*, vol. 9, no. 4, pp. 695–701, 2014.

[24] E. Howley, D. R. Bassett, and H. G. Welch, "Criteria for maximal oxygen uptake: review and commentary," *Medicine and Science in Sports and Exercise*, vol. 27, no. 9, pp. 1292–1301, 1995.

[25] K. Wasserman, B. J. Whipp, S. N. Koyl, and W. L. Beaver, "Anaero bic threshold and respiratory gas exchange during exercise," *Journal of Applied Physiology*, vol. 35, no. 2, pp. 236–243, 1973.

[26] PLUX Wireless Biosignals, "Biosignalsplux hub-data sheet," Tech. Rep., 2015.

[27] H. J. Hermens, B. Freriks, C. Disselhorst-Klug, and G. Rau, "Development of recommendations for SEMG sensors and sensor placement procedures," *Journal of Electromyography and Kinesiology*, vol. 10, no. 5, pp. 361–374, 2000.

[28] S. Thongpanja, A. Phinyomark, P. Phukpattaranont, and C. Limsakul, "Mean and median frequency of EMG signal to determine muscle force based on time-dependent power spectrum mean and median frequency of EMG signal to determine muscle force based on time- dependent power spectrum," *Electronics and Electrical Engineering*, vol. 19, no. 3, pp. 51–56, 2013.

[29] B. J. Becker and M.-J. Wu, "The synthesis of regression slopes in meta-analysis," *Statistical Science*, vol. 22, no. 3, pp. 414–429, 2007.

[30] A. Pimentel, R. Gomes, B. H. Olstad, and H. Gamboa, "A new tool for the automatic detection of muscular voluntary contractions in the analysis of electromyographic signals," *Interacting with Computers*, vol. 27, no. 5, pp. 492–499, 2015.

[31] J. Pan and W. J. Tompkins, "A real-time QRS detection algorithm," *IEEE Transactions on Biomedical Engineering*, vol. BME-32, no. 3, pp. 230–236, 1985.

[32] J. Rodrigues, D. Belo, and H. Gamboa, "Noise detection on ECG based on agglomerative clustering of morphological features," *Computers in Biology and Medicine*, vol. 87, pp. 322–334, 2017.

[33] U. R. Acharya, K. P. Joseph, N. Kannathal, C. M. Lim, and J. S. Suri, "Heart rate variability: a review," *Medical and Biological Engineering and Computing*, vol. 44, no. 12, pp. 1031–1051, 2006.

[34] Task Force of the European Society Electrophysiology, "Heart rate variability-standards of measurement, physiological interpretation, and clinical use task," *Circulation*, vol. 93, no. 5, pp. 1043–1065, 1996.

[35] N. Otsu, "A threshold selection method from gray-level histograms," *IEEE Transactions on Systems, Man, and Cybernetics*, vol. 9, no. 1, pp. 62–66, 1979.

[36] M. Borenstein, L. V. Hedges, J. P. T. Higgins, and H. R. Rothstein, "A basic introduction to fixed-effect and random-effects models for meta-analysis," *Research Synthesis Methods*, vol. 1, no. 2, pp. 97–111, 2010.

[37] S. Lewis and M. Clarke, "Forest plots: trying to see the wood and the trees," *BMJ*, vol. 322, no. 7300, pp. 1479-1480, 2001.

[38] D. M. Rouffet and C. A. Hautier, "EMG normalization to study muscle activation in cycling," *Journal of Electromyography and Kinesiology*, vol. 18, no. 5, pp. 866–878, 2008.

[39] T. V. Camata, L. R. Altimari, and H. Bortolotti, "Electromyographic activity and rate of muscle fatigue of the quadriceps Femoris during cycling exercise in the severe domain," *Journal of Strength and Conditioning Research*, vol. 25, no. 9, pp. 2537–2543, 2011.

[40] M. Knaflitz and P. Bonato, "Time-frequency methods applied to muscle fatigue assessment during dynamic contractions," *Journal of Electromyography and Kinesiology*, vol. 9, no. 5, pp. 337–350, 1999.

[41] A. Koumarianou, P. Pelekasis, M. Kontogoni, and C. Darviri, "How to encounter the development of panic disorder during adjuvant breast cancer chemotherapy: a case study," *Journal of Clinical Case Reports*, vol. 5, no. 1, pp. 1-2, 2015.

[42] R. K. Binder, M. Wonisch, and U. Corra, "Methodological approach to the first and second lactate threshold in incremental cardiopulmonary exercise testing," *European Journal of Cardiovascular Prevention & Rehabilitation*, vol. 15, no. 6, pp. 726–734, 2008.

[43] O. Faude, W. Kindermann, and T. Meyer, "Lactate threshold concepts," *Sports Medicine*, vol. 39, no. 6, pp. 469–490, 2009.

[44] M. A. Hearst, S. T. Dumais, E. Osuna, J. Platt, and B. Scholkopf, "Support vector machines," *IEEE Intelligent Systems and Their Applications*, vol. 13, no. 4, pp. 18–28, 1998.

[45] C. Cortes and V. Vapnik, "Support-vector networks," *Machine Learning*, vol. 20, no. 3, pp. 273–297, 1995.

[46] P. M. Granitto, C. Furlanello, F. Biasioli, and F. Gasperi, "Recursive feature elimination with random forest for PTR-MS analysis of agroindustrial products," *Chemometrics and Intelligent Laboratory Systems*, vol. 83, no. 2, pp. 83–90, 2006.

[47] P. Bonato, S. H. Roy, M. Knaflitz, and C. J. de Luca, "Time-frequency parameters of the surface myoelectric signal for assessing muscle fatigue during cyclic dynamic contractions," *IEEE Transactions on Biomedical Engineering*, vol. 48, no. 7, pp. 745–753, 2001.

[48] D. Farina, "Interpretation of the surface electromyogram in dynamic contractions," *Exercise and Sport Sciences Reviews*, vol. 34, no. 3, pp. 121–127, 2006.

[49] M. Vitor-Costa, H. Bortolotti, and T. V. Camata, "EMG spectral analysis of incremental exercise in cyclists and non-cyclists using Fourier and Wavelet transforms," *Revista Brasileira de Cineantropometria & De-sempenho Humano*, vol. 14, no. 6, pp. 660–670, 2012.

[50] J. L. Dantas, T. V. Camata, M. A. O. C. Brunetto, A. C. Moraes, T. Abrão, and L. R. Altimari, "Fourier and wavelet spectral analysis of EMG signals in isometric and dynamic maximal effort exercise," in *Proceedings of the 2010 Annual International Conference of the IEEE Engineering in Medicine and Biology*, vol. 2010, pp. 5979–5982, Buenos Aires, Argentina, September 2010.

[51] A. Phinyomark, C. Limsakul, and P. Phukpattaranont, "Application of wavelet analysis in EMG feature extraction for pattern classification," *Measurement Science Review*, vol. 11, no. 2, pp. 45–52, 2011.

[52] M. Bigliassi, P. R. Scalassara, T. F. D. Kanthack, T. Abrão, A. C. d. Moraes, and L. R. Altimari, "Fourier and wavelet spectral analysis of EMG signals in 1-km cycling time-trial," *Applied Mathematics*, vol. 05, no. 13, pp. 1878–1886, 2014.

[53] D. MacIsaac, P. A. Parker, and R. N. Scott, "The short-time Fourier transform and muscle fatigue assessment in dynamic contractions," *Journal of Electromyography and Kinesiology*, vol. 11, no. 6, pp. 439–449, 2001.

[54] R. A. da Silva, C. Lariviére, A. B. Arsenault, S. Nadeau, and A. Plamondon, "The comparison of wavelet- and Fourier-based electromyographic indices of back muscle fatigue during dynamic contractions: validity and reliability results," *Electromyography and Clinical Neurophysiology*, vol. 48, no. 3-4, pp. 147–162, 2008.

[55] B. Makivić, M. Nikić Djordjević, and M. S. Willis, "Heart rate variability (HRV) as a tool for diagnostic and monitoring performance in sport and physical activities," *Journal of Exercise Physiology Online*, vol. 16, no. 3, 2013.

[56] S. Sarmiento, J. M. García-Manso, J. M. Martín-González, D. Vaamonde, J. Calderón, and M. E. Da Silva-Grigoletto, "Heart rate variability during high-intensity exercise," *Journal of Systems Science and Complexity*, vol. 26, no. 1, pp. 104–116, 2013.

[57] Y. Tran, N. Wijesuriya, M. Tarvainen, P. Karjalainen, and A. Craig, "The relationship between spectral changes in heart rate variability and fatigue," *Journal of Psychophysiology*, vol. 23, no. 3, pp. 143–151, 2009.

[58] M. Patel, S. K. L. Lal, D. Kavanagh, and P. Rossiter, "Applying neural network analysis on heart rate variability data to assess

driver fatigue," *Expert Systems with Applications*, vol. 38, no. 6, pp. 7235–7242, 2011.

[59] J. Murgoitio Larrauri, J. L. G. Teminõ, and M. J. G. Larrea, "Heart rate variability-knowing more about HRV analysis and fatigue in transport studies," *Proceedings of the International Congress on Cardiovascular Technologies*, pp. 107–114, 2013.

[60] F. O. Cottin, C. MéDigue, P.-M. LeprêTre, Y. Papelier, J.-P. Koralsztein, and V. R. Billat, "Heart rate variability during exercise performed below and above ventilatory threshold," *Medicine & Science in Sports & Exercise*, vol. 36, no. 4, pp. 594–600, 2004.

[61] A. P. Pichon, C. de Bisschop, M. Roulaud, A. Denjean, and Y. Papelier, "Spectral analysis of heart rate variability during exercise in trained subjects," *Medicine & Science in Sports & Exercise*, vol. 36, no. 10, pp. 1702–1708, 2004.

[62] R. M. Enoka, "Mechanisms of muscle fatigue: central factors and task dependency," *Journal of Electromyography and Kinesiology*, vol. 5, no. 3, pp. 141–149, 1995.

[63] D. Ioannis, "Potential adverse biological effects of excessive exercise and overtraining among healthy individuals," *Acta Medica Martiniana*, vol. 14, no. 3, pp. 5–12, 2014.

[64] G. Vilhena de Mendonca, C. Teodósio, and P. M. Bruno, "Sexual dimorphism in heart rate recovery from peak exercise," *European Journal of Applied Physiology*, vol. 117, no. 7, pp. 1373–1381, 2017.

Hindawi
Journal of Healthcare Engineering
Volume 2019, Article ID 4159676, 13 pages
https://doi.org/10.1155/2019/4159676

Research Article

Removal of EMG Artifacts from Multichannel EEG Signals Using Combined Singular Spectrum Analysis and Canonical Correlation Analysis

Qingze Liu,[1] **Aiping Liu**,[1] **Xu Zhang**,[1] **Xiang Chen**,[1] **Ruobing Qian**,[2] **and Xun Chen**[3]

[1]*Department of Electronic Science and Technology, University of Science and Technology of China, Hefei 230027, China*
[2]*Department of Neurosurgery, The First Affiliated Hospital of University of Science and Technology of China (Anhui Provincial Hospital), Hefei 230036, China*
[3]*Department of Electronic Engineering and Information Science, University of Science and Technology of China, Hefei 230026, China*

Correspondence should be addressed to Aiping Liu; aipingl@ece.ubc.ca and Ruobing Qian; qianruobing@fsyy.ustc.edu.cn

Received 20 August 2019; Accepted 29 November 2019; Published 31 December 2019

Academic Editor: Rafael Morales

Electroencephalography (EEG) signals collected from human scalps are often polluted by diverse artifacts, for instance electromyogram (EMG), electrooculogram (EOG), and electrocardiogram (ECG) artifacts. Muscle artifacts are particularly difficult to eliminate among all kinds of artifacts due to their complexity. At present, several researchers have proved the superiority of combining single-channel decomposition algorithms with blind source separation (BSS) to make multichannel EEG recordings free from EMG contamination. In our study, we come up with a novel and valid method to accomplish muscle artifact removal from EEG by using the combination of singular spectrum analysis (SSA) and canonical correlation analysis (CCA), which is named as SSA-CCA. Unlike the traditional single-channel decomposition methods, for example, ensemble empirical mode decomposition (EEMD), SSA algorithm is a technique based on principles of multivariate statistics. Our proposed approach can take advantage of SSA as well as cross-channel information. The performance of SSA-CCA is evaluated on semisimulated and real data. The results demonstrate that this method outperforms the state-of-the-art technique, EEMD-CCA, and the classic technique, CCA, under multichannel circumstances.

1. Introduction

As a representatively noninvasive technique of reflecting electrical activities generated by the cerebral cortex, electroencephalography (EEG) is widely used for numerous practical applications in the biomedical engineering field. It owns the benefits of low cost, easy usability, and high temporal resolution. For example, EEG recordings are important for the description of the irritant and ictal onset zones in the presurgical evaluation of refractory partial epilepsy [1]; motor imagery EEG signals provide an important basis for designing a way to communicate between the brain and computer [2]; by making use of sparse EEG compressive sensing, person identification is possible [3]; and EEG can be utilized with other physiological data of different types to make a study of brain functions [4]. Nevertheless, with relatively low amplitudes, EEG is often polluted by many kinds of nonbrain artifacts mainly from the electromyogram (EMG), electrooculogram (EOG), and electrocardiogram (ECG) interferences. Thus, it is difficult to continue subsequent signal analysis. If the pollution is very heavy, the EEG waves may be completely masked so that we cannot interpret the brain activity contained in EEG signals [5]. Therefore, it has been attracting increasing attention that how to effectively eliminate these artifacts in the last few decades [6, 7].

Compared with EOG and ECG artifacts, there are more troubles in the domain of removing EMG artifacts [8, 9]. As we all know, many kinds of movements involving but not limited to eye movement, mastication, and facial expression

are generated by a number of muscles around the head. EEG can be easily influenced anywhere on the human scalp by the activity of each muscle via volume conduction. EMG artifacts have the characteristics of high amplitude, non-stereotyped scalp topographies, and extensive frequency domain distributions, which increase the difficulty in denoising.

In previous studies, researchers have successfully explored blind source separation (BSS) approaches to handle multichannel EEG data for accomplishing artifact elimination. Both independent component analysis (ICA) and canonical correlation analysis (CCA) belong to the most classic methods. ICA exploits higher-order statistics (HOS) of data to decompose the multichannel signals into independent components (ICs). The ICs representing the underlying sources are reserved, but artifact-related ICs are identified and discarded; hence, we can reconstruct relatively artifact-free EEG subsequently. As a well-known and effective BSS method, ICA is widely adopted for artifact removal from EEG since its first application in the field of brain electrical noise reduction [10, 11]. A study comparing fifteen diverse algorithms of ICA for denoising muscle artifacts has been published, which provides us with a helpful reference [12]. However, when it comes to the EMG removal problem of EEG, ICA might not perform well [9]. By making use of HOS information, ICA is better at eliminating the artifacts whose scalp topographies are stereotyped such as EOG. Muscle artifacts usually own a lot of different scalp topographies involving the activities of a group of muscles. Moreover, ICA does not exploit the temporal structure of muscle activities. Later on, canonical correlation analysis (CCA) has been advised to achieve EMG artifact removal [13]. By utilizing second-order statistics (SOS) information, CCA is able to obtain sources which are autocorrelated to the great extent and mutually uncorrelated. Since EMG artifacts have a broad frequency spectrum, their autocorrelation is low while the autocorrelation of EEG rhythms is high relatively. CCA can utilize this obvious characteristic to eliminate EMG artifacts. Simulation studies [13–15] and clinical studies [16, 17] have proved the superiority of CCA beyond ICA frequently for suppressing muscle artifacts in EEG.

However, with low signal-to-noise ratio (SNR) and complex contamination, ICA and CCA cannot perform well enough when denoising noisy EEG [6, 15]. As application scenarios of EEG devices tend to change from the traditional experimental condition to the realistic complex dynamic environment, muscle artifacts are inevitably generated due to the head movement and they are often pretty heavy. In recent years, studies show that combining more than one algorithm might obtain optimal results for removing artifacts from the EEG signals [7, 18, 19]. Usually, combining single-channel decomposition methods with BSS is highly recommended.

It is common that the combination mentioned above is applied to process single-channel EEG [20]. Since BSS implicitly has the limitation that potential sources must be not more than utilizable channels in number, the single-channel EEG can be decomposed into multidimensional data sets by single-channel decomposition methods to satisfy the requirements of BSS. For example, the combination of the wavelet transform (WT) with ICA [21], ensemble empirical mode decomposition (EEMD) with multiset CCA (MCCA) [22], and so on. In order to eliminate muscle artifacts from multichannel EEG recordings, if we process the multichannel EEG by means of channel by channel using the combination mentioned above, the relationship between channels may be ignored. To overcome this shortcoming, an EEMD-ICA approach has been suggested to improve the artifact elimination effect for multichannel EEG signals [23]. The EEMD-ICA approach employs ensemble empirical mode decomposition (EEMD) [24] to firstly obtain a number of intrinsic mode functions (IMFs) from each channel of EEG data. Then, the acquired IMFs relating to EMG artifacts are selected according to predefined rules. When applied to the chosen IMFs, ICA has the ability of concentrating the contents involving artifacts into several specific ICs. By discarding the ICs related to artifacts, we can obtain the relatively artifact-free data ultimately in the reconstruction step. It has been proved that this EEMD-ICA approach outperforms ICA and wavelet-ICA [25]. The superior performance over ICA demonstrates that exploring the information of every signal channel by single-channel decomposition methods first is of great significance to the contaminated multichannel EEG. The superior performance over wavelet-ICA is not hard to explain. While wavelet transform (WT) decomposes a signal adopting the method of determining in advance, and it is not easy in practice to select the best mother wavelets, EEMD is an entirely data-driven method, where no prior knowledge is required during decomposition. As we have discussed, CCA is better suited to eliminate muscle artifacts with complex and multiform scalp topographies. Very recently, replacing ICA with CCA, the EEMD-CCA method outperforms different techniques, including ICA, CCA, and EEMD-ICA, for eliminating muscle artifacts from EEG with multiple channels [26]. As far as we know, it gets the best results on multichannel EEG denoising. But EEMD decomposes the signal merely in terms of the amplitude and frequency information [15], and it cannot separate EEG contents from EMG artifacts overlapping in the relatively higher-frequency band. The IMFs relating to EMG artifacts usually represent high-frequency bands. Since the amplitude of EEG contents in the IMFs mainly containing muscle artifacts is much lower than the amplitude of EMG artifacts, it is extremely difficult to extract brain activity drowned in artifacts. Therefore in this article, we utilize singular spectrum analysis (SSA) to accomplish single-channel decomposition and propose a new architecture to process multichannel EEG data.

Singular spectrum analysis (SSA) is a kind of spectrum estimation technique with no need for parameters to do the decomposition for the raw signal according to the covariance property of data [27] and the characteristic of original signal [28]. In addition to its great success in terms of handling climatic, meteorological, and geophysical data [29], the SSA-based algorithm has been used to analyse EEG signals. Maddirala and Shaik made use of the method based on SSA to eliminate EOG [30] and motion artifacts [31] from

EEG in the case of only one channel; Teixeira et al. presented an approach to extract high-amplitude artifacts [32]; Hu et al. suggested utilizing the method derived from SSA to extract desired brain rhythms [33]. On the basis of these studies, we know that SSA can succeed in separating EEG composed of different sources, which are mixed with each other in the time-frequency domain. Cheng et al. have demonstrated that SSA is more powerful than EEMD in decomposing single-channel EEG [34].

In our proposed method, with the goal of eliminating EMG artifacts from multichannel EEG data, SSA algorithm is utilized twice. It decomposes each channel of multichannel EEG signals to acquire a collection of interpretable components. The two data sets of relatively clean EEG reconstructed from the process of two-time SSA decomposition are handled with CCA to get further noise reduction. Here, we set a suitable threshold value for the autocorrelation to select the components containing EEG information automatically. Our proposed SSA-CCA approach is applied to semisimulated data and real-life data, respectively; meanwhile, we make a comparison with the most effective technique, EEMD-CCA, and the classic technique, CCA.

The main contribution of our study is that we successfully solved the problem for removing EMG artifacts from EEG data in the multichannel situation. Our proposed technique is novel and performs very well. This scheme not only takes advantage of SSA to conduct time series analysis better than EEMD, but also utilizes a new framework to seek crosschannel interdependence with the help of BSS. It is also novel that we distinguished components of different content types by calculating the autocorrelation coefficients of SSA components.

The organization of the remaining paper is as follows: the proposed method and the methods used to do the comparison are described in Section 2. In Section 3, the synthetic and real-life data are briefly introduced. Section 4 presents the denoising results. Section 5 offers an intensive discussion and summarizes the work in this paper in the end.

2. Methods

We will introduce the suggested SSA-CCA method and the methods used to compare, i.e., CCA and EEMD-CCA in the following text of this section. The notations will be employed throughout the article as follows: lowercase italic letters (x, y, ...) are on behalf of scalars, lowercase boldface letters ($\mathbf{x}$, $\mathbf{y}$, ...) take the place of vectors, boldface capitals ($\mathbf{X}$, $\mathbf{Y}$, ...) represent matrices, and furthermore italic capitals (C, T, ...) are on behalf of the number of rows and columns. Vector or matrix transposition can be represented by the uppercase superscript T (e.g., $\mathbf{x}^T$ as well as $\mathbf{Y}^T$). In our study, the multichannel EEG signal is written as a matrix $\mathbf{X}$ whose size is $C \times T$. It means that this signal includes C channels and T sampling points. The time course is represented as $\mathbf{X}(t) = [\mathbf{x}_1(t), \mathbf{x}_2(t), \ldots, \mathbf{x}_C(t)]^T$ $(t = 1, 2, \ldots, T)$.

The entire flow diagram of the suggested SSA-CCA scheme is as shown in Figure 1. As it can be seen, SSA-CCA contains the following five steps: (1) utilizing SSA to decompose each channel into a collection of reconstructed components (RCs); (2) selecting RCs related to EEG activity to reconstruct a multichannel relatively clean EEG, mrcEEG, and the multichannel relatively clean EMG, mrcEMG, in the meanwhile; (3) decomposing mrcEMG by SSA again to extract possible EEG content just like step (1) and step (2); (4) applying CCA to the two data sets of mrcEEG from step (1) and step (3) for removing artifacts and obtaining cleaned mrcEEG; and (5) adding the two cleaned mrcEEG data up to get the desired artifact-free EEG. The description of details about our proposed approach is provided as follows.

2.1. Decomposition of Each Channel Using SSA. SSA is a very effective approach for analyzing time series. Considering a N sampled signal of one dimension as $\mathbf{x}(t) = (x_1, x_2, \ldots, x_N)$, the SSA algorithm is composed of two stages, which are named as decomposition and reconstruction, respectively. There are also two independent steps at each stage. To be more specific, the decomposition stage involves time-delay embedding and singular value decomposition (SVD). First, when conducting the embedding step, the original one-dimensional signal $\mathbf{x}$ can be mapped into a trajectory matrix $\mathbf{X}$ whose size is $L \times K$:

$$\mathbf{X} = (\mathbf{x}_1, \mathbf{x}_2, \ldots, \mathbf{x}_K) = \begin{bmatrix} x_1 & x_2 & \cdots & x_K \\ x_2 & x_3 & \cdots & x_{K+1} \\ \vdots & \vdots & \ddots & \vdots \\ x_L & x_{L+1} & \cdots & x_N \end{bmatrix}, \quad (1)$$

where L is on behalf of the window length for segmenting the data and $\mathbf{x}_i (1 \le i \le K)$ denotes the lagged vector as one column in the matrix $\mathbf{X}$ and here, we define $K = N - L + 1$. In the obtained trajectory matrix, all the antidiagonal elements are the same, and the matrix of this type is called Hankel matrix. Then, with the purpose of calculating SVD of matrix $\mathbf{X}$, the SVD step can be accomplished by utilizing the eigenvalue decomposition (EVD) of the covariance matrix $\mathbf{C}$, where $\mathbf{C} = \mathbf{X}\mathbf{X}^T$. Here, all eigenvalues and eigenvectors of the covariance matrix $\mathbf{C}$ are denoted as $\lambda_1, \lambda_2, \ldots, \lambda_L$ and $\mathbf{v}_1, \mathbf{v}_2, \ldots, \mathbf{v}_L$, respectively. It must be pointed out that the eigenvalues and corresponding eigenvectors are sorted inherently following the order of magnitude decrease, i.e., $\lambda_1 \ge \lambda_2 \ge, \ldots, \ge \lambda_L \ge 0$. The elementary matrices are defined as

$$\mathbf{X}_i = \sqrt{\lambda_i}\mathbf{v}_i\mathbf{u}_i, \quad (i = 1, 2, \ldots, L), \quad (2)$$

where $\mathbf{u}_i = \mathbf{X}^T\mathbf{v}_i/\sqrt{\lambda_i}$. Now, the trajectory matrix $\mathbf{X}$ can be expressed as

$$\mathbf{X} = \sum_{i=1}^{L} \mathbf{X}_i = \sum_{i=1}^{L} \sqrt{\lambda_i}\mathbf{v}_i\mathbf{u}_i. \quad (3)$$

Reconstruction consists of grouping and diagonal averaging. The SSA grouping involves dividing the indices $I_n = 1, 2, \ldots, L$ into G different groups. The trajectory matrix after the grouping step is denoted by

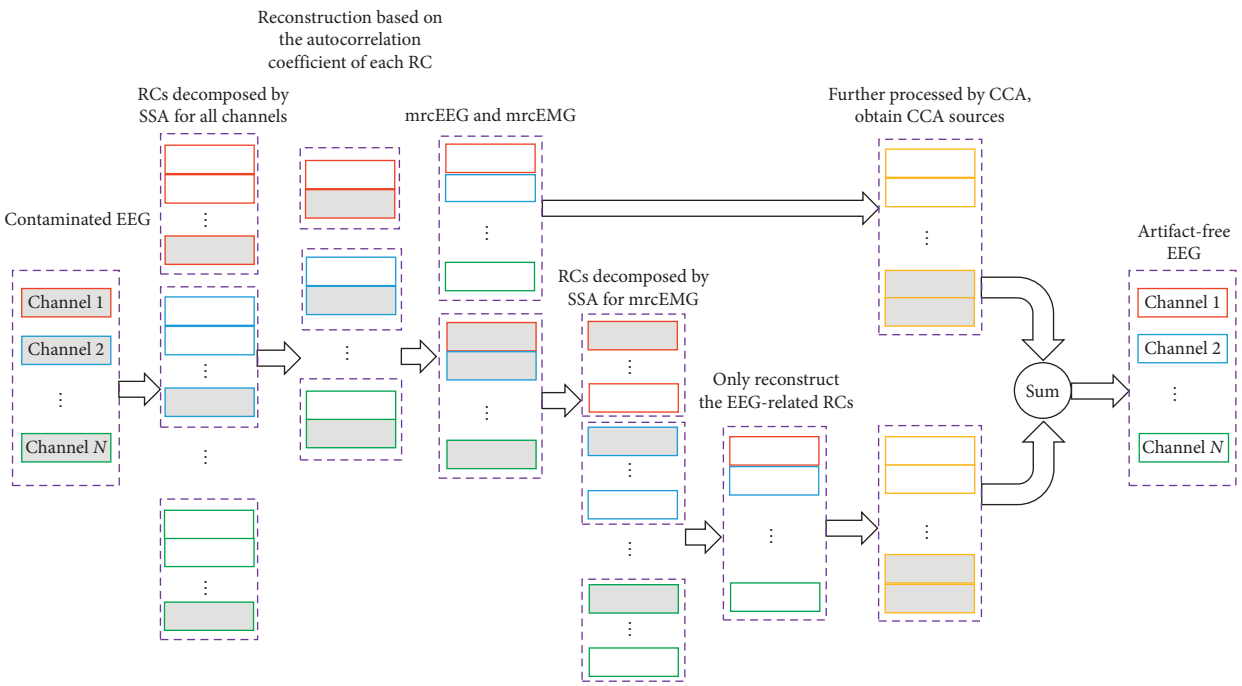

Figure 1: A flow diagram for the SSA-CCA approach. Here, the grey rectangles represent artifact-related components.

$$\mathbf{X} = \sum_{j=1}^{G} \mathbf{X}_{I_j}, \tag{4}$$

where $\mathbf{X}_{I_j}$ is the trajectory matrix and I_j is an ensemble of indices for the j^{th} group, $j = 1, \ldots, G$. In the condition of $G = L$, grouping of this type is known as elementary grouping. We conduct elementary grouping in this paper, i.e., $j = 1, \ldots, L$. In the final step called diagonal averaging since each submatrix $\mathbf{X}_{I_j}$ is hankelized, we can transform the acquired Hankel matrix into a new series through the operation of changing the antidiagonal elements of the matrix. The element values on the opposite diagonal of the Hankel matrix will be replaced with their mean value, which will be used to generate the signal of one dimension later. The reconstructed time series are referred to as reconstructed components (RCs) or SSA components in general. Thus, the original N sampled signal $\mathbf{x}(t)$ can be presented by

$$\mathbf{x}(t) = \sum_{j=1}^{L} \mathbf{x}_j^{\text{rc}}(t), \tag{5}$$

where $\mathbf{x}_j^{\text{rc}}(t)$ denotes the j^{th} RC with elementary grouping.

2.2. RCs Selection. According to our introduction to the SSA decomposition principle, it can be seen that there is no difference between choosing indices one wants at the grouping step and selecting proper RCs after elementary grouping while extracting a desired signal. However, there is no general criterion for indices or RCs selection [35]. When the energy of our expected signal is high enough and the signal that we need can be well defined in advance, the minimum description length (MDL) criterion works well for automatic grouping of trajectory matrices according to the magnitude of the eigenvalues [32]. Besides, in order to extract the dominating rhythms contained in EEG, researchers group the eigenvectors by exploring the characteristic of the eigenvalue pairs [36].

As we all know, muscle artifacts have a wide spectrum in the frequency domain and they behave very much like white noise, whose autocorrelation is much lower in comparison. The group rules above have a bad performance when applied to EMG artifact removal. Here, we recommend calculating the autocorrelation coefficient of each RC. The autocorrelation coefficient is a widely adopted indicator for the muscle artifact removal issue to select artifact-related components generated by EEMD [26]. Picking out RCs with relatively higher autocorrelation values can ensure that the useful information of EEG signals is reserved. We set an appropriate threshold value for the autocorrelation to identify and pick out RCs related to EEG rhythms before reconstruction automatically. Suppose one RC is represented as $\mathbf{c}(t)$, let $\mathbf{c}_1(t)$ equal to $\mathbf{c}(t)$ and $\mathbf{c}_2(t)$ be the time-delayed version, i.e., $\mathbf{c}_2(t) = \mathbf{c}(t-1)$. The calculation formula of autocorrelation R is as follows:

$$R = \frac{E\left[\left(\mathbf{c}_1(t) - E\left(\mathbf{c}_1(t)\right)\right)\left(\mathbf{c}_2(t) - E\left(\mathbf{c}_2(t)\right)\right)\right]}{\sqrt{E\left[\left(\mathbf{c}_1(t) - E\left(\mathbf{c}_1(t)\right)\right)^2\right]E\left[\left(\mathbf{c}_2(t) - E\left(\mathbf{c}_2(t)\right)\right)^2\right]}}, \tag{6}$$

where E is the operator that computes the expectation.

The RCs with autocorrelation values less than the threshold are picked out to generate relatively clean EEG. When one has finished this process channel by channel, the multichannel relatively clean EEG, denoted as mrcEEG, is obtained. And the multichannel relatively clean EMG, denoted as mrcEMG, can be obtained by subtracting mrcEEG from the original mixed EEG. Here, a relatively

lower threshold is suggested in order to avoid too much loss of brain activity information.

2.3. Further Treatment of Muscle Artifact with CCA. The mrcEEG is processed by CCA to achieve further artifact elimination. Let $\mathbf{Z}_1(t)$ be equal to the mrcEEG matrix $\mathbf{Z}(t)$, which includes C channels and T sampling points, meanwhile $\mathbf{Z}_2(t)$ be the time-delayed version, i.e., $\mathbf{Z}_2(t) = \mathbf{Z}(t-1)$. CCA maximizes the correlation coefficient (CC) between the related sources generated from $\mathbf{Z}_1(t)$ and $\mathbf{Z}_2(t)$. This results in an objective function as follows, which aims at strengthening the correlation as best as it can between the mixtures of the variates from $\mathbf{Z}_1$ and $\mathbf{Z}_2$:

$$\max_{\mathbf{w}_1,\mathbf{w}_2} \frac{\mathbf{w}_1^T \sum_{12} \mathbf{w}_2}{\sqrt{\mathbf{w}_1^T \sum_{11} \mathbf{w}_1} \sqrt{\mathbf{w}_2^T \sum_{22} \mathbf{w}_2}}, \tag{7}$$

where $\sum_{11}$ the autocovariance matrices of $\mathbf{Z}_1$, $\sum_{22}$ is the autocovariance matrices of $\mathbf{Z}_2$, and $\sum_{12}$ is the cross-covariance matrix of $\mathbf{Z}_1$ and $\mathbf{Z}_2$, in addition $\mathbf{w}_1$ and $\mathbf{w}_2$ are the weight vectors. In our definition, $\widetilde{S}_1$ denotes the whole canonical variates generated from $\mathbf{Z}_1$ and $\widetilde{S}_2$ denotes those generated from $\mathbf{Z}_2$. Traditionally, CCA is considered as a BSS technique by making the estimated sources highly correlated between $\widetilde{S}_1$ and $\widetilde{S}_2$ and mutually uncorrelated within each respective matrix. By this means, the rows in $\widetilde{S}_1$ are arranged in the decreasing order of autocorrelation. In comparison to EEG content, the autocorrelation of EMG artifacts is relatively lower. Therefore, CCA has the ability to concentrate these artifacts into the last several sources. Finally, we can set sources relating to artifacts to zero in the reconstruction step to achieve further artifact elimination.

2.4. Artifact Removal and Signal Reconstruction. In this part, by letting the artifact-related sources to be zero and operating the inverse process of CCA, the denoised mrcEEG data can be acquired. Then, the mrcEMG in Section 2.2 should be processed the same way as the original mixed EEG using the combination of SSA and CCA. We find that twice is enough for applying this combination. Finally, add the two cleaned mrcEEG data up. The desired artifact-free multichannnel EEG is done.

2.5. Introduction to State-of-the-Art Methods

2.5.1. CCA for Muscle Artifact Elimination. The CCA method has been described in Section 2.3. One can also consult the original work [13].

2.5.2. EEMD-CCA Method for Muscle Artifact Elimination. First, there is an introduction to EEMD. Empirical mode decomposition (EMD), as one well-known decomposition method firstly suggested by Huang et al., is suitable to process many kinds of time variable and complex signals. EMD can decompose a one-dimensional signal into a number of intrinsic mode functions (IMFs), refer to [37] for decomposition details. A single-channel signal $\mathbf{x}(t)$ can be decomposed in the form of

$$\mathbf{x}(t) = \sum_{j=1}^{N} \mathbf{c}_j + \mathbf{r}_n, \tag{8}$$

where $\mathbf{c}_j$ denotes the j^{th} IMF, $j = 1, 2, \ldots, N$ and $\mathbf{r}_n$ denotes the residual component after extracting all N IMFs. But the original EMD algorithm has its own inherent disadvantage. It is easily influenced by noise, and the phenomenon of mode-mixing is possible to occur among diverse IMFs. Therefore, Wu and Huang [24] came up with a noise-assisted method for data analysis, known as ensemble EMD (EEMD), to solve this problem. EEMD independently adds white noise to the raw signal with a number of individual trials when applying the original EMD. At last, EEMD takes the mean of a collection of IMFs as the definition of its IMFs. In this paper, we have tried different ensemble numbers when utilizing EEMD (i.e., 10, 50, and 100) and there is no significant difference when the number of ensembles is not less than 50. Considering the computational cost and to get the best possible result, 50 ensembles were used. The noise standard deviation was determined as 0.2 times the standard deviation of the raw data according to experience as recommended [24]. The implementation of EEMD-CCA includes six steps. The details of this algorithm are provided in the work [26].

3. Data Generation and Description

In order to conduct performance evaluation of different techniques appearing in this article, we made use of semi-simulated data and real-life data. The semisimulated EEG signals are derived by mixing real pure EEG with pure EMG, both collected from different subjects. The real-life data set comes from a patient suffering from epileptic seizures. The details of these data are shown as follows.

3.1. Semisimulated Data. The semisimulated data set was generated from real EEG and EMG data, which were derived from different people. The 19-channel pure EEG data were recorded when 20 subjects in good health participated in the experiment, whose sampling rate was 500 Hz and processed by a high-passed filter with 1 Hz cutoff frequency to eliminate the baseline noise. The original EMG signals acting as muscle artifact sources were collected with 23 healthy volunteers involved, whose sampling rate was also 500 Hz to match with EEG data. The length of data is 10 seconds for both types of data. The instrument and details of data acquisition can be found in [26].

To make sure that the sources were independent with each other and randomly chosen, each EMG source was selected among diverse EMG recordings across different subjects. Thus, an independent EMG source matrix $\mathbf{S}_{\text{EMG}}$ could be formed, and it includes 19 channels with 10 seconds of data in each channel. By multiplying a 19×19 mixing matrix $\mathbf{A}$ with the EMG source matrix $\mathbf{S}_{\text{EMG}}$, a simulated EMG matrix $\mathbf{X}_{\text{EMG}}$ containing 19 channels was generated. To ensure sufficient spatial structure, there were 5 to 8 nonzero

elements in each column of the matrix **A**. Thus, each EMG source from the source matrix **S** synchronously exists in 5 to 8 channels of the simulated EMG matrix $\mathbf{X}_{\mathrm{EMG}}$. The number, values, and positions of nonzero entries in each column of the matrix **A** were decided at random on the basis of uniform distribution [6]. At last, the data generated above were utilized to form the mixed EEG signal **X** as follows:

$$\mathbf{X} = \mathbf{X}_{\mathrm{EEG}} + \lambda \cdot \mathbf{X}_{\mathrm{EMG}}, \tag{9}$$

where λ determines the contribution of EMG artifacts. The contamination levels can be controlled by adjusting the SNR values. SNR is calculated as

$$\mathrm{SNR} = \frac{\mathrm{RMS}(\mathbf{X}_{\mathrm{EEG}})}{\mathrm{RMS}(\lambda \cdot \mathbf{X}_{\mathrm{EMG}})}, \tag{10}$$

where we define the root mean square (RMS) as

$$\mathrm{RMS}(\mathbf{X}) = \sqrt{\frac{1}{C \cdot T} \sum_{c=1}^{C} \sum_{t=1}^{T} \mathbf{X}^2(c,t)}, \tag{11}$$

where C represents how many channels there are and T represents how many time sampling points there exist. The values of SNR were within a range from 0.5 to 4.5, which are changed taking 0.5 as the step length. As an example, data of pure EEG, pure simulated EMG, and mixed EEG are presented in Figure 2.

In our study, two evaluation indexes were adopted for the semisimulated experiment. The first evaluation indicator was called the relative root mean squared error (RRMSE), which was expressed as

$$\mathrm{RRMSE} = \frac{\mathrm{RMS}(\mathbf{X}_{\mathrm{EEG}} - \tilde{X}_{\mathrm{EEG}})}{\mathrm{RMS}(\mathbf{X}_{\mathrm{EEG}})}, \tag{12}$$

where $\tilde{X}_{\mathrm{EEG}}$ is the EEG data after being processed to eliminate artifacts. The second evaluation measure was the correlation coefficient (CC) between the pure EEG served as ground truth in each channel and its denoised version. We calculated the average CC (ACC) values over all channels to estimate the ability of the methods for preserving true brain activity. Note that these two indicators were applied to mean-removed signals.

3.2. Real Data. An available real-life ictal EEG recording was utilized to evaluate the performance between our proposed method and the other two methods on data of the real person. As shown in Figure 3, these data are scalp EEG signal, which contains 21 channels, lasts for 10 s, and has a sampling rate of 250 Hz. It was processed by a band-pass filter from 0.3 to 35 Hz. Muscle artifacts can be found in channels F7, T3, T5, C3, and T1 between 0 and 4 s and in channels F8, T4, F4, C4, and P4 between 5 and 10 s.

Since real data lacks the ground truth to serve as a reference, both RRMSE and ACC cannot be utilized to perform evaluation. Power spectral density (PSD) is an effective and well-known way to describe the energy distribution of time series in the frequency domain. Different from muscle artifacts, the EEG components are mainly at a lower frequency. Hence, the values of PSD belong to a well-denoised EEG signal which have a tendency to decrease at high frequencies (e.g., above 30 Hz) and at the same time they follow more closely the PSD values of the raw EEG signal at low frequencies (e.g., below 25 Hz).

4. Results

4.1. Semisimulated Data. To make a quantitative comparison, the semisimulated data were handled by all the methods in this paper to automatically eliminate EMG artifacts. There were a total of 20 collected EEG recordings generated from 20 different subjects. In order to sufficiently utilize each EEG recording, 10 independent results were obtained by adding 10 respective simulated EMG matrices, which were randomly produced by the recorded EMG signals. Thus, there were 200 mutually independent results in all per SNR value, and the mean as well as standard deviation at the corresponding SNR value were calculated. According to the method description in Section 2, CCA can isolate the final obtained components related to muscle artifacts into the last several components. Since we own the ground truth here, all the methods will definitely receive their best performance by discarding the optimal number of components at each SNR value. The meaning of the optimal number is that removing fewer or more last components cannot get better results than removing the last components of this number.

The window length L for SSA is empirically recommended as 200. At the SNR value of 1, after the raw mixed EEG signal is decomposed by SSA, the autocorrelation coefficients of reconstructed components (RCs) are shown in Figure 4(a). We recommend setting the threshold to be 0.82. The RCs whose autocorrelation coefficients are above the threshold are selected to reconstruct multichannel relatively clean EEG, mrcEEG. The left RCs generate multichannel relatively clean EMG, mrcEMG. Then, mrcEMG is also decomposed by SSA and the autocorrelation coefficients of RCs are described in Figure 4(b). Now, the RCs related to EEG are isolated relatively behind. With eigenvalues and the corresponding RCs arranged in the decreasing order of magnitude, according to reference [38], the SSA algorithm can be regarded as a bank of finite impulse response (FIR) filters. The filters are data adaptive, and the filter corresponding to the higher-energy component is located in the relatively front position of the RC sequence. In Figure 4(b), the sum of eigenvalues corresponding to EEG-related RCs accounts for 3.13% of the sum of all eigenvalues, which means that after picking out EEG-related RCs, the reconstructed EMG signal contains almost no EEG information. Thus, there is no need to further decompose the EMG signal reconstructed from mrcEMG, considering the time cost of the SSA algorithm.

The final obtained results are displayed in Figure 5. The threshold of EEMD-CCA at step (2) in Section 2.5.2 is 0.95 as recommended [26]. It can be seen that SSA-CCA performs best per SNR value in terms of RRMSE and ACC. EEMD-CCA has a better performance than CCA, reproducing the results in [26].

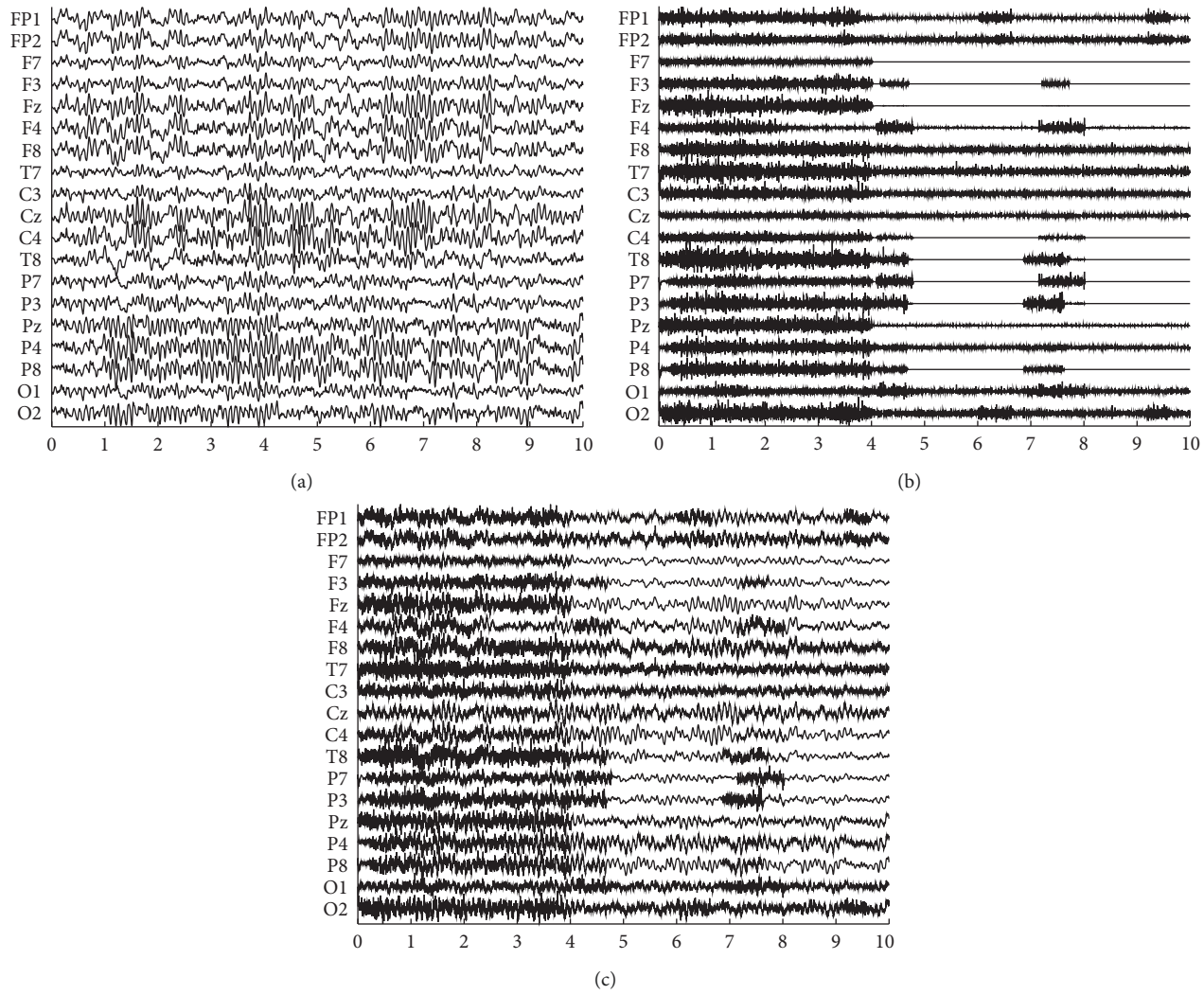

Figure 2: (a) Pure EEG data $\mathbf{X}_{\text{EEG}}$, (b) pure simulated EMG data $\mathbf{X}_{\text{EMG}}$, and (c) mixed EEG data $\mathbf{X}$ contaminated with SNR = 1.5. The horizontal axis is on behalf of time variation with the second as the unit.

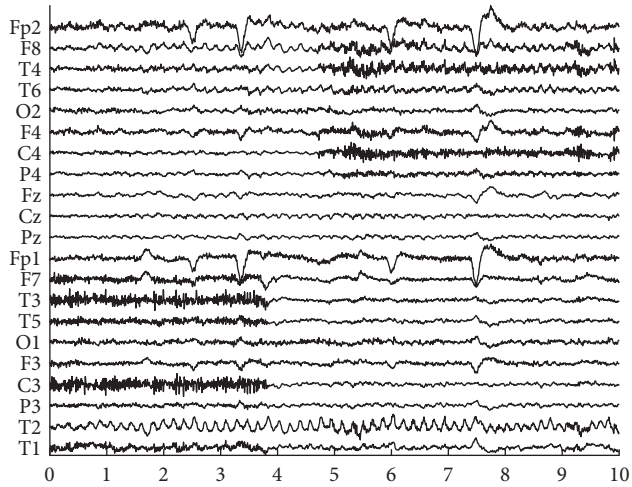

Figure 3: Real EEG data polluted by muscle artifacts. The horizontal axis is on behalf of time variation with the second as the unit.

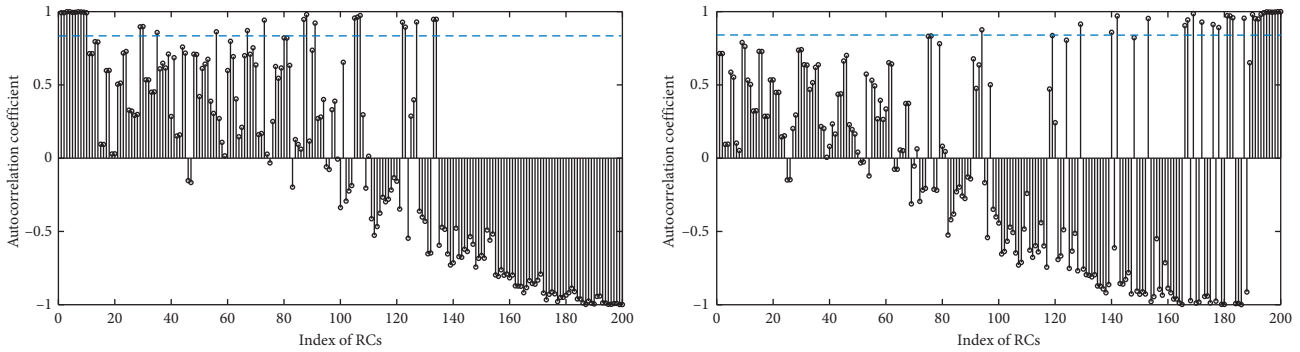

Figure 4: (a) The autocorrelation coefficients of RCs for the original mixed EEG signal at SNR 1, and (b) the autocorrelation coefficients of RCs for the mrcEMG. The blue line is threshold 0.82.

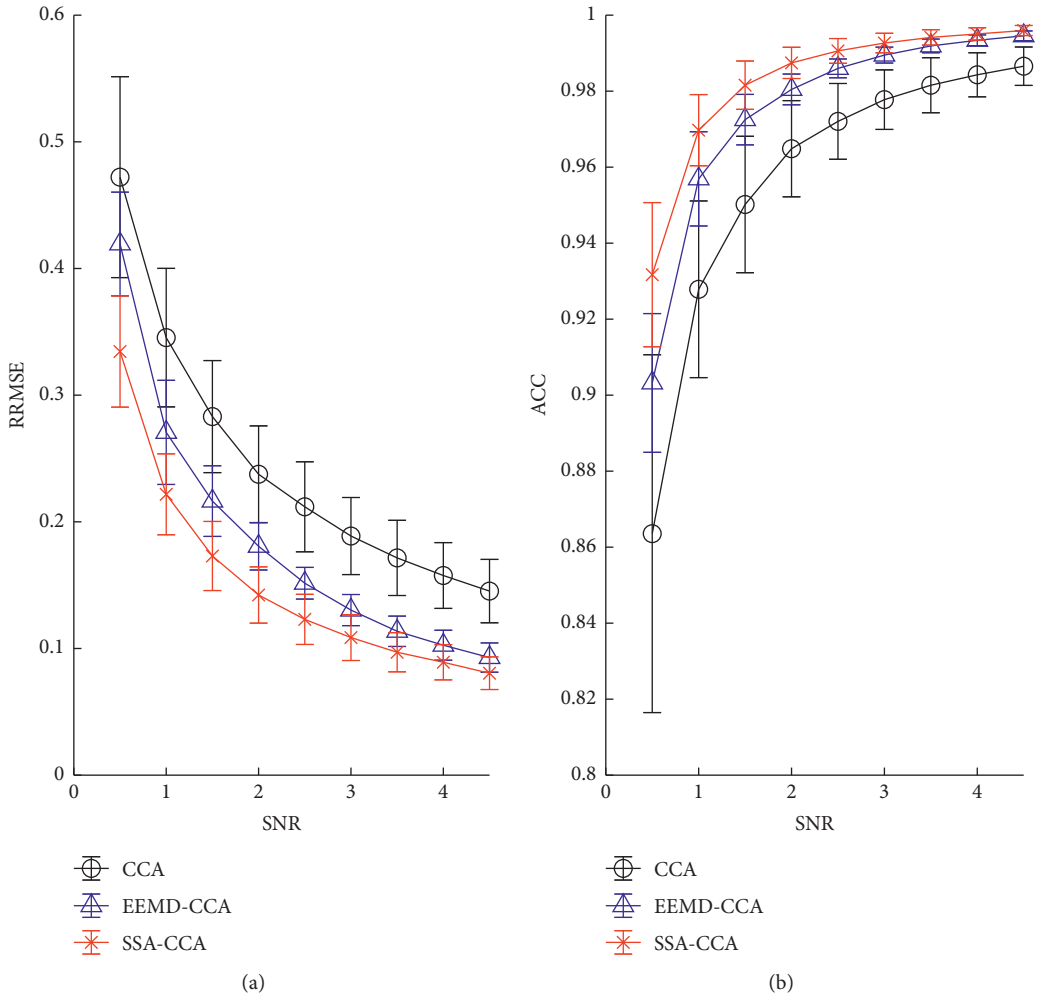

Figure 5: For the semisimulated experiment, the quantitative comparison of methods per different SNR value of (a) RRMSE and (b) ACC.

4.2. Real-Life Data. When it comes to the real data, without the ground truth, the two evaluation indexes of RRMSE and ACC cannot be employed to illustrate the denoising effects of these methods. Here, the comparative results on qualitative time domain waveforms and the PSD values before and after artifact removal are applied. In order to get a closer look, a channel lightly polluted and a channel heavily contaminated by muscle artifacts were picked out, they were T2 and T5, respectively. The temporal waveforms after applying three different methods to the real EEG are described in Figures 6 and 7.

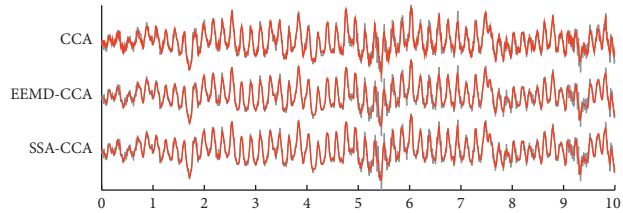

Figure 6: The denoised EEG (red) of channel T2 presented together with the raw EEG (grey) by applying (a) CCA, (b) EEMD-CCA, and (c) SSA-CCA. The horizontal axis is on behalf of time variation with the second as the unit.

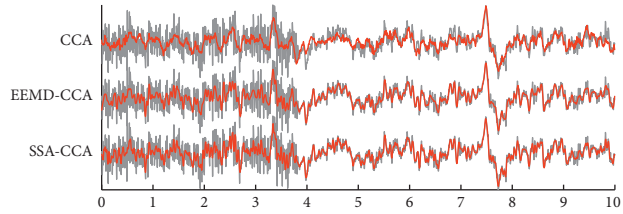

Figure 7: The denoised EEG (red) of channel T5 presented together with the raw EEG (grey) by applying (a) CCA, (b) EEMD-CCA, and (c) SSA-CCA. The horizontal axis is on behalf of time variation with the second as the unit.

The grey color denotes the original real-life data, and the red color denotes the cleaned data. From Figure 6, EEMD-CCA and SSA-CCA could perfectly deal with lightly contaminated EEG since the artifacts appearing at around 5.3 s and 9.2 s were removed and the seizure activity was reserved very well. The resulting signal of CCA could also follow the original waveform, but the artifacts were not eliminated very cleanly. From Figure 7, when EEG was corrupted with heavy artifacts, it could be seen that there were still a lot of visible artifacts in the result of CCA. In addition, the cleaned signal failed to go after the raw signal at the segment free from artifacts between 4 s and 10 s. But EEMD-CCA and SSA-CCA can deal with this situation successfully. The denoised signals closely followed the raw signal segments where there were no artifacts and visible artifacts could not be found. By carefully examining the waveform details in Figures 6 and 7, we are able to conclude that SSA-CCA is more powerful than EEMD-CCA in preserving brain activity. There are more details in the waveform of SSA-CCA, meaning that more EEG information can be preserved. For further illustration of this point, we also computed the values of PSD for the raw EEG data and the artifact-attenuated EEG data processed by these three methods. The PSD values are plotted channel by channel in Figure 8.

As it can be seen in Figure 8, the EEG signals in channels Fz, Cz, and Pz are merely lightly polluted. Therefore, the PSD values (black) of these channels are relatively higher at low frequencies and lower at high frequencies. Noticing the characteristics of the spectrum distribution in Fz, Cz, and Pz, we can note that true EEG contents in the raw EEG are originally concentrated at low frequencies (e.g., 1–25 Hz). There are obvious EEG rhythms at about 10 Hz and between 1 and 5 Hz. For the channels polluted by heavy artifacts, such as T4, C4, T3, and C3, the PSD values at high frequencies are relatively higher. The goal of denoising is to maximally suppress the effects of muscle activity and meanwhile minimally cause a loss to brain activity.

From Figure 8, the performance of CCA is unsatisfactory. CCA does not have enough effect on removing muscle artifacts (e.g., F7 and P4), causing the insufficient energy decrease in the high-frequency band, or removes both brain and muscle contents, resulting in the energy decrease in almost all frequency bands (e.g., T3 and C4). This is because the sources decomposed by CCA are mainly the mixture of muscle artifacts and ongoing EEG signals. On the contrary, both EEMD-CCA and SSA-CCA can largely remove muscle artifacts, comparing the PSD values at high frequencies with those of the original EEG signal. And the PSD values between 1 and 5 HZ and around 10 Hz are nearly unchanged from the raw EEG signal in almost all channels, demonstrating the ability of retaining EEG content for the two methods. However, when observing the results between EEMD-CCA and SSA-CCA more closely, we are able to see that the PSD values in terms of EEMD-CCA decrease sharply from about 15 Hz while the PSD values in terms of SSA-CCA tend to keep relatively higher between 15 and 25 Hz in almost all channels. Thus, SSA-CCA can preserve EEG information not only in the low-frequency band but also in the relatively higher frequency band. To be more specific, in the frequency band of 15–25 Hz, the PSD values of SSA-CCA are very close to those of the original EEG signal with little contamination in channels Fz, Cz, Pz, T6, and O2, indicating that EEG information is well retained; meanwhile, taking the PSDs of the original EEG signal heavily contaminated in channels T3, C3, C4, and T4 as a reference, the PSD values of SSA-CCA are lower, indicating that muscle artifacts are removed. EEMD-CCA thoughtlessly ignores the brain activity in the frequency band of 15–25 Hz. Hence, SSA-CCA is more powerful than EEMD-CCA in extracting EEG information of higher frequency.

In addition, by using the proposed SSA-CCA method, the final denoised EEG data are shown in Figure 9. As we can see, compared with the raw EEG data, muscle artifacts

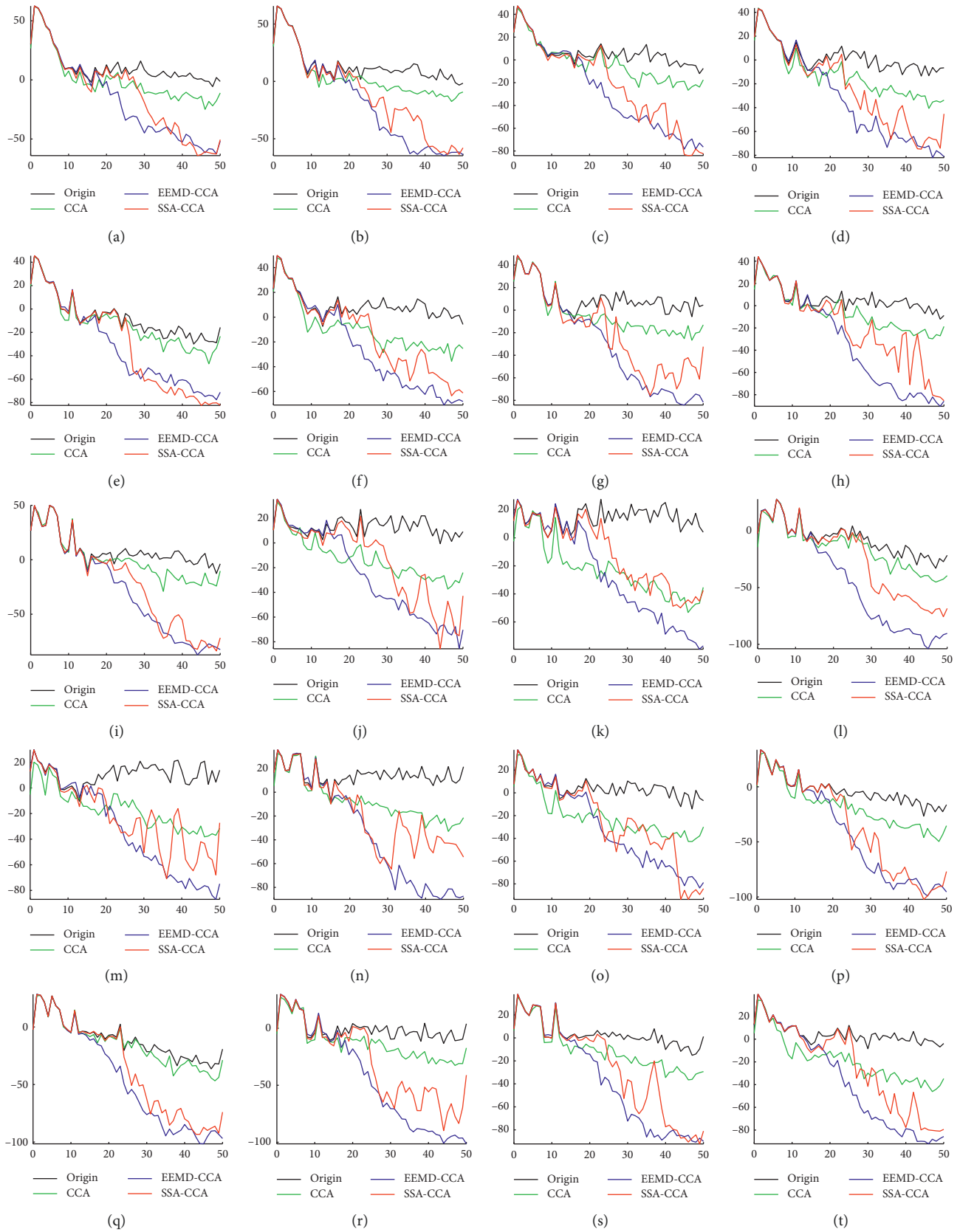

Figure 8: Continued.

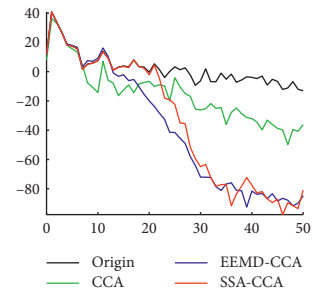

(u)

Figure 8: Power spectral density of the raw EEG and the denoised EEG processed by different methods in our study. The horizontal axis is frequency with unit Hz, and the vertical axis is PSD with unit dB: (a) Fp1; (b) Fp2; (c) F7; (d) F3; (e) Fz; (f) F4; (g) F8; (h) T1; (i) T2; (j) T3; (k) C3; (l) Cz; (m) C4; (n) T4; (o) T5; (p) P3; (q) Pz; (r) P4; (s) T6; (t) O1; (u) O2.

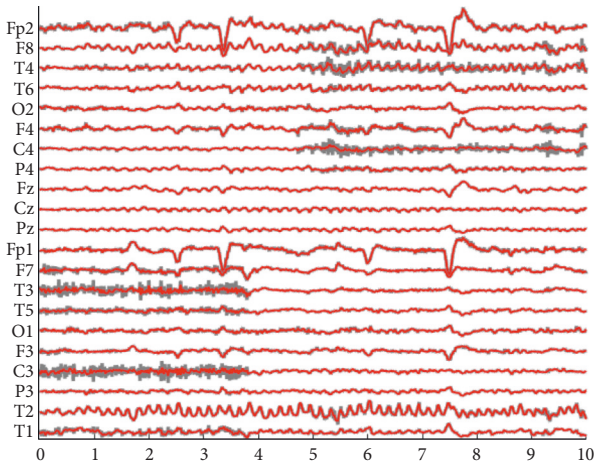

Figure 9: The reconstructed EEG (red) after eliminating EMG artifacts presented together with the raw EEG (grey).

completely disappeared while the EEG content was well reserved.

5. Discussion and Conclusion

According to the relevant discussions in [26, 39], it is crucially important to guarantee the signal quality of EEG by means of muscle artifact removal. Different from ocular and cardiac artifacts, muscle artifacts with highly nonstereotyped scalp topographies are especially challenging to be eliminated. This may be the reason why ICA, a well-known and widely used tool, does not perform well for removing muscle artifacts. Although ICA has a good effect on ocular and cardiac artifact removal, based on previous studies [9, 13–17, 23, 26], there is no need to apply ICA for comparison in the multichannel EMG artifact removal task in this paper. Instead, CCA makes use of the unique characteristics of muscle activity such as low autocorrelation, resulting in an improved performance. However, the traditional multichannel BSS techniques, like CCA, are capable of extracting the underlying myogenic sources as many as the number of EEG channels at most. When the SNR is very low with complex and severe contamination, the potential sources might be more than utilizable channels in number. Under these circumstances, combining single-channel decomposition methods with BSS is recommended, for example, EEMD-CCA.

As we all know, the architecture of the human head is often regarded as a volume conductor, so that the interference of each muscle can readily appear anywhere on the scalp. Thus, the signal in each channel generates from the mixture of different underlying sources, bringing in cross-channel dependence. The main advantage of single-channel decomposition may be that this technique fully explores single-channel information to discover independent EEG sources. The subsequent division of sources in each channel reduces the complexity of the EEG signal, and the following BBS method is applied to conduct further noise reduction with the crosschannel information. The algorithm architectures of EEMD-CCA and SSA-CCA are different, but they both take advantage of combining single-channel decomposition with BSS. Since EEMD decomposes signals merely according to amplitude and frequency, the frequency spectrum of the artifact sources derived from EEMD often overlaps with that of EEG sources. The identified artifact-related IMFs absolutely contain EEG content, which is drowned in the artifacts. Even CCA cannot completely extract the EEG content from the artifact-related IMFs. The high-frequency EEG is mixed with the last sources abandoned by CCA. This explains why a lot of loss was caused by EEMD-CCA in the frequency band of 15–25 Hz processing the real data. However, taking advantage of the information of eigenvalues, SSA is able to distinguish diverse sources even mixed in the time-frequency domain. It can be seen that EEG-related RCs with low eigenvalues, accounting for a small portion of EEG contents, are nicely separated by SSA in Figure 4. The high-frequency EEG part is not dominant in the pure EEG; thus, it tends to be the EEG-related RCs with low eigenvalues and is well retained by SSA. As for muscle artifacts owning extensive frequency domain distributions, SSA can get better results than EEMD.

The window length L of SSA is selected according to the condition, i.e., $L > f_s/f_1$, where f_1 is the lowest frequency of the desired component and f_s is the sampling frequency [40]. This choice can make sure that the size of L is large enough to include one period of the desired source at least. Therefore, we set the L to be 200 and 100 for semisimulated

data and real data, respectively. In practical applications, the real data recordings are complicated and it is hard to select a proper window length. Fortunately, we tested different window length values (i.e., 200, 150, 100, and 50) with all other parameters unchanged. The results on semisimulated data and real data were very similar, all leading to advantages over EEMD-CCA. It demonstrates that in our proposed method, SSA is not sensitive to L, showing the generality of the method. We recommend choosing the window length L according to the condition $L > f_s/f_1$ if one wants to obtain a detailed decomposition by SSA. But in practice, L is proposed to be between 50 and 100, considering the good decomposition effect and low time cost. It must be mentioned that Maddirala et al. grouped the eigenvectors on the basis of the local mobility of the eigenvectors to eliminate muscle artifacts from EEG [41]. We also used the local mobility to distinguish RCs and found the results were totally consistent with the criterion of calculating the autocorrelation. In our proposed method, two thresholds of the autocorrelation coefficient should be determined, one for choosing EEG-related RCs and the other for CCA discarding artifact-related sources. In [26] for EEMD, to preserving EEG content as much as possible in the early processing step, the first threshold is relatively higher (0.95 used in our study) for selecting artifact-related IMFs. While in our proposed method, the first threshold is set to be lower, in order to pick out EEG-related RCs as possible. Through experiments, the thresholds around 0.8 are recommended (0.82 used in our study). In the semisimulation study, with ground truth, the optimally selected number of abandoned components can be determined for all the methods, thus the second threshold is not needed. In the real-life data study, the second threshold values ranged from 0.80 to 0.99 were examined through direct visual inspection of both temporal and spectral contents before and after muscle artifact elimination. All the methods adopt 0.9 as the second threshold for a fair comparison.

For practical applications, we tested the time cost of conducting CCA, EEMD-CCA, and SSA-CCA. In SSA, calculating the eigenvalues of the trajectory matrix is time-consuming work. On the premise of not affecting the effect of denoising, L was set to be 50 for comparison. The realization was completed in MATLAB (MathWorks Inc., Novi, MI, USA) and operated under Microsoft Windows 10×64 on a computer with Intel(R) and Core(TM) i5-8400 2.80 GHz CPU and 16.0 GB RAM. At each SNR from 0.5 to 4.5 changing with a 0.5 step, there were 200 independent implementations for semisimulated data mentioned above. The average time costs for CCA, EEMD-CCA, and SSA-CCA over the EEG data with 19 channels and the length of 10 seconds were 0.0118 s, 4.4469 s, and 3.6665 s with standard deviations 0.0007, 0.1529, and 0.0218. As you can see, the computational cost of SSA-CCA can be completely accepted.

We have proved that SSA-CCA is a satisfactory tool for muscle artifact elimination when processing the multichannel EEG signals. Nowadays, with portable or wearable EEG devices for long-term mobile monitoring becoming increasingly prevalent, the present EEG devices have a tendency to own only a small number of channels [18]. Unfortunately, our method might not be the optimal choice due to the channel limitation in the few-channel situation [39]. Thus, we might improve the current processing architecture of SSA-CCA to satisfy the needs of removing muscle artifacts from few-channel EEG signals in the near future.

Data Availability

There are two data sets used, semisimulated data and real-life data. The semisimulated data used to support the findings of this study are available from the authors Qingze Liu and Aiping Liu upon request, who can be contacted via qingze@mail.ustc.edu.cn and aipingl@ece.ubc.ca, respectively. The real-life data are publicly available from the BioSource database, and one can access this data set at "http://www.esat.kuleuven.be/sista/members/biomedng/biosource.html."

Conflicts of Interest

The authors declare that they have no conflicts of interest.

Acknowledgments

This work was supported by the National Natural Science Foundation of China (grants 61922075 and 61701158) and the Young Elite Scientists Sponsorship Program by CAST (grant 2017QNRC001).

References

[1] M. De Vos, A. Vergult, L. De Lathauwer et al., "Canonical decomposition of ictal scalp EEG reliably detects the seizure onset zone," *NeuroImage*, vol. 37, no. 3, pp. 844–854, 2007.

[2] H. wang and Y. Zhang, "Detection of motor imagery EEG signals employing Naïve Bayes based learning process," *Measurement*, vol. 86, pp. 148–158, 2016.

[3] Y. Dai, X. Wang, X. Li, and Y. Tan, "Sparse EEG compressive sensing for web-enabled person identification," *Measurement*, vol. 74, pp. 11–20, 2015.

[4] X. Chen, Z. J. Wang, and M. McKeown, "Joint blind source separation for neurophysiological data analysis: multiset and multimodal methods," *IEEE Signal Processing Magazine*, vol. 33, no. 3, pp. 86–107, 2016.

[5] M. Fatourechi, A. Bashashati, R. K. Ward, and G. E. Birch, "EMG and EOG artifacts in brain computer interface systems: a survey," *Clinical Neurophysiology*, vol. 118, no. 3, pp. 480–494, 2007.

[6] X. Chen, A. Liu, J. Chiang, Z. J. Wang, M. J. Mckeown, and R. K. Ward, "Removing muscle artifacts from EEG data: multichannel or single-channel techniques?," *IEEE Sensors Journal*, vol. 16, no. 7, pp. 1986–1997, 2015.

[7] J. A. Urigüen and B. Garcia-Zapirain, "EEG artifact removal—state-of-the-art and guidelines," *Journal of Neural Engineering*, vol. 12, no. 3, Article ID 031001, 2015.

[8] E. Urrestarazu, J. Iriarte, M. Alegre, M. Valencia, C. Viteri, and J. Artieda, "Independent component analysis removing artifacts in ictal recordings," *Epilepsia*, vol. 45, no. 9, pp. 1071–1078, 2004.

[9] B. W. McMenamin, A. J. Shackman, L. L. Greischar, and R. J. Davidson, "Electromyogenic artifacts and electroencephalographic inferences revisited," *Neuroimage*, vol. 54, no. 1, pp. 4–9, 2011.

[10] M. J. McKeown, S. Makeig, G. G. Brown et al., "Analysis of fMRI data by blind separation into independent spatial components," *Human Brain Mapping*, vol. 6, no. 3, pp. 160–188, 1998.

[11] T.-P. Jung, S. Makeig, C. Humphries et al., "Removing electroencephalographic artifacts by blind source separation," *Psychophysiology*, vol. 37, no. 2, pp. 163–178, 2000.

[12] L. Albera, A. Kachenoura, P. Comon et al., "ICA-based EEG denoising: a comparative analysis of fifteen methods," *Bulletin of the Polish Academy of Sciences: Technical Sciences*, vol. 60, no. 3, pp. 407–418, 2012.

[13] W. De Clercq, A. Vergult, B. Vanrumste, W. Van Paesschen, and S. Van Huffel, "Canonical correlation analysis applied to remove muscle artifacts from the electroencephalogram," *IEEE Transactions on Biomedical Engineering*, vol. 53, no. 12, pp. 2583–2587, 2006.

[14] J. Gao, C. Zheng, and P. Wang, "Online removal of muscle artifact from electroencephalogram signals based on canonical correlation analysis," *Clinical EEG and Neuroscience*, vol. 41, no. 1, pp. 53–59, 2010.

[15] M. R. Mowla, S. C. Ng, M. S. Zilany, and R. Paramesran, "Artifacts-matched blind source separation and wavelet transform for multichannel EEG denoising," *Biomedical Signal Processing and Control*, vol. 22, pp. 111–118, 2015.

[16] A. Vergult, W. De Clercq, A. Palmini et al., "Improving the interpretation of ictal scalp EEG: BSS-CCA algorithm for muscle artifact removal," *Epilepsia*, vol. 48, no. 5, pp. 950–958, 2007.

[17] D. M. Vos, S. Riès, K. Vanderperren et al., "Removal of muscle artifacts from EEG recordings of spoken language production," *Neuroinformatics*, vol. 8, no. 2, pp. 135–150, 2010.

[18] J. Minguillon, M. A. Lopez-Gordo, and F. Pelayo, "Trends in EEG-BCI for daily-life: requirements for artifact removal," *Biomedical Signal Processing and Control*, vol. 31, pp. 407–418, 2017.

[19] X. Chen, X. Xu, A. Liu et al., "Removal of muscle artifacts from the EEG: a review and recommendations," *IEEE Sensors Journal*, vol. 19, no. 14, pp. 5353–5368, 2019.

[20] X. Chen, A. Liu, H. Peng, and R. Ward, "A preliminary study of muscular artifact cancellation in single-channel EEG," *Sensors*, vol. 14, no. 10, pp. 18370–18389, 2014.

[21] J. Lin and A. Zhang, "Fault feature separation using wavelet-ICA filter," *NDT & E International*, vol. 38, no. 6, pp. 421–427, 2005.

[22] X. Chen, C. He, and H. Peng, "Removal of muscle artifacts from single-channel EEG based on ensemble empirical mode decomposition and multiset canonical correlation analysis," *Journal of Applied Mathematics*, vol. 2014, Article ID 261347, 10 pages, 2014.

[23] K. Zeng, D. Chen, G. Ouyang, L. Wang, X. Liu, and X. Li, "An EEMD-ICA approach to enhancing artifact rejection for noisy multivariate neural data," *IEEE Transactions on Neural Systems and Rehabilitation Engineering*, vol. 24, no. 6, pp. 630–638, 2015.

[24] Z. Wu and N. E. Huang, "Ensemble empirical mode decomposition: a noise-assisted data analysis method," *Advances in Adaptive Data Analysis*, vol. 1, no. 1, pp. 1–41, 2009.

[25] N. Mammone, F. La Foresta, and F. C. Morabito, "Automatic artifact rejection from multichannel scalp EEG by wavelet ICA," *IEEE Sensors Journal*, vol. 12, no. 3, pp. 533–542, 2011.

[26] X. Chen, Q. Chen, Y. Zhang, and Z. J. Wang, "A novel EEMD-CCA approach to removing muscle artifacts for pervasive EEG," *IEEE Sensors Journal*, vol. 19, no. 19, pp. 8420–8431, 2018.

[27] N. Golyandina and A. Zhigljavsky, *Singular Spectrum Analysis for Time Series*, Springer Science & Business Media, Berlin, Germany, 2013.

[28] E. Cantú-Paz, S. Newsam, and C. Kamath, "Feature selection in scientific applications," in *Proceedings of the Tenth ACM SIGKDD International Conference on Knowledge Discovery and Data Mining*, pp. 788–793, Seattle, WA, USA, August 2004.

[29] N. Golyandina, V. Nekrutkin, and A. A. Zhigljavsky, *Analysis of Time Series Structure: SSA and Related Techniques*, Chapman and Hall/CRC, Boca Raton, FL, USA, 2001.

[30] A. K. Maddirala and R. A. Shaik, "Removal of EOG artifacts from single channel EEG signals using combined singular spectrum analysis and adaptive noise canceler," *IEEE Sensors Journal*, vol. 16, no. 23, pp. 8279–8287, 2016.

[31] A. K. Maddirala and R. A. Shaik, "Motion artifact removal from single channel electroencephalogram signals using singular spectrum analysis," *Biomedical Signal Processing and Control*, vol. 30, pp. 79–85, 2016.

[32] A. R. Teixeira, A. M. Tomé, E. W. Lang, P. Gruber, and A. Martins da Silva, "Automatic removal of high-amplitude artefacts from single-channel electroencephalograms," *Computer Methods and Programs in Biomedicine*, vol. 83, no. 2, pp. 125–138, 2006.

[33] H. Hu, S. Guo, R. Liu, and P. Wang, "An adaptive singular spectrum analysis method for extracting brain rhythms of electroencephalography," *PeerJ*, vol. 5, Article ID e3474, 2017.

[34] J. Cheng, L. Li, C. Li et al., "Remove diverse artifacts simultaneously from a single-channel EEG based on SSA and ICA: a semi-simulated study," *IEEE Access*, vol. 7, pp. 60276–60289, 2019.

[35] F. Ghaderi, H. R. Mohseni, and S. Sanei, "Localizing heart sounds in respiratory signals using singular spectrum analysis," *IEEE Transactions on Biomedical Engineering*, vol. 58, no. 12, pp. 3360–3367, 2011.

[36] S. M. Mohammadi, S. Enshaeifar, M. Ghavami, and S. Sanei, "Classification of awake, REM, and NREM from EEG via singular spectrum analysis," in *Proceedings of the 2015 37th Annual International Conference of the IEEE Engineering in Medicine and Biology Society (EMBC)*, pp. 4769–4772, Milano, Italy, August 2015.

[37] N. E. Huang, Z. Shen, S. R. Long et al., "The empirical mode decomposition and the Hilbert spectrum for nonlinear and non-stationary time series analysis," *Proceedings of the Royal Society of London. Series A: Mathematical, Physical and Engineering Sciences*, vol. 454, no. 1971, pp. 903–995, 1998.

[38] N. Figueiredo, P. Georgieva, E. W. Lang, I. M. Santos, A. R. Teixeira, and A. M. Tomé, "SSA of biomedical signals: a linear invariant systems approach," *Statistics and Its Interface*, vol. 3, no. 3, pp. 345–355, 2010.

[39] X. Chen, X. Xu, A. Liu, M. J. McKeown, and Z. J. Wang, "The use of multivariate EMD and CCA for denoising muscle artifacts from few-channel EEG recordings," *IEEE Transactions on Instrumentation and Measurement*, vol. 67, no. 2, pp. 359–370, 2017.

[40] C. J. James and D. Lowe, "Extracting multisource brain activity from a single electromagnetic channel," *Artificial Intelligence in Medicine*, vol. 28, no. 1, pp. 89–104, 2003.

[41] A. K. Maddirala and R. A. Shaik, "Removal of EMG artifacts from single channel EEG signal using singular spectrum analysis," in *Proceedings of the 2015 IEEE International Circuits and Systems Symposium (ICSyS)*, pp. 111–115, Langkawi, Malaysia, September 2015.

Hindawi
Journal of Healthcare Engineering
Volume 2019, Article ID 8597606, 10 pages
https://doi.org/10.1155/2019/8597606

Research Article

DMCNN: A Deep Multiscale Convolutional Neural Network Model for Medical Image Segmentation

Lin Teng,[1] **Hang Li**,[1] **and Shahid Karim**[2]

[1]*Software College, Shenyang Normal University, Shenyang 110034, China*
[2]*Institute of Image and Information Technology, Harbin Institute of Technology, Harbin 150000, China*

Correspondence should be addressed to Hang Li; lihangsoft@163.com and Shahid Karim; shahidhit@yahoo.com

Received 29 September 2019; Revised 21 November 2019; Accepted 28 November 2019; Published 27 December 2019

Guest Editor: Liang Zhao

Medical image segmentation is one of the hot issues in the related area of image processing. Precise segmentation for medical images is a vital guarantee for follow-up treatment. At present, however, low gray contrast and blurred tissue boundaries are common in medical images, and the segmentation accuracy of medical images cannot be effectively improved. Especially, deep learning methods need more training samples, which lead to time-consuming process. Therefore, we propose a novelty model for medical image segmentation based on deep multiscale convolutional neural network (CNN) in this article. First, we extract the region of interest from the raw medical images. Then, data augmentation is operated to acquire more training datasets. Our proposed method contains three models: encoder, U-net, and decoder. Encoder is mainly responsible for feature extraction of 2D image slice. The U-net cascades the features of each block of the encoder with those obtained by deconvolution in the decoder under different scales. The decoding is mainly responsible for the upsampling of the feature graph after feature extraction of each group. Simulation results show that the new method can boost the segmentation accuracy. And, it has strong robustness compared with other segmentation methods.

1. Introduction

Medical imaging makes a critical difference in clinical diagnosis [1–3]. Recently, with the progress of medical imaging technology and the continuous development of artificial intelligence image processing, medical image processing technology has gradually developed into a key research field. It is vital in clinical application. The aim of medical image segmentation technology is to segment the interested part by some deep automatic segmentation algorithms and make the segmentation results as close as possible to the original structure of the region [4]. Segmentation of medical image has big significance in clinical diagnosis and pathological diagnosis. Measuring lesion volume with segmented images can assist doctors to determine the disease and make treatment plans [5].

Medical imaging segmentation (MIS) is an indispensable stage in ROI (region of interest) extraction, quantitative analysis, and 2D reconstruction. The images will be segmented with the same or similar features (such as intensity, color, and texture) into separated areas, particularly to extract the lesion areas with special meanings or other regions of interest (ROI) from the complex background, so as to provide basis for clinical analysis [6]. Magnetic Resonance Imaging (MRI) uses the principle of nuclear magnetic resonance, which not only has high soft tissue resolution but also provides rich and high-resolution three-dimensional brain tissue information. Therefore, how to segment the medical images accurately in MRI images is becoming a challenging task in medical image research [7].

Through the analysis of research status, we summarize three kinds of traditional MIS methods: (1) manual segmentation method, which is tedious, excessive labor, subjective, prone to error, and not suitable for large-scale research [8]; (2) semiautomatic segmentation method, which requires accurate control of prior parameters and consumes much time in the process of parameter tuning [9]; (3) the traditional segmentation methods such as graph-based, deformation model, and active appearance model [10–12], which is based on simple registration method.

However, due to the differences between the hippocampus, in terms of the segmentation efficiency and accuracy, a simple registration method is still not ideal.

Currently, deep learning has attracted more attention, and the model based on deep CNN and its variants have been diffusely used in various fields of medical image processing and also achieved better results [13–15]. For example, Cha [16] presented MR brain image automatic segmentation method using a CNN network. The method was independent on explicit features only requiring a single MR (magnetic resonance) image. Lu et al. [17] used two-dimensional convolutional neural network to evaluate the segmentation of electron microscope images. Zhang et al. [18] adopted deep CNN to evaluate the segmentation of multimodal brain images. Although the models based on CNN have obtained better performance, these methods have a common problem, namely, all networks take image block as input, due to a large amount of overlapping image blocks, the redundant computation will increase the time cost for testing the network, and the image block size will influence the capability of the trained network. To solve the problem of image segmentation, many researchers have come up with many approaches based on the fully convolutional network (FCN) model to remedy limitations of image segmentation. FCN can take the entire image as the input of the network and generate the corresponding output of the whole image, thus avoiding the problems caused by the use of image blocks. However, it had low efficiency. So, a deep multiscale CNN model is put forward for medical image segmentation. The major contributions are illustrated as follows:

(1) First, we extract the regions of interest from the raw medical images. Then, the data augmentation is operated to obtain more training dataset. The encoder, U-net, and decoder models are used for constructing our proposed segment framework.

(2) Encoder is mainly responsible for feature extraction of 2D image slice.

(3) In different scales of the decoder, it will acquire the features of each encoder's block by deconvolution operation, and then the U-net joins them together.

(4) The decoding is mainly responsible for the upsampling of the feature graph after feature extraction of each group.

This paper is originated as follows. In Section 2, related works are introduced for the image segmentation. Section 3 describes the proposed DMCNN in detail. In Section 4, we conduct experiments and give analysis. Section 5 concludes the work.

2. Related Works

2.1. Inception Model. In order to make the convolutional neural network have better learning ability, the most direct and effective method is to make the network layer deeper. However, there are some disadvantages in this operation: (1) if the training number and dataset are limited, more parameters will easily lead to overfitting; (2) if the network is larger, it is hard to utilize due to the greater endless computation; (3) the deeper the network is, the gradient will disappear, which leads to the diffusion of gradient. Under this situation, it is difficult to optimize the network model. Inception v1 is proposed in 2014 [19], the convolution layer of 1×1, 3×3, and 5×5, and pooling layer of 3×3 are stacked together, which increases the width of the network and also enhances the adaptability of the network in terms of the scale. This operation can extract features from different scales. An important improvement in Inception v31 is decomposition, the two-dimensional convolution of $N \times N$ is divided into two-dimensional convolutions of $1 \times \mathrm{N}$ and $N \times 1$. The advantage of this method is that it can not only accelerate the computation but also increase the nonlinearity of the network.

2.2. Batch Normalization. BN aims to add a standardized processing for the input data of each layer in the training process of neural network, which also belongs to the network layer. Previously, we mentioned that in addition to the output layer of the network, the parameters of the lower layer of the network are updated during the training, which caused the change of the distribution of the input data in the latter layer. In each layer, it is better to add a preprocessing operation. For example, the data in the third layer of network are normalized. Then, it inputs the third layer for calculation, so that we can solve the problem of "Internal Covariate Shift" [20–22]. By introducing batch standardization method, the network's convergence speed will be greatly increased. The overfitting can also be controlled. The dropout and regularization operation will be realized with little utilization.

2.3. End-To-End Models and Jump Connections. Compared to the traditional image block-based convolutional neural network model, the end-to-end model utilizes the entire image as input. The entire image will be generated as output [23, 24]. The image block-based model needs to foretell each size of pixel in the slice separately. Therefore, the end-to-end model adopted in this paper can evidently decrease the time consumption when segmenting images. Generally, end-to-end models primarily include fully CNN and faster CNN. It combines the feature maps of different levels. Unlike FCN, the U-net model adopts jump connection to join the feature information obtained from the shrinking coding path and the deconvolution operation in the expanded path together which is favourable for obtaining multiscale feature information to strengthen the network's feature extraction ability.

3. Proposed DMCNN

3.1. Data Preprocessing. For the acquired medical images, the region of interest should be extracted and preprocessed to serve as the samples for training and testing the network. After that, gray level regularization is carried out on all acquired ROIs. And, the mean and SD (standard deviation)

are measured. The gray level regularization is assessed by subtracting mean value and dividing by SD. In the subsequent training and testing process, the extracted images are transported into the network model as samples, and the extracted region is shown in Figure 1. For example, the size of the raw image is 256×256, and after ROI extraction, we get the 128×128 patch and input it into network for training.

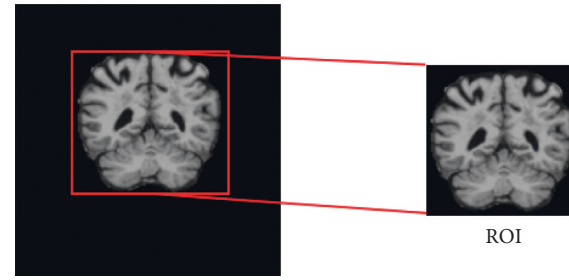

Figure 1: Extracted ROI.

3.2. Data Extension. Since labeled public medical image datasets are little online and they are inconvenient to use, training a deep CNN model is troublesome [25]. In our proposed model, we first adopt some newest data argumentation methods to expand the raw data in order to increase the number of available training samples. In this paper, five data expansion methods are adopted including vertical direction reversal, random angle rotation, random translation, horizontal direction reversal, and image deformation. Figure 2 shows an example of the image expansion.

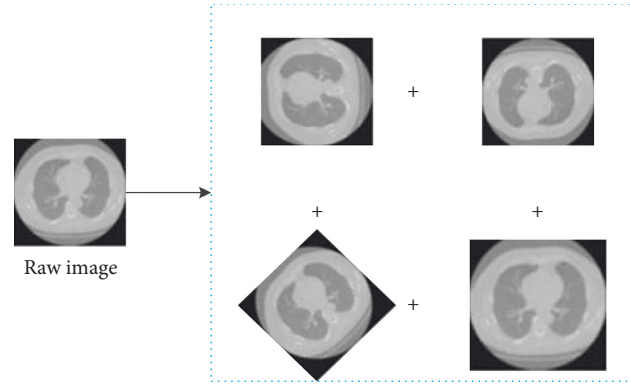

Figure 2: Proposed medical image segment model.

3.3. Proposed Network Model. To raise the accuracy of medical image segmentation, spatial information of images and relevant information between 2D slices are effectively utilized. The proposed deep multiscale convolutional neural network model contains three parts: encoder, U-net, and decoder as shown in Figure 3.

3.3.1. Encoder. It is mainly responsible for feature extraction of 2D slices, whose network structure is shown in Figure 4. Small convolution kernel in convolutional network is conducive to capturing local information, while large convolution kernel is conducive to capturing global information. However, ROIs are different in 2D slices, and it is difficult to select an accurate and universal convolution kernel. For this purpose, we use three different convolution layers (1×1, 3×3, 5×5) to extract information of multiple scales in Inception V1, which can extract more features. Additionally, to reduce the amount of computation, asymmetric convolution kernel is used in this experiment to decompose the $N \times N$ two-dimensional convolution into two one-dimensional convolutions with $1 \times N$ and $N \times 1$.

Meanwhile, to expand the receptive field of convolution and perfectly obtain multiscale information without increasing the size of parameters, this paper adds dilated convolutions with expansion coefficients of 2 and 4, respectively. For an ordinary convolution layer of 3×3, the receptive field of its convolution kernel is 3×3. In this paper, after the employment of dilated convolution (DC), the size of parameters remains unchanged, but the receptive field of the convolution kernel becomes 7×7 and 15×15. It can be seen that DC greatly increases the receptive field of the convolution layer without increasing parameters number. As shown in Figure 4, there are three kinds of dilated convolution with expansion coefficients of 1, 2, and 4, respectively, in the encoded part, and the receptive fields of the corresponding convolution kernel are 3×3, 7×7 and 15×15, respectively. After using the three receptive fields with different sizes, it is not only conducive to feature extraction but also conducive to better capturing the pathological area features.

Then, after cascading the feature graphs extracted from five different convolution layers, we utilize two ordinary 3×3 convolution layers in feature extraction process. Finally, to reduce the size of the feature map, it connects a maximum pooling layer. In Figure 4, the number of channels in each convolution layer is 16. Considering the convergence of networks, batch normalization is added behind the convolution layer, and ReLu layer is used as the activation function.

3.3.2. U-Net Model. Figure 5 shows the proposed U-net network structure employed. The U-net network structure contains two parts as follows:

(a) Contractile encoder part on the left. It processes input medical images.

(b) Decoder part on the right. It produces labeled output.

(c) The skip connection. It can cascade the features of each block in the encoder. Features are obtained by deconvolution operation in the decoder.

The U-net model in this paper is displayed as Figure 5.

The proposed entire U-net network consists of twenty-eight convolution layers. In here, twenty-four convolution layers are spread over four convolution blocks and four deconvolution blocks. The contraction encoder in deep

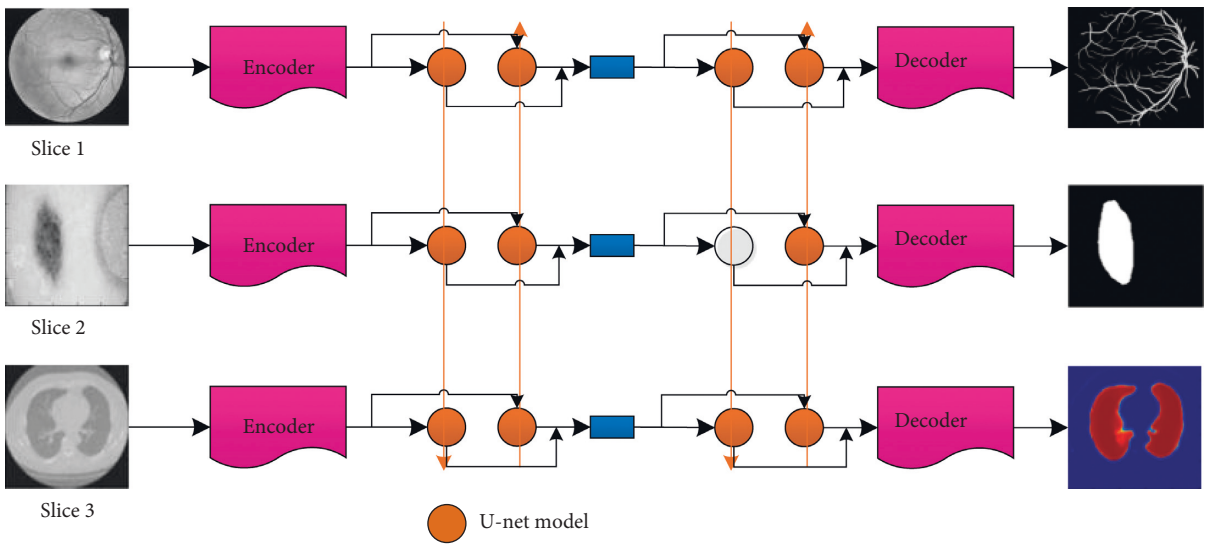

Figure 3: Proposed medical image segment model.

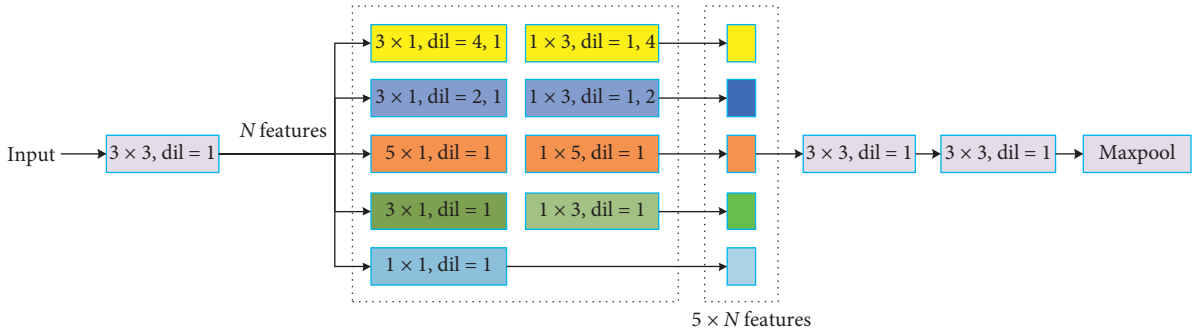

Figure 4: Encoder structure.

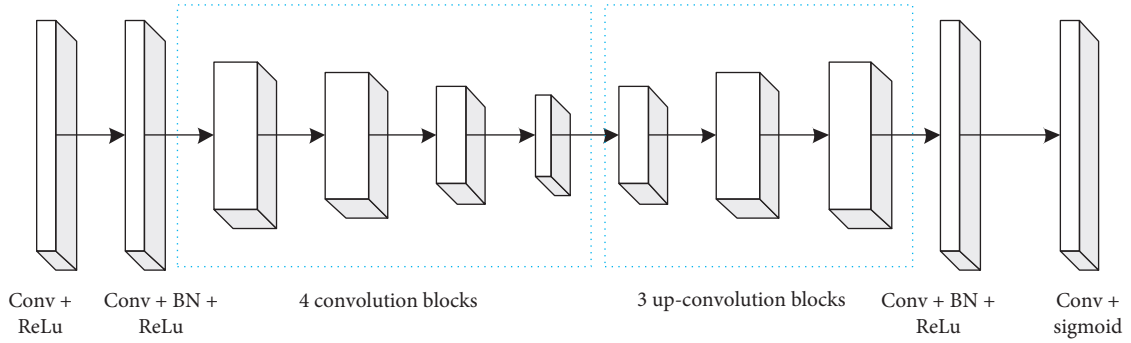

Figure 5: Deep multiscale U-net model.

multiscale U-net covers four convolution blocks shown in left of Figure 4. Each convolutional block contains two convolutional layers (conv). Each convolutional layer utilizes a 3×3 convolutional kernel to carry out the convolution. The step size is 1. Synchronously, each convolutional layer follows a BN layer and a ReLu layer to modify the network performance. ReLu activation function has sparse ability, and it can better learn the relatively sparse features from the effective data dimension and play the role of feature automatic decoupling. In each convolution block, its first convolution layer can double feature graphs. The number of feature graphs will be increased to 64. After four convolution layers, the number of feature graphs is increased from 64 to 1024. Between each convolution block, the sampling method of traditional U-net adopts maximum pooling. In this paper, we use the 2×2 convolution kernel with step length 2 for down-conv operation to achieve a convolution block feature on the image of the sampling operation. Through this down-

conv operation, the size of feature graph is reduced by half with iterative deepening, so that the size of input original image is decreased from 128×128 layer by layer to 8×8.

The expansion decoder of the U-net model contains three deconvolution blocks as shown in the right of Figure 6. The deconvolution up-conv operation adopts the 3×3 convolution kernel. The step size is 2, and the size of the feature graph is increased by twice the original size through the deconvolution operation. This process can recover the feature graph as the raw input image in the last deconvolution block. Meanwhile, the number of feature graphs is halved after each deconvolution operation. The feature graphs obtained by deconvolution are cascaded with the corresponding feature graphs in the convolution block as the feature input of the deconvolution block. Two convolution layers are in each deconvolution block. The 3×3 convolution kernel is utilized (the step size is 1). The first convolution layer will reduce the number of feature graphs by half after every cascading. Not exactly the same as the original U-net structure, the presented U-net structure is filled with zero filler in each convolution layer. According to formula (1), the output size of the deep multiscale CNN model can be guaranteed to be consistent with the input image data size by using zero padding:

$$I_{\text{output}} = \frac{\left(I_{\text{input}} - F + 2P\right)}{S + 1}, \tag{1}$$

where I_{input} and I_{output} are on behalf of the input and output images' size in DMCNN, respectively. F represents the convolution kernel with size 3×3. P denotes the fill size with 1×1. $S = 1$ stands for step size in this paper.

At the end of the proposed U-net model in this paper, we skillfully adopt a convolution layer (whose size is 1×1) to lessen the number of feature graphs to 1. The final output will be disposed by the Sigmoid function. We can obtain the value of each pixel between 0 and 1. The lesion area is a probability distribution. Through the above processing, the final image is considered as the probability graph of DMCNN. The value corresponding to each pixel indicates the probability that the point belongs to the lesion.

3.3.3. Decoding Part. It is mainly responsible for upsampling the feature graph after extracting each group feature, and the structure is shown in Figure 7. The decoder section contains one deconvolution layer and one convolution layer. Both deconvolution and convolution have batch-normalization and ReLu. After the upsampling, the feature graph becomes the same resolution as the input image. Finally, the final segmentation result is obtained by softmax classifier to analyze the end-to-end segmentation.

3.4. Loss Function. Different from the commonly used pixel point-based softmax loss function [26, 27], Dice loss function is based on region loss function. In medical image segmentation, Dice index is often used to measure the overlap rate between the object and the detection area. If the Dice value is larger, then the overlap degree is higher, and the segmentation effect is better. However, Dice index cannot be directly used as a loss function, so we use the improved Dice function. Dice function is a function that gives feedback to network parameters after independent evaluation for each area [28]. The calculation form and process of Dice function are in good agreement with medical image segmentation. Therefore, Dice loss function used in this paper is defined as follows:

$$\text{Dice}(g, p) = 1 - \frac{2\sum_i^v p_i g_i}{\sum_i^v \left(p_i^2 + g_i^2\right)}, \tag{2}$$

where g stands for the ground truth. p is the predicted value. v is the number of pixels in each image block. Dice always is used as a loss function, when comparing the probability graph with the labeled. The background part whose labeled value is 0 will not be calculated into the loss to avoid the situation of unbalanced category and accelerate the convergence of the network and improve the segmentation accuracy.

4. Results and Discussion

4.1. Dataset and Evaluation Index. The dataset is from ADNI (Alzheimer's Disease Neuroimaging Initiative: adni.loni.usc.edu) [29, 30]. In this advanced researches, 100 groups of brain MRI images and segmented hippocampal tags are obtained from ADNI library. From this group, 80 groups are randomly selected for cross-validation, and the remaining 20 groups are for testing.

To improve the segmentation veracity, this study preprocesses the data with three steps. First, consider that the hippocampus only accounts for a small part of the whole brain MRI image and other parts are invalid areas. The pixel values in brain MRI are statistically analyzed, and the images are cropped into $80 \times 80 \times 40$ including the hippocampus and the blank area around it. In this way, invalid background information can be reduced without any influence on the integrity of valid information. Second, to accelerate the convergence of the network and consider the inconsistency of the pixel values of MRI images in ADNI, the mean and SD methods are utilized to normalize the images. Thirdly, making allowances for the small number of samples in the dataset, we enhance the obtained MRI images by left rotation and right rotation and finally obtain 400 MRI images.

To accurately reflect the performance differences between algorithms, we use uniform platform. The hardware environment of the experiment is NVIDIA GTX1060Ti, Intel Corei7 processor, and the software environment was Keras2.2.4. In the experiment, glorot normal distribution method is used to initialize the weight. The image size is 300×300 pixel used in this section. Execution environment is GPU and Geforce GTX 1060. The parameters used in DMCNN are given in Table 1.

To quantitatively evaluate the performance of the new approach, dice similarity coefficient (DSC), sensitivity (SEN), and predictive positivity value (PPV) are selected as the evaluation indexes for the medical image segmentation result. They are defined as follows:

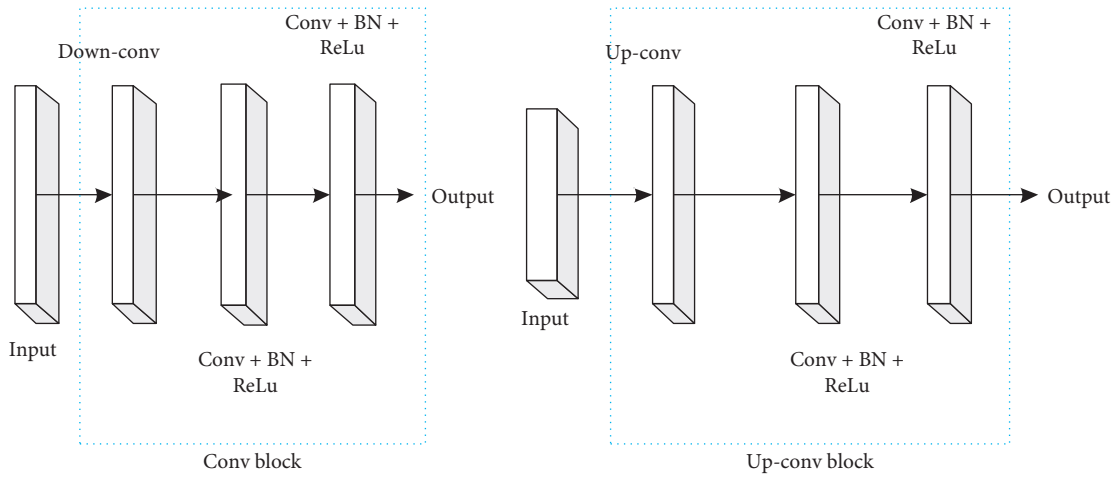

Figure 6: Convolution block and Up-convolution block structure.

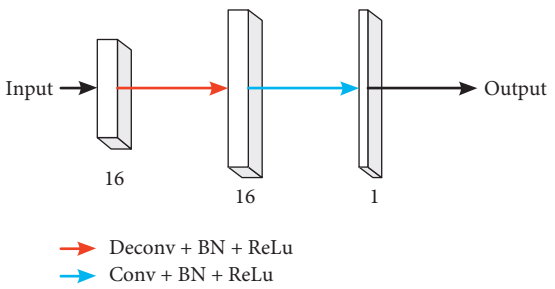

Figure 7: Decoder structure.

Table 1: Parameters in this experiment.

Learning rate	0.001
Batch size	8
L2 regularization	0.0001

Table 2: *Hippocampus* segment results with DMCNN.

Images	DSC	SEN	PPV
100	88.37	89.65	89.54
400	**90.58**	**91.92**	**92.73**

$$\mathrm{DSC} = 2\frac{P \cap T}{P + T},$$
$$\mathrm{SEN} = \frac{P \cap T}{T}, \quad (3)$$
$$\mathrm{PPV} = \frac{P \cap T}{P},$$

where P denotes the lesion region segmented by the presented algorithm. T expresses the region of Ground truth. $P \cap T$ represents the pixel region of the intersection between the algorithm's segmentation region and the true segmentation region.

Table 3: *Hippocampus* segment results with DMCNN and single-scale CNN.

Method	DSC	SEN	PPV
Single-scale CNN	86.54	86.95	87.31
Multiscale CNN	**91.26**	**90.89**	**91.57**

Table 4: *Hippocampus* segment results with different U-net models.

Method	DSC	SEN	PPV
U-net	89.26	88.73	89.45
2D U-net	89.65	89.21	90.14
Proposed	**91.23**	**90.87**	**91.58**

Table 5: *Hippocampus* segment results with different methods.

Method	DSC	SEN	PPV	Time
TLWK	84.62	83.17	86.54	11.5 s
MNF	87.13	86.45	87.53	11.8 s
SUSAN	88.62	88.92	89.85	10.2 s
DMCNN	**92.54**	**91.87**	**92.08**	**8.5 s**

4.2. Comparative Analysis of Segmentation. In this paper, 100 images before augmentation and 400 images after augmentation are segmented by the proposed method. The evaluation indexes in above section are used for evaluation. The comparison results of DSC, SEN, and PPV are given in Table 2.

From Table 2, it reveals that data augmentation can greatly improve the segmentation accuracy. This also fully proves the importance of datasets in the deep learning model construction process. The size of the datasets can directly affect the learning capability of the model.

To verify that DMCNN can effectively capture information between slices, we conduct the comparison between multiscale convolutional neural network and single-scale CNN in this paper. Other conditions remain unchanged.

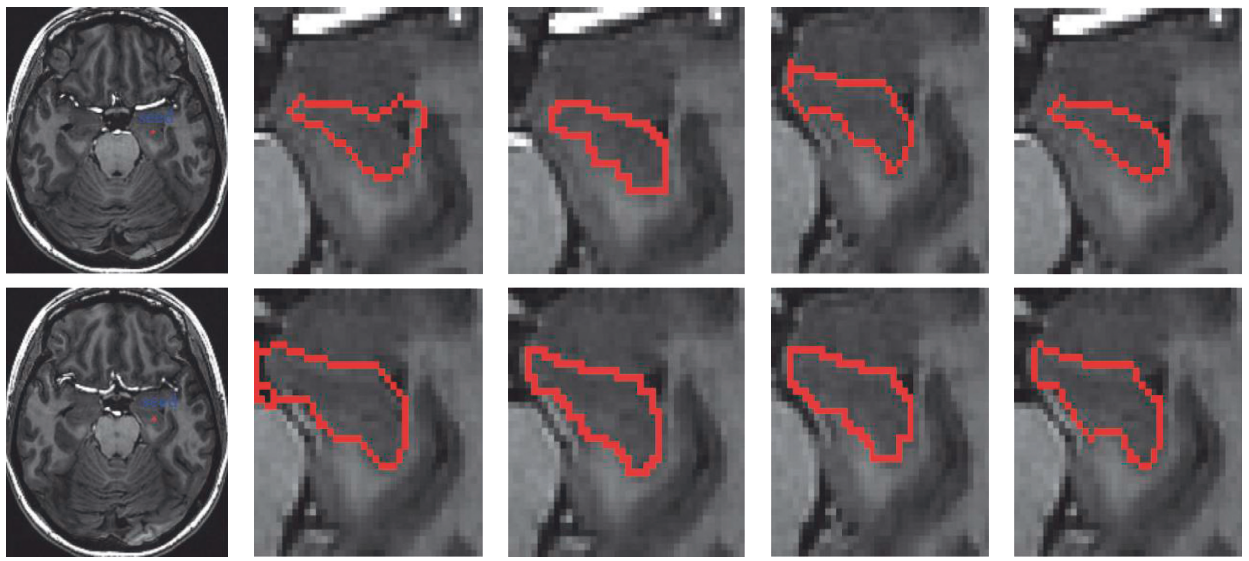

Figure 8: Segmentation of hippocampus with different algorithms. (a) Original images of hippocampus with initial seed points (blue). Results of the (b) TLWK model; (c) MNF method; (d) SUSAN method; (e) DMCNN method.

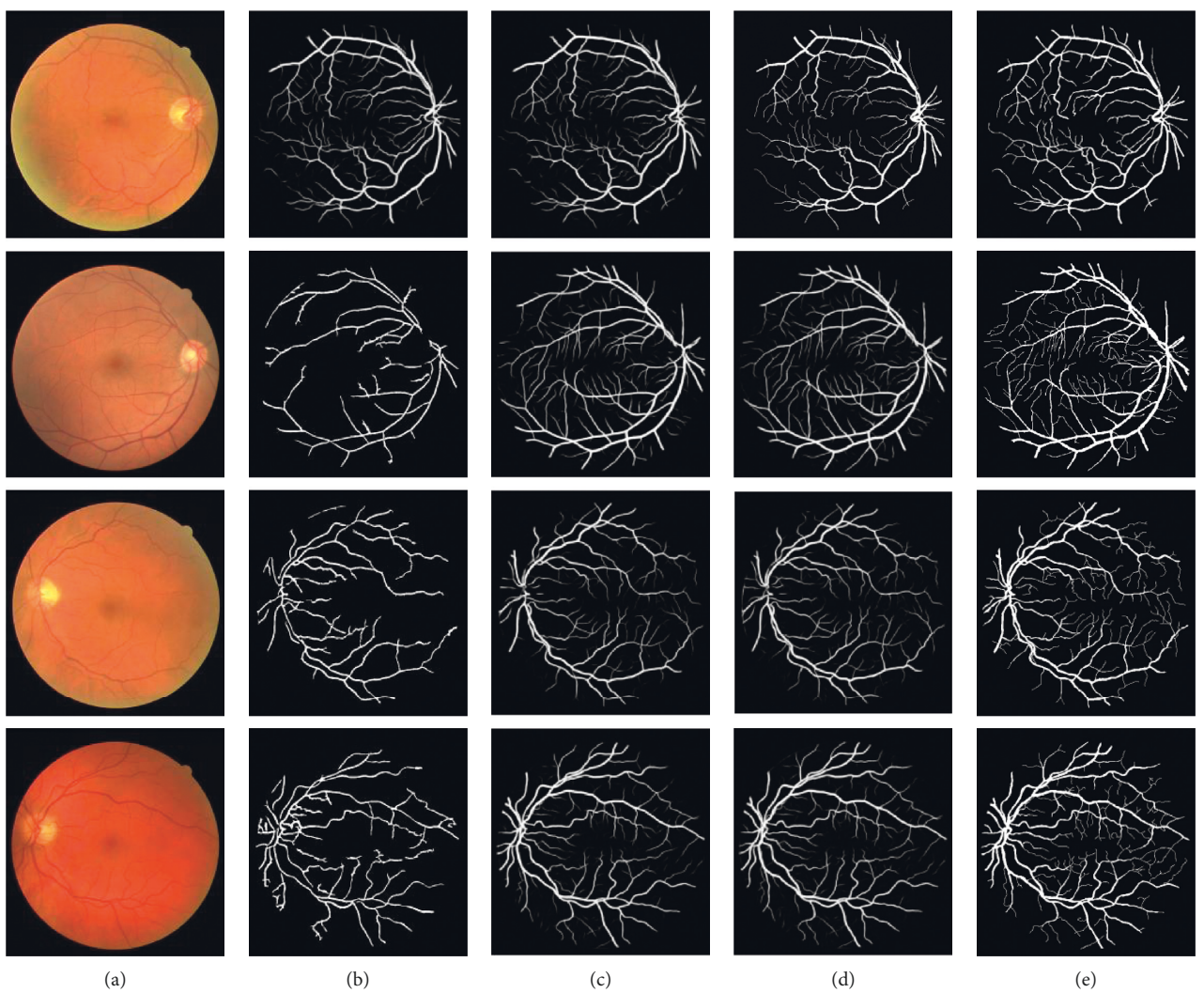

Figure 9: Segmentation results: (a) original image; (b) TLWK method; (c) MNF method; (d) SUSAN method; (e) DMCNN method.

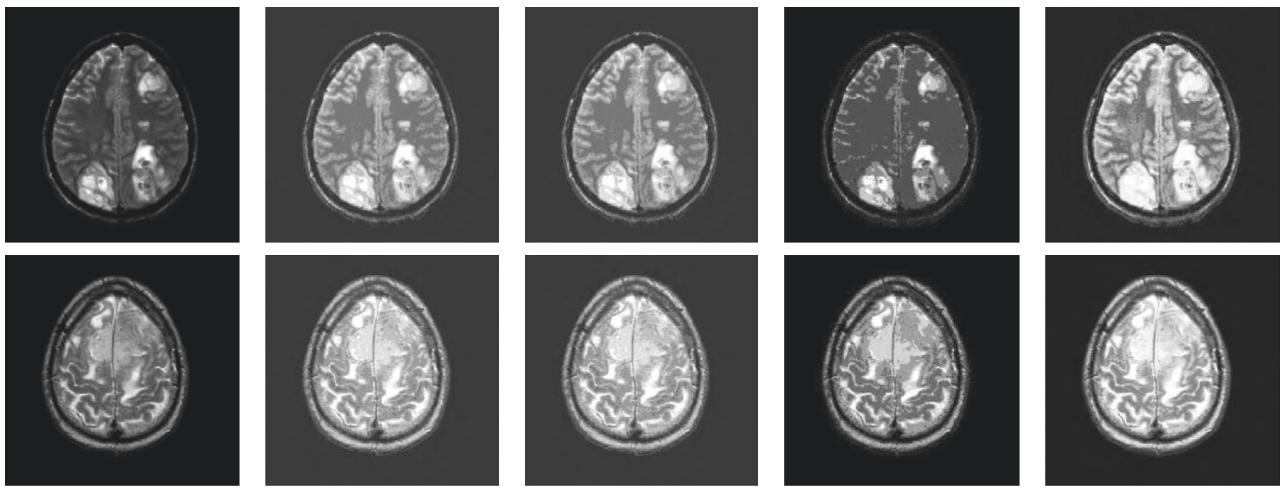

(a) (b) (c) (d) (e)

Figure 10: Segmentation results: (a) original image; (b) TLWK method; (c) MNF method; (d) SUSAN method; (e) DMCNN method. The first row is sarcoma, and the second is meningioma.

Table 6: IoU results with different methods.

Method	*Hippocampus*	Retina	Sarcoma	Meningioma
TLWK	72.48	81.73	75.48	73.69
MNF	78.31	84.56	79.35	78.24
SUSAN	82.37	88.57	82.54	81.53
DMCNN	**89.62**	**90.24**	**89.66**	**88.74**

The effectiveness of the proposed model can be observed from Table 3.

We can see that the segmentation accuracy of DMCNN is significantly higher than that of single-scale CNN, which further verifies that DMCNN can better learn more feature information between slice sequences than single-scale CNN.

Meanwhile, we study the effect of different network models on experiment results. Two representative segmentation methods including U-net and 2D U-net network model are compared with our deep multiscale U-net given in Table 4. The segmentation accuracy obtained by the DMCNN method is higher than that of the other two methods, indicating that it can extract features more efficiently and improve the segmentation accuracy.

Compared with the multiple groups of up- and downsampling layers in U-net and 2D U-net networks, the proposed network model only contains one up- and downsampling layer, which greatly reduces the size of the parameters. The number of parameters of the encoding part and decoding part is below 5000, which significantly reduces the computation time in this article.

We also conduct comparison experiment with state-of-the-art segment methods including TLWK [31], MNF [32], and SUSAN [33] on our medical data. The results are given in Table 5.

TLWK adopted the traditional random forest regression method, and MNF adopted the multiscale method. They are all automatic segmentation methods, due to the large gap between different individuals, and the accuracy and efficiency of segmentation are often not ideal, which is not as high as the precision of the automatic segmentation method in this paper. SUSAN simply improves 2D U-net, so the results are not very good. In general, the proposed method combining convolution neural network and multiscale U-net model is superior to other current methods for medical image segmentation. And, the time consumption is shorter than other methods too.

Figures 8–10 are the segmentation comparison results in terms of hippocampus, retinal blood vessel, sarcoma, and meningioma.

Given the segmented image, the IoU measure gives the similarity between the predicted region and the ground truth region for an object and is defined by following equation:

$$\text{IoU} = \frac{\text{TP}}{\text{FP} + \text{TP} + \text{FN}}, \tag{4}$$

where TP, FP, and FN denote the true positive, false positive, and false negative counts, respectively. The results are given in Table 6. We can see that the proposed segment method has the better result.

5. Conclusions

This paper proposes a medical image segmentation method based on multiscale convolutional neural network. This method can realize automatic segmentation of medical images and has high accuracy of segmentation. The CNN model in this paper not only reduces the amount of computation but also effectively captures multiscale information. In addition, the use of U-net fully mines the relevant information between slice sequences. Taking relevant medical image segmentation as an example, the experimental results on ADNI database show that the segmentation method in this paper is superior to other methods. The proposed method can perform segmentation tasks more easily and accurately. In the future, studying on deeply deep learning methods to segment images and applying them into different

types of images and different practical engineering are warranted.

Data Availability

The data used to support the findings of this study are available from the corresponding author upon request.

Conflicts of Interest

The authors declare that there are no conflicts of interest regarding the publication of this paper.

References

[1] S. Yin and B. Jing, "Medical image annotation based on deep transfer learning," *Journal of Applied Science and Engineering*, vol. 22, no. 2, pp. 385–390, 2019.

[2] L. Zhao, Z. Chen, Y. Yang, L. Zou, and Z. J. Wang, "ICFS clustering with multiple representatives for large data," *IEEE Transactions on Neural Networks and Learning Systems*, vol. 30, no. 3, pp. 728–738, 2019.

[3] L. Peng, Z. Chen, L. T. Yang, Q. Zhang, and J. Deen, "Deep convolutional computation model for feature learning on big data in Internet of Things," *IEEE Transactions on Industrial Informatics*, vol. 14, no. 2, pp. 790–798, 2018.

[4] Q. Zhang, C. Bai, L. T. Yang, Z. Chen, P. Li, and H. Yu, "A unified smart Chinese medicine framework for healthcare and medical services," *IEEE/ACM Transactions on Computational Biology and Bioinformatics*, vol. 129, pp. 1–8, 2019.

[5] S. M. Mousavi, A. Naghsh, A. A. Manaf, and S. A. R. Abu-Bakar, "A robust medical image watermarking against salt and pepper noise for brain MRI images," *Multimedia Tools and Applications*, vol. 76, no. 7, pp. 10313–10342, 2017.

[6] S. Kurtek, J. Su, C. Grimm, M. Vaughan, R. Sowell, and A. Srivastava, "Statistical analysis of manual segmentations of structures in medical images," *Computer Vision and Image Understanding*, vol. 117, no. 9, pp. 1036–1050, 2013.

[7] L. Zhao, Z. Chen, L. T. Yang, M. Jamal Deen, and Z. Jane Wang, "Deep semantic mapping for heterogeneous multimedia transfer learning using co-occurrence data," *ACM Transactions on Multimedia Computing, Communications, and Applications*, vol. 15, no. 1, pp. 9–21, 2019.

[8] X. Chen, J. Yao, Z. Ying, and U. Bagci, "3D automatic anatomy segmentation based on graph cut-oriented active appearance models," in *Proceedings of the IEEE International Conference on Image Processing*, Hong Kong, China, September 2010.

[9] Q. Zhang, C. Bai, Z. Chen et al., "Deep learning models for diagnosing spleen and stomach diseases in smart Chinese medicine with cloud computing," *Concurrency and Computation: Practice and Experience*, p. e5252, 2019.

[10] K. Y. Lim and R. Mandava, "A multi-phase semi-automatic approach for multisequence brain tumor image segmentation," *Expert Systems with Applications*, vol. 112, no. 1, pp. 288–300, 2018.

[11] M. Nielsen, K. Petersen, M. Nielsen, and M. Lillholm, "A unifying framework for automatic and semi-automatic segmentation of vertebrae from radiographs using sample-driven active shape models," *Machine Vision & Applications*, vol. 24, no. 7, pp. 1421–1434, 2013.

[12] L. Zhao, Z. Chen, Y. Yang, Z. Jane Wang, and V. C. M. Leung, "Incomplete multi-view clustering via deep semantic mapping," *Neurocomputing*, vol. 275, pp. 1053–1062, 2018.

[13] M. G. Roberts, E. M. B. Pacheco, R. Mohankumar, T. F. Cootes, and J. E. Adams, "Detection of vertebral fractures in DXA VFA images using statistical models of appearance and a semi-automatic segmentation," *Osteoporosis International*, vol. 21, no. 12, pp. 2037–2046, 2010.

[14] G. Wang, W. Li, M. A. Zuluaga et al., "Interactive medical image segmentation using deep learning with image-specific fine tuning," *IEEE Transactions on Medical Imaging*, vol. 37, no. 7, pp. 1562–1573, 2018.

[15] J. Gao, P. Li, and Z. Chen, "A canonical polyadic deep convolutional computation model for big data feature learning in Internet of Things," *Future Generation Computer Systems*, vol. 99, pp. 508–516, 2019.

[16] K. H. Cha, L. Hadjiiski, R. K. Samala, H.-P. Chan, E. M. Caoili, and R. H. Cohan, "Urinary bladder segmentation in CT urography using deep-learning convolutional neural network and level sets," *Medical Physics*, vol. 43, no. 4, pp. 1882–1896, 2016.

[17] H. Lu, H. Wang, Q. Zhang, D. Won, and S. W. Yoon, "A dual-tree complex wavelet transform based convolutional neural network for human thyroid medical image segmentation," in *Proceedings of the IEEE International Conference on Healthcare Informatics*, vol. 1, pp. 191–198, New York, NY, USA, June 2018.

[18] W. Zhang, R. Li, H. Deng et al., "Deep convolutional neural networks for multi-modality isointense infant brain image segmentation," *NeuroImage*, vol. 108, pp. 214–224, 2015.

[19] L. Zhao, Z. Chen, and Z. J. Wang, "Unsupervised multiview nonnegative correlated feature learning for data clustering," *IEEE Signal Processing Letters*, vol. 25, no. 1, pp. 60–64, 2018.

[20] P. Moeskops, M. A. Viergever, A. M. Mendrik, L. S. de Vries, M. J. N. L. Benders, and I. Isgum, "Automatic segmentation of MR brain images with a convolutional neural network," *IEEE Transactions on Medical Imaging*, vol. 35, no. 5, pp. 1252–1261, 2016.

[21] C. Szegedy, V. Vanhoucke, S. Ioffe, J. Shlens, and Z. Wojna, "Rethinking the inception architecture for computer vision," in *Proceedings of the IEEE 2016 IEEE Conference on Computer Vision and Pattern Recognition (CVPR)*, pp. 2818–2826, Las Vegas, NV, USA, June 2016.

[22] S. Ioffe and C. Szegedy, "Batch normalization: accelerating deep network training by reducing internal covariate shift," in *Proceedings of the 32nd International Conference on International Conference on Machine Learning ICML'15*, vol. 37, pp. 448–456, Lille, France, July 2015.

[23] P. Li, Z. Chen, L. T. Yang, J. Gao, Q. Zhang, and M. J. Deen, "An incremental deep convolutional computation model for feature learning on industrial big data," *IEEE Transactions on Industrial Informatics*, vol. 15, no. 3, pp. 1341–1349, 2019.

[24] C. Liu, Z. Xiao, and N. Du, "Application of improved convolutional neural network in medical image segmentation," *Journal of Frontiers of Computer Science and Technology*, vol. 13, no. 9, pp. 1593–1603, 2019.

[25] P. Pan, Y. Wang, Y. Luo, and J. Zhou, "Automatic segmentation of nasopharyngeal neoplas in MR image based on U-net model," *Journal of Computer Applications*, vol. 39, no. 4, pp. 1183–1188, 2019.

[26] B. Gaonkar, D. Hovda, N. Martin, and L. Macyszyn, "Deep learning in the small sample size setting: cascaded feed forward neural networks for medical image segmentation," *Medical Imaging: Computer-Aided Diagnosis*, vol. 9785, 2016.

[27] J. Gao, J. Li, and Y. Li, "Approximate event detection over multi-modal sensing data," *Journal of Combinatorial Optimization*, vol. 32, no. 4, pp. 1002–1016, 2016.

[28] P. Li, Z. Chen, L. T. Yang, J. Gao, Q. Zhang, and M. J. Deen, "An improved stacked auto-encoder for network traffic flow classification," *IEEE Network*, vol. 32, no. 6, pp. 22–27, 2018.

[29] R. C. Jack, M. A. Bernstein, N. C. Fox et al., "The Alzheimer's disease neuroimaging initiative (ADNI): MRI methods," *Journal of Magnetic Resonance Imaging*, vol. 27, no. 4, pp. 685–691, 2010.

[30] D. Lu, K. Popuri, G. W. Ding, R. Balachandar, and M. F. Beg, "Multimodal and multiscale deep neural networks for the early diagnosis of Alzheimer's disease using structural MR and FDG-PET images," *Scientific Reports*, vol. 8, no. 1, p. 5697, 2018.

[31] A. V. Opbroek, H. C. Achterberg, M. W. Vernooij, and M. De Bruijne, "Transfer learning for image segmentation by combining image weighting and kernel learning," *IEEE Transactions on Medical Imaging*, vol. 38, no. 1, pp. 213–224, 2019.

[32] F. Liu, "SUSAN: segment unannotated image structure using adversarial network," *Magnetic Resonance in Medicine*, vol. 81, no. 5, pp. 3330–3345, 2019.

[33] Y. Wu, Y. Xia, Y. Song, Y. Zhang, and W. Cai, "Multiscale network followed network model for retinal vessel segmentation," in *Medical Image Computing and Computer Assisted Intervention-MICCAI*, pp. 119–126, Springer, Cham, Switzerland, 2018.

Hindawi
Journal of Healthcare Engineering
Volume 2019, Article ID 6320651, 10 pages
https://doi.org/10.1155/2019/6320651

Research Article

An Effective LSTM Recurrent Network to Detect Arrhythmia on Imbalanced ECG Dataset

Junli Gao,[1] **Hongpo Zhang**,[1,2] **Peng Lu**,[3] **and Zongmin Wang**[1]

[1]*Cooperative Innovation Center of Internet Healthcare, Zhengzhou University, Zhengzhou 450000, China*
[2]*State Key Laboratory of Mathematical Engineering and Advanced Computing, Zhengzhou 450001, China*
[3]*Department of Automation, School of Electrical Engineering, Zhengzhou University, Zhengzhou 450001, China*

Correspondence should be addressed to Zongmin Wang; zmwang@zzu.edu.cn

Received 19 April 2019; Revised 4 June 2019; Accepted 19 June 2019; Published 13 October 2019

Guest Editor: Liang Zou

To reduce the high mortality rate from cardiovascular disease (CVD), the electrocardiogram (ECG) beat plays a significant role in computer-aided arrhythmia diagnosis systems. However, the complex variations and imbalance of ECG beats make this a challenging issue. Since ECG beat data exist in heavily imbalanced category, an effective long short-term memory (LSTM) recurrence network model with focal loss (FL) is proposed. For this purpose, the LSTM network can disentangle the timing features in complex ECG signals, while the FL is used to resolve the category imbalance by downweighting easily identified normal ECG examples. The advantages of the proposed network have been verified in the MIT-BIH arrhythmia database. Experimental results show that the LSTM network with FL achieved a reliable solution to the problem of imbalanced datasets in ECG beat classification and was not sensitive to quality of ECG signals. The proposed method can be deployed in telemedicine scenarios to assist cardiologists into more accurately and objectively diagnosing ECG signals.

1. Introduction

Cardiovascular diseases (CVDs) are the leading cause of death worldwide [1]. According to the World Health Organization, about 17.9 million people died of CVD in 2016, accounting for 31% of all deaths. Arrhythmia is caused by improper intracardiac conduction or pulse formation, which can affect heart shape or disrupt the heart rate [2]. An electrocardiogram (ECG) is a comprehensive manifestation of the electrical signal activity of the human heart. Obtaining the detailed physiological state of various parts of the heart by collecting signals is an indispensable means of clinical objective diagnosis. Automated analysis and diagnosis based on ECG data have a reliable clinical diagnostic reference value for arrhythmia [3].

Many methods for automatic classification of ECGs have been proposed. The type of ECG beat can be distinguished by the time-domain [4], wavelet transform [5], genetic algorithm [6], support vector machine (SVM) [7], Bayesian [8], or other methods. Although the above classification methods achieve high accuracy on experimental datasets, their performance is highly dependent on the extraction characteristics of fixed or manual design methods. Manually designing extracted features may increase computational complexity throughout the process, especially in the transform domain.

Deep learning constitutes the mainstream of machine learning and pattern recognition. It provides a structure in which feature extraction and classification are performed together [9]. Deep learning has been widely used in many fields, such as image classification [10], target detection [11], and disease prediction [12]. It is also effectively used to analyze bioinformatics signals [13–17]. Acharya et al. [13] proposed a nine-layer convolutional neural network (CNN) to automatically identify five ECG beat types. Yildirim et al. [15] designed an end-to-end 1D-convolutional neural network (1D-CNN) model for arrhythmia detection. Hannun et al. [16] developed a deep neural network (DNN) to detect 12 rhythm ECG classes. Oh et al. [17] used U-Net autoencoder to detect five arrhythmias. The input of CNN

through its unique weight-sharing mechanism is a spatial change, that is, the spatial data with the image as a typical example perform well. However, recurrent neural networks (RNNs) are more appropriate for chronological changes in the appearance of sample sequences.

Long short-term memory (LSTM) network is a special type of RNN that is widely used for time series analysis. It can effectively retain historical information and realize learning of long-term dependence information of text. It has been used in many fields, such as natural language processing [18] and speech recognition [19]. LSTM is also used for the detection of ECG arrhythmias. [20–23]. Yildirim [20] proposed a new model for deep bidirectional LSTM network- (BLSTM-) based wavelet sequences (WS) to classified electrocardiogram (ECG) signals. Oh et al. [22] proposed a combined network model using CNN and LSTM for ECG arrhythmia diagnosis. Hou et al. [23] introduced a new algorithm based on deep learning that combines LSTM with SVM for ECG arrhythmia classification.

The imbalance of the ECG dataset is an additional challenge to accurately classify ECG beats. There are two problems in the training process: (1) low training efficiency, because normal ECG beats occupying a large proportion of the dataset are prone to negative effects, and (2) degeneration of the model when a normal ECG beat overwhelms training. Some researchers have attempted to address imbalance in the ECG beat data when diagnosing arrhythmia. Sanabila et al. [24] used the generated oversampling method (GenOMe) to solve the problem of imbalanced arrhythmias, which generated new data points with specific distributions (beta, gamma, and Gaussian) as constraints. Rajesh and Dhuli [25] employed three data-level preprocessing techniques on an extracted feature set to balance the distribution of ECG heartbeats. These were random oversampling and undersampling (ROU), synthetic minority oversampling technique with random undersampling (SMOTE + RU), and distribution-based balancing (DBB). As an alternative to resampling the input ECG beat data or feature set, focal loss addresses imbalanced dataset classification by downweighting easy normal ECG beat examples so that their contribution to the loss is small even if their number is large, that is, focal loss concentrates network training on hard ECG beat types, which may constitute a small part of the dataset.

Inspired by the idea of FL to solve the problem of imbalanced category classification and LSTM popularization technology, an effective LSTM with FL is proposed to handle imbalanced ECG beat data on the MIT-BIH arrhythmia database. LSTM automatically extracts the timing characteristics of complex ECG signals, and FL mitigates the problem of ECG class imbalanced distribution faced by the LSTM network, enabling the network to effectively train all categories. The experimental results show that the proposed model achieved state-of-the-art performance on imbalanced ECG beat data and outperformed previous results. Furthermore, we conduct experiments on both denoised and without denoised ECG datasets, and results demonstrate the proposed model is not sensitive to quality of ECG signals.

2. Methodology

Arrhythmia classification using deep learning generally includes two basic stages: preprocessing and classification. In the preprocessing stage, the Daubechies 6 (db6) discrete wavelet transform is used to remove noise from the ECG signal. The ECG heartbeat is then extracted using the sliding window search method, and the data are normalized using Z-score. The LSTM network is proposed for ECG heartbeat classification. The details and theoretical background of these methods are discussed in the following sections.

2.1. Preprocessing. Preprocessing includes denoising and segmentation of ECG signals.

2.1.1. Noise Removal. We denoised the raw data with the Daubechies 6 (db6) discrete wavelet transform [26], and the denoised ECG signals were input to the LSTM network. The original and denoised ECG signals are shown in Figure 1.

2.1.2. ECG Beat Segmentation. We used the sliding window search method on the sample map extraction (see Figure 2). The MIT-BIH arrhythmia database provided annotations for ECG beat class information verified by independent experts. Since R-peak detection algorithms achieved more than 99% specificity and sensitivity [27–29], we used the R-peak annotation file directly. All ECG signals were segmented into sequences that were 250 samples long and centered on the annotated R-peaks. Note that we used an ECG beat with a length of 250 points by default, but there is no common standard for their size.

2.2. Method

2.2.1. Problem Description. To achieve the detection of arrhythmia, the softmax regression model is used as the last layer of the LSTM network structure. For the input training set, $\mathfrak{R} = \{(x^{(1)}, y^{(1)}), \ldots, (x^{(i)}, y^{(i)}), \ldots, (x^{(n)}, y^{(n)})\}$. n is the number of ECG beats containing the class labels. $x^{(i)}$ is an ECG beat. $y^{(i)} \in \{0, 1, 2, 3, 4, 5, 6, 7\}$ is the category label of the $x^{(i)}$. 0, 1, 2, 3, 4, 5, 6, and 7 are the representations of N, LBBB, RBBB, APC, NESC, ABERR, NPC, and AESC, respectively. If $y = 0$, $x^{(i)}$ is a N (normal); otherwise, $x^{(i)}$ is one of the arrhythmia types. For an ECG beat $x^{(i)}$, the output through the LSTM network is $z^{(i)}$, as shown in

$$z^{(i)} = g\left(x^{(i)}; \theta\right), \tag{1}$$

where $g(\cdot)$ is a process function, describing the process of an ECG signal from the input layer to the last full connection layer, and θ is the relevant parameter in the LSTM network.

The last output vector $z^{(i)}$ of full connection layer is ECG signal feature extracted by LSTM network. It is fed to the softmax layer which calculates the probability of each ECG beat category. Equation (2) is the softmax function used in the proposed network:

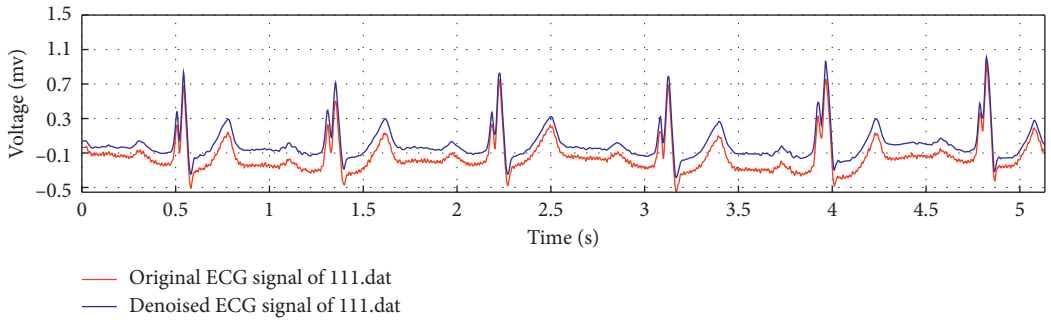

Figure 1: ECG signal denoised by db6 wavelet.

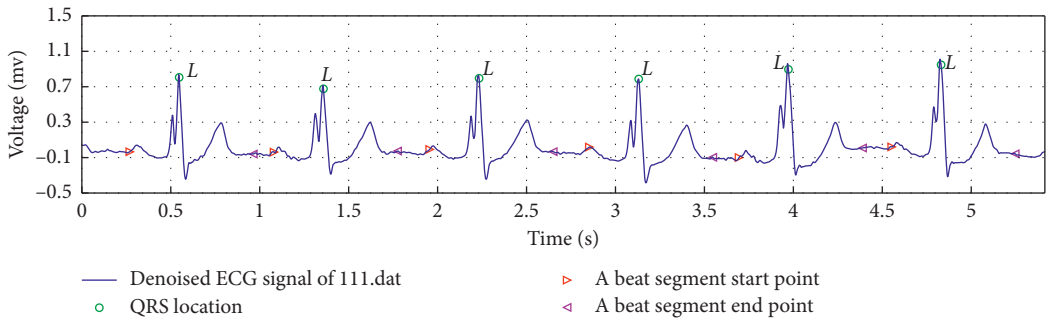

Figure 2: Sliding window search method extracts ECG beats.

$$\hat{y}^{(i)} = \frac{\exp\left(z^{(i)}\right)}{\sum_{j=1}^{C}\exp\left(z^{(j)}\right)}, \tag{2}$$

where C is the number of ECG beat categories. $\hat{y}^{(i)}$ is the class probability that the LSTM gives to the input feature vector $z^{(i)}$.

2.2.2. LSTM Recurrent Network. Long short-term memory (LSTM) is a time-recurrent neural network. It is suitable for time-series prediction of important events, and the delay interval is relatively long [30]. The neural network can effectively retain historical information and realize learning of long-term dependence information of text. The LSTM network consists of an input gate, forget gate, output gate, and cell unit to update and retain historical information. Figure 3 shows an LSTM block.

The forget gate f_t in the LSTM memory block is controlled by a simple single neuron. It determines which information must be retained or discarded to enable the storage of historical information. The input gate i_t is a section where the LSTM block is created by a neuron and previous memory unit effects. It is activated to determine whether to update the historical information to the LSTM block. The candidate update content c_{in} is calculated by a tanh neuron. The current time memory cell state value c_t is calculated from the current candidate cell c_{in}, the previous time state c_{t-1}, the input gate information i_t, and the forget gate information f_t. o_t of the LSTM block at the current time is generated at the output gate. Finally, a_t determines the amount of information about the current cell state that will

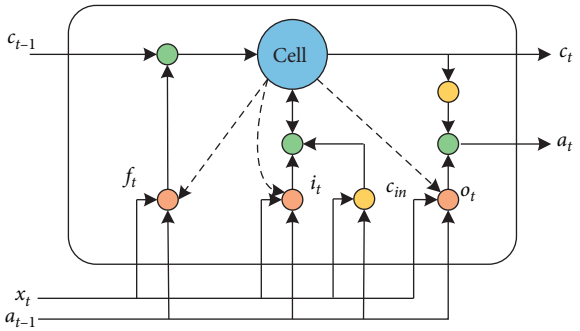

Figure 3: Long short-term memory block.

be output. The activation of each gate and the update of the current cell state can be calculated as follows:

$$\begin{aligned} f_t &= \text{sigmoid}\left(W_f \cdot \left[a_{t-1}, x_t, c_{t-1}\right] + b_f\right), \\ i_t &= \text{sigmoid}\left(W_i \cdot \left[a_{t-1}, x_t, c_{t-1}\right] + b_i\right), \\ c_{\text{in}} &= \tanh\left(W_c \cdot \left[a_{t-1}, x_t, c_{t-1}\right] + b_c\right), \\ c_t &= f_t \cdot c_t + i_t \cdot c_{\text{in}}, \\ o_t &= \text{sigmoid}\left(W_o \cdot \left[a_{t-1}, x_t, c_{t-1}\right] + b_o\right), \\ a_t &= o_t \cdot \tanh\left(c_t\right). \end{aligned} \tag{3}$$

After calculating the hidden vector for each position, we considered the last hidden vector as the ECG signal representation. We fed it to a linear layer with an output length of the classification number and added a softmax output layer to classify the ECG beat as N, LBBB, RBBB, APC, NESC, ABERR, NPC, or AESC.

In this paper, we use the four-layer LSTM architecture including an input layer, an LSTM layer, and two fully connected layers. The structure of the proposed LSTM for imbalanced ECG signal feature extraction and classification tasks is shown in Figure 4.

2.2.3. Focal Loss for Imbalanced ECG Beat Data. Focal loss is a more effective way to deal with the issue of imbalanced datasets. It is obtained by transforming the cross-entropy (CE) loss function. The CE is calculated by

$$\mathrm{CE}(\widehat{y}) = -\log(\widehat{y}). \tag{4}$$

The focal loss [31] is a dynamically scaled CE, where the scaling factor decays to zero as the confidence of the classification increases. Intuitively, this scaling factor can automatically downweight the contribution of normal ECG examples during training, and model training focuses quickly on the hard examples. The FL can be calculated by

$$\mathrm{FL}(\widehat{y}) = -(1-\widehat{y})^{\gamma} \cdot \log(\widehat{y}), \quad \gamma \geq 0, \tag{5}$$

where $(1-\widehat{y})^{\gamma}$ is a modulating factor and γ is a focusing parameter. The purpose of the modulation factor is to reduce the weights of easily categorizable ECG beats so that the model is more focused on ECG beats that are difficult to classify during training. When an ECG beat is misclassified and $\widehat{y}$ is small, the value of the modulation factor is close to 1 and the loss is barely affected. Loss value is calculated using FL according to the block diagram in Figure 5.

Optimization of the network parameters is important. There are many types of gradient descent optimization algorithms, such as Adagrad, Adadelta, Adam, and Nadam. This work uses the Nadam algorithm. This is an effective gradient descent optimization algorithm that combines the Adam and NAG algorithms to calculate adaptive learning rates for different parameters. Overall, Nadam performs better than other gradient descent optimization methods in practical applications [32].

3. Experiment and Results

3.1. Experiment Setup. The LSTM network proposed in this study ran on the deep learning framework Tensorflow 1.12.0 in the Microsoft Windows 10 64 bit operating system. The computer server was configured with an 8-GB Intel (8) Core (TM) i5-7000 processor. Considering the effectiveness of the classification results, we set the epochs to 350. The loss curve and accuracy curve during the training and verification process of the LSTM network using FL ($\gamma = 2$) are shown in Figure 6. By observing the curve of Figure 6, after 350 epochs, the network converged and the overall classification accuracy was stable. The average time required to train the model in one epoch was approximately 191 s. Please note that this epoch setting was only used to easily evaluate the impact of other learning parameters on the network classification results and is not guaranteed to be the best configuration for LSTM network.

3.2. Materials. We used the MIT-BIH arrhythmia database provided by the Massachusetts Institute of Technology [33]. It comes from 47 clinical patients and contains 48 annotated ECG records. Each group is approximately 30 minutes long and is sampled at a rate of 360 Hz by a 0.1–100 Hz band pass filter, for a total of approximately 650,000 sample points.

There are more than 109,000 marker beats from 16 heartbeat categories. All beats are marked by two or more cardiologists. The normal category has the most data volume, and the category with the least data are supraventricular premature beats (only two samples). This study used eight ECG beat types: N, LBBB, RBBB, APC, NESC, ABERR, NPC, and AESC. These beat types and their statistics are listed in Table 1.

From Table 1, it is found that there is a heavy imbalance between normal and abnormal ECG beats. Because of imbalanced ECG beat data, the network model tends to learn the distribution of major ECG beat data, while there is insufficient learning of minority ECG beat data, and we are often concerned with the lesser categories of abnormal ECG beats.

The dataset had a total of 93,371 ECG beats. We used 10% of all ECG data as the testing set. In the remaining ECG data, 90% of the data were used as the training set and 10% as the validation set. The training and validation sets were used to adjust the parameters and determine the optimal number of elements of the designed model. The model performance was evaluated using a testing set that was not previously used.

3.3. Evaluation Metrics. We used five metrics to evaluate the performance of the proposed network: accuracy, recall, precision, specificity, and $F1$ score. Accuracy is the proportion of correctly classified ECG beats of all ECG beats, which reflects the consistency between test results and real results. However, recall, precision, and specificity are less biased in evaluating the performance of the classifier on the imbalanced dataset. The $F1$ score is the harmonic mean of precision and recall. Five evaluation metrics can be calculated as follows:

$$\begin{aligned}
\mathrm{ACC}(\text{accuracy}) &= \frac{\mathrm{TPs} + \mathrm{TNs}}{\mathrm{TPs} + \mathrm{TNs} + \mathrm{FPs} + \mathrm{FNs}},\\
\mathrm{RE}(\text{recall}) &= \frac{\mathrm{TPs}}{\mathrm{TPs} + \mathrm{FNs}},\\
\mathrm{PR}(\text{precision}) &= \frac{\mathrm{TPs}}{\mathrm{TPs} + \mathrm{FPs}},\\
\mathrm{SP}(\text{specificity}) &= \frac{\mathrm{TNs}}{\mathrm{TNs} + \mathrm{FPs}},\\
F1 &= \frac{2 \times \mathrm{RE} \times \mathrm{PR}}{\mathrm{RE} + \mathrm{PR}}.
\end{aligned} \tag{6}$$

The classification categories in this study are not binary, so we use the confusion matrix to express the TP, FP, TN, and FN metrics built for a classification test. The confusion matrix makes it easy to generate the above four metrics.

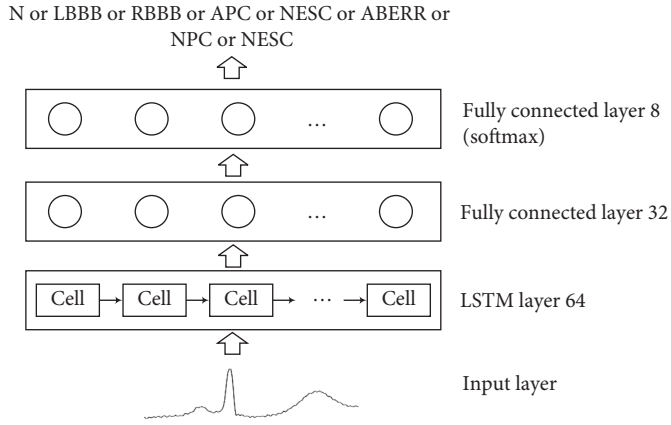

Figure 4: LSTM recurrent network architecture.

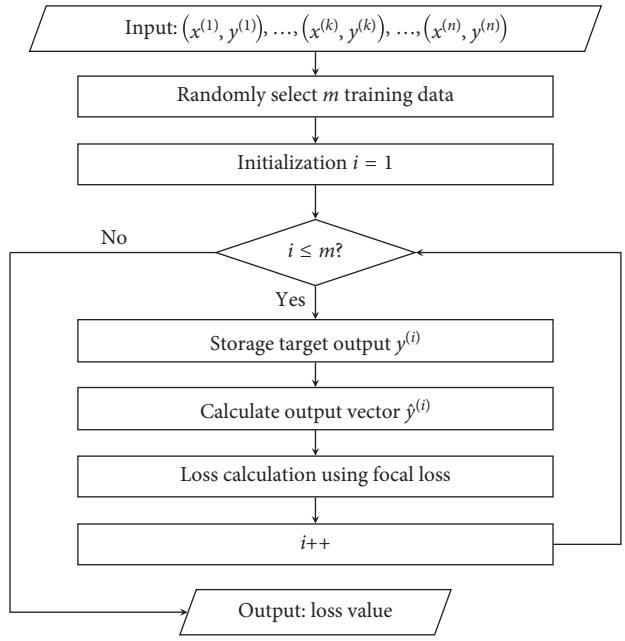

Figure 5: Block diagram to calculate loss value using focal loss.

3.4. Network Parameter Configuration. To obtain the best learning parameters of our proposed LSTM network, we quantitatively analyzed the impact of different learning parameters on the experimental results. The optimal parameter value was determined by evaluating the classification accuracy of the experimental results of multiple cases on the testing set.

After 350 epochs, the LSTM network converged and the classification accuracy was stable. The settings of the LSTM network parameters to obtain the best classification accuracy are shown in Table 2.

In this experiment, we analyzed the impact of various learning parameters on the classification performance of the proposed LSTM network with FL. The primary network parameters included the dropout, batch size, and γ parameter of FL.

We evaluated different dropouts for the proposed network with an increasing dropout proportion. The other learning parameter settings took the default values in Table 2. Table 3 shows the classification accuracy on the testing set with different dropout proportions after 350 epochs.

By comparing the results of Table 3, we can see that the performance of our proposed LSTM network is not improved by increasing the dropout proportion. Therefore, the optimal dropout value of the LSTM network structure is around zero.

Then, we studied the effect on the LSTM network performance of changing the initial settings of the batch size. We evaluated the performance of five different batch sizes, as shown in Table 4.

Based on the results of Table 4, increasing or decreasing the size of the batch does not necessarily improve the performance of our proposed LSTM network. A larger batch size allows for more accurate estimation of the gradient, but it is prone to overfitting. The small batch size has a standardizing effect, but there is a risk of inefficiency, and it is not possible to stop or to not match the strategy early. For the

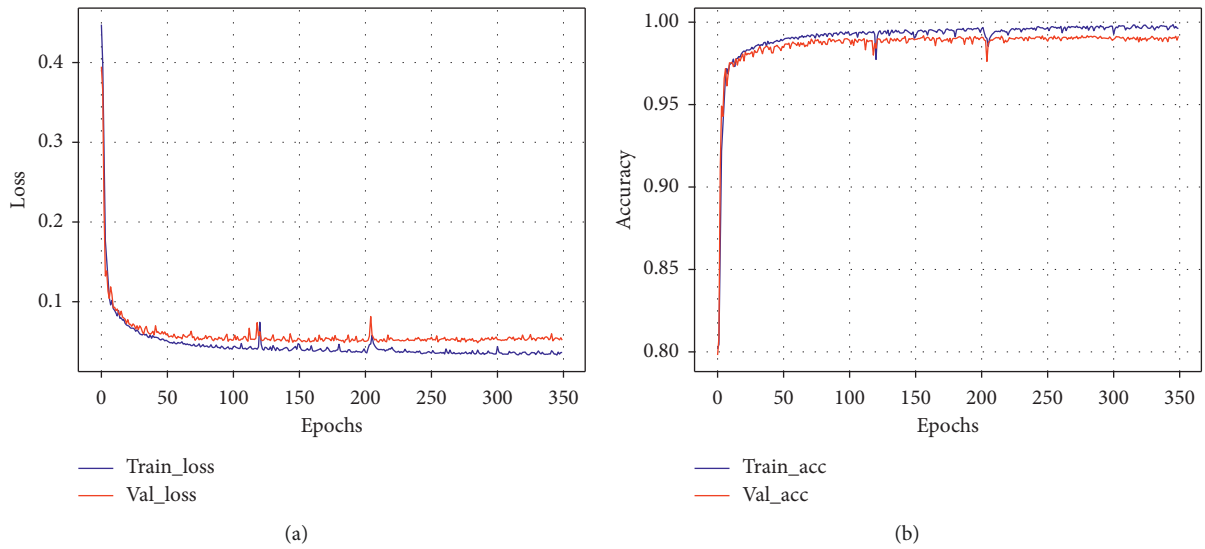

Figure 6: Training of the LSTM with FL ($\gamma = 2$). (a) Loss curve. (b) Accuracy curve.

Table 1: ECG beat types used in this work.

ECG beat types	Annotation	Number of beats
Normal beat	N	75,020
Left bundle branch block	LBBB	8,072
Right bundle branch block	RBBB	7,255
Atrial premature contraction	APC	2,546
Nodal (junctional) escape beat	NESC	229
Aberrated atrial premature beat	ABERR	150
Nodal (junctional) premature beat	NPC	83
Atrial escape beat	AESC	16
Total	—	93,371

Table 2: LSTM network default parameter settings.

LSTM cells	Network layers	Optimizer	Dropout	Epoch	Batch size	Cost function	γ
64	4	Nadam	0	350	128	Focal loss	2

Table 3: Classification accuracy of different dropout proportions.

Dropout	0	0.10	0.15	0.20	0.25	0.30
ACC of testing set (%)	99.26	98.7	99.21	98.46	99.09	99.07

Table 4: Classification accuracy of different batch sizes.

Batch size	32	64	128	256	512
ACC of testing set (%)	81.20	97.87	99.26	99.11	98.72

dataset and network structure used in this paper, the optimal batch size is 128.

The γ parameter is the most critical parameter for FL. The effect of changing γ on the performance of our proposed LSTM network was investigated. The effect on the distribution of the loss for abnormal ECG beats was minor. For normal beats, however, increasing the value of the parameter γ heavily reduced the loss of correctly classified normal beats, allowing the model to focus on the misclassified abnormal ECG beats. After 350 epochs, the classification accuracy associated with the testing dataset was calculated and is given in Table 5 for six γ values. The other learning parameters are the same as in Table 2.

From the results shown in Table 5, we can see that increasing or decreasing γ did not improve the performance of the LSTM network with FL. The best γ parameter value is 2 for the proposed network.

4. Results and Discussion

In this study, we proposed a LSTM network structure to achieve the goal of imbalanced ECG signal classification. The ECG beat data were classified by the LSTM network, and then, we trained the LSTM network using FL. By setting the CE as the benchmark, the feasibility of using the FL to classify the imbalanced ECG beats was proved. We verified the effectiveness of the LSTM network structure by comparing with state-of-the-art methods.

Performance measures of the model were evaluated using a confusion matrix. The cost function of the LSTM

Table 5: Overall accuracy of FL over different γ parameter.

γ parameter	0	0.5	1	2	3	4
ACC of testing set (%)	98.85	99.08	99.03	99.26	99.11	98.82

network uses CE to calculate the confusion matrix on the testing set, as shown in Figure 7(a). The diagonal values in the confusion matrix represent the correct classification of ECG beats. Other LSTM network structure parameters (except γ) are the same as in Table 2. The cost function of the LSTM network uses FL to calculate the confusion matrix on the testing set, as shown in Figure 7(b). Other LSTM network parameters are the same as in Table 2.

By comparing and analyzing the confusion matrix of LSTM network with CE and LSTM network with FL in Figure 7, we can see that the LSTM network with FL performs better on the imbalanced ECG dataset than the LSTM network with CE. When the FL is examined, it appears that the LSTM network provides better recognition performance over most classes. Examining the CE, the LSTM network appears to provide lower recognition performance over most class. Also, for the CE, 41 APC beats are misclassified into *N* beats, while for the FL ($\gamma = 2$), 32 APC beats are misclassified into *N* beats. This is because there is no big difference in the shape of the two beats, but there is a specific, difficult-to-position wave anomaly (e.g., the PR segment is extended). Table 6 shows the PR, RE, SP, and *F*1 of the LSTM network with CE and LSTM network with FL on the testing set.

By comparing the results in Table 6, the validity of the LSTM network with FL is verified on imbalanced ECG data. From this table, it can be observed that the LSTM network with FL ($\gamma = 2$) achieves an ACC of 99.26%, a RE of 99.26%, a PR of 99.30%, a SP of 99.14%, and an F1 score of 99.27%. The LSTM network with CE achieves 98.70% ACC, 98.70% RE, 98.05% PR, a SP of 98.75%, and 98.36% *F*1 score. Although the performance improvement by the LSTM network with FL seems not to be large compared to that of the LSTM network with CE, in a real diagnosis, even a minor accuracy improvement can hold great value for human health and life.

To more intuitively compare the effectiveness of the above two methods (CE and FL), we next analyze the results using the precision-recall curve (PR curve). For the category imbalance problem, the PR curve is considered to be superior to the receiver operating characteristic curve (ROC curve) [34]. As shown in Figure 8, for the input of the imbalanced ECG data, the PR curve of each category is drawn from the classification results using the CE (shown in Figure 8(a)) and the FL (shown in Figure 8(b)), respectively. Compared with the CE, when the LSTM network proposed in this paper uses the FL, most categories obtain a relatively high area under the PR curve (AUC). Therefore, our proposed LSTM network with FL is effective in solving the category imbalance ECG dataset.

To verify the robustness of the proposed LSTM network with FL in a noisy environment, the network is also analyzed without denoised and the results are listed in Table 7. The performance measurements in Table 7 show that the LSTM network with FL ($\gamma = 2$) achieved a classification result close to the result of denoised ECG recordings. It shows the advantages of denoised network and also illustrates the robustness of the network.

The proposed network can be deployed in telemedicine scenarios. The ECG data of heart patients are collected through wearable devices and transmitted to the cloud via the Internet. Data analysis is carried out through the proposed model in this study to assist cardiologists into more accurately and objectively diagnose ECG signals.

The proposed model was primarily studied on the MIT-BIH arrhythmia database. According to the AAMI standards (ANSI/AAMI EC57: 1998), all the beats in the MIT-BIH arrhythmia database are grouped into five main classes. However, this is not always desirable. The type of arrhythmia can be judged by the specific ECG beat and the regularity of the beat type. Repeated APC beats can become dangerous arrhythmias such as atrial fibrillation when a patient has a potential structural heart problem. Bundled branch blocks impede the normal pathway of electrical impulses through the conduction system to the ventricles. This causes asynchronous ventricular contractions and heart function deterioration, which may lead to life-threatening situations.

To assess the performance of the proposed network, we compared it to some state-of-the-art methods in the literature. We record the performance of the proposed network model (in bold) and the recent representative techniques for ECG beat classification using the MIT-BIH arrhythmia database in Table 8.

From Table 8, it is evident that our proposed LSTM network with FL achieved good performance. The difference between our study and other studies in the literature is that we used deep learning to classify category-imbalanced ECG beat data. For the classification of class-imbalanced ECG arrhythmias, we proposed a LSTM network with FL. There are also studies in the literature on the classification of imbalanced ECG data [24, 25]. The main difference is that our study uses FL that modifies the loss function, which makes the LSTM network more focused on feature learning of abnormal ECG beats that are prone to misclassification and improves the accuracy of arrhythmia classification. Regarding the RE, our proposed LSTM network with FL achieved a best result on the testing set. This means that it has a smaller number of false negatives, i.e., abnormal ECG beats which are erroneously classified as normal ECG beats. Furthermore, this method avoids the problem of the effective information reduction caused by the undersampling method or the problem of the network training time increase caused by the oversampling method.

The highlights of our proposed network are as follows:

(i) Feature extraction and selection techniques are not needed

(ii) Our important finding is that the proposed method can improve the classification accuracy rate of categories with arrhythmia

(iii) Our proposed method is robust under without denoised ECG recordings

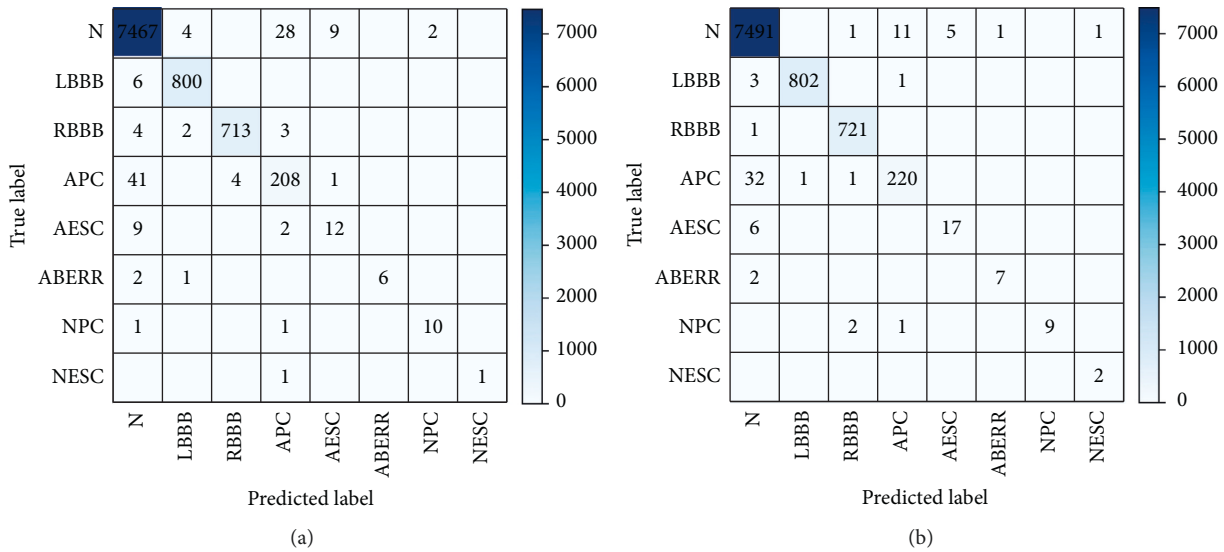

Figure 7: Confusion matrix obtained by the LSTM network using different loss functions on the testing set: (a) CE and (b) FL ($\gamma = 2$).

Table 6: LSTM network classification results on the testing set using two different loss methods.

Cost function	ACC (%)	RE (%)	SP (%)	PR (%)	$F1$ (%)
Cross entropy	98.70	98.70	98.05	98.75	98.36
Focal loss ($\gamma = 2$)	99.26	99.26	99.14	99.30	99.27

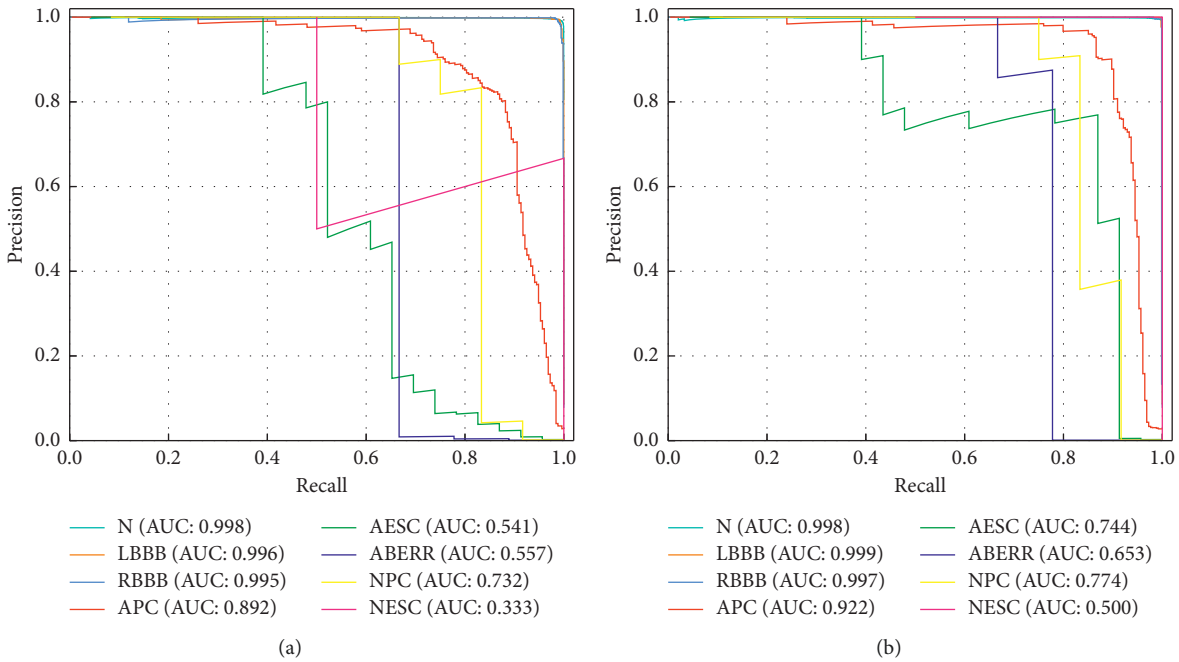

Figure 8: Precision-recall curves for every class. (a) Using CE and (b) using FL ($\gamma = 2$) method.

Table 7: LSTM network with FL ($\gamma = 2$) classification results on the testing set.

	ACC (%)	RE (%)	SP (%)	PR (%)	$F1$ (%)
Denoised	99.26	99.26	99.14	99.30	99.27
Without denoised	99.07	99.07	98.99	99.13	99.09

Table 8: Comparison between the related work and the method proposed in this work.

Works	Year	Classes	Methods	ACC (%)	RE (%)	SP (%)
Martis et al. [35]	2013	5 beat types	DCT + PCA, PNN	99.52	98.69	99.91
Raj et al. [7]	2016	16 beat types	DOST, SVM-PSO	99.18	—	—
Sharma and Ray [36]	2016	6 beat types	EMD, HHT, SVM	99.51	98.64	99.77
Gutiérrez-Gnecchi et al. [37]	2017	8 beat types	PNN	98.89	—	—
Jung and Lee [38]	2017	4 beat types	WKNN	96.12	96.12	99.97
Li et al. [6]	2017	6 beat types	GA-BPNN	97.78	97.86	99.54
Rajesh and Dhuli [25]	2018	5 beat groups	DBB, AdaBoost	99.10	97.90	99.40
W. Li and J. Li [14]	2018	16 beat types	LDP, DNN	98.37	—	—
Yildirim. [20]	2018	5 beat types	DULSTM-WS2	99.25	—	—
Oh et al. [22]	2018	5 beat types	CNN-LSTM	98.10	97.50	98.70
Pławiak and Acharya [39]	2019	17 classes	DGEC	99.37	94.62	99.66
Yildirim et al. [21]	2019	5 beat types	LSTM	99.23	99.00	99.00
Our work	**2019**	**8 beat types**	**LSTM, FL**	**99.26**	**99.26**	**99.14**

DCT: discrete cosine transform; GMM + EM: Gaussian mixture modeling with enhanced expectation maximization; DOST: discrete orthogonal stockwell transform; SVM-PSO: PSO-tuned support vector machine; EMD: empirical mode decomposition; HHT: Hilbert–Huang transform; PNN: probabilistic neural network; WKNN: weighted k-nearest neighbor; NRSC: neighborhood rough set; DWT: discrete wavelet transform; GA-BPNN: genetic algorithm-backpropagation neural network; DNN: deep neural network; DULSTM-WS: deep unidirectional LSTM network-based wavelet sequences; DBLSTM-WS: deep bidirectional LSTM network-based wavelet sequences; LDP: local deep field; DBB: distribution-based balancing; FL: focal loss; DGEC: deep genetic ensemble of classifiers.

The disadvantages of our proposed network are as follows:

(i) This study is conducted only on eight ECG beat types

(ii) The proposed network is the time cost of the training phase

5. Conclusions and Future Work

In this study, we proposed a LSTM network with FL to improve the training effect by inhibiting the impact of a large number of easy normal ECG beat data on model training. The results show that the LSTM network with FL achieved an accuracy, recall, precision, specificity, and $F1$ score of 99.26%, 99.26%, 99.30%, 99.14%, and 99.27%, respectively. Experimental results of the MIT-BIH arrhythmia database demonstrate the effectiveness and robustness of the proposed network. The proposed method can be deployed in telemedicine scenarios to assist cardiologists into more accurately and objectively diagnosing ECG signals.

The study was conducted only on eight ECG beat types. To generalize the results, various types and numerous beats should be incorporated in future research. And, we also plan to add different levels of noise to ECG signals to discuss the performance of the LSTM with the FL model.

Data Availability

The data used to support the findings of this study are included in the article. Further data can be requested from the corresponding author.

Conflicts of Interest

The authors declare that there are no conflicts of interest.

Acknowledgments

This research was partly supported by the Integration of Cloud Computing and Big Integration of Cloud Computing and Big Data, Innovation of Science and Education (grant no. 2017A11017), the CERNET Innovation Project (grant no. NGII20161202), the Key Research, Development, and Dissemination Program of Henan Province (Science and Technology for the People) (grant no. 182207310002), and the Key Science and Technology Project of Xinjiang Production and Construction Corps (grant no. 2018AB017).

References

[1] World Health Organization, *Cardiovascular Diseases (CVDs)*, WHO, Geneva, Switzerland, 2019, https://www.who.int/en/news-room/fact-sheets/detail/cardiovascular-diseases-(cvds).

[2] National Heart, Lung, and Blood Institute, *Arrhythmia*, National Heart, Lung, and Blood Institute, Bethesda, MA, USA, 2019, https://www.nhlbi.nih.gov/health-topics/arrhythmia.

[3] S. Min, B. Lee, and S. Yoon, "Deep learning in bioinformatics," *Briefings in Bioinformatics*, vol. 18, pp. 851–869, 2017.

[4] D. Katircioglu-Öztürk, H. A. Güvenir, U. Ravens, and N. Baykal, "A window-based time series feature extraction method," *Computers in Biology and Medicine*, vol. 89, pp. 466–486, 2017.

[5] Y. Jung and H. Kim, "Detection of PVC by using a wavelet-based statistical ECG monitoring procedure," *Biomedical Signal Processing And Control*, vol. 36, pp. 176–182, 2017.

[6] H. Li, D. Yuan, X. M. Ma, D. Cui, and L. Cao, "Genetic algorithm for the optimization of features and neural networks in ECG signals classification," *Scientific Reports*, vol. 7, no. 1, Article ID 41011, 2017.

[7] S. Raj, K. C. Ray, and O. Shankar, "Cardiac arrhythmia beat classification using DOST and PSO tuned SVM," *Computer Methods and Programs in Biomedicine*, vol. 136, pp. 163–177, 2016.

[8] M. M. Casas, R. L. Avitia, F. F. Gonzalez-Navarro, J. A. Cardenas-Haro, and M. A. Reyna, "Bayesian classification models for premature ventricular contraction detection

on ECG traces," *Journal Of Healthcare Engineering*, vol. 2018, Article ID 2694768, 7 pages, 2018.

[9] Y. Bengio, "Learning deep architectures for AI," *Foundations and Trends® in Machine Learning*, vol. 2, no. 1, pp. 1–127, 2009.

[10] E. Maggiori, Y. Tarabalka, G. Charpiat, and P. Alliez, "Convolutional neural networks for large-scale remote-sensing image classification," *IEEE Transactions on Geoscience and Remote Sensing*, vol. 55, no. 2, pp. 645–657, 2017.

[11] O. Russakovsky, J. Deng, H. Su et al., "ImageNet large scale visual recognition challenge," *International Journal of Computer Vision*, vol. 115, no. 3, pp. 211–252, 2015.

[12] P. Lu, S. Guo, H. Zhang et al., "Research on improved depth belief network-based prediction of cardiovascular diseases," *Journal of Healthcare Engineering*, vol. 2018, Article ID 8954878, 9 pages, 2018.

[13] U. R. Acharya, S. L. Oh, Y. Hagiwara et al., "A deep convolutional neural network model to classify heartbeats," *Computers In Biology And Medicine*, vol. 89, pp. 389–396, 2017.

[14] W. Li and J. Li, "Local deep field for electrocardiogram beat classification," *IEEE Sensors Journal*, vol. 18, no. 4, pp. 1656–1664, 2018.

[15] O. Yıldırım, P. Pławiak, R.-S. Tan, and U. R. Acharya, "Arrhythmia detection using deep convolutional neural network with long duration ECG signals," *Computers in Biology and Medicine*, vol. 102, pp. 411–420, 2018.

[16] A. Y. Hannun, P. Rajpurkar, M. Haghpanahi et al., "Cardiologist-level arrhythmia detection and classification in ambulatory electrocardiograms using a deep neural network," *Nature Medicine*, vol. 25, no. 1, pp. 65–69, 2019.

[17] S. L. Oh, E. Y. K. Ng, R. S. Tan, and U. R. Acharya, "Automated beat-wise arrhythmia diagnosis using modified U-net on extended electrocardiographic recordings with heterogeneous arrhythmia types," *Computers in Biology and Medicine*, vol. 105, pp. 92–101, 2019.

[18] L. Ferrone and F. M. Zanzotto, "Symbolic, distributed and distributional representations for natural language processing in the era of deep learning: a survey," 2017, https://arxiv.org/abs/1702.00764.

[19] A. Graves, A.-R. Mohamed, and G. Hinton, "Speech recognition with deep recurrent neural networks," in *Proceedings of the 2013 IEEE International Conference on Acoustics, Speech and Signal Processing*, pp. 6645–6649, IEEE, Vancouver, Canada, May 2013.

[20] Ö. Yildirim, "A novel wavelet sequence based on deep bidirectional LSTM network model for ECG signal classification," *Computers in Biology and Medicine*, vol. 96, pp. 189–202, 2018.

[21] O. Yildirim, U. B. Baloglu, R.-S. Tan, E. J. Ciaccio, and U. R. Acharya, "A new approach for arrhythmia classification using deep coded features and LSTM networks," *Computer Methods and Programs in Biomedicine*, vol. 176, pp. 121–133, 2019.

[22] S. L. Oh, E. Y. K. Ng, R. S. Tan, and U. R. Acharya, "Automated diagnosis of arrhythmia using combination of CNN and LSTM techniques with variable length heart beats," *Computers in Biology and Medicine*, vol. 102, pp. 278–287, 2018.

[23] B. Hou, J. Yang, P. Wang, and R. Yan, "LSTM based auto-encoder model for ECG arrhythmias classification," *IEEE Transactions on Instrumentation and Measurement*, 2019, In press.

[24] H. R. Sanabila, I. Kusuma, and W. Jatmiko, "Generative oversampling method (GenOMe) for imbalanced data on apnea detection using ECG data," in *Proceedings of the 2016 International Conference on Advanced Computer Science and Information Systems*, pp. 572–577, Malang, Indonesia, October 2016.

[25] K. N. V. P. S. Rajesh and R. Dhuli, "Classification of imbalanced ECG beats using re-sampling techniques and AdaBoost ensemble classifier," *Biomedical Signal Processing and Control*, vol. 41, pp. 242–254, 2018.

[26] B. N. Singh and A. K. Tiwari, "Optimal selection of wavelet basis function applied to ECG signal denoising," *Digital Signal Processing*, vol. 16, no. 3, pp. 275–287, 2006.

[27] E. Arrais Junior, R. A. de Medeiros Valentim, and G. Bezerra Brandao, "Real time QRS detection based on redundant discrete wavelet transform," *IEEE Latin America Transactions*, vol. 14, no. 4, pp. 1662–1668, 2016.

[28] Q. Qin, J. Li, Y. Yue, and C. Liu, "An adaptive and time-efficient ECG R-peak detection algorithm," *Journal of Healthcare Engineering*, vol. 2017, Article ID 5980541, 14 pages, 2017.

[29] F.-M. Melgarejo-Meseguer, E. Everss-Villalba, F.-J. Gimeno-Blanes et al., "On the beat detection performance in long-term ECG monitoring scenarios," *Sensors*, vol. 18, no. 5, p. 1387, 2018.

[30] H. Sak, A. Senior, and F. Beaufays, "Long short-term memory recurrent neural network architectures for large scale acoustic modeling," in *Proceedings of the Fifteenth Annual Conference of the International Speech Communication Association*, pp. 338–342, Singapore, September 2014.

[31] T.-Y. Lin, P. Goyal, R. Girshick, K. He, and P. Dollar, "Focal loss for dense object detection," in *Proceedings of the IEEE Transactions on Pattern Analysis and Machine Intelligence*, pp. 2999–3007, Venice, Italy, 2017.

[32] T. Dozat, "Incorporating Nesterov Momentum into Adam," in *Proceedings of the 2016 International Conference on Learning Representations*, San Juan, Puerto Rico, May 2016.

[33] A. L. Goldberger, L. A. N. Amaral, L. Glass et al., "PhysioBank, PhysioToolkit, and PhysioNet: components of a new research resource for complex physiologic signals," *Circulation*, vol. 101, no. 23, pp. E215–E220, 2000.

[34] J. Davis and M. Goadrich, "The relationship between precision-recall and roc curves," in *Proceedings of the 23rd International Conference on Machine Learning*, pp. 233–240, ACM, Pittsburgh, PA, USA, June 2006.

[35] R. J. Martis, U. R. Acharya, C. M. Lim, and J. S. Suri, "Characterization of ECG beats from cardiac arrhythmia using discrete cosine transform in PCA framework," *Knowledge-Based Systems*, vol. 45, pp. 76–82, 2013.

[36] P. Sharma and K. C. Ray, "Efficient methodology for electrocardiogram beat classification," *IET Signal Processing*, vol. 10, no. 7, pp. 825–832, 2016.

[37] J. A. Gutiérrez-Gnecchi, R. Morfin-Magaña, D. Lorias-Espinoza et al., "DSP-based arrhythmia classification using wavelet transform and probabilistic neural network," *Biomedical Signal Processing and Control*, vol. 32, pp. 44–56, 2017.

[38] W.-H. Jung and S.-G. Lee, "An arrhythmia classification method in utilizing the weighted KNN and the fitness rule," *IRBM*, vol. 38, no. 3, pp. 138–148, 2017.

[39] P. Pławiak and U. R. Acharya, "Novel deep genetic ensemble of classifiers for arrhythmia detection using ecg signals," *Neural Computing and Applications*, pp. 1–25, 2019, In press.

Hindawi
Journal of Healthcare Engineering
Volume 2019, Article ID 5068283, 12 pages
https://doi.org/10.1155/2019/5068283

Research Article

G-Causality Brain Connectivity Differences of Finger Movements between Motor Execution and Motor Imagery

Chao Chen,[1,2] **Jiaxin Zhang**,[1] **Abdelkader Nasreddine Belkacem**,[3] **Shanting Zhang**,[1] **Rui Xu**,[2] **Bin Hao**,[4] **Qiang Gao**,[1] **Duk Shin**,[5] **Changming Wang**,[6,7] **and Dong Ming**[2]

[1]*Key Laboratory of Complex System Control Theory and Application, Tianjin University of Technology, Tianjin 300384, China*
[2]*Academy of Medical Engineering and Translational Medicine, Tianjin University, Tianjin 300072, China*
[3]*Department of Computer and Network Engineering, College of Information Technology, UAE University, P.O. Box 15551, Al Ain, UAE*
[4]*Zhonghuan Information College Tianjin University of Technology, Tianjin 300380, China*
[5]*Department of Electronics and Mechatronics, Tokyo Polytechnic University, Kanagawa 243-0297, Japan*
[6]*Beijing Key Laboratory of Mental Disorders, Beijing Anding Hospital, Capital Medical University, Beijing 100088, China*
[7]*North China University of Science and Technology, Tangshan, Hebei 063000, China*

Correspondence should be addressed to Changming Wang; superwcm@163.com and Dong Ming; richardming@tju.edu.cn

Received 4 July 2019; Accepted 9 September 2019; Published 2 October 2019

Guest Editor: Yu Zhang

Motor imagery is one of the classical paradigms which have been used in brain-computer interface and motor function recovery. Finger movement-based motor execution is a complex biomechanical architecture and a crucial task for establishing most complicated and natural activities in daily life. Some patients may suffer from alternating hemiplegia after brain stroke and lose their ability of motor execution. Fortunately, the ability of motor imagery might be preserved independently and worked as a backdoor for motor function recovery. The efficacy of motor imagery for achieving significant recovery for the motor cortex after brain stroke is still an open question. In this study, we designed a new paradigm to investigate the neural mechanism of thirty finger movements in two scenarios: motor execution and motor imagery. Eleven healthy participants performed or imagined thirty hand gestures twice based on left and right finger movements. The electroencephalogram (EEG) signal for each subject during sixty trials left and right finger motor execution and imagery were recorded during our proposed experimental paradigm. The Granger causality (G-causality) analysis method was employed to analyze the brain connectivity and its strength between contralateral premotor, motor, and sensorimotor areas. Highest numbers for G-causality trials of 37 ± 7.3, 35.5 ± 8.8, 36.3 ± 10.3, and 39.2 ± 9.0 and lowest Granger causality coefficients of 9.1 ± 3.2, 10.9 ± 3.7, 13.2 ± 0.6, and 13.4 ± 0.6 were achieved from the premotor to motor area during execution/imagination tasks of right and left finger movements, respectively. These results provided a new insight into motor execution and motor imagery based on hand gestures, which might be useful to build a new biomarker of finger motor recovery for partially or even completely plegic patients. Furthermore, a significant difference of the G-causality trial number was observed during left finger execution/imagery and right finger imagery, but it was not observed during the right finger execution phase. Significant difference of the G-causality coefficient was observed during left finger execution and imagery, but it was not observed during right finger execution and imagery phases. These results suggested that different MI-based brain motor function recovery strategies should be taken for right-hand and left-hand patients after brain stroke.

1. Introduction

EEG-based brain-computer interfaces (BCIs) have been used for building an advanced communication or control pathway between brain and computer using noninvasive measurements [1, 2]. Several classical BCI paradigms were developed for helping handicapped people to interact with the environment by controlling a smart home, robotic arm,

and a wheelchair using brain activity based on event-related potential (ERP) such as the P300 wave [3, 4] or based on steady-state visually evoked potential (SSVEP) [5] and motor imagery [6, 7].

The mental process during motor execution or motor imagery has been widely used for building BCI systems in several domains [8–10]. This mental process has also showed the potential applications in the rehabilitation field for patients who suffered from brain strokes [11, 12]. These patients who lost some motor functions after brain stroke might be able to reactivate some brain areas such as sensorimotor area [13] by using BCI based on motor imagery as one of the most effective surrogate motor training methods [14]. When patients perform or imagine hand gestures or finger movements during rehabilitation exercise sessions, they activate more areas of the brain and therefore maximize the neuroplastic benefits. These kinds of movement require a greater overall activation of muscle contraction and therefore probably require the firing of a greater number of cortical cells. Furthermore, the sophisticated movements of fingers are important to accomplish many complex tasks in daily life. Unfortunately, the patient who suffered contralateral hemiparesis after brain stroke lose the ability of moving their fingers which means they lose the ability of motor execution [15, 16]. Stroke is a kind of impaired cerebrovascular diseases. The number of patients who suffered from this disease in recent years was about 2 million per year, age standardized incidence is about 21/6250, and 70%~80% of stroke patients have different degrees of movement disorders. Based on the motion, performing physical therapy is helpful for the recovery of motor function in patients with cerebral apoplexy but requires patients to have a certain ability of independent movement. Most stroke patients have poor exercise ability in the early rehabilitation stage, during which exercise imagination therapy can play an important role [17, 18]. However, the ability of motor imagery might be a useful option for restoring and recovering the motor functions [19, 20]. Which kind of motor imagery strategy is more suitable according to the patients' condition, e.g., subject-dependent recovery protocol, and which kind of feature is more suitable to evaluate subject-dependent motor function can be evaluated and can be employed to build a neurofeedback system to improve the motor recovery protocol. Whether the brain connectivity can be used as an effective feature for motor function evaluation and motor recovery is found. The efficacy of motor imagery for neural prosthetics control and motor recovery after brain stroke is still very much an open question.

Beta-band activities play an important role in motor imagery. In previous research papers, researchers noticed that event-related desynchronization occurs during left hand, right hand, foot, and tongue motor imagery tasks [21–23]. They showed a significant usage of beta-band activities for motor recovery in stroke patients [17–24].

Brain function is increasingly understood to be a result of extensively interconnected neurons which means the brain connection reflects the brain function such as decision-making [25–27] and motor function recovery [28–31]. Asymmetry also exists in the perspective of functional connectivity [32]. It has been shown that right-handed subjects who completed the motor imagination tasks with the right hand had more effective connections between the auxiliary motor area and other brain regions than those who completed the motor imagination tasks with the left hand and so on. This lateralization of the cerebral cortex may be related to the asymmetry of the brain structure of right-handed subjects [33].

To investigate the brain connectivity during finger motor execution and motor imagery tasks, a new EEG experimental paradigm using thirty finger gestures was designed. Right-handed subjects only participated in the proposed experiment. First, they were instructed to watch a short video and mimic the finger movements by performing the movements. Second, they were asked to imagine the finger movements for sixty trials for each movement. However, we investigated beta-band activity of EEG signals which was recorded and extracted from both scenarios: motor execution and motor imagery. Also, the Granger causality (G-causality) analysis method was applied to calculate the brain network between contralateral primary motor area, premotor area, and primary sensory area. G-causality coefficients of motor execution and imagery under left-hand and right-hand conditions were computed and analyzed. G-causality is the most adopted criterion for causal inference in brain recordings knowing that the number of G-causality over many trials or observation epochs means how many times statistically significant brain connection was built and the coefficients of G-causality indicate the strength of the brain connections. Using these G-causality characteristics, we were able to investigate the efficacy of motor imagery of finger movements using noninvasive measurements and compare it with motor execution.

2. Method

2.1. Data Recording and Experimental Paradigm. For reducing signal interferences, EEG experiments were held in the electromagnetic shielding room (Figure 1) at Beijing Anding Hospital, Capital Medical University, China. This study was approved by the Ethics Committee of North China University of Science and Technology, Hebei Province, China (Number: 2019002). All participants provided written informed consent. Eleven healthy people (7 males and 4 females) were recruited to participate in this study. All of them are right-handed and have no experience in motor execution and/or motor imagery EEG-based BCI experiments. Chirality is determined by the Edinburgh handedness inventory (EHI). EHI produces scores ranging from −100 (strongly left handed) to 0 (unbiased handedness) and 100 (strongly right handed). The average score of handedness of the subjects is 90.84, and the standard deviation is 5.79. The average age of them is 25 years (the range is from 22 to 27).

The subjects were instructed to sit down on a comfortable chair in front of the computer screen which was about 50 cm away from their eyes. Before the experiment, a clear explanation of the framework of experimental paradigm was given to the subjects. The experimental paradigm was designed by using *E-prime* which is a software package

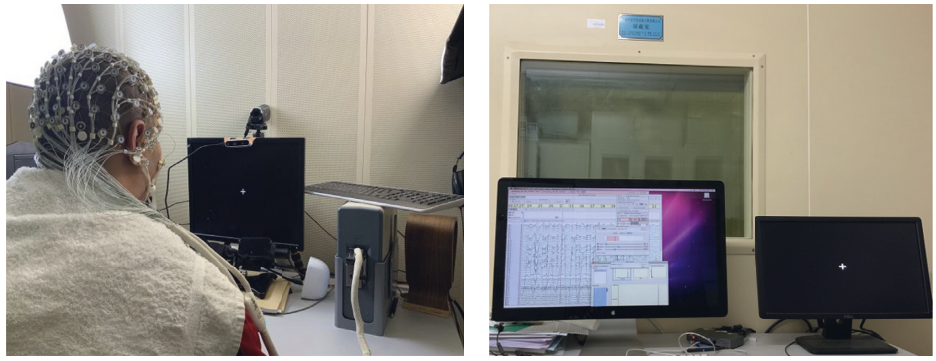

(a) (b)

Figure 1: Experiment setup of real-time recording of EEG signals during performing or imagining finger movements. We can see in this picture, two subfigures from left to right: the experimental electromagnetic shielding room and the data collection and analysis platform Net Station (i.e., real-time streaming, recording, and some preprocessing of multichannel EEG data) and experimental paradigm interface.

used to design and run simulation experiments, with a focus on psychological and cognitive science.

The 128 EEG channels were recorded during two scenarios: motor execution and motor imagery of finger movements by using EGI signal acquisition system (Brain products, Germany). The sampling rate was 1000 Hz, where oversampling produced no significant changes in timing and amplitude. As recording setting, EEG signals were band passed from 0.1 Hz to 50 Hz and saved with the Net Station system, as shown in Figure 1. We removed high frequency bands such as high and low gamma bands because it is hard to get them in a single trial using noninvasive measurements such as EEG.

In the beginning of each session, a clear guideline of the proposed experiment was shown in the screen to guide the subjects and make them more familiar with the experimental paradigm process. The subjects were able to understand fully the experimental paradigm and complete the whole instructions more attentively. The subjects could take few minutes' rest after each session.

For each trial, the finger gestures during execution and imagery phases were arranged within 15 s, containing three instructions or tips of 2 seconds for each task, gesture video of 3 s, finger motor execution of 3 s, and motor imagery of 3 s. Task tip 1 indicates that the video will start. One of thirty finger movements was shown randomly during the gesture video time. Task tips 2 and 3 indicated the subjects to perform or imagine the same finger movement at motor execution and motor imagery phases, respectively. Then, the subject can take a rest at a duration from 6 seconds to 8 seconds. Then, the next trial will be conducted (Figure 2).

2.2. Brain Region of Interest Selection. In this research, the difference between motor execution and motor imagery was investigated. The premotor area, primary motor area, and primary sensory area might be the most relevant brain areas during performing and imagining a finger movement. The position of 128 channels is shown in Figure 3. Due to the low spatial resolution of EEG signals, two electrodes E13 and E20 and E112 and E118 were averaged to calculate the brain activities of the left and right premotor area, respectively, according to location of the premotor area in previous EEG-TMS research [34]. The electrodes E36 correspond to the left motor areas. The electrodes E104 correspond to the primary right motor areas. The electrodes E52 correspond to the left primary sensory areas. The electrodes E92 correspond to the right primary sensory areas.

2.3. EEG Data Processing. The EEGLab toolbox [35] was used for the preprocessing phase of raw EEG data. In this phase, we have checked the quality of EEG signals by checking the signal-to-noise ratio. Then, the bad channels with obvious artifacts (e.g., clear muscles artifact or strong blink) were removed using EEGLab functions and were not included in results analysis. However, few trials only were not recorded correctly. In our proposed experiment, 60 trials of EEG signals for each subject were recorded for left and right finger movements during motor execution and motor imagery phases. The numbers of valid trials of each subject are shown in Table 1.

The 128 EEG signals were down sampled from 1 KHz to 500 Hz for reducing data size. Then, the baseline of EEG signals was reset called baseline drift [36]. There are several methods to remove baseline drift, such as the median filtering method [37], wavelet transform method [38], high-pass filtering method [39, 40], and curve fitting method [41]. In this paper, weighted least squares- (WLS-) [42] based local linear regression method is employed to fit the original data of each segment to zero. Figures 4 and 5 show EEG signals before and after removing baseline drift, respectively.

The ICA method was used to remove the artifact in EEG signals such as eye movements (EOG signal) per session. At first, EEG signals were decomposed by ICA, and the limited number of components was determined through the whitening stage of PCA. The ICA decomposed components in spatial distribution map of each EEG signal are shown in Figure 6, respectively. It was clear that the energy of the second component was mainly concentrated in the area around the eyes, which was consistent with the EOG signal area in the prefrontal cortex. Thus, artifact of the eye

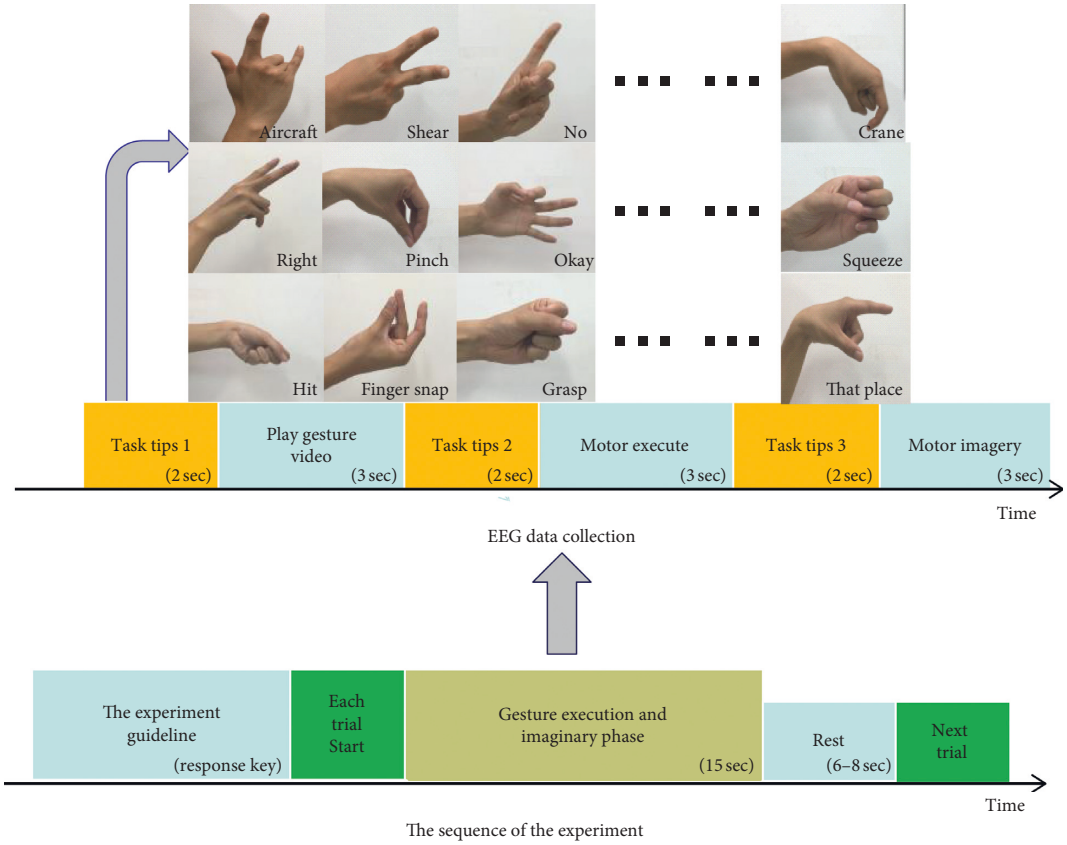

Figure 2: The experimental paradigm. The gesture execution and imaginary phase contains three task tips and three duration of playing gesture video (3 seconds), motor execution, and imagery (2 seconds), in which each of thirty finger movements were used. Thirty finger movements are okay, no, begun to refer, phase modulation, crane, right, scope, aircraft, geometry, crowded, scissors, cut, there, kneading, clap, planer, money, broom, fan, double, frost, question marks, grip, rain, circuitous, approximately equal to, blame, recruit, at noon, and catch.

movement can be removed from EEG signals by deleting the second component.

After removing the eye movements' artifacts, the beta-band activities (14–30 Hz) during −0.5 to 3 second periods of the motor execution and imagery onset were feature selected for Granger causality brain connectivity calculation.

2.4. Granger Causality Brain Connectivity Calculation. The Granger causality analysis model is based on the autoregressive model, which depends on the time priority of signals and can be used to measure the degree of mutual influence between signals. And it can be used to explore the temporal relationship between regions of interest in order to reveal the directional information flow between brain regions. The Granger causality analysis model was already used for computing the brain connection of decision-making and motor recovery [25–29], which showed that the Granger causality analysis is effective for analyzing the brain.

Given the two wide-sense stationary time series X and Y, which have constant means and variances. If the predictive effect of the variable X by using the past information of X and Y is better than the predictive effect using the past information of X significantly, then the variable X is the Granger cause by the variable Y [43]. The autoregressive model of X can be calculated by the following equation.

Constrained regression model:

$$X_t = \alpha_0 + \sum_{i=1}^{p} \alpha_i X_{t-i} + \varepsilon_x. \tag{1}$$

Unconstrained regression mode (u):

$$X_t = \alpha_0 + \sum_{i=1}^{p} \alpha_i X_{t-i} + \sum_{i=1}^{q} \beta_i Y_{t-i} + \varepsilon_y, \tag{2}$$

where α_0 represents the constant term; p and q are the maximum lag number of variables X and Y, respectively; and ε_x and ε_y denoted residuals of constrained and unconstrained regression models, respectively. The Bayesian information criterion (BIC), Akaike information criterion (AIC), and experiential method are usually used to calculate the lag number of the regression model. In the study, the max lag of X and Y was set to 20.

The sum of squared residuals of constrained regression models can be calculated by the following equation:

$$\mathrm{RSS}_r = (p+1)\varepsilon_x^2. \tag{3}$$

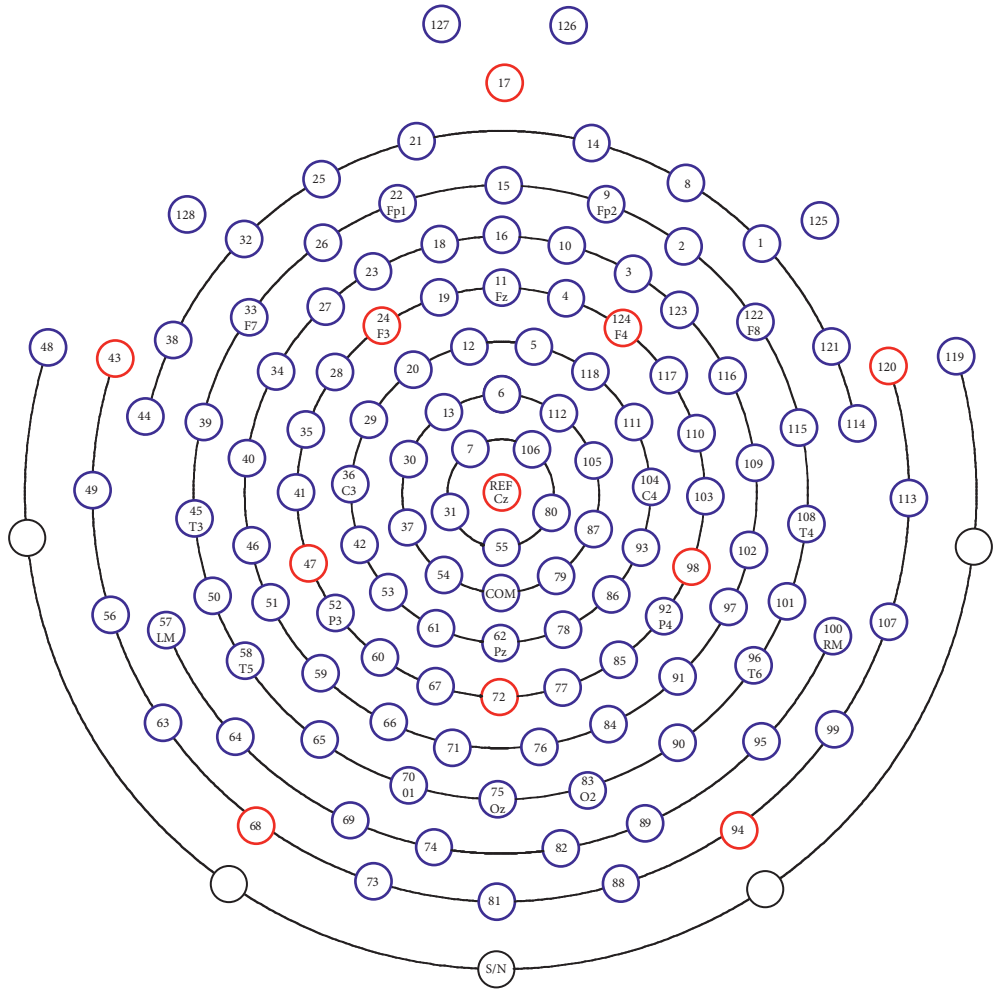

Figure 3: The EEG electrode position of 128 channels. Using the EGI signal acquisition system Net Station (Brain product, Germany), 128 EEG channels were recorded.

Table 1: Number of valid trials.

	Left finger execution	Left finger imagery	Right finger execution	Right finger imagery
Subject 1	55	53	58	56
Subject 2	54	50	52	54
Subject 3	56	56	49	53
Subject 4	50	48	54	54
Subject 5	56	58	52	54
Subject 6	46	52	54	50
Subject 7	54	54	56	56
Subject 8	58	58	56	58
Subject 9	53	54	57	55
Subject 10	53	54	53	57
Subject 11	30	44	58	55

The sum of squared residuals of unconstrained regression models can be calculated by the following equation:

$$\mathrm{RSS}_{ur} = (p+1)\varepsilon_y^2. \tag{4}$$

Then, the F test was applied to confirm the statistics significant of the residuals:

$$F = \frac{(\mathrm{RSS}_r - \mathrm{RSS}_{ur})/p}{\mathrm{RSS}_{ur}/(T-p-q-1)}, \tag{5}$$

where T is the number of sample size which used to estimate X. p and q are the maximum lag number in the regression model. If the signification is confirmed, variable Y Granger causes variable X.

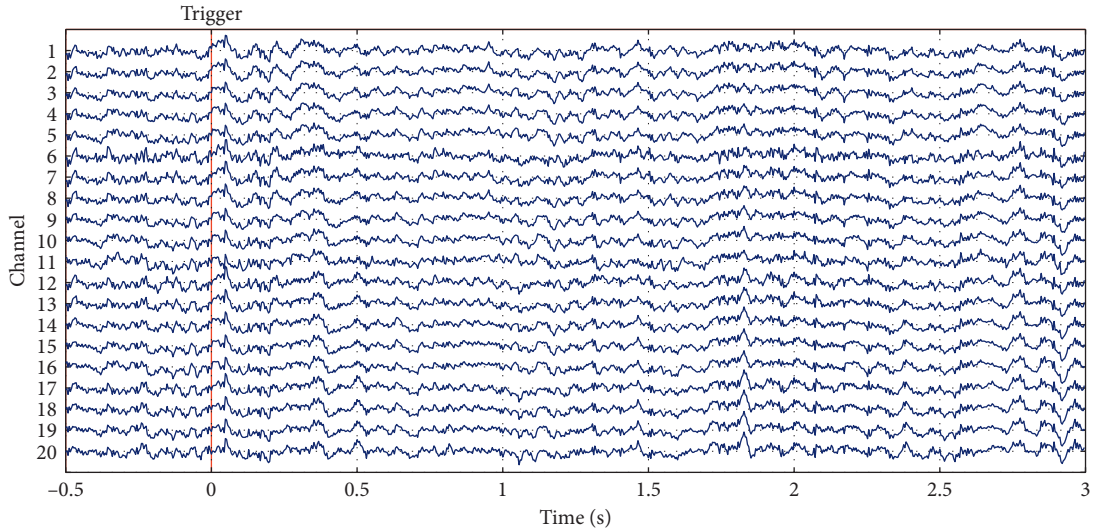

Figure 4: Representative EEG signals before baseline drift. There is a total of 128 channels of data. The figure shows the EEG waveform of 1–20 channels.

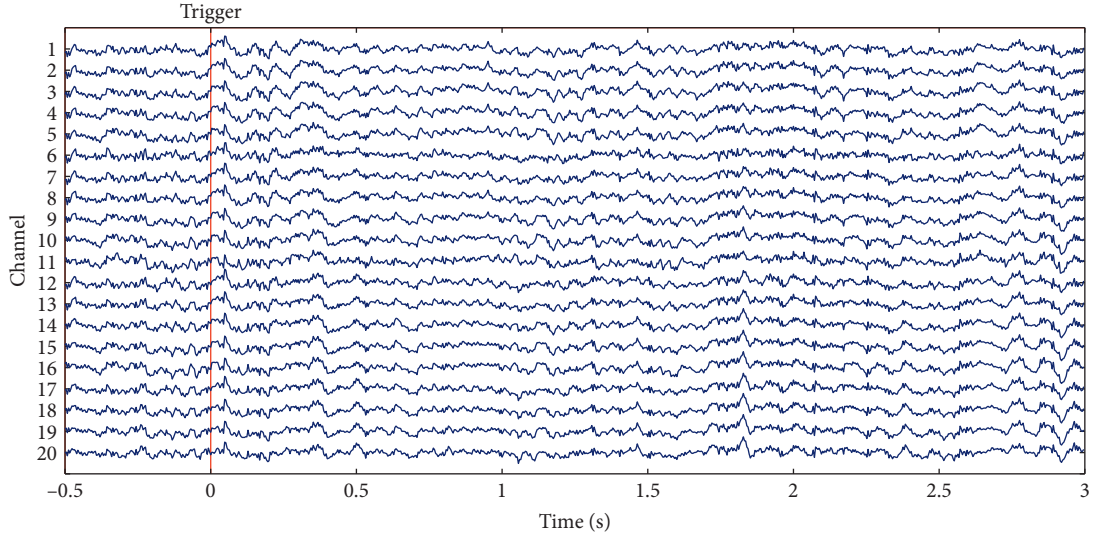

Figure 5: EEG signals after baseline drift. There is a total of 128 channels of data. The figure shows the EEG waveform of 1–20 channels.

According to the definition of Granger, the causality coefficient of Y on X can be calculated as

$$F_{Y\longrightarrow X} = \ln \frac{\operatorname{var}(\varepsilon_x)}{\operatorname{var}(\varepsilon_y)}. \tag{6}$$

Noted that there exists two kinds of Granger causality interrelations $F_{X\longrightarrow Y}$ and $F_{Y\longrightarrow X}$, but $F_{Y\longrightarrow X} \neq \pm F_{X\longrightarrow Y}$.

In this study, EEG signals which were recorded from contralateral premotor, primary motor, and primary sensory area in motor execution and imagery experiment were set as X and Y, and Granger causality relation was calculated trial by trial.

For example, EEG signal in the premotor area was set as Y, and EEG signal in the motor area was set as X. If $F_{Y\longrightarrow X}$, we noted this relationship as Granger causality from the premotor to motor area.

There are six Granger causality relations between contralateral different brain areas: from premotor to motor, from premotor to sensory, from motor to sensory, from motor to premotor, from sensory to premotor, and from sensory to motor. Because some trials do not have any static significant relation, the number of Granger causality trials was computed. Then, the Granger causality coefficient of significant Granger causality trials was calculated.

3. Result

The G-causality result of one trial from premotor to motor is shown in Figure 7. In Figure 7(a), the beta-band activities of premotor and motor EEG signals are shown. In Figure 7(b), the original motor EEG and predicted signal only from motor EEG and predicted signal from premotor EEG and

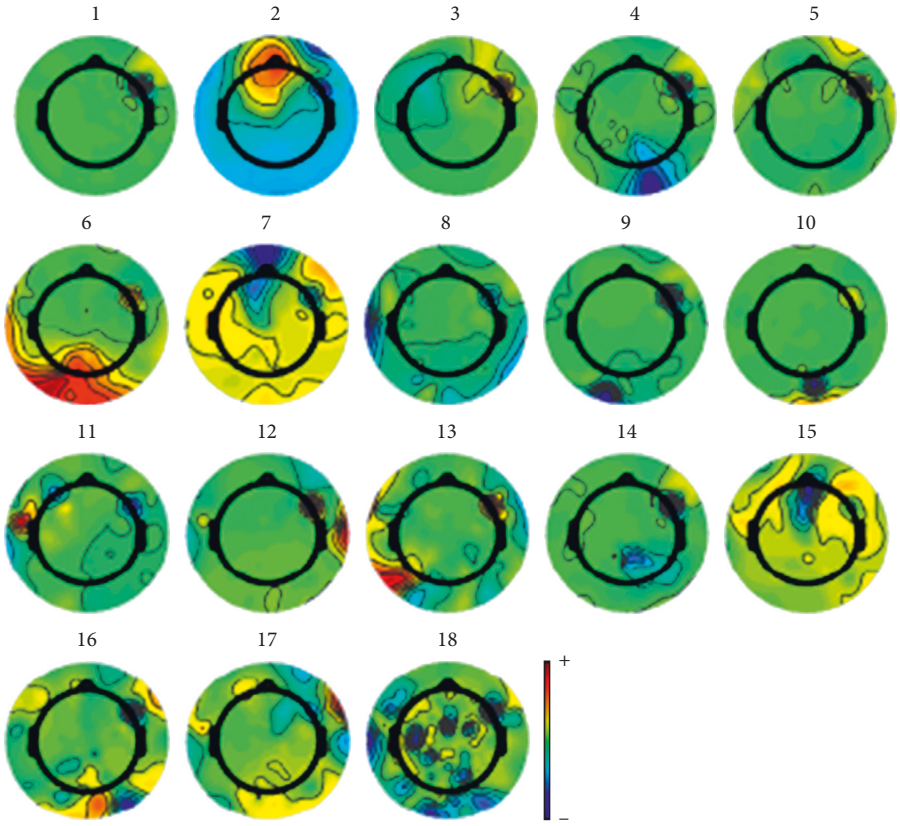

Figure 6: Spatial distribution map of ICA decomposition components. After ICA processing, 18 independent components are obtained, which can be seen as eye electrical components from the second component.

motor EEG are shown, respectively. From Figure 7(c), the predicted error reduced by using premotor EEG and motor EEG. Thus, significant Granger causality exists in this trial.

The number of trials which has Granger causality relation during left finger execution, left finger imagery, right finger execution, and right finger imagery experiment is shown in Tables 2–5, respectively. The bold number showed the highest number of Granger causality trial between the premotor to motor area. The number of trials from right premotor to motor area was 37 ± 7.3 (mean $\pm$ standard deviation), from premotor to sensory area was 29.7 ± 11.3, from motor to sensory area was 27.8 ± 10.6, from motor to premotor area was 23.5 ± 7.9, from sensory to premotor area was 23.4 ± 7.5, and from sensory to motor area was 28.5 ± 12.9 during left finger execution.

A two-way ANOVA is then applied to analyze the number of Granger causality trials between different brain areas. The number of Granger causality from right premotor to right motor area is significantly higher than from right motor to right premotor and from right sensory to right premotor area ($F_{10,5} = 4.51$, $p = 1.8 \times 10^{-3}$), and no other significant differences are observed between the number of Granger causality trials between brain areas during the left finger execution phase.

The number of Granger causality from the right premotor to right motor area is significantly higher than that from the right sensory to right premotor area ($F_{10,5} = 2.41$, $p = 4.92 \times 10^{-2}$), and no other significant differences are observed between the number of Granger causality between brain areas during the left finger imagery phase.

No significant differences are observed between the number of Granger causality between the whole brain areas ($F_{10,5} = 1.99$, $p = 9.67 \times 10^{-2}$) during the right finger execution phase.

The number of valid Granger causality trials from left premotor to left motor area, left motor to left sensory area, and left premotor to left sensory are significantly higher than that from right sensory to right premotor area ($F_{10,5} = 11.03$, $p = 3.44 \times 10^{-7}$), from left motor to left motor area is significantly higher than left motor to left premotor area, and no other significant differences are observed between the number of Granger causality between brain areas during the right finger imagery phase.

The Granger causality coefficient of the Granger causality trial during left finger execution, left finger imagery, right finger execution, and right finger imagery experiment is shown in Tables 6–9, respectively. The bold number showed the lowest Granger causality coefficient between the premotor to motor area. The number of trials from right premotor to motor area was 9.1 ± 3.2, from premotor to sensory area was 13.9 ± 0.6, from motor to sensory area was 13.8 ± 0.7, from motor to premotor area was 14.1 ± 0.5, from sensory to premotor area was 13.6 ± 0.7, and from sensory to motor area was 13.2 ± 0.8 during left finger execution.

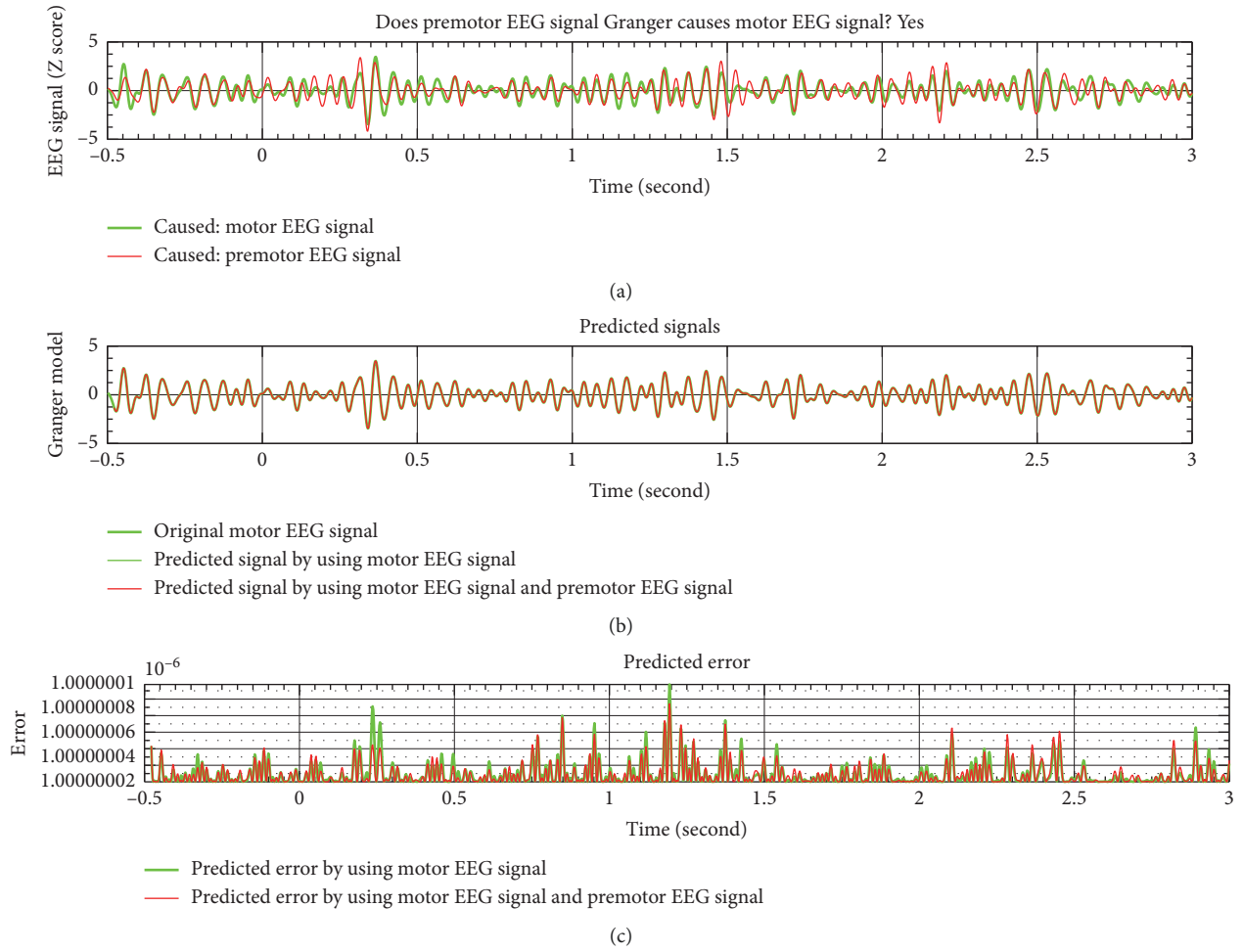

Figure 7: Granger causality result of one finger movement trial.

Table 2: The number of Granger causality trials in left finger execution.

From	To		
	PMA right	MA right	SA right
PMA right	NAN	**37 ± 7.3**	29.7 ± 11.3
MA right	23.5 ± 7.9	NAN	27.8 ± 10.6
SA right	23.4 ± 7.5	28.5 ± 12.9	NAN

A two-way ANOVA is then applied to analyze the Granger causality coefficient between different brain areas. The Granger causality coefficient from right premotor to right motor area is significantly lower than other brain areas ($F_{10,5} = 23.09$, $p = 6.16 \times 10^{-12}$), and no other significant Granger causality coefficient differences are observed between brain areas during the left finger execution phase.

The Granger causality coefficient from right premotor to right motor area is significantly lower than other brain areas ($F_{10,5} = 6.03$, $p = 1.93 \times 10^{-4}$), and no other significant Granger causality coefficient differences are observed between brain areas during the left finger imagery phase.

No other significant Granger causality coefficient differences are observed between brain areas ($F_{10,5} = 0.89$, $p = 0.49$) during the right finger execution phase.

No other significant Granger causality coefficient differences are observed between brain areas ($F_{10,5} = 0.39$, $p = 0.85$) during the right finger imagery phase.

4. Discussion

The brain areas involved in motor execution and motor imagery were investigated by using fMRI [44–46] and PET [44]. Stephan et al. suggested that imaginative motion activated medial and lateral premotor areas, anterior cingulate areas, and ventral motor anterior areas. The motor execution associated with imaginative movement leads to additional activity in the left primary sensory cortex and premotor area, the premotor cingulate area, and the rostral portion of the left superior parietal cortex [44]. Porro et al. also supports the hypothesis that motor imagery and motor execution are involved in overlapping neural networks in peripheral cortical regions [45]. Ehrsson et al. demonstrated that voluntary motion images of fingers, toes, and tongue activated specific motion representations of corresponding body parts especially in the lateral primary motor cortex [46]. These researches showed that the motor execution and motor imagery of finger movement shared some common brain areas and can be distinguished in premotor areas.

Table 3: The number of Granger causality trials in left finger imagery.

From	To		
	PMA right	MA right	SA right
PMA right	NAN	**35.5 ± 8.8**	29.3 ± 8.8
MA right	27.1 ± 9.2	NAN	28.3 ± 10.7
SA right	25.5 ± 7.4	31.4 ± 12.4	NAN

Table 4: The number of Granger causality trials in right finger execution.

From	To		
	PMA left	MA left	SA left
PMA left	NAN	**36.3 ± 10.3**	34.5 ± 8.2
MA left	24.5 ± 10.9	NAN	30.5 ± 9.3
SA left	25.6 ± 9.6	31.8 ± 9.4	NAN

Table 5: The number of Granger causality trials in right finger imagery.

From	To		
	PMA left	MA left	SA left
PMA left	NAN	**39.2 ± 9.0**	36.1 ± 7.7
MA left	24.2 ± 5.7	NAN	33.1 ± 9.1
SA left	22.3 ± 5.6	31.4 ± 7.4	NAN

Table 6: Granger causality coefficient of left finger execution.

From	To		
	PMA right	MA right	SA right
PMA right	NAN	**9.1 ± 3.2**	13.9 ± 0.6
MA right	14.1 ± 0.5	NAN	13.8 ± 0.7
SA right	13.6 ± 0.7	13.2 ± 0.8	NAN

Table 7: Granger causality coefficient of left finger imagery.

From	To		
	PMA right	MA right	SA right
PMA right	NAN	**10.9 ± 3.7**	14.0 ± 0.6
MA right	14.0 ± 0.4	NAN	13.9 ± 0.7
SA right	13.5 ± 0.9	13.3 ± 0.5	NAN

Table 8: Granger causality coefficient of right finger execution.

From	To		
	PMA left	MA left	SA left
PMA left	NAN	**13.2 ± 0.6**	13.4 ± 0.9
MA left	13.6 ± 0.7	NAN	13.6 ± 1.1
SA left	13.7 ± 0.9	13.7 ± 0.6	NAN

Motor imagery may serve as a potential motor training to the rehabilitation of motor control [47] for the patients who suffered from severe upper limb contralateral hemiparesis after brain stroke [48, 49].

Table 9: Granger causality coefficient of right finger imagery.

From	To		
	PMA left	MA left	SA left
PMA left	NAN	**13.4 ± 0.6**	13.4 ± 0.8
MA left	13.7 ± 0.8	NAN	13.6 ± 1.0
SA left	13.6 ± 0.8	13.5 ± 0.6	NAN

In this paper, we investigated the neural mechanism of thirty finger movements in two scenarios: motor execution and motor imagery using the G-causality analysis model. Eleven subjects joined the experiment and performed and imagined left and right finger gestures. EEG signals were recorded simultaneously during motor execution and movement imagery tasks. Beta-band activities of primary motor area, premotor area, and primary sensory area were the most relevant selected feature and then analyzed. We aimed to investigate whether the Granger causality relation can be used for motor function evaluation and motor recovery.

Previous magnetoencephalography studies observed clear movement-related power decreases in the alpha (8–13 Hz) and beta (13–30 Hz) band to 0.5 s during bilateral hand movements in both scenarios: motor execution and motor imagery. In addition, a clear postmovement beta rebound between 0.5 and 1 s was observed when someone moves his/her bilateral hands [50]. Thus, the beta-band EEG signals from −0.5 to 3 seconds of the motor execution and imagery onset were feature selected and analyzed.

We mainly investigated the number of Granger causality trials and Granger causality coefficient between different brain areas during finger motor execution and imagery experiment. The highest number of Granger causality trials 37 ± 7.3, 35.5 ± 8.8, 36.3 ± 10.3, and 39.2 ± 9.0 was achieved from premotor to motor area during left motor execution and imagery and right finger motor execution and imagery, respectively, as shown in Tables 2–5.

These results suggested the most important connection in motor function was from premotor to motor area, which is consistent with previous research on the neuronal population activity model [51]. It suggested Granger causality results were related to motor function and might be used as an efficient feature for motor function evaluation.

Hammer et al. showed the neurons in premotor and motor area activities in the neuronal population level according to the balance of excitatory and inhibitory synaptic input. In addition, significant difference of the Granger causality trial number was observed during left finger execution and imagery and right finger imagery, but not observed during the right finger execution phase.

Meanwhile, the lowest Granger causality coefficients 9.1 ± 3.2, 10.9 ± 3.7, 13.2 ± 0.6, and 13.4 ± 0.6 were achieved from premotor to motor area during left motor execution and imagery and right finger motor execution and imagery, respectively, as shown in Tables 6–9. Significant difference of the Granger causality coefficient was observed during left finger execution and imagery, but not observed during right finger execution and imagery phase.

Several researches showed the significant difference in the brain cortex between left-handed and right-handed subjects. Male right handers showed a significant deeper central sulcus on the left hemisphere than on the right in previous research study [52]. The asymmetry of central sulcus depth is significantly different between left-handed and right-handed individuals in the contralateral hemisphere [53]. In addition, when right-handed subjects performed motor tasks with their right hand, the activation intensity of the cortex in the left hemisphere of the brain was higher than that in the right hemisphere [54–56].

The results in this study also suggested the significant differences between left and right finger motor Granger connection and coefficient may be caused by the reason that all of participants in this study were right-handed. These results also suggested that different MI-based brain motor function recovery strategy should be taken for right-hand subjects and left-hand patients to build an efficient motor recovery protocol after brain stroke. The left-hand subjects should be enrolled to confirm the results in the future. In the future study, we would like to measure the Granger causality in the contralateral motor, motor, and sensorimotor areas of the right and left hemispheres of patients with stroke and then calculate the Granger causality intensity between the brain areas. The efficacy of the motor imagery paradigm might be obtained by the Granger causality model comparing heal people with patients.

There are some limitations in this research. Only beta-band activity of EEG signals was calculated to build the brain network. Compared with ECoG signals, the gamma activity in EEG signals was not so clear and high quality [1, 57]. The alpha band and gamma band were not included although beta-band activity was known to reflect motor function well. Although these areas including the main parts of motor functions are still not enough for free voluntary movement [58, 59], the brain network in present work only focus on left and right sides of the primary motor area, premotor area, and primary sensory area, in totally six points. More areas should be considered, and the brain connectivity should be more investigated in the future work.

Data Availability

The datasets generated and analyzed during the current study are not publicly available due to the policy of Tianjin University of Technology, Capital Medical University, and North China University of Science and Technology, but are available from the corresponding author on reasonable request.

Conflicts of Interest

The authors declare that there are no conflicts of interest regarding the publication of this paper.

Authors' Contributions

D. Ming and C. Wang designed the research, supervised the project, and revised the article. J. Zhang, S. Zhang, A. N. Belkacem, and C. Chen performed the research, analyzed data, and drafted the article. R. Xu, B. Hao, Q. Gao, and D. shin collected and interpreted the data. A. N. Belkacem, L. Lu, and C. Chen interpreted data and revised the draft. All authors reviewed the paper and approved for submitting.

Acknowledgments

This work was financially supported by the National Key R&D Program of China (2018YFC1314500), National Natural Science Foundation of China (61806146 and 61971118), Natural Science Foundation of Tianjin City (15JCZDJC32800 and 18JCYBJC95400), Belt and Road International Scientific and Technological Cooperation Demonstration Project (17PTYPHZ20060), and Young and Middle-Aged Innovation Talents Cultivation Plan of Higher Institutions in Tianjin.

References

[1] R. Zhang, D. Yao, P. A. Valdés-Sosa et al., "Efficient resting-state EEG network facilitates motor imagery performance," *Journal of Neural Engineering*, vol. 12, no. 6, Article ID 066024, 2015.

[2] T. Yan, W. Wang, L. Yang, K. Chen, R. Chen, and Y. Han, "Rich club disturbances of the human connectome from subjective cognitive decline to Alzheimer's disease," *Theranostics*, vol. 8, no. 12, pp. 3237–3255, 2018.

[3] B. Wittevrongel and M. M. Van Hulle, "Faster P300 classifier training using spatiotemporal beamforming," *International Journal of Neural Systems*, vol. 26, no. 3, Article ID 1650014, 2016.

[4] F. Li, B. Chen, H. Li et al., "The time-varying networks in P300: a task-evoked EEG study," *IEEE Transactions on Neural Systems and Rehabilitation Engineering*, vol. 24, no. 7, pp. 725–733, 2016.

[5] M. Xu, X. Xiao, Y. Wang, H. Qi, and D. Ming, "A brain-computer interface based on miniature-event-related potentials induced by very small lateral visual stimuli," *IEEE Transactions on Biomedical Engineering*, vol. 65, no. 5, pp. 1166–1175, 2018.

[6] Y. R. Tabar and U. Halici, "A novel deep learning approach for classification of EEG motor imagery signals," *Journal of Neural Engineering*, vol. 14, no. 1, Article ID 016003, 2017.

[7] E. Dong, C. Li, L. Li, S. Du, A. N. Belkacem, and C. Chen, "Classification of multi-class motor imagery with a novel hierarchical SVM algorithm for brain-computer interfaces," *Medical & Biological Engineering & Computing*, vol. 55, no. 10, pp. 1809–1818, 2017.

[8] R. Bauer, M. Fels, M. Vukelić, U. Ziemann, and A. Gharabaghi, "Bridging the gap between motor imagery and motor execution with a brain-robot interface," *NeuroImage*, vol. 108, pp. 319–327, 2015.

[9] M. Li, Y. Liu, Y. Wu, S. Liu, J. Jia, and L. Zhang, "Neurophysiological substrates of stroke patients with motor imagery-based brain-computer interface training," *International Journal of Neuroscience*, vol. 124, no. 6, pp. 403–415, 2014.

[10] K. K. Ang, K. S. G. Chua, K. S. Phua et al., "A randomized controlled trial of EEG-based motor imagery brain-computer interface robotic rehabilitation for stroke," *Clinical EEG and Neuroscience*, vol. 46, no. 4, pp. 310–320, 2015.

[11] S. de Vries and T. Mulder, "Motor imagery and stroke rehabilitation: a critical discussion," *Journal of Rehabilitation Medicine*, vol. 39, no. 1, pp. 5–13, 2007.

[12] S. Bajaj, A. J. Butler, D. Drake, and M. Dhamala, "Brain effective connectivity during motor-imagery and execution following stroke and rehabilitation," *NeuroImage: Clinical*, vol. 8, pp. 572–582, 2015.

[13] S. Boe, A. Gionfriddo, S. Kraeutner, A. Tremblay, G. Little, and T. Bardouille, "Laterality of brain activity during motor imagery is modulated by the provision of source level neurofeedback," *NeuroImage*, vol. 101, pp. 159–167, 2014.

[14] A. J. Szameitat, S. Shen, A. Conforto, and A. Sterr, "Cortical activation during executed, imagined, observed, and passive wrist movements in healthy volunteers and stroke patients," *NeuroImage*, vol. 62, no. 1, pp. 266–280, 2012.

[15] H. Alkadhi, P. Brugger, S. H. Boendermaker et al., "What disconnection tells about motor imagery: evidence from paraplegic patients," *Cerebral Cortex*, vol. 15, no. 2, pp. 131–140, 2005.

[16] A. R. Anwar, M. Muthalib, S. Perrey et al., "Effective connectivity of cortical sensorimotor networks during finger movement tasks: a simultaneous fNIRS, fMRI, EEG study," *Brain Topography*, vol. 29, no. 5, pp. 645–660, 2016.

[17] L. He, D. Hu, M. Wan, Y. Wen, and M. C. Zhou, "Common Bayesian network for classification of EEG-based multiclass motor imagery BCI," *IEEE Transactions on Systems, Man, and Cybernetics: Systems*, vol. 46, no. 6, pp. 843–854, 2016.

[18] M. Arvaneh, C. Guan, K. K. Ang et al., "Facilitating motor imagery-based brain-computer interface for stroke patients using passive movement," *Neural Computing and Applications*, vol. 28, no. 11, pp. 3259–3272, 2016.

[19] D. V. Sjoerd, T. Marga, O. Bert, and M. Theo, "Recovery of motor imagery ability in stroke patients," *Rehabilitation Research and Practice*, vol. 2011, Article ID 283840, 9 pages, 2011.

[20] V. Kaiser, A. Kreilinger, G. R. Müller-Putz, and C. Neuper, "First steps toward a motor imagery based stroke BCI: new strategy to set up a classifier," *Frontiers in Neuroscience*, vol. 5, 2011.

[21] W. Deng, M. Duoqian, and B. Gunnar, "Multi-class motor imagery EEG decoding for brain-computer interfaces," *Frontiers in Neuroscience*, vol. 6, 2012.

[22] G. Pfurtscheller, "Event-related synchronization (ERS): an electrophysiological correlate of cortical areas at rest," *Electroencephalography and Clinical Neurophysiology*, vol. 83, no. 1, pp. 62–69, 1992.

[23] W. J. Tan, Y. Kang, Z. W. Dong et al., "An Approach to Extraction Midsagittal Plane of Skull From Brain CT Images for Oral and Maxillofacial Surgery," *IEEE Access*, vol. 7, pp. 118203–118217, 2019.

[24] E. R. Buch, A. Modir Shanechi, A. D. Fourkas, C. Weber, N. Birbaumer, and L. G. Cohen, "Parietofrontal integrity determines neural modulation associated with grasping imagery after stroke," *Brain*, vol. 135, no. 2, pp. 596–614, 2012.

[25] Y. Si, X. Wu, F. Li et al., "Different decision-making responses occupy different brain networks for information processing: a study based on EEG and TMS," *Cerebral Cortex*, vol. 29, no. 10, pp. 4119–4129, 2018.

[26] U. Basten, G. Biele, H. R. Heekeren, and C. J. Fiebach, "How the brain integrates costs and benefits during decision making," *Proceedings of the National Academy of Sciences*, vol. 107, no. 50, pp. 21767–21772, 2010.

[27] M. J. Mulder, W. Boekel, R. Ratcliff, and B. U. Forstmann, "Cortico-subthalamic connection predicts individual differences in value-driven choice bias," *Brain Structure and Function*, vol. 219, no. 4, pp. 1239–1249, 2014.

[28] Z. C. Chao, M. Sawada, T. Isa, and Y. Nishimura, "Dynamic reorganization of motor networks during recovery from partial spinal cord injury in monkeys," *Cerebral Cortex*, vol. 29, no. 7, pp. 3059–3073, 2019.

[29] S. R. M. Almeida, J. Vicentini, L. Bonilha, B. M. De Campos, R. F. Casseb, and L. L. Min, "Brain connectivity and functional recovery in patients with ischemic stroke," *Journal of Neuroimaging*, vol. 27, no. 1, pp. 65–70, 2017.

[30] K. P. Westlake and S. S. Nagarajan, "Functional connectivity in relation to motor performance and recovery after stroke," *Frontiers in Systems Neuroscience*, vol. 5, 2011.

[31] Q. Gao, X. Duan, and H. Chen, "Evaluation of effective connectivity of motor areas during motor imagery and execution using conditional granger causality," *NeuroImage*, vol. 54, no. 2, pp. 1280–1288, 2011.

[32] K. Cohen Kadosh, Q. Luo, C. De Burca et al., "Using real-time fMRI to influence effective connectivity in the developing emotion regulation network," *NeuroImage*, vol. 125, no. 6, pp. 616–626, 2016.

[33] Z. Tamás Kincses, H. Johansen-Berg, V. Tomassini, R. Bosnell, P. M. Matthews, and C. F. Beckmann, "Model-free characterization of brain functional networks for motor sequence learning using fMRI," *NeuroImage*, vol. 39, no. 4, pp. 1950–1958, 2008.

[34] Z. Marco, P. P. Battaglini, J. Joanna, P. Gilberto, and B. Pierpaolo, "Long-range neural activity evoked by premotor cortex stimulation: a TMS/EEG co-registration study," *Frontiers in Human Neuroscience*, vol. 7, 2013.

[35] A. Delorme, T. Mullen, C. Kothe et al., "EEGLAB, SIFT, NFT, BCILAB, and ERICA: new tools for advanced EEG processing," *Computational Intelligence and Neuroscience*, vol. 2011, Article ID 130714, 12 pages, 2011.

[36] P.-C. Lo and J.-S. Leu, "Adaptive baseline correction of meditation EEG," *American Journal of Electroneurodiagnostic Technology*, vol. 41, no. 2, pp. 142–155, 2001.

[37] J. Echauz, D. A. Padovani, R. Esteller, B. Litt, and G. Vachtsevanos, "Median-based filtering methods for EEG seizure detection," in *Proceedings of the First Joint BMES/EMBS Conference. 1999 IEEE Engineering in Medicine and Biology 21st Annual Conference and the 1999 Annual Fall Meeting of the Biomedical Engineering Society (Cat. No.99CH37015)*, IEEE, Piscataway, NJ, USA, October 1999.

[38] Y. Fei-Long and L. Zhi-Zeng, "The EEG de-noising research based on wavelet and Hilbert transform method. Computer science and electronics engineering (ICCSEE)," in *Proceedings of the 2012 International Conference on Computer Science and Electronics Engineering (ICCSEE)*, Hangzhou, China, March 2012.

[39] B. Maess, E. Schröger, and A. Widmann, "High-pass filters and baseline correction in M/EEG analysis. Commentary on: "how inappropriate high-pass filters can produce artefacts and incorrect conclusions in ERP studies of language and cognition"," *Journal of Neuroscience Methods*, vol. 266, pp. 164-165, 2016.

[40] B. Maess, E. Schröger, and A. Widmann, "High-pass filters and baseline correction in M/EEG analysis-continued discussion," *Journal of Neuroscience Methods*, vol. 266, pp. 171-172, 2016.

[41] J. Wu, D. Yang, and L. Shen, "Research on the curve-fitting method based on curvature data," *Journal of Applied Sciences*, vol. 21, no. 3, pp. 258–262, 2003.

[42] S. M. Haas, M. G. Frei, I. Osorio, B. Pasik-Duncan, and J. Radel, "EEG ocular artifact removal through ARMAX model system identification using extended least squares," *Communications in Information and Systems*, vol. 3, no. 1, pp. 19–40, 2003.

[43] A. K. Seth, "A MATLAB toolbox for granger causal connectivity analysis," *Journal of Neuroscience Methods*, vol. 186, no. 2, pp. 262–273, 2010.

[44] K. M. Stephan, G. R. Fink, R. E. Passingham et al., "Functional anatomy of the mental representation of upper extremity movements in healthy subjects," *Journal of Neurophysiology*, vol. 73, no. 1, pp. 373–386, 1995.

[45] C. A. Porro, M. P. Francescato, V. Cettolo et al., "Primary motor and sensory cortex activation during motor performance and motor imagery: a functional magnetic resonance imaging study," *The Journal of Neuroscience*, vol. 16, no. 23, pp. 7688–7698, 1996.

[46] H. H. Ehrsson, S. Geyer, and E. Naito, "Imagery of voluntary movement of fingers, toes, and tongue activates corresponding body-part-specific motor representations," *Journal of Neurophysiology*, vol. 90, no. 5, pp. 3304–3316, 2003.

[47] N. Sharma, V. M. Pomeroy, and J.-C. Baron, "Motor imagery," *Stroke*, vol. 37, no. 7, pp. 1941–1952, 2006.

[48] M. Ietswaart, M. Johnston, H. C. Dijkerman et al., "Mental practice with motor imagery in stroke recovery: randomized controlled trial of efficacy," *Brain*, vol. 134, no. 5, pp. 1373–1386, 2011.

[49] P. Langhorne, F. Coupar, and A. Pollock, "Motor recovery after stroke: a systematic review," *The Lancet Neurology*, vol. 8, no. 8, pp. 741–754, 2009.

[50] A. N. Belkacem, S. Nishio, T. Sazuki, H. Ishiguro, and M. Hirata, "Neuromagnetic decoding of simultaneous bilateral hand movements for multidimensional brain-machine interfaces," *IEEE Transactions on Neural Systems and Rehabilitation Engineering*, vol. 26, no. 6, pp. 1301–1310, 2018.

[51] J. Hammer, T. Pistohl, J. Fischer et al., "Predominance of movement speed over direction in neuronal population signals of motor cortex: intracranial EEG data and a simple explanatory model," *Cerebral Cortex*, vol. 26, no. 6, pp. 2863–2881, 2016.

[52] K. Amunts, L. Jäncke, H. Mohlberg, H. Steinmetz, and K. Zilles, "Interhemispheric asymmetry of the human motor cortex related to handedness and gender," *Neuropsychologia*, vol. 38, no. 3, pp. 304–312, 2000.

[53] K. A. Phillips and C. C. Sherwood, "Primary motor cortex asymmetry is correlated with handedness in capuchin monkeys (cebus apella)," *Behavioral Neuroscience*, vol. 119, no. 6, pp. 1701–1704, 2005.

[54] C. Malagelada, F. De Iorio, F. Azpiroz et al., "New insight into intestinal motor function via noninvasive endoluminal image analysis," *Gastroenterology*, vol. 135, no. 4, pp. 1155–1162, 2008.

[55] M. Gurney, H. Pu, A. Chiu et al., "Motor neuron degeneration in mice that express a human Cu, Zn superoxide dismutase mutation," *Science*, vol. 264, no. 5166, pp. 1772–1775, 1994.

[56] Y. Tianyi, D. Xiaonan, M. Nan et al., "Positive classification advantage: tracing the time course based on brain oscillation," *Frontiers in Human Neuroscience*, vol. 11, p. 659, 2018.

[57] Y. Nakanishi, T. Yanagisawa, D. Shin et al., "Decoding fingertip trajectory from electrocorticographic signals in humans," *Neuroscience Research*, vol. 85, pp. 20–27, 2014.

[58] D. P. Hanes and J. D. Schall, "Neural control of voluntary movement initiation," *Science*, vol. 274, no. 5286, pp. 427–430, 1996.

[59] C. J. Hasson, "Neural representation of muscle dynamics in voluntary movement control," *Experimental Brain Research*, vol. 232, no. 7, pp. 2105–2119, 2014.